SAPIENZA
UNIVERSITÀ DI ROMA

$B \to J/\psi\, X \to \mu^+\mu^- X$ Production Cross-Section and Lifetime Determination with the ATLAS Detector at LHC

Scuola di dottorato in fisica

Dottorato di Ricerca in Fisica – XXIV Ciclo

Candidate

Camilla Maiani

ID number 699084

Thesis Advisors

Prof. Carlo Dionisi

Prof. Stefano Giagu

Dr. Marco Rescigno

A thesis submitted in partial fulfillment of the requirements for the degree of Doctor of Philosophy in Physics

December 2011

CERN-THESIS-2012-131
14/02/2012

Thesis defended on 14 February 2012
in front of a Board of Examiners composed by:

Prof. Antonello Polosa (chairman)

Prof. Mauro Dell'Orso

Prof. Giovanni Ridolfi

Camilla Maiani. $B \to J/\psi\, X \to \mu^+\mu^- X$ *Production Cross-Section and Lifetime Determination with the ATLAS Detector at LHC.*
Ph.D. thesis. Sapienza – University of Rome
© 2011

VERSION: 12 December 2011

EMAIL: camilla.maiani@roma1.infn.it

Abstract

Contents

Introduction

The *Large Hadron Collider* (LHC) at CERN has provided proton–proton (pp) collisions at 7 TeV centre-of-mass energy since March 2010, and the first lead-lead collisions at 2.76 TeV centre-of-mass energy per nucleon in December 2010. A very fast progression in the performances of the machine allowed the four main LHC experiments, ATLAS, CMS, ALICE and LHCb, to perform a complete commissioning of the detectors and providing competitive physics results within the first year of LHC run. The LHC reached in 2010 a peak instantaneous luminosity, in pp collisions, of $2 \times 10^{32}\,\mathrm{cm}^{-2}\mathrm{s}^{-1}$, and a total integrated luminosity of 41 pb^{-1} has been recorded at ATLAS. ATLAS is a multi-purpose experiment located in one of the four interaction points of the LHC beams. It has been designed to perform a broad programme of high energy physics studies, from Standard Model precision measurements to new physics searches, using both pp and $PbPb$ collisions. Also, the detector, trigger and reconstruction are optimized to keep high level performances in the very wide kinematic range spanned by the LHC data.

For my master thesis, I worked on the ATLAS muon trigger development and commissioning; it was thus immediate to study $J/\psi \to \mu^+\mu^-$ events when the LHC pp collisions first started. Since the beginning of 2010, tracking and muon system commissioning has been performed at ATLAS using the J/ψ resonance, the lightest of the $c\bar{c}$ bound states; because of the large number of $J/\psi \to \mu^+\mu^-$ events produced at the LHC and of the resonance very small decay width, J/ψ is well suited for the calibration of muon and tracking trigger, detector systems and reconstruction.

The detector and trigger commissioning activities naturally evolved, as documented in the present Ph.D. thesis, in measurements at the frontier of J/ψ physics at the LHC, in both pp and heavy ion collisions. Indeed, J/ψ is the subject of many interesting physics studies. To begin with, despite the large amount of data collected at colliders such as LEP and the Tevatron, the production mechanisms of heavy quark–antiquark bound states (*quarkonia*) are still not well understood today; it is thus important to perform measurements of the J/ψ production cross-section and, in perspective when statistics will make it possible, spin-alignment, in the kinematic range covered by the LHC. On the other hand, quarkonia bound-states production is one of the fundamental ingredients of heavy ion physics, since J/ψ yield suppression, due to colour screening effects, might indicate the production of a quark–gluon plasma during the collision. Reconstruction of $J/\psi \to \mu^+\mu^-$ allows the clean separation of inclusive and exclusive B-hadron samples, through the decay $B \to J/\psi\, X$. A vast majority of the B-physics program of the ATLAS experiment is based in fact on final states including J/ψ (e.g. $B_s \to J/\psi\phi$).

In this document, we present the first J/ψ studies performed on 2010 data recorded at ATLAS. Although the 2010 pp data sample represents a small fraction of

the total amount of data produced by the LHC up to now, it is sufficient in this case, because of the large $J/\psi \to \mu^+\mu^-$ cross-section, to perform precision measurements, already dominated by systematic uncertainties. The three introductory chapters contain an overview of the LHC accelerator and its performances in the first year of data taking, a review of the J/ψ physics that can be studied in that energy range (Chapter 1), and a description of the ATLAS detector (Chapter 2) and reconstruction algorithms (Chapter 3) relevant to the analyses presented.

In Chapter 4, the inclusive differential J/ψ cross-section and non-prompt to prompt cross-section fraction measurements are presented in rapidity bins and as a function of the resonance p_T. I have been main author of the J/ψ non-prompt to prompt cross-section fraction measurement, fundamental to extract the exclusive differential production J/ψ cross-sections from the inclusive measurement. These analyses have been published in [1].

I exploited the experience acquired in the cross-section measurement, notably the technique used to separate non-prompt and prompt J/ψ mesons to provide the measurement of the average B lifetime in inclusive $B \to J/\psi\ X \to \mu^+\mu^- X$ decays. This measurement, presented in Chapter 5, is described in an ATLAS public conference note [2], and will be presented in winter conferences.

Finally, Chapter 6 is dedicated to dimuon reconstruction in $PbPb$ collisions. In particular, the measurement of J/ψ suppression in highly central events, and the first observation of Z bosons in heavy ion collisions, published in [3], are presented. I have given my contribution, exploiting the skills acquired on dimuon reconstruction in pp collisions, performing the yield extraction procedure, providing the efficiency maps and studying the sources of systematic uncertainties or biases on this very delicate measurement.

Chapter 1

Physics at the Large Hadron Collider

1.1 The Large Hadron Collider

The *Large Hadron Collider* [4] (LHC) is a proton-proton (pp) collider located at the CERN laboratories in Geneva. It has been placed in the same underground tunnel, 27 Km long, where the previous CERN e^+e^- collider, the LEP (*Large Electron Positron*), was hosted.

The LHC has been designed to accelerate two proton beams at 7 TeV of energy, for a total of $\sqrt{s} = 14$ TeV in their centre-of-mass. This is approximately seven times higher than the maximum energy previously reached ($\sim$ 2 TeV) at the Tevatron proton-antiproton collider at the Fermilab laboratories.

A key parameter in accelerators design is their luminosity, since it is proportional to the event rate $\frac{dN}{dt}$:

$$\frac{dN}{dt} = \mathcal{L} \cdot \sigma, \tag{1.1}$$

where σ is the cross-section of the process considered. At the LHC, where searches and studies on rare events are performed, it is thus very important to reach the higher instantaneous luminosity possible. The instantaneous luminosity of a particle collider depends on its intrinsic properties, and is defined as:

$$\mathcal{L} = \frac{N_1 N_2 f k}{4\pi R^2}, \tag{1.2}$$

where N_1 and N_2 are the number of particles (protons at the LHC) per bunch, f is the revolution frequency of protons in the accelerator ring, k is the number of bunches in the beam that circulate at the same time, R is the mean radius of the spatial protons distribution in the plane orthogonal to the beam direction.

This requirement justifies the LHC strategic choice of making protons collide with protons. In principle a proton-antiproton ($p\bar{p}$) collider has the advantage of exploiting the valence quark interactions, whereas in the case of a pp collider such as the LHC the sea partons are the ones that produce the interesting physics events, with a consequent lower cross-section of the interaction [5]. This is not a problem at the centre-of-mass energies reached by the LHC, since, at such high energies, the cross-section distributions in the two cases converge, as it can be seen from the

distributions in Figure 1.1. On the other hand, the use of antiprotons is limited by their low production efficiency and by the long times needed for their accumulation, that make it difficult to operate a $p\bar{p}$ collider at the needed luminosities (see eq. 1.1).

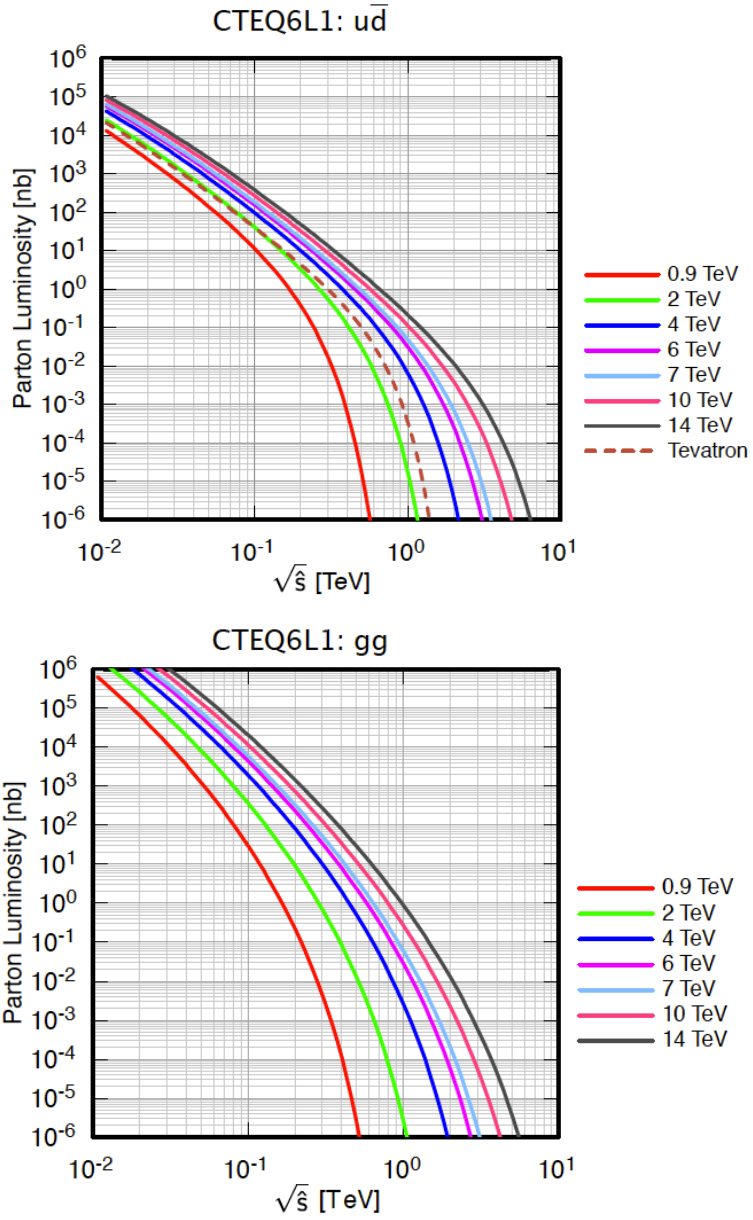

Figure 1.1. Parton luminosities for $u\bar{d}$ (top) and gg (bottom) interactions at different centre-of-mass energies. The first case is the dominant interaction in $p\bar{p}$ collisions, whereas the second in pp collisions.

The design parameters of the LHC are presented in Table 1.1. The very high collision rate, one every 25 ns at design luminosity, and the elevated instantaneous luminosity have been a true challenge for the design of the accelerator and of the LHC experiments.

The LHC design includes collisions between beams of lead ions ($^{208}Pb^{82+}$). With

circumference	26.7 Km
$\sqrt{s}$	14 TeV
protons per bunch	$1.67 \cdot 10^{11}$ at $\int \mathcal{L}\ dt = 10^{34} cm^{-2} s^{-1}$
length σ_z of the bunches	56 mm
radius $\sigma_x = \sigma_y$ of the bunches	16 μm
maximum number of bunches	3564 (of which 2835 are used)
space between the bunches	7.48 m $\sim$ 25 ns $\sim$ 40 MHz

Table 1.1. Design parameters of the LHC.

the nominal field produced by the LHC dipole magnets, these interactions will have a centre-of-mass energy of 5.52 TeV/nucleon, and a nominal instantaneous luminosity of 1.0×10^{27} cm^{-2}s^{-1}.

The four main experiments of the LHC, ATLAS (*A Toroidal LHC ApparatuS*) [6], CMS (*Compact Muon Solenoid*) [7], ALICE (*A Large Ion Collider Experiment*) [8] and LHCb (*Large Hadron Collider beauty*) [9], are located at the four collision points of the beams. ATLAS and CMS are multi-purpose experiments, LHCb studies the physics of the b-quark, whereas ALICE is designed for the study of heavy ion collisions.

The LHC has been operational since december 2009. In march 2010 the first pp collisions with a centre-of-mass energy of 7 TeV were provided at an instantaneous luminosity of approximately 1.1×10^{27} cm^{-2}s^{-1}. The LHC performances have been improving quickly and in the last months of 2010 the LHC reached a peak luminosity of 2×10^{32} cm^{-2}s^{-1}. This allowed to perform J/ψ and B-physics analyses on a very large statistical sample quite fast after collisions started. In Figure 1.2 (top) the luminosity provided by the LHC (green) and integrated by ATLAS (yellow) per day in 2010 are shown. For a total integrated luminosity of 41 pb^{-1} collected in 2010, the ratio of the recorded to delivered luminosity gives the ATLAS data taking efficiency of 93.6%. The residual inefficiency depends on the dead times of the detector and, most of all, to the requirement that all detectors should be ready when recording data. In 2010 LHC provided also the first heavy ion collisions, at a centre-of-mass energy of 2.76 TeV/nucleon. The run lasted for about three weeks, during which 9.17 μb^{-1} were integrated.

In 2011 the instantaneous luminosity provided by the LHC is still growing, as shown in the bottom plot in Figure 1.2, and has reached, up to the 25th of July 2011, a peak value of approximately 1.75×10^{33} cm^{-2}s^{-1}, as shown in Figure 1.3. The record parameters of the LHC as of the 25th of July 2011 are listed in Table 1.2. LHC has integrated 2.68 fb^{-1}, and is expected to provide a total of about 4 fb^{-1} by the end of the year, while a second heavy ions run is foreseen for december 2011.

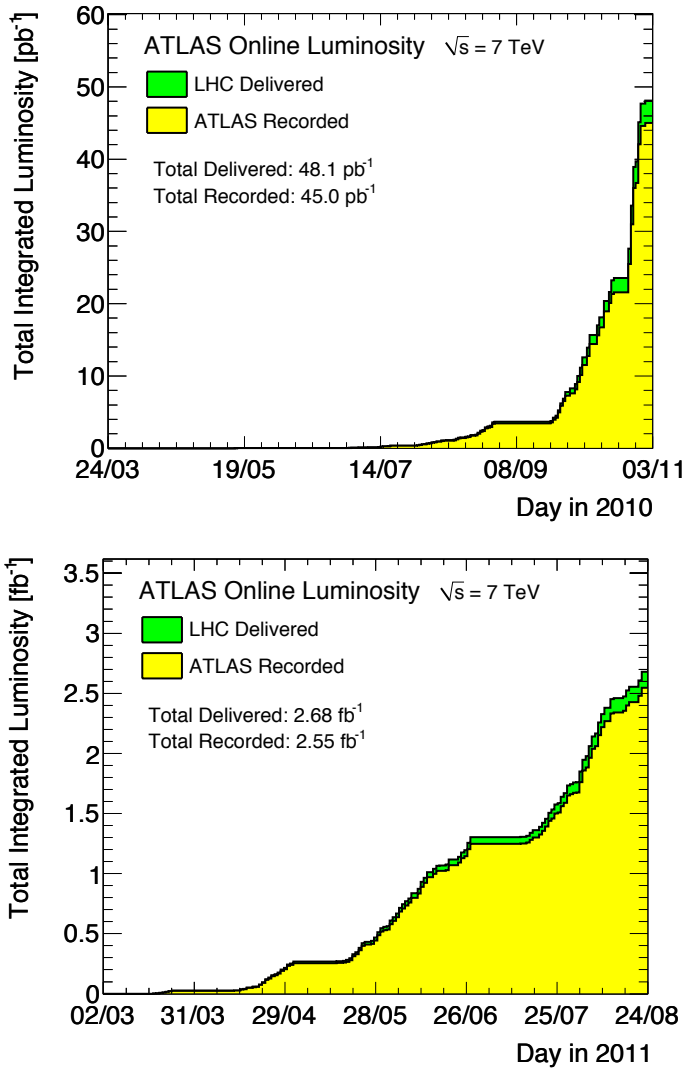

Figure 1.2. Integrated luminosity provided by the LHC (green) and integrated by ATLAS (yellow) in 2010 (top) and in 2011 (bottom).

$\sqrt{s}$	7 TeV
protons per beam	$1.65 \cdot 10^{14}$
maximum number of colliding bunches	1331
space between the bunches	$\sim$ 50 ns $\sim$ 20 MHz
peak luminosity	$1.75 \cdot 10^{33}$ cm^{-2}s^{-1}
maximum integrated luminosity delivered in one day	62.85 pb^{-1}

Table 1.2. Record parameters of the LHC as of July 25 2011.

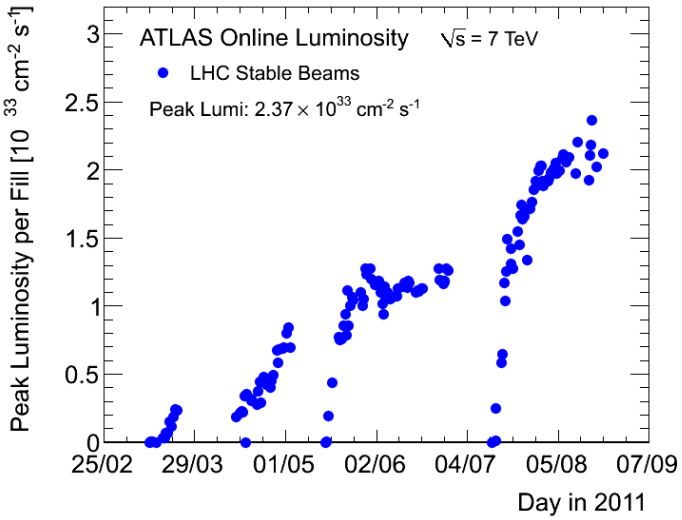

Figure 1.3. Peak luminosity reached by the LHC in 2011 per day.

1.2 Physics of the J/ψ at the LHC

The J/ψ resonance was first discovered in November 1974 simultaneously at the Brookhaven National Laboratory (BNL), by Ting *et al.* [10], and at the Stanford Linear Accelerator Center (SLAC), by Richter *et al.* [11]. The first group observed a peak in the invariant mass distribution of e^+e^- pairs at 3.1 GeV, with the events produced in the reaction $p + Be \rightarrow J/\psi \; X \rightarrow e^+ e^- X$, whereas at SLAC a peak in the cross-section of e^+e^-, $\mu^+\mu^-$ and hadrons production from e^+e^- interactions was observed in correspondence to the same mass value. When a second resonance, the ψ', was found quickly after by the SLAC group at slightly higher mass [12], it became clear that these were bound states of $c\bar{c}$ pairs, named "charmonium", and that the J/ψ was the lowest mass system. The observation of charmonium was the first direct experimental evidence of the existence of the charm quark, predicted in 1970 by Glashow, Iliopoulos and Maiani [13].

During the first years of data taking at the LHC, the importance in studying $J/\psi \rightarrow \mu^+\mu^-$ events is threefold. First of all, the facts that the J/ψ is the most abundant resonance decaying to two muons that one encounters at a collider, and its very small decay width, make of it an invaluable instrument for the commissioning and calibration of the muon and tracking detectors, trigger and reconstruction. Secondly, the production mechanisms of the quarkonia resonances is still an open problem, and new measurements will lead to progresses in various QCD calculations both in perturbative and non-perturbative regimes. Thirdly, J/ψ mesons can be clean signatures to events of interest and new physics searches. This is the case, for example, of B-physics studies, where J/ψ are the product of B-hadrons decays, and are invaluable instruments to estimate their lifetimes and widths. Another interesting example is heavy ions physics, where quarkonia states can be used to study the medium they are produced in and improve our knowledge, for example, on deconfined matter production.

The commissioning work performed at ATLAS on J/ψ on early data is outlined in chapters 2 and 3, whereas the theoretical background related to the physics studies are briefly presented in the following Sections.

1.2.1 J/ψ Production at Hadron Colliders

After their discovery, J/ψ mesons have been produced and studied widely at hadron colliders, at BNL, CERN and Fermilab laboratories. Models describing their production mechanism have been developed, but none of them is yet successful at fitting experimental data satisfactorily. A brief overview of the most popular production mechanisms of J/ψ (for more details see [14, 15] and references therein) will be provided below, but first a distinction between the different production types of charmonium states needs to be made.

J/ψ Production Types

In high energy collisions, J/ψ can be produced either through *prompt* or through *non-prompt* processes. In the former case J/ψ comes from Quantum Chromo Dynamics (QCD) $c\bar{c}$ production, where we can distinguish J/ψ that come directly from the primary interaction (*direct* production) or that come from the decays of excited

charmonium states (*indirect* production), ψ' and $\chi_{c(0,1,2)}$. J/ψ are said to be non-prompt if they come instead from the decays of B-hadrons, that can be detected thanks to the presence of a secondary displaced vertex in the event, as explained in Section 4.5.1.

Quarkonia Production Puzzle

The Colour Singlet Model (CSM) [16] was developed right after the discovery of J/ψ to describe the production processes of charmonium and bottomonium bound states. It is based on the factorisation theorem of QCD [17], that allows to separate the cross-section of a process in two parts: the short distance one, where *perturbative QCD* can be applied due to its asymptotic freedom, and the long distance one, dominated by *non-perturbative* effects. The soft part is factorised in a universal wave function.

The assumption that the quark pair is produced with the same quantum numbers as the final bound state, that is in a colour singlet, leads to the name of the model. The CSM's greatest advantage is that it is a very predictive model. It was considered to describe reasonably well the production mechanism of charmonium and bottomonium for decades, until the CDF experiment at the Tevatron, in 1997 [18], showed that it predicts a prompt charmonium production cross-section over an order of magnitude lower than the measured one. In Figure 1.4, a comparison is provided between the direct (top) and prompt, from χ_c decays, (bottom) J/ψ differential cross-section as a function of the p_T measured at CDF (solid points) and the CSM predictions (dotted line). It is observed that the colour singlet prediction at the Leading Order (LO) in α_s reproduces the shape of the CDF points, but under-estimates the overall normalization of the cross-section. An even bigger discrepancy is measured on the $\psi(2S)$ differential cross-section (middle plot), ruling out the CSM as a credible theoretical description of charmonium production.

On the other hand, according to the Non Relativistic QCD (NRQCD) factorization approach, the charmonium production cross-section not only contains colour singlet but also colour octet terms. The Colour Octet Model (COM) thus includes $c\bar{c}$ pairs produced in a colour octet state, that become colourless radiating soft gluons during hadronization. In Figure 1.4, the total NRQCD factorization fits are represented as solid lines, and the colour octet terms by dashed lines. The COM matrix elements have been extracted from CDF data [18] since, unlike CSM matrix elements, they cannot be derived from theory. Therefore, COM accomodates for the large production cross-section measured in data, but is not predictive since the normalization of those terms is determined by the matrix elements.

The normalization and shape of the charmonium production cross-section can also be reasonably well predicted using the Colour Evaporation Model (CEM) [19]. First proposed in 1977, the CEM uses a phenomenological approach to describe the charmonium production, where the charmonium states with an invariant mass below the $D\bar{D}$ threshold (since D is the lightest meson containing a c-quark) are formed in proportions determined by experimental results. In analogy with the COM, here too $c\bar{c}$ pairs can be formed in colour octet states; the pair is then assumed to neutralize its colour emitting soft gluons by interaction with the collision-induced colour field, hence by *colour evaporation*. In Figure 1.5 a comparison between the differential cross-section as a function of the resonance p_T measured at CDF (solid points) and

CEM predictions at Next to Leading Order (NLO) (solid line) are shown. The comparison is provided for $\psi(2S)$ decays (top right), and for direct (top left) and prompt (bottom) decays of the J/ψ.

At the LHC, new experimental input in very wide kinematic ranges with respect to the previous experimental studies, is being provided. This is very useful to improve our understanding of the mechanisms that regulate quarkonium production. Other stringent indications might also come from the measurement of quarkonia spin-alignment, already measured by the CDF experiment [20], and which will improve at the LHC with a larger statistical sample. All of the previously outlined models provide some predictions on the subject, that will be tested on LHC data collected in 2011.

1.2.2 B-Hadrons Lifetime Measurements

J/ψ reconstruction leads, with enough statistics, to precise measurements of B-hadron lifetimes, which allow tests of theoretical predictions based on the Heavy Quark Expansion (HQE) [21] technique. In this framework, inclusive observables, such as lifetimes, are calculated using a power expansion of the decay rate $\Gamma(H_b)$, where H_b represents any hadron containing a single b-quark and any of the light u, s or d quarks, in terms of $\Lambda_{\rm QCD}/m_b$. Here $\Lambda_{\rm QCD}$ is the fundamental scale of QCD, and m_b is the b-quark mass. At the third order of the expansion in $\Lambda_{\rm QCD}/m_b$, effects related to the weak interaction between the b-quark and the valence quark introduce differences among different b-flavoured hadrons. The measurement of these differences can thus be used to test the HQE formalism.

The mismatch between the low experimental value of the ratio $\tau(\Lambda_b)/\tau(B_d)$ and the HQE predictions has long been a puzzle. Only recently, Next-to-Leading Order (NLO) calculations of perturbative QCD, $1/m_b$ corrections to spectator effects as well as recent Tevatron measurements reduced the dicrepancy, and today a very good agreement between experimental results and theoretical predictions is assessed [15].

In particular, lifetime ratios for the different species of B-hadrons are predicted with accuracies at the per cent level. The lifetime difference between the light and heavy eigenstates of the B_s^0 meson are also predicted with roughly 30% precision, which is comparable to the present world average from the Tevatron experiments.

Theoretically, predictions are usually made for ratios of lifetimes rather than for individual lifetimes, as this allows to cancel out several uncertainties. Experimentally, on the other hand, a ratio measurement would allow as well certain sources of systematic to cancel.

Among lifetime measurements, inclusive ones, which do not distinguish the B-hadron flavour, are usually the first to be performed by an experiment. The inclusive B-hadron lifetime, defined as $\tau_b = \sum_i f_i \tau_i$, where τ_i are the individual species lifetimes and f_i are the fractions of the various species present in the sample, is not as fundamental a quantity as exclusive lifetimes are for comparing with the theoretical predictions. In particular this quantity is sensitive to the B-hadrons mixture composition, which is dependent on how the B is produced at the collider, on the final states used to reconstruct it, etc..., hence the average B lifetime is a quite experiment-dependent observable. On the other hand, this measurement can usually be performed very soon with a large statistical sample: this allows to perform an estimate of detector-dependent systematic effects which paves the way

for all exclusive lifetime measurements.

As it was said, inclusive lifetime measurements depend on the B-hadrons mixture, hence they depend on the way the decay is reconstructed. Many experiments have previously provided estimates of τ_b using different techniques, at LEP, SLD and Tevatron. Grouping analysis which are expected to select the same mixtures, one can separate experimental results in three categories:

- fully inclusive measurements, performed at LEP [22–25] and SLD [26], that accept any B-hadron decay, based on topological reconstruction;
- measurements, performed at LEP [24, 27, 28], relying on the identification of a lepton from a B decay;
- measurements, performed at the Tevatron [29], using inclusive $H_b \to J/\psi\ X$ samples, where the J/ψ is fully reconstructed.

The mixture defined by the last kind of measurements is well defined, since, in the limits where the J/ψ reconstruction efficiency does not depend on the type of the decaying hadron, it is given by the product of the production fractions and the inclusive branching fractions for each H_b to give a J/ψ. The averages obtained by the Heavy Flavour Averaging Group (HFAG) [30] for the sets defined above are:

$$\begin{aligned} \tau(b\,\text{vertex}) &= 1.572 \pm 0.009\,\text{ps}, \\ \tau(b \to l) &= 1.537 \pm 0.020\,\text{ps}, \\ \tau(b \to J/\psi\ ) &= 1.533\ ^{+0.038}_{-0.034}\,\text{ps}, \end{aligned}$$

whereas an average of all measurements, ignoring mixture differences, yields 1.568 ± 0.009 ps.

1.2.3 Quarkonia Production in Heavy Ion Collisions and J/ψ Suppression

At the LHC, the production of J/ψ mesons is not only studied in pp collisions, but also in lead-lead collisions. With this type of interactions, one hopes to recreate a state similar to matter at the very beginning of the Universe: a hot system with deconfined quarks and gluons. This allows to test and develop the theoretical and phenomenological description of effects such as the screening and deconfinement, furthering at the LHC the work done by collaborations at the CERN SPS and at RHIC at an higher centre-of-mass energy per nucleon.

In this setting, quarkonia play a very important role [14] as an instrument to study the properties of the medium. In particular, quarkonia suppression was suggested as a signal of deconfinement [31]. It is expected, according to both theoretical predictions and simulations, that in strongly interacting matter a transition to quark–gluon plasma takes place when reaching very high temperature and pressure conditions. One of the fundamental mechanisms that characterize this state of matter is the screening of colour forces between static quarks: $q\bar{q}$ bound states, in these conditions, cannot be formed.

Heavy quarkonia can, in principle, survive the deconfinement phase transition because of their small sizes. On the other hand, the screening radius becomes smaller

than the typical bound-state size when reaching a given temperature, and as a consequence heavy quarkonia pairs dissolve. The quarkonia suppression in heavy ions collisions was proposed to be a symptom of matter deconfinement [31].

The interpretation of J/ψ suppression in terms of colour screening is generally complicated by the quantitative agreement between the overall levels of J/ψ suppression measured by the NA50 experiment at the CERN SPS [32] ($\sqrt{s_{NN}} = 17.3$ GeV) and the PHENIX experiment at RHIC [33] ($\sqrt{s_{NN}} = 200$ GeV). Data from proton-nucleus and deuteron-gold collisions also show decreased rates of J/ψ production [34], indicating that other mechanisms may come into play.

Finally, proposals for J/ψ *enhancement* exist at high energies from charm quark recombination [35]. Measurements at higher energies, with concomitantly higher temperatures and heavy quark production rates, are clearly needed to address these debates with new experimental input. The production of vector bosons (W, Z), only available in heavy ion collisions at LHC energies, can serve as a reference process for J/ψ production, since they are not expected to be affected by the hot, dense medium, although modifications to the nuclear parton distribution functions must be considered [36].

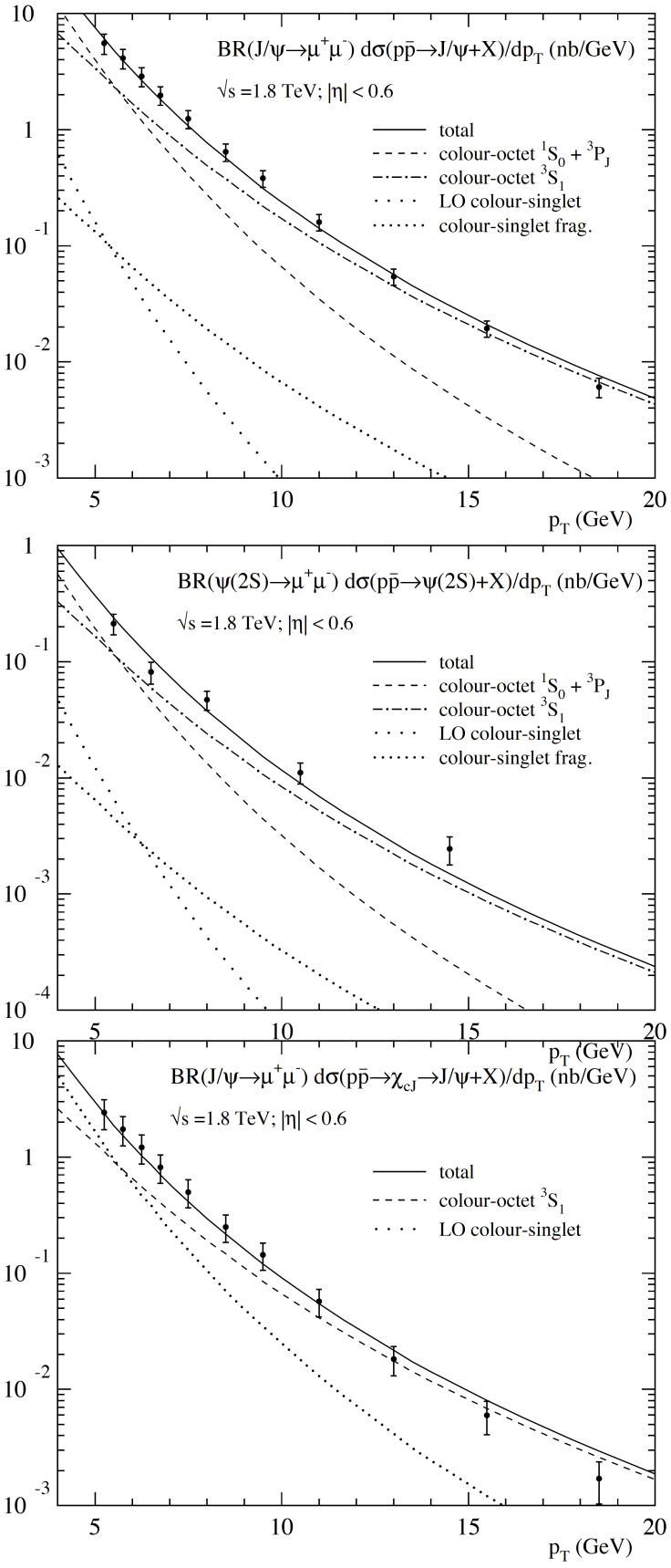

Figure 1.4. Direct (top) and indirect (bottom) J/ψ and $\psi(2S)$ (middle) differential prodution cross-sections as a function of the transverse momentum from [18]. The data points are from CDF Run I measurement, and are compared to the NRQCD factorization fits (solid curves). The other curves (dotted) are the colour singlet and colour octet terms presented separately.

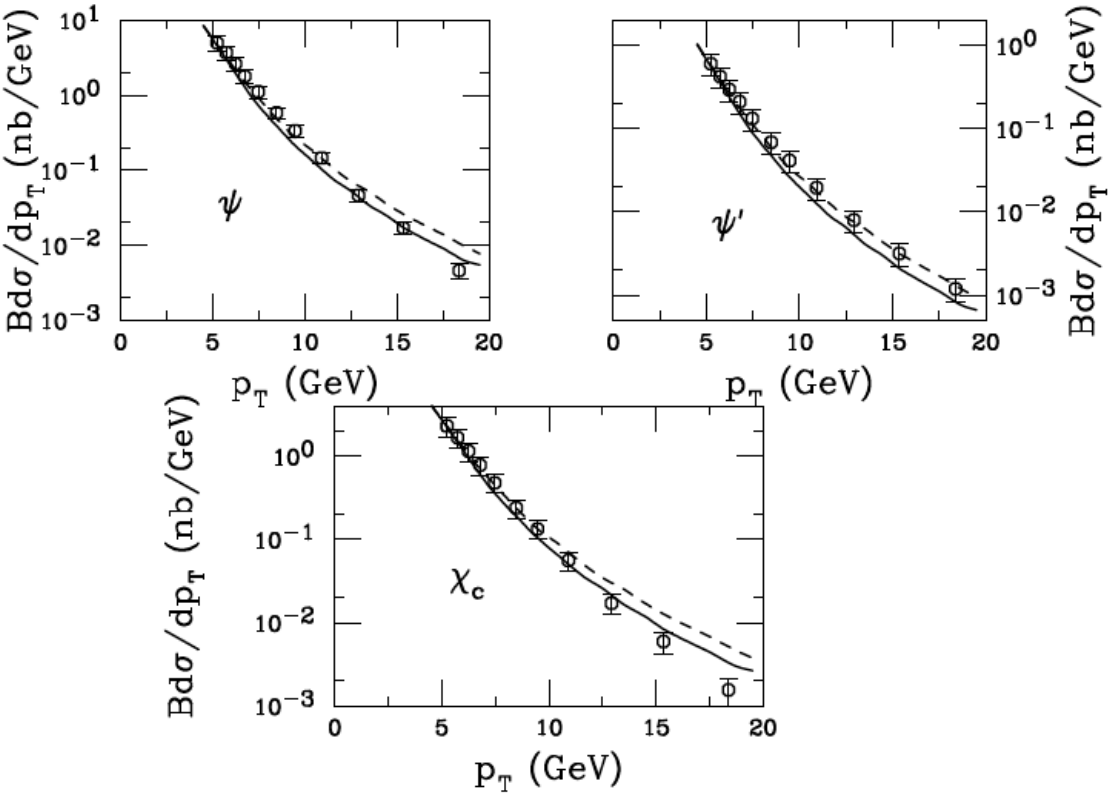

Figure 1.5. Direct (top left), indirect (bottom) J/ψ and $\psi(2S)$ (top right) differential cross-section as a function of the transverse momentum from [18]. The data points (empty dots) are from CDF measurements, and are compared to the CEM predictions at next to leading order in α_s (solid line).

Chapter 2

The ATLAS Experiment

ATLAS [6], shown in Figure 2.1, is a multi-purpose experiment located underneath the Geneva region at one of the four interaction points of the LHC. It has a cylindrical structure, with its axis along the direction of the collider's beam-pipes. ATLAS is hermetic, composed by a central barrel closed at the extremities by two end-caps, and of gigantic dimensions: 45 meters long, 25 meters high and weighting more than 7000 tons.

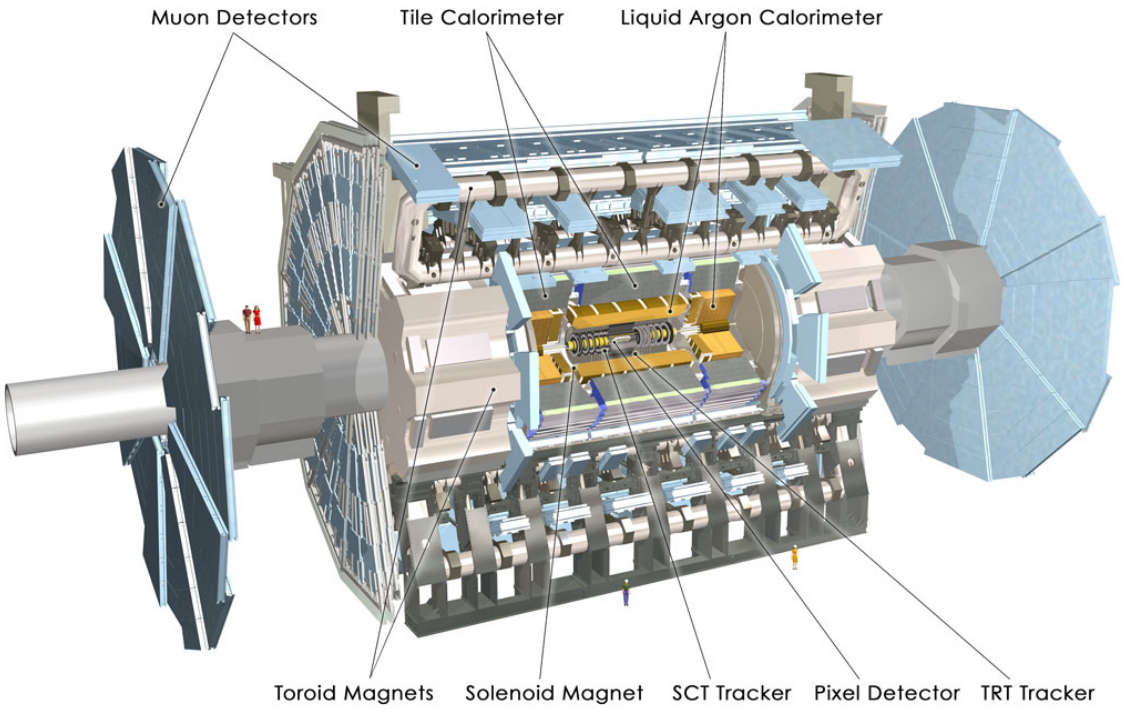

Figure 2.1. Drawing of the ATLAS experiment.

Following the tradition of high-energy physics multi-purpose experiments design, ATLAS is composed by layers of concentric detectors. Each of these detectors is specialized in the detection of one or more signatures. From the innermost to the outermost layer, the ATLAS experiment is composed by:

- an inner tracker system to detect charged particles;
- a solenoidal superconducting magnet producing a uniform 2 tesla field in the direction of the beam axis;
- an electromagnetic calorimeter to measure the energy deposited by electrons and photons;
- an hadronic calorimeter to measure the energy deposited by jets and hadrons;
- a muon spectrometer, i.e. an outer tracker system for the measurement of muons;
- a system of air-core superconducting toroidal magnets.

In the following sections a more detailed description of the detectors will be provided, with a particular attention to the systems used in the presented analyses.

2.1 ATLAS Reference System and Nomenclature

It is important, before coming to the description of ATLAS, to define the experiment reference system and a number of variables of common use at hadronic colliders.

The reference system used in ATLAS is represented in Figure 2.2. The z direction is defined along the beam axis, and the x-y plane is the one transverse to the beams. The x axis is directed towards the center of the accelerator's ring, and the y axis is pointing upwards. The azimuthal angle ϕ is defined around the beam axis in the transverse (x-y) plane, and the polar angle θ is the angle from the beam axis in the y-z plane.

One can define the rapidity of a particle (y) as a function of the polar angle, as:

$$y = \frac{1}{2}\ln\left(\frac{E + p_L}{E - p_L}\right) \tag{2.1}$$

where p_L is the longitudinal (i.e. along the z axis) component of its momentum. In the ultra-relativistic limit, for particles with a negligible mass and $E \simeq p_L$, equation 2.1 simplifies to the so-called *pseudo*-rapidity, defined as:

$$\eta = -\ln\left[\tan\left(\frac{\theta}{2}\right)\right] \tag{2.2}$$

Pseudo-rapidity is commonly used at hadronic colliders as it is a relativistic invariant under longitudinal boosts. This variable, when θ is equal to zero, tends to infinity, whereas when θ is equal to $\frac{\pi}{2}$ η is zero, as shown in Figure 2.3.

It is common to all experiments at hadronic colliders that observables projected in the plane transverse to the beam axis, characterized by a "T" subscript, as it is the case for the transverse momentum p_T for example, or the transverse energy E_T, are used. This is due to the observation that hadrons, and in the specific LHC case protons, are non-elementary particles. Therefore the centre-of-mass energy of the quarks and gluons that compose the hadrons is unknown, and the kinematic of their interactions is, in general, not closed. On the other hand it is possible to neglect the transverse component of the partons' momentum, which is on average zero, with

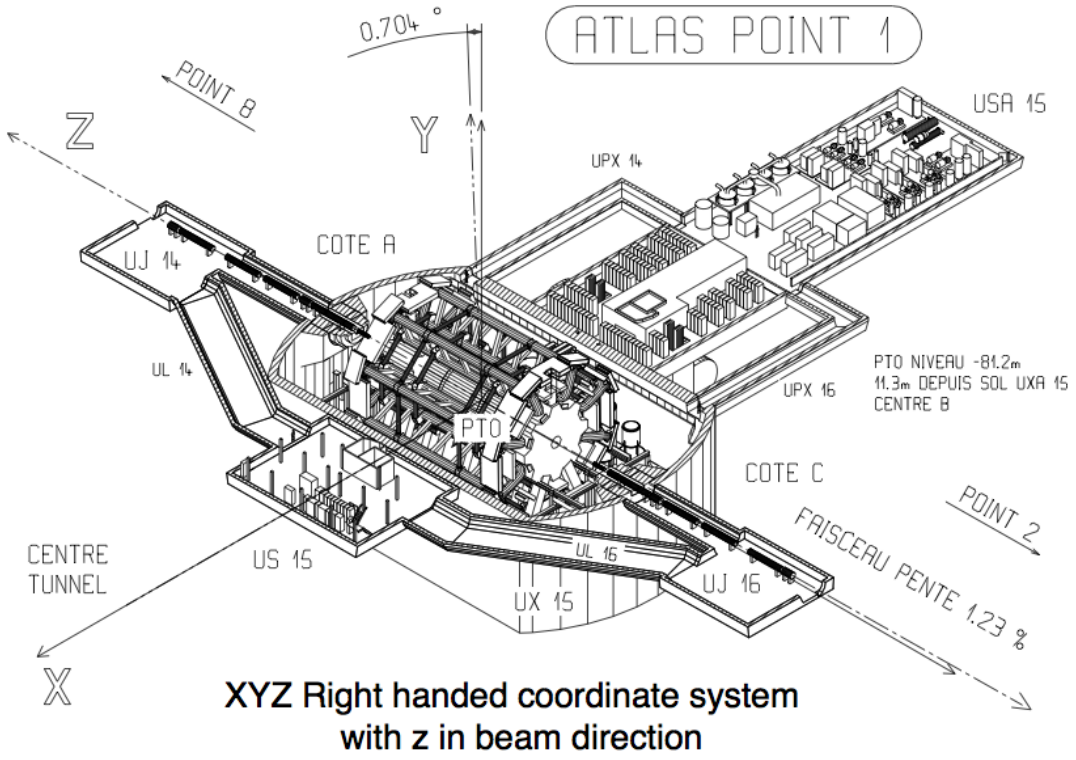

Figure 2.2. Reference frame used at the ATLAS experiment.

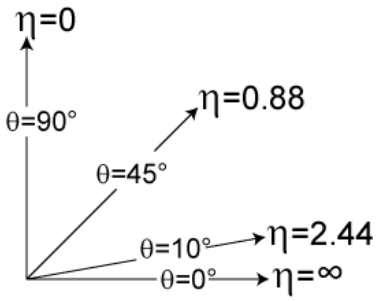

Figure 2.3. Pseudo-rapidity (η) definition as a function of the polar angle θ.

respect to the longitudinal one. It is hence possible to reconstruct the particles in the event using its parameters projected onto the transverse plane, since there the kinematic of the event is closed.

2.2 Magnets Systems

Two magnetic fields [37] are used in ATLAS, produced by: a superconducting solenoid [38] enveloping the barrel region of the inner detector tracker, and a system of air-core superconducting toroidal magnets [39, 40] located outside the muon spectrometer, as shown in Figure 2.4.

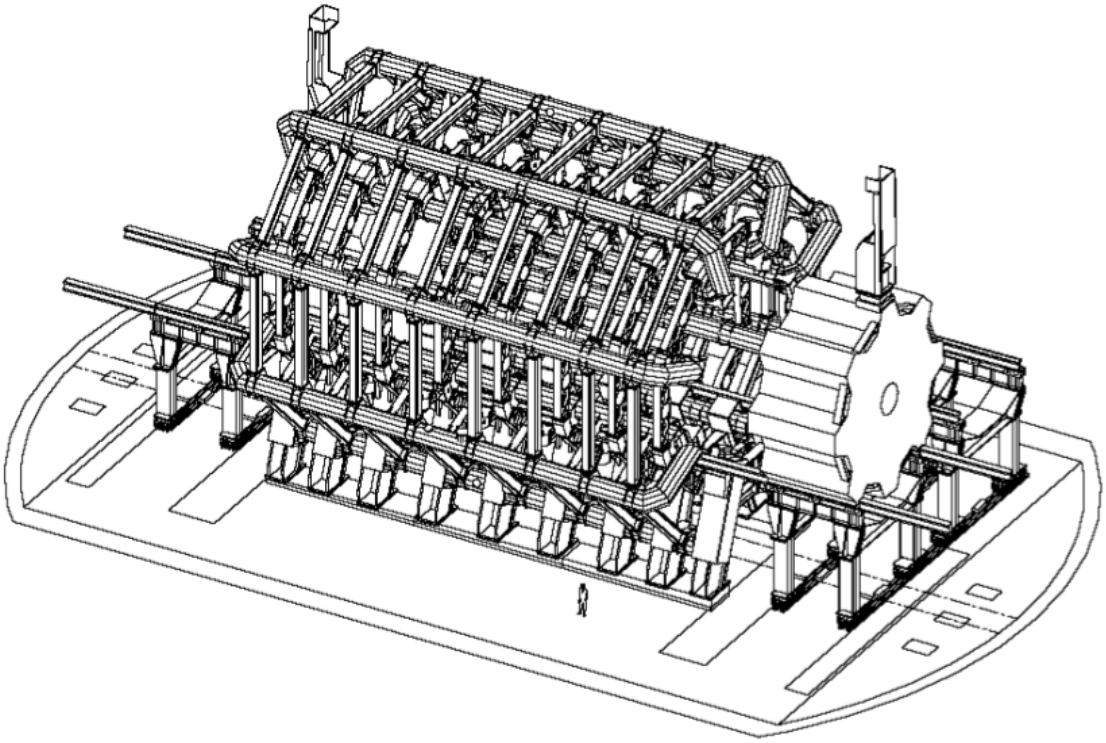

Figure 2.4. ATLAS superconducting air-core toroidal magnets.

This complicated system has been designed to provide an accurate measurement of muon momenta from a few GeV up to the TeV scale thanks to the two independent measurements in the inner tracker and muon chambers, and to the large lever arm of the external field. The toroids have been built "in air" in order to obtain a better momenta and position measurement minimizing the muons' multiple scattering within the detector.

The solenoid provides a uniform magnetic field in the inner tracker of approximately 2 tesla along the z direction, bending the charged particles' tracks in the transverse plane. The toroidal magnets, eight in the barrel and eight in each of the two end-caps, produce a variable field in the detector, shown in Figure 2.5, reaching peak intensities of 3.9 tesla in the barrel region and 4.1 tesla in the end-cap regions.

2.3 Inner Detector Tracker

The ATLAS Inner Detector tracker (ID) [41], shown in Figure 2.6, is composed by three concentric detectors of cylindrical geometry, with its axis, $\Delta z = \pm 345$ cm long, on the beam line and a total radius of 115 cm. It is enveloped in the magnetic solenoid described in Section 2.2.

The three detectors that compose the ID are:

- **Pixel Detector:** three layers of silicon pixels, each provides a measurement with resolution of $\sim$10 μm in the transverse plane, and approximately 115

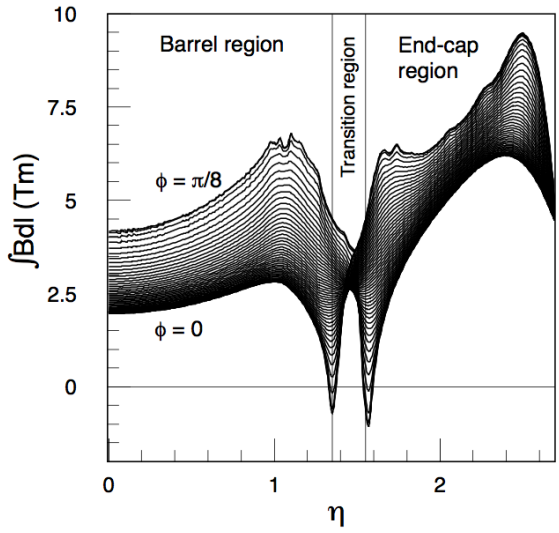

Figure 2.5. Variation of the toroids' magnetic field integrated in a straight line given as a function of pseudo-rapidity for different ϕ values.

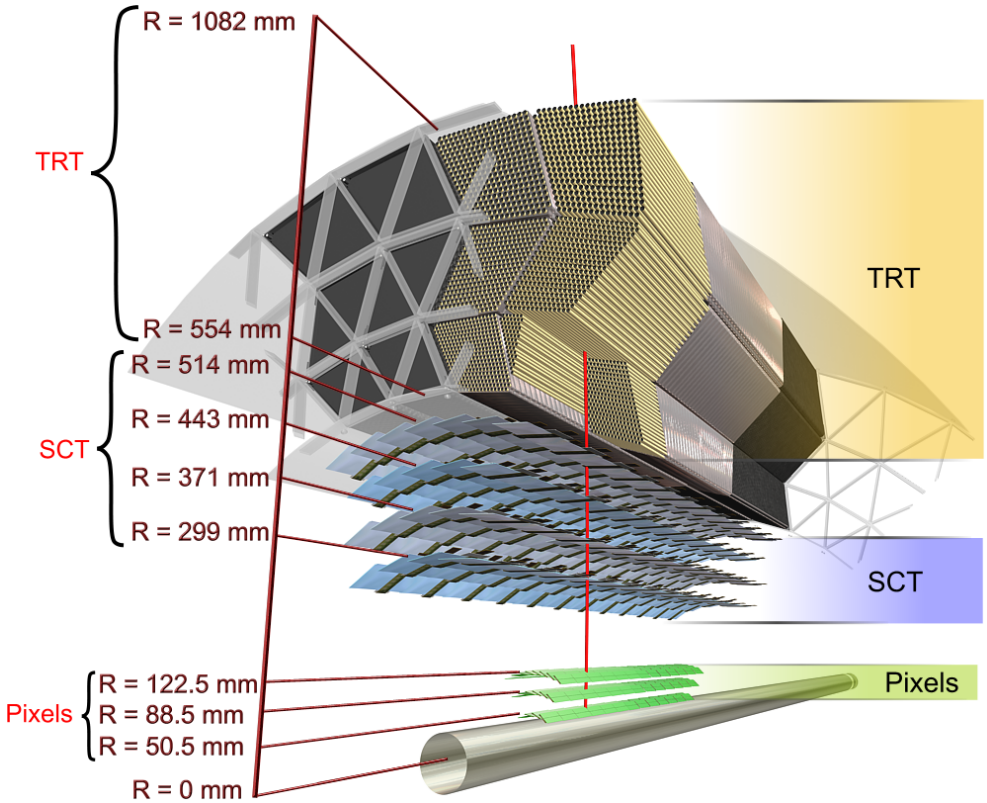

Figure 2.6. Sketch representing the ATLAS ID. The Pixel, SCT and TRT detectors are shown.

μm in the z coordinate. The innermost layer of the Pixel detector is called B-layer.

- **Semi-Conductor Tracker (SCT):** eight layers of silicon strips with a resolution of 17 μm in the transverse plane and 580 μm in the longitudinal one each. The Pixel and SCT detectors provide on average a total of four high precision measurements on the track.

- **Transition Radiation Tracker (TRT):** is composed by straw tubes chambers extending in the transverse plane up to $|\eta| \leq 2.5$. Here the low resolution, $\sim$ 130 μm per straw, is compensated by the high number of measured points on track, on average thirty-six.

The ATLAS ID has been designed to identify the primary and secondary vertices of the interactions, to reconstruct the tracks of the charged particles passing through it and to measure their momentum. The momentum measurement relies on the solenoid magnetic field, described in 2.2, that bends the particles' trajectories on the $r - \phi$ plane thanks to the Lorentz force:

$$\vec{F}_L = q\vec{v} \times \vec{B} \tag{2.3}$$

where q is the electric charge of the particle, $\vec{v}$ is its velocity, and $\vec{B}$ is the magnetic field.

The resolution on the momentum measurement is a function of many detector-related parameters:

$$\frac{\Delta p}{p^2} = \frac{8}{0.3 \cdot B \cdot L^2} \cdot \Delta s \tag{2.4}$$

where B is the magnetic field (in tesla), L is the lenght of the reconstructed track (in meters). Δs is provided by Gluckstern's formula:

$$\Delta s = \frac{\epsilon}{8}\sqrt{\frac{720}{N+4}} \tag{2.5}$$

where ϵ is the resolution on the measurement and N is the number of measured points on the track. The ATLAS intense magnetic field, the high precision measurements from the Pixel and SCT detectors and the high number of measurements of the TRT detector all contribute to provide a better momentum resolution on the tracks.

2.4 Calorimetric Apparatus

The ATLAS calorimetric system is composed by an ElectroMagnetic (EM) calorimeter [42], for the identification of electrons and photons and the reconstruction of electromagnetic showers, and by an hadronic calorimeter [42, 43] to measure hadronic jets. It has a cylindrical structure developing around the solenoid magnet. The external radius of the electromagnetic calorimeter measures 2.25 m, and its longitudinal axis $\pm$ 6.65 m around the interaction point. The hadronic calorimeter that envelopes it has an external radius measuring 4.25 m, and is $\pm$6.10 m long in the z direction around the interaction point. The ATLAS calorimetry is represented in the drawing in Figure 2.7, whereas the absorption lengths relative to its material are shown in Figure 2.8 as a function of the detector pseudo-rapidity.

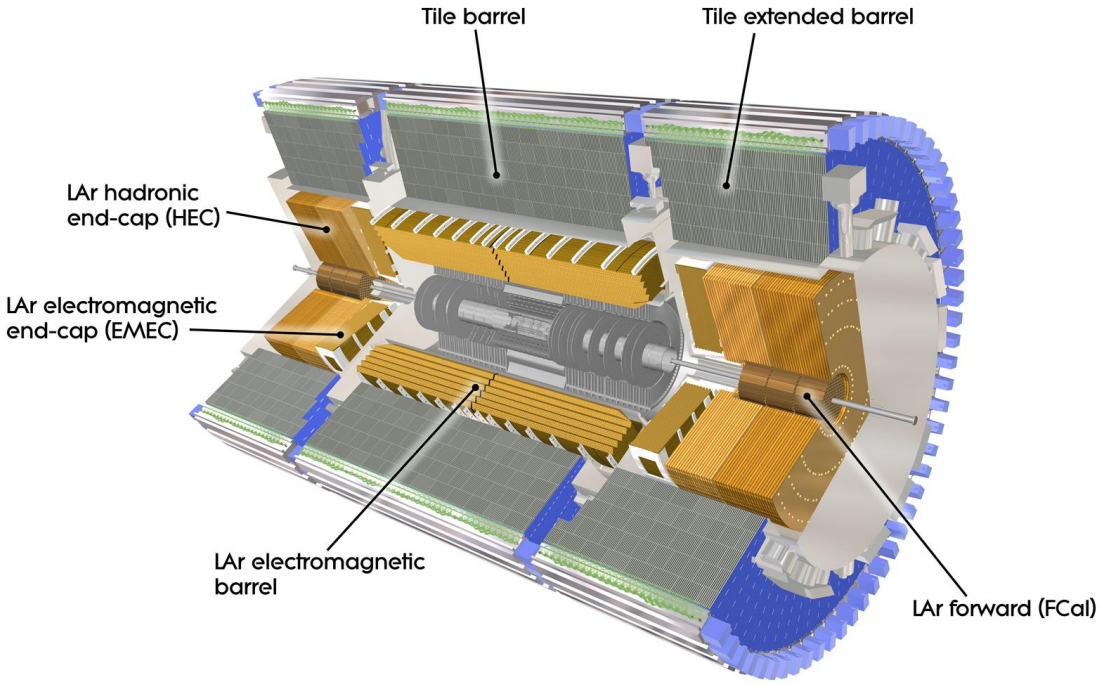

Figure 2.7. Layout of the ATLAS calorimetric apparatus.

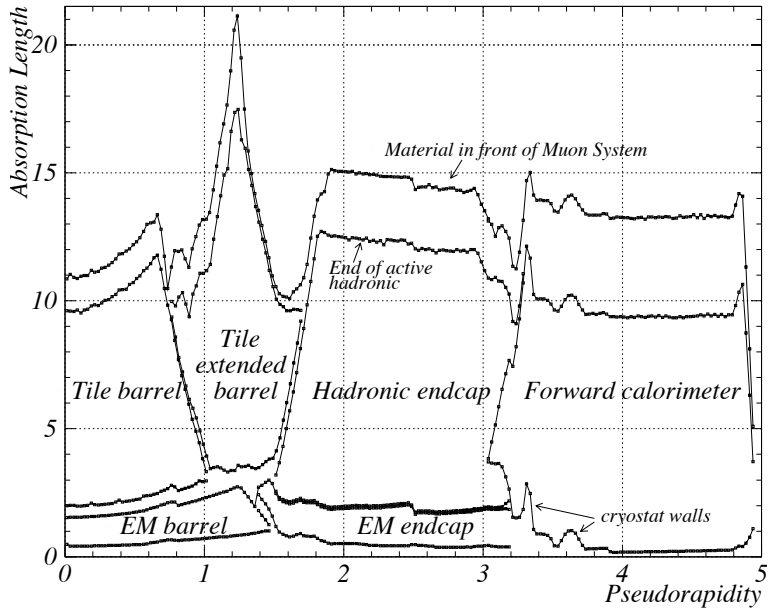

Figure 2.8. Amount of material in absorption lenghts in the ATLAS calorimetry as a function of η.

2.4.1 Electromagnetic Calorimeter

The EM calorimeter is a sampling detector. It is characterized by the accordion geometry of its Kapton electrodes and lead absorber plates, shown in Figure 2.9, designed in order to maximize the geometric acceptance of the detector in ϕ. The active material is given by 2.1 mm thick layers of liquid argon, alternated to the lead absorbers plates of a thickness that varies as a function of η to optimize the energy resolution.

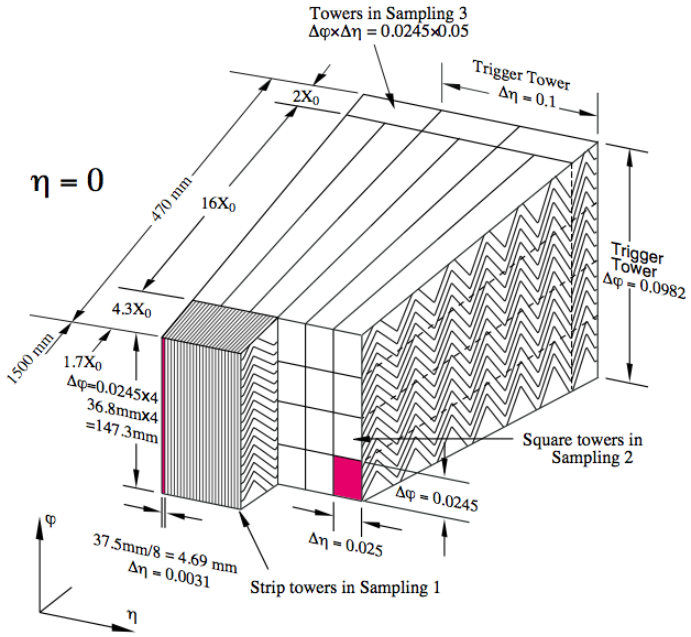

Figure 2.9. Sketch of the accordion geometry that characterizes the ATLAS EM calorimeter.

The EM calorimeter is segmented in cells of variable dimensions depending on the pseudo-rapidity region they're installed in. In most of the volume, in the middle region, granularity is approximately $\Delta\eta \times \Delta\phi \simeq 0.025 \times 0.025$. The total thickness of the electromagnetic calorimeter is $> 24(X_0)$ radiation lenghts in the barrel and $> 26X_0$ in the end-caps.

The ATLAS EM calorimeter resolution in energy is given by

$$\frac{\Delta E}{E} = \frac{10\%}{\sqrt{E[\text{GeV}]}} \bigoplus 0.3\% \tag{2.6}$$

whereas the η resolution is:

$$\frac{40 \text{ mrad}}{\sqrt{E[\text{GeV}]}}. \tag{2.7}$$

The electromagnetic calorimeter is located outside the central solenoid, covering a pseudo-rapidity region of $|\eta| \leq 3.2$. Over the pseudo-rapidity range $|\eta| < 1.8$ it is preceded by a pre-sampler detector, used to correct for the energy lost in the material (ID, magnet) upstream of the calorimeter.

2.4.2 Hadronic Calorimeter

The hadronic calorimeter is composed by a barrel detector, covering $|\eta| < 1.7$, by two end-cap detectors, covering $1.5 < |\eta| < 3.2$, and by two Forward Calorimeters (FCal), covering $3.1 < |\eta| < 4.9$. The hadronic barrel detector is a sampling calorimeter, with plastic scintillator plates (*tiles*) as sensitive material, alternated with layers of iron absorber. At larger pseudo-rapidities, where a higher radiation level is reached, the liquid argon technology is used: a copper-LAr detector with parallel-plate geometry in the end-caps, and a dense LAr calorimeter with rod-shaped electrodes in a tungsten matrix for the forward calorimeter.

The hadronic calorimeter has to provide good containment for hadronic showers to provide precision measurements. It also has to stop all particles (but muons) going through it to minimize punch-through effects in the muon spectrometer (see Section 2.5). Hence, the thickness is one of the fundamental parameters that characterize it. ATLAS hadronic calorimeter provides approximately 10 interaction lengths (λ) of active material, and around 1.5λ of dead material at $\eta = 0$.

2.4.3 Minimum Bias Trigger Scintillators and Zero Degree Calorimeters

The Minimum Bias Trigger Scintillator (MBTS) [44] detectors are used to obtain a minimally biasing trigger selection. They consist of 32 scintillator counters, 2 cm thick, organised in two disks as shown in Figure 2.10. The two disks are installed, with their surface perpendicular to the beam line, on the inner face of the end-cap calorimeters cryostats, at z = ±3560 mm. Each disk is composed of an inner ($153 < |z| < 426$ mm) and an outer ($426 < |z| < 890$ mm) disk, both divided in 8 identical ϕ sectors.

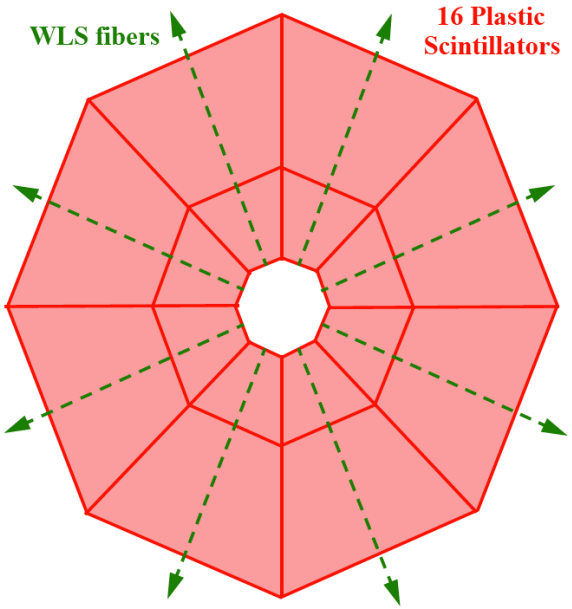

Figure 2.10. Schematization of an MBTS disk.

When stimulated by a particle flow, the scintillators emit light, that is then

amplified and read out by the Tile Calorimeter electronics. A MBTS hit is defined as a signal above a 60 mV threshold. A description of the MBTS trigger system is provided in Section 2.6.1.

In addition, in order to select *PbPb* interactions with minimal bias, two Zero-Degree Calorimeters (ZDCs) have been placed in ATLAS, at 140m from the collision point, along the z axis. These detectors are used to detect neutrons and photons at $|\eta| > 8.3$. The ZDCs have been used in heavy ion collisions studies, and notably in the analysis presented in Chapter 6.

2.5 Muon Spectrometer

The ATLAS Muon Spectrometer (MS) system [45], shown in Figure 2.11, is instrumented with separate trigger and high precision chambers, immersed in the magnetic field provided by the superconducting air-core toroid magnets, described in Section 2.2. The magnetic field allows the measurement of the transverse momentum of muons passing through the spectrometer, and is provided by the barrel toroid over the range $|\eta| \leq 1$, by the end-caps magnets in the range $1.4 \leq |\eta| \leq 2.7$, and by the combination of the two fields in the so-called transition region, over $1 \leq |\eta| \leq 1.4$. Such a configuration provides a field that is orthogonal to the muon's trajectory in most of the cases, deflecting it along the longitudinal plane.

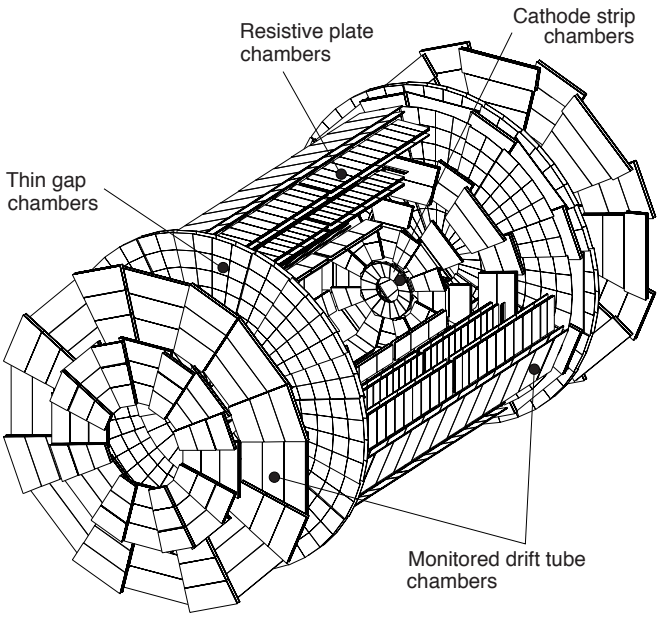

Figure 2.11. Sketch of the muon spectrometer, the four different chamber technologies are indicated.

The precision measurement of the track parameters is provided, up to $|\eta| < 2$, by Monitored Drift Tubes (MDTs). The MDT chambers are composed by aluminium

tubes of 30 mm diameter and 400 μm thickness, with a 50 μm diameter central wire. The tubes contain a non-flammable mixture of Argon and CO_2 at high pressure (3 bar). The single-wire resolution of MDT chambers is 80 μm.

At large pseudo-rapidities, where a more radiation resistant technology is needed, the higher granularity Cathode Strip Chambers (CSCs) are used, and provide measurements up to $|\eta| \leq 2.7$. CSC chambers are multi-wire proportional chambers. The readout is performed using strips forming a grid on the cathode plane, both in the parallel and orthogonal direction with respect to the wires. The position resolution provided by this detector are of approximately 60 μm

In the barrel region the spectrometer chambers are arranged in projective towers on three cylindrical layers, or stations, concentric with the beam axis, at radii of about 5, 7.5 and 10 meters. In the end-caps they are installed vertically, forming four disks at 7, 10, 14 and 21-23 meters from the interaction point. The chambers provide almost complete coverage of the pseudo-rapidity range $1 < |\eta| < 2.7$. There is an efficiency drop corresponding to $\eta = 0$, where an opening was built for the passage of cables and services of the ID, cryostats and calorimeters.

The trigger system chambers cover the pseudo-rapidity range $|\eta| \leq 2.4$. In the barrel Resistive Plate Chambers (RPC) are used, whereas in the end-caps Thin Gap Chambers (TGC) are used. In the barrel there are three stations of RPC, located on both sides of the middle MDT station, and inside the outer MDT station. In the end-cap regions three stations of TGCs are used, located near to the middle MDT station.

The basic RPC unit is composed by two parallel resistive bakelite plates defining a 1 mm gas gap, filled with a gas mixture (97% $C_2H_2F_4$ and 3% C_4H_1O). The system provides a time resolution of 1.5 ns. TGCs are multi-wire proportional chambers using a gas mixture of CO_2 and $n - C_5H_{12}$. They provide a time resolution of about 5 ns.

2.6 Trigger System

The LHC design bunch-crossing rate is of approximately 40 MHz, with an average of 25 interactions per bunch-crossing at the design instantaneous luminosity of $10^{34}\,\mathrm{cm}^{-2}\mathrm{s}^{-1}$, for a total rate of $\sim$ 1 GHz. On the other hand, the event rate that can be written on disk is of approximately 200 Hz, corresponding to an average data rate of $\sim$300 MB/s. This means that a reduction of the rate of the order of 10^6 needs to be applied on the events, before the data writing process. During runs with instantaneous luminosity $\sim 10^{32}\,\mathrm{cm}^{-2}\mathrm{s}^{-1}$, the average event size recorded was $\sim$ 1.3 MB.

The rate reduction is applied online on the events by the ATLAS trigger and data acquisition systems [46]. In ATLAS the online selection process is performed on three levels, as shown in Figure 2.12. Each of the levels contributes to reduce the event flow refining the previous level's cuts or, in some cases, introducing new selection criteria.

The first level trigger (L1) [47] can receive in input a maximum rate of about 75 kHz, and has to make its event selection in less than $\sim$ 2.5 μm because of the high bunch-crossing frequency. In order to meet the very limited time available, the first level trigger selection is hard-ware based. The L1 operates in particular

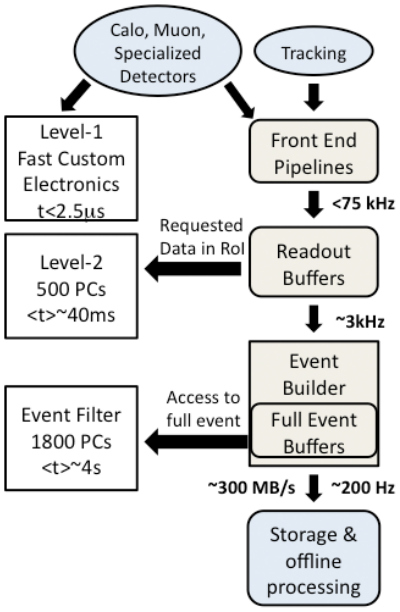

Figure 2.12. Diagram representing the ATLAS trigger system.

in the muon spectrometer, using only RPCs in the barrel regions and TGCs in the end-cap regions (described in Section 2.5), and in the calorimeters, using a reduced granularity, integrating on blocks of cells to reduce the time needed for the readout. The L1 triggers identify Regions of Interest (RoI) within the detector to be investigated by the next trigger levels.

The second (L2) and third level, also called Event Filter (EF), form the High Level Trigger (HLT) system [48]. They make use of all of the ATLAS sub-detectors using them with full-granularity, and combining their information to get higher precision measurements. Reconstruction and selection of the events is performed by software algorithms running, for both levels, on the same computer farms. The software algorithms allow to get a more precise estimate of the particles' parameters with respect to the previous level, and to apply a more sophisticated selection on them in the limited time at disposal. The L2 has to apply the selection within 20 to 40 ms, whereas the EF has a few seconds of time to confirm the second level decision. During runs with instantaneous luminosity $\sim 10^{32}\,\mathrm{cm}^{-2}\mathrm{s}^{-1}$, the average processing time of the L2 was $\sim$ 50 ms/event, whereas the one of the EF was $\sim$ 0.4 s/event.

A 15 hours long pp run corresponding to an integrated luminosity of 6.4 pb^{-1} and instantaneous luminosity ranging from $180 \times 10^{10}\,\mathrm{cm}^{-2}\mathrm{s}^{-1}$ to $85 \times 10^{10}\,\mathrm{cm}^{-2}\mathrm{s}^{-1}$ was used to study the general performances of the ATLAS trigger in 2010 [49]. In Figure 2.13 some of the results of this study are shown. On the left, the total trigger rates for all three levels as a function of the instantaneous luminosity shows that the trigger rate is kept stable at $\sim$ 30 kHz for L1, $\sim$ 4 kHz for L2 and $\sim$450 Hz for EF, well within the expectations. On the right, the fraction of CPU used in the HLT farm shows that the HLT farm is well within its CPU capacity. Discontinuities in the rate and CPU usage are due to changes in the prescale, used to control the trigger rate.

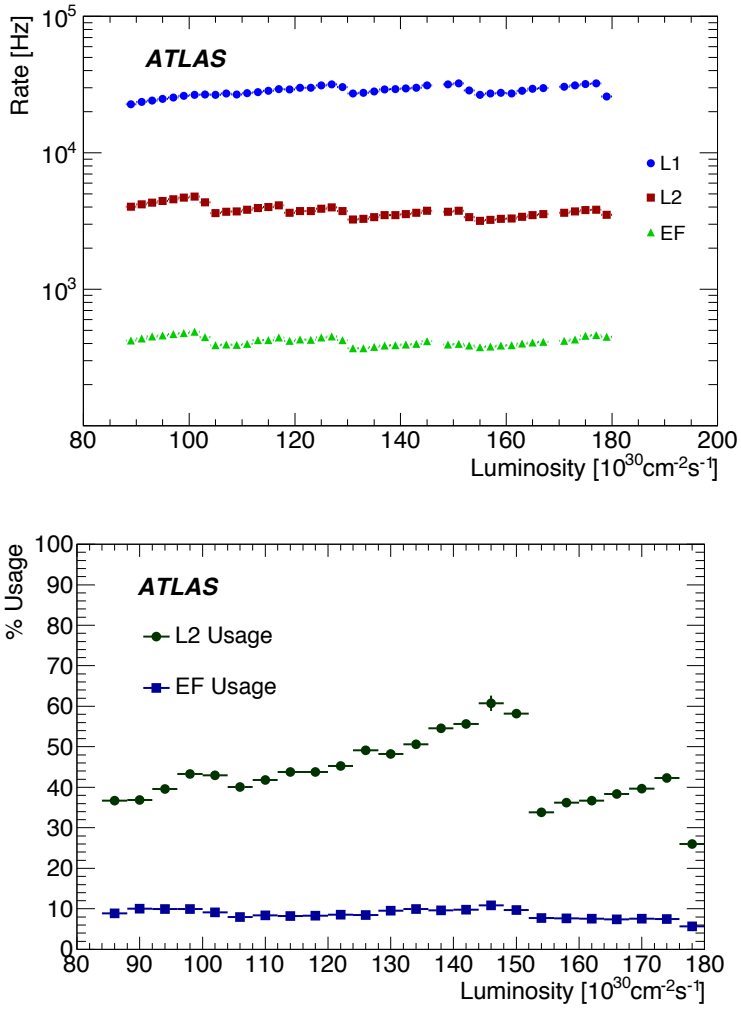

Figure 2.13. Total trigger rates (top) and fraction of HLT CPU usage (bottom) as a function of istantaneous luminosity in a 2010 sample run.

2.6.1 Minimum Bias Trigger

The minimum bias trigger [49] makes use of the MBTS system described in Section 2.4.3. It is used to provide a trigger selection of inelastic interactions as inclusive as possible, and was used in particular in early *pp* and *PbPb* analyses, when the trigger rate was not too elevated.

The MBTS trigger works on a single hard-ware based level. Its basic requirement is that at least one of the 32 MBTS counters on either side of the detector emits a signal above the 60 mV threshold. A coincidence with colliding bunches is also required. Additional requirements have been optimized for the different analysis.

The efficiency of the MBTS trigger selection was measured in inelastic *pp* collisions at $\sqrt{s} = 7$ TeV [49]. The result of this study is shown in Figure 2.14, where the efficiency as a function of the number of tracks in the event passing an offline selection is provided. This efficiency is computed using a random L1 trigger and requirements on the space-points measured in the ID at HLT, and applying offline a

quality selection on the events. The efficiency of the MBTS trigger is measured to be ∼100%, except for events with lower track multiplicity.

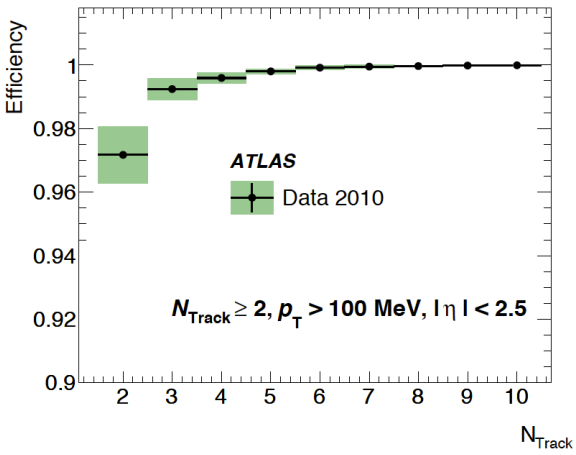

Figure 2.14. Efficiency of the MBTS trigger, that requires one hit above threshold in the MBTS in coincidence with the colliding bunches, as measured on inelastic *pp* collisions at $\sqrt{s} = 7$ TeV. The vertical bars represent the statistical uncertainty, whereas the shaded areas represent the statistical and systematic uncertainties added in quadrature.

2.6.2 Muon Trigger

Since some of the presented analyses rely on the muon trigger [50], a more detailed description of this system will be provided below. The muon trigger is divided in three levels following the general structure of the ATLAS trigger.

Level 1

At the L1, muons are triggered using RPC in the barrel region ($|\eta| < 1.05$) and TGC in the end-cap regions ($1.05 < |\eta| < 2.4$), as described in Section 2.5. The trigger chambers provide a rough measurement of the muon candidate p_T, η and ϕ. The geometrical coverage of the muon trigger system is $\sim 99\%$ in the end-caps, and $\sim 80\%$ in the barrel due to the $\eta = 0$ crack. The trigger chambers are arranged in three planes both in the barrel and in the end-caps. The coincidences of signatures between the muon planes are used to identify the muon candidates.

The muon search starts from hits in a specific muon trigger plane, called *pivot plane* (corresponding to the middle chambers in the RPCs and the outer ones in the TGCs), and continues to search for coincidences in additional planes, called *low p_T confirmation* (corresponding to the inner chambers in the RPCs and the middle ones in the TGCs) or *high p_T confirmation* (corresponding to the outer chambers in the RPCs and the inner ones in the TGCs). These algorithms are implemented in a similar way in the RPCs and TGCs. In the RPC system, a low-p_T trigger logic is obtained by requiring a coincidence of hits in at least three of the four layers of the two inner planes, whereas the high-p_T trigger logic is given by the requirement of a low-p_T trigger combined with hits in one of the two layers of the high-p_T confirmation plane. In the TGC system, the low-p_T trigger logic is defined as in the RPCs, while

the high-p_T one requires at least one ϕ-strip layer and two out of three wire layers in coincidence with the low-p_T trigger in the high-p_T plane. The low-p_T and high-p_T trigger logics in both RPC and TGC systems are schematized in Figure 2.15.

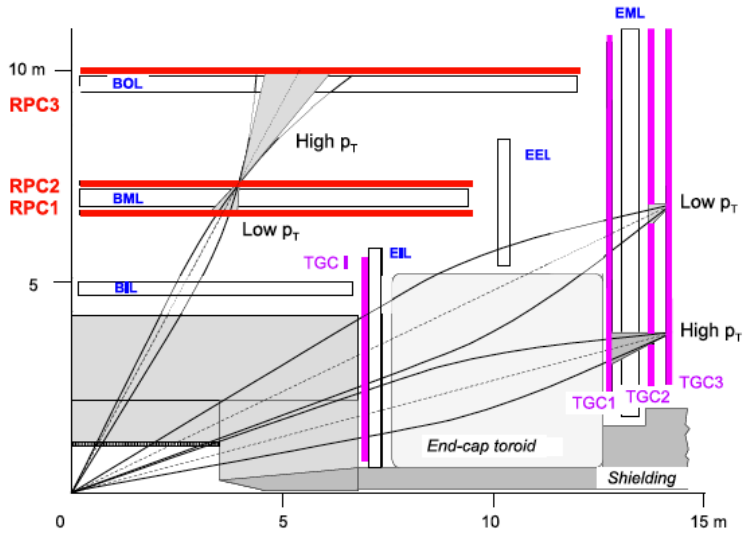

Figure 2.15. Section view of the ATLAS L1 muon trigger chambers.

According to what described above, six main L1 trigger thresholds have been defined for the 2010 data taking period, corresponding to three low p_T (L1_MU0, L1_MU6 and L1_MU10) and three high p_T (L1_MU0_COMM, L1_MU15 and L1_MU20) triggers. The lowest trigger thresholds, in both low-p_T (L1_MU0) and high-p_T (L1_MU0_COMM) logics, only require that the hits in the different planes are in the same trigger tower, within $\eta \times \phi \sim 0.1 \times 0.1$. The efficiencies of these triggers were measured on the 2010 data sample for the different p_T thresholds [49]. Results for RPC (top) and TGC (bottom) triggers are shown in Figure 2.16. In the barrel region, the efficiency was computed using an orthogonal L1 calorimeter trigger, whereas in the end-cap regions the tag and probe method was used on $J/\psi \to \mu\mu$ and $Z \to \mu\mu$ decays. The label MUX corresponds to the different triggers, where X indicates the nominal p_T threshold relative to the efficiency curve.

Two different *plateaux* are found in the RPC (TGC) efficiency curves, one at ∼80% (∼95%) for the low-p_T triggers, and one at ∼65% (∼90%) for the high-p_T ones. The plateaux of the low-p_T RPC triggers are as expected from the geometrical acceptance of the L1 trigger in the barrel. The RPC high-p_T threshold are less efficient: part of this (∼6%) is due to an intrinsic reduced geometrical acceptance of high-p_T thresholds, the rest of the discrepancy depends on detector inefficiencies that should be improved in 2011. As for the TGCs, the plateaux of the distributions are as expected from their geometrical acceptance.

High Level Trigger

The HLT is composed by two independent trigger levels: the Level 2 and the Event Filter. In addition to the L1 RPCs and TGCs, the HLT makes use of the MDT precision chambers, covering a range of $|\eta| < 2.4$. The L2 algorithms are designed

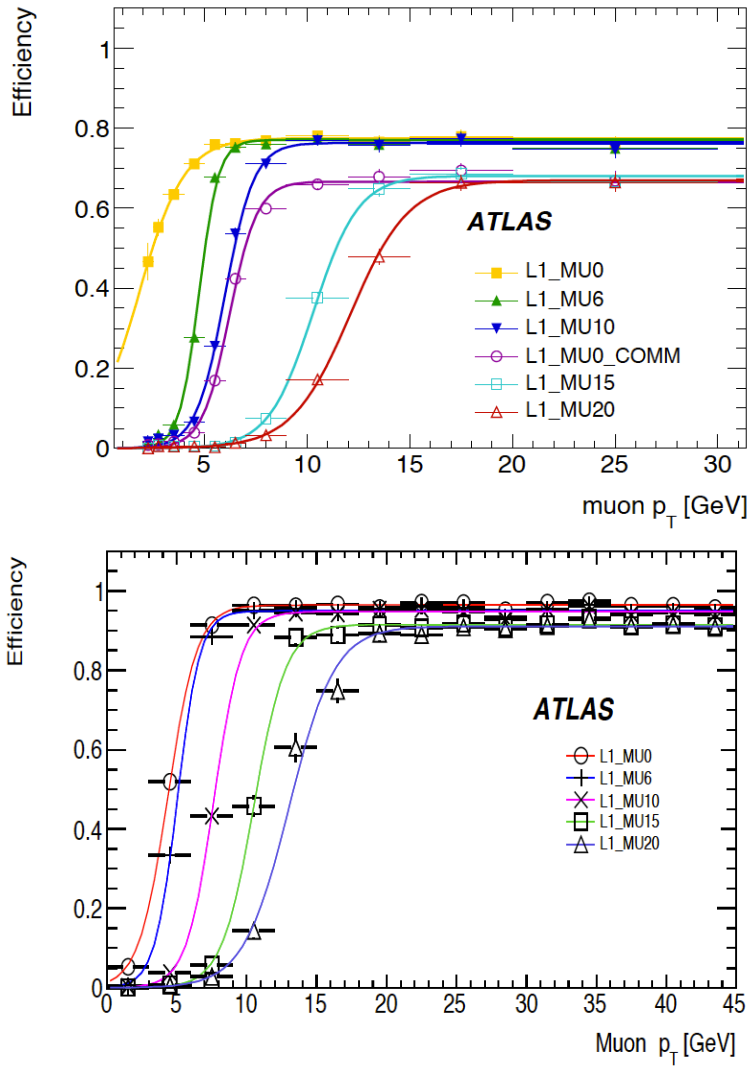

Figure 2.16. L1 trigger efficiency computed with respect to the combined muons reconstructed offline for different RPC (top) and TGC (bottom) trigger thresholds. A Fermi function is fitted to each of the trigger efficiency measurement.

to be fast, whereas the EF algorithms, having more time to take a decision, rely on offline muon reconstruction software.

The L2 algorithms search for muon candidates within the Region of Interest defined by the L1 trigger. L2 makes use of three sequential algorithms, that build a muon track from the outside muon spectrometer chambers to the inner detector ones:

- *L2 MS-Only*: The MS-Only algorithm uses, to reconstruct the muon track, only the signals contained in the RoI defined by the L1 in the muon spectrometer. A fit is performed on the spectrometer track, where the fitting algorithm uses Look Up Tables (LUTs) to minimize the time needed in the process.

- *L2 Muon Combined*: This algorithm combines the MS-Only muon track with L2 ID tracks [51] reconstructed at the inner detector to form a muon candidate

with better track parameters resolution.

- *L2 Isolated Muon*: The muon isolation algorithm, starting from the combined muon built by the previous algorithm, makes use of calorimetric and tracking information in order to select only isolated muons. This algorithm is helpful especially to select high p_T muons from Z and W decays from the ones coming from b and c-quark semi-leptonic decays, which are produced within jets.

At the EF, the muon reconstruction starts from the RoI identified by the L1 and confirmed by the L2 to build a more refined muon track. Here three reconstruction strategies are used:

- *EF MS-Only*: Tracks are reconstructed at the muon spectrometer and extrapolated back to the nominal interaction point, forming a stand-alone muon track.

- *EF Combined*: MS-Only candidates are combined to ID tracks forming a combined muon candidate.

- *EF Inside-Out*: Independent strategy that builds a muon candidate starting from the inner detector tracks, extrapolating them to the entrance of the muon spectrometer chambers and searching for MS-only candidates to form combined muons.

The first two steps work as a chain, if no spectrometer muon is reconstructed, no combined muon can be built. On the other hand, the inside-out strategy is an independent reconstruction, and is used to highen the muon reconstruction efficiency, in particular for low p_T muons, or for muons that fall in the spectrometer inefficient regions. The overlap between the different reconstructions is then removed offline.

In Figure 2.17 the HLT efficiencies as a function of the offline reconstructed muon p_T in the barrel (top) and end-cap (bottom) regions obtained on 2010 data (black) and Monte Carlo (MC) (red) is shown [49]. The efficiency is computed for the HLT trigger with a nominal p_T threshold of 6 GeV (the lowest possible threshold being 4 GeV, determined by the L1 acceptance), using the tag and probe method on J/ψ and Z di-muon decays, with respect to offline reconstruction. Good agreement is found in data with the expected MC results.

2.6.3 B-Physics Trigger

The B-physics triggers [49] complement the low-p_T muon triggers applying additional invariant mass selections for J/ψ, Υ and B-mesons. There are two categories of B-physics triggers:

- *Topological Triggers*: Topological di-muon triggers start from two muon RoIs that have been found by the muon L1 and HLT (see Section 2.6.2). The B-physics algorithms in the HLT combine the information from the two muons fitting them to a common vertex in the hypothesis that the candidates come from a di-muon resonance. Requiring two muons at L1 reduces the rate with respect to the low-p_T single muon triggers, but also their efficiency.

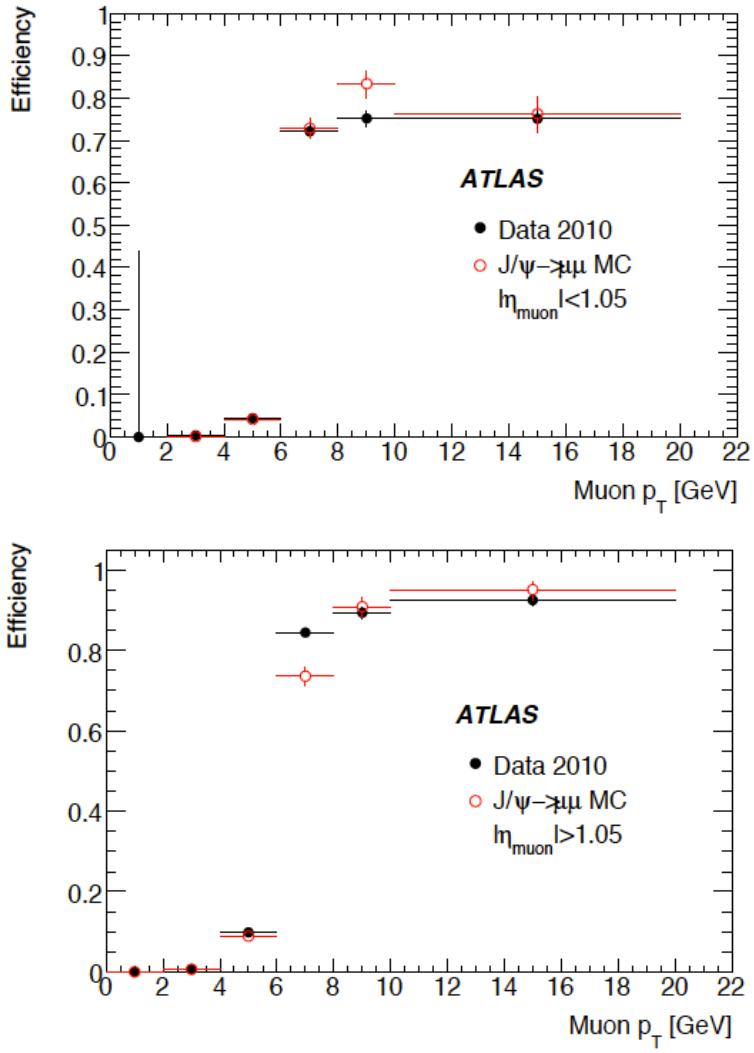

Figure 2.17. Trigger efficiencies for the 6 GeV nominal p_T threshold as a function of the offline reconstructed muon transverse momentum for $J/\psi \to \mu\mu$ decays in data and in simulation in the barrel (top) and end-cap (bottom) regions. Statistical uncertainties are represented by the vertical bars.

- *Single RoI Seeded Triggers*: These triggers start from a L1 muon and associate it to a second muon only at the HLT, highening the efficiency on signal events. At L2, tracks found in a region of $\Delta\eta \times \Delta\phi = 1.5 \times 1.5$ around the L1 muon are extrapolated to the muon spectrometer. The algorithm searches for muon spectrometer hits in correspondence to the extrapolated ID track, and if enough hits are found, the track is flagged as muon. No additional selection is applied at the EF.

For both strategies, additional selections can be applied on the charge, invariant mass or vertex quality of the di-muon pair. For example, the invariant mass cut used in 2010 for J/ψ triggers was: $2.5 < m_{\mu\mu} < 4.3$ GeV, very loose compared to the mass resolution of ∼40 GeV for the J/ψ mass peak.

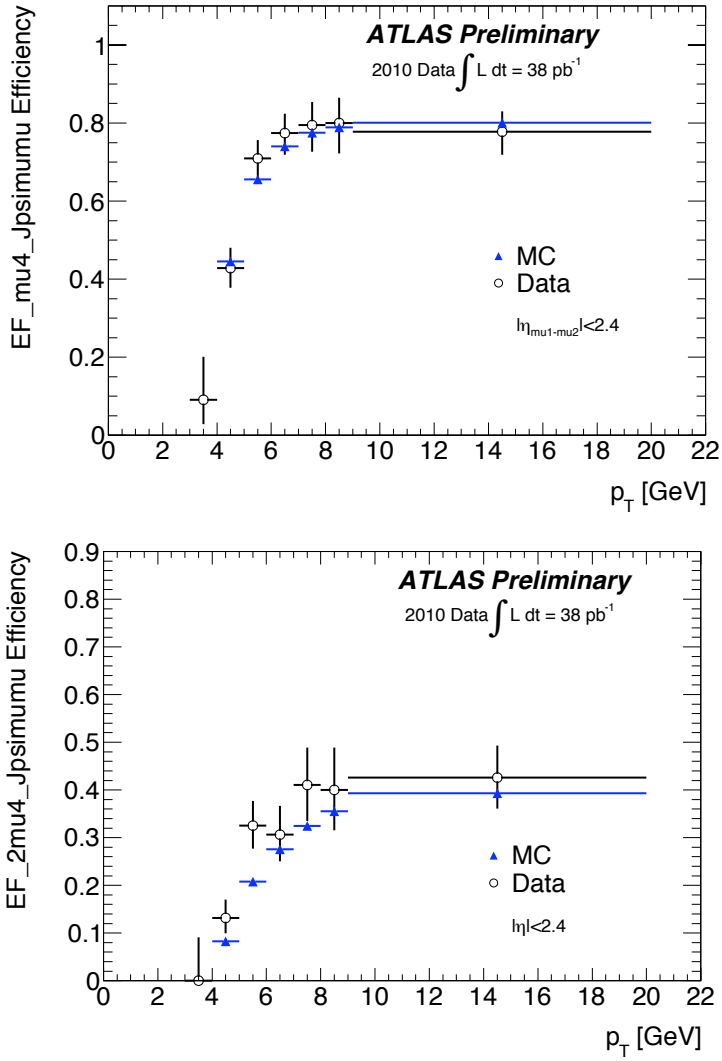

Figure 2.18. Efficiency in 2010 data (empty dots) and MC (blue triangles) of B-physics single RoI seeded (top) and topological (bottom) triggers corresponding to a 4 GeV nominal p_T threshold on one or both muons are provided as a function of the transverse momentum of the leading combined muon of the pair reconstructed offline.

The efficiencies obtained on 2010 data for the topological and single RoI seeded triggers, with one or both muon's transverse momentum of at least 4 GeV, are shown in Figure 2.18 as a function of the leading muon offline p_T respectively. The vertical error bars represent the statistical uncertainty on the measurements, whereas the systematic ones are estimated to be less than 1%. The efficiency estimated at plateau for the single RoI seeded trigger, for muons with $p_T > 8$ GeV, is found to be 0.787 ± 0.005 in data and 0.786 ± 0.003 in MC, whereas for topological trigger it is 0.41 ± 0.05 in data and 0.39 ± 0.04 in MC, statistical uncertainties only. The two strategies provide an almost fully overlapping sample of di-muon candidates, with the single RoI seeded trigger being more efficient in particular for very boosted J/ψ, for which the ΔR of the two muons is smaller than the L1 RoI dimension, but

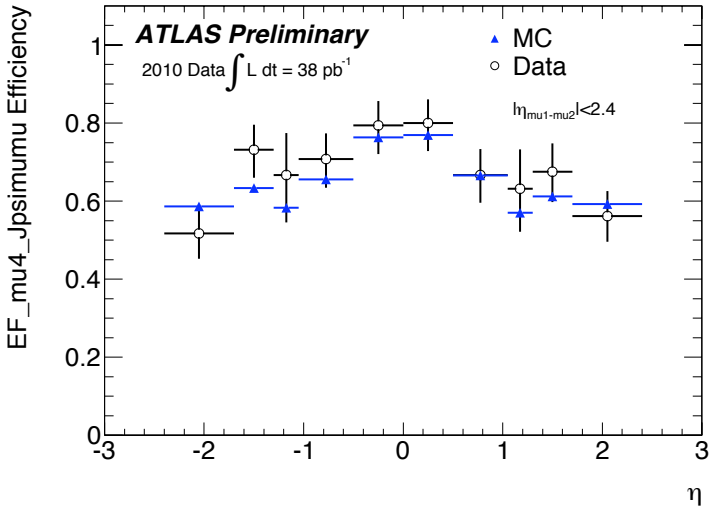

Figure 2.19. Efficiency in 2010 data (empty dots) and MC (blue triangles) of B-physics single RoI seeded trigger corresponding to a 4 GeV nominal p_T threshold on one of the muons is provided as a function of the η of the leading muon of the pair reconstructed offline.

corresponding also to a higher, not always sustainable, trigger rate.

For the single RoI seeded trigger, on the same data and MC samples, the efficiency as a function of the leading muon η is also shown in Figure 2.19, a similar distribution is obtained for the topological trigger. A reduction in efficiency at high η is given by the fact that all muon p_T are integrated in this distribution, and the end-cap detectors of the ATLAS muon spectrometer have an acceptance corresponding to a lower muon p_T threshold than the barrel region ones.

Chapter 3

Reconstruction

Track, vertex and muon reconstruction are critical for most of the physics studies performed in this thesis. This is all the more true in the case of $J/\psi \to \mu\mu$ reconstruction and of long-lived particles lifetime measurements. The muons momentum estimate is the main ingredient of the J/ψ resonance invariant mass reconstruction and, on the other hand, a correct primary and secondary vertex identification is fundamental for all lifetime studies.

In this chapter a description of the ATLAS tracking, vertex and muon reconstruction algorithms is provided, and their performances on first collision data are shown. A full account of the ATLAS reconstruction and its expected performance, estimated using simulation, can be found in [52]. Moreover a first report on the ATLAS performances on first collision data can be found in [53].

3.1 Track Reconstruction

The track reconstruction [52] in ATLAS uses the Pixel, SCT and TRT sub-detectors described in section 2.3. It happens on three levels:

- *Pre-processing*: the raw data from the pixel, SCT and TRT detectors is converted into clusters, space-points and calibrated drift circles respectively.
- *Track finding*: different tracking algorithms are employed. The default one finds track seeds combining space-points in the three pixel layers and in the first SCT layer. These seeds are then extended to all the SCT layers, to form a track candidate, as schematized in Figure 3.1. The selected tracks are then extended to the TRT, and refitted with the full ID information. Hits in the TRT extended track that worsen the fit quality are not included in the final track fit, but are kept, labelled as outliers of the track, to provide information for the offline rejection of π and k through the reconstruction of the distinctive kink in the decay.

  A complementary track finding strategy looks for unused track segments in the TRT. The found segments are extrapolated to the silicon detectors to improve the tracking efficiency on secondary tracks from conversions or long-lived particles decays.

The track reconstruction performance on data was first validated using test beam [54] and cosmic-ray commissioning runs [55]. Additional studies have been

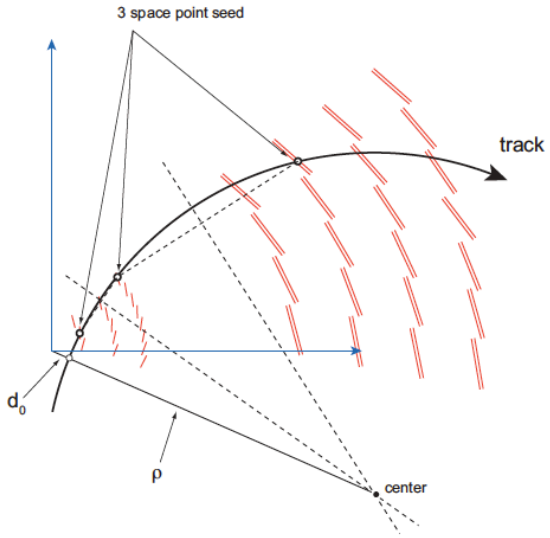

Figure 3.1. Sketch of the technique used to estimate the track parameters of the seed.

performed on collision pp [56] and $PbPb$ data, some results of the latter studies are shown here.

In Figure 3.2, the transverse (top) and longitudinal (bottom) impact parameters of tracks in 2010 $PbPb$ collision data (black dots) and in MC (yellow histogram) are compared. In Figure 3.3, the number of pixel hits (top) and the average number of pixel hits versus η are shown in $PbPb$ collision data (black dots) and MC (yellow histogram). The striking agreement between data and MC distributions highlight the very good understanding of the ID and tracking reconstruction already reached in 2010, even in the difficult heavy ions environment.

3.2 Primary Vertex Reconstruction

The reconstruction of primary vertices [57] is, in ATLAS, organised in two steps:

- An iterative primary vertex finding algorithm associates the reconstructed tracks (see section 3.1), passing a quality selection, to the vertex candidates;
- A vertex fitting algorithm finds the vertex position and error matrix.

A constraint to the beam-spot position, estimated as described in [58], is used in both steps, run by run. The transverse beam-spot width in 7 TeV runs varies, in 2010 data, between 60 μm in the first runs and 30 μm in the latest ones with squeezed beams. This constraint has an impact especially on low multiplicity vertices, where the transverse resolution is dominated by the one of the beam-spot. In the longitudinal direction, instead, the constraint has nearly no effect since the resolution on the beam-spot z coordinate is much worse than the one of the reconstructed primary vertex.

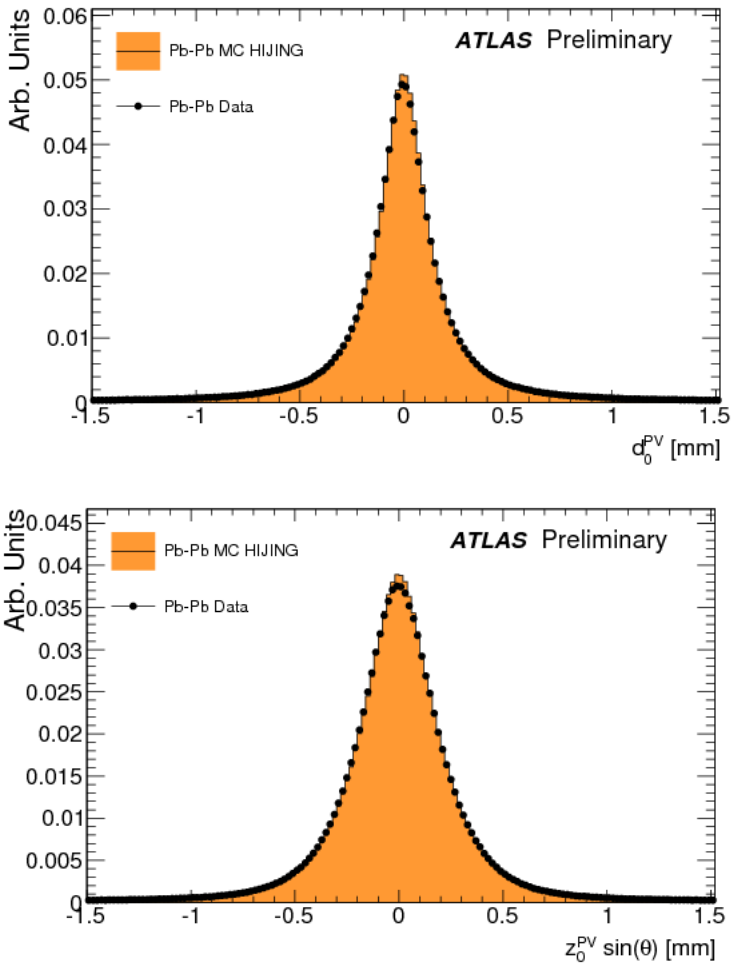

Figure 3.2. Top: transverse impact parameter (d_0) of tracks in 2010 $PbPb$ collision data (black dots) and MC (yellow histogram). Bottom: longitudinal impact parameter (z_0) of tracks in 2010 $PbPb$ data (black dots) and MC (yellow histogram)

The two dimensional distributions of the vertex position as measured [57] on approximately $3.4 \cdot 10^6$ 7 TeV minimum bias events taken at ATLAS in the spring of 2010 are shown in Figure 3.4, projected both in the transverse plane (top) and in the $x - z$ plane (bottom). An average beam size of 24 μm (40 μm) is measured on the x (y) coordinate, whereas the size of the z coordinate is measured to be 27.9 mm.

The resolutions vary with the number of tracks associated to the vertex, and with their sum of transverse momenta, as shown, for the x coordinate, respectively in the top and bottom plots in Figure 3.5. For events with at least 70 tracks, or $\sqrt{\sum_{trk} p_T^2} > 8$ GeV a resolution of $\sim 30\,\mu$m is measured in the transverse plane, and of $\sim 50\,\mu$m in the longitudinal direction. In 2011, vertex reconstruction performances are much better due to the improved ID alignment and material description in the MC simulation, but the new results on vertex reconstruction will not be presented here since the analyses presented in the next chapters use the 2010 data sample.

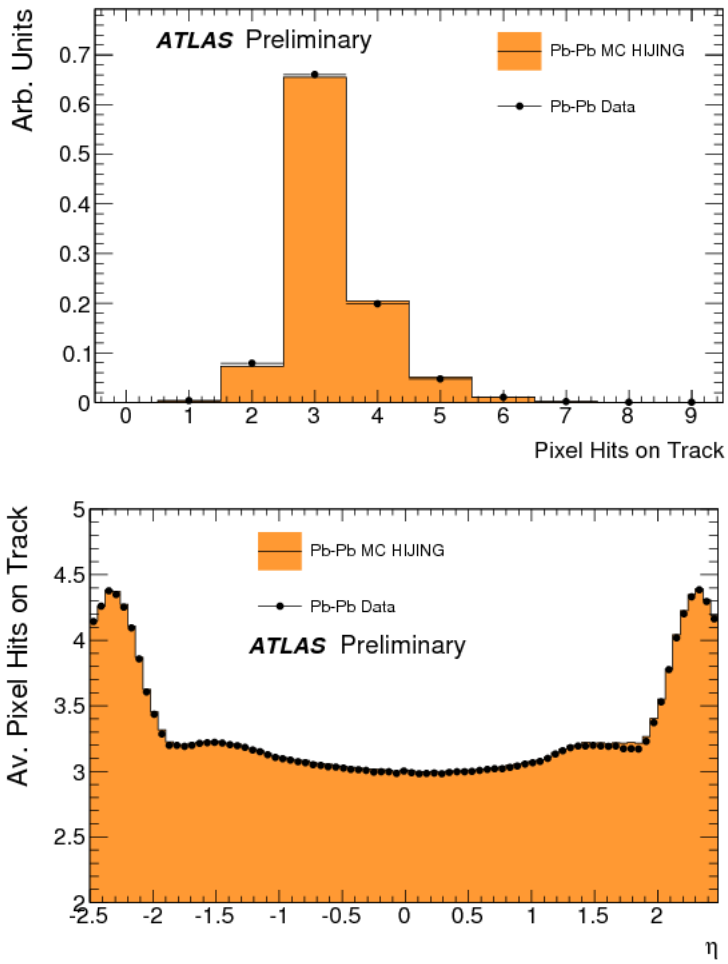

Figure 3.3. Top: number of pixel hits on tracks in 2010 *PbPb* data (black dots) and MC (yellow histogram). Bottom: average number of pixel hits on tracks as a function of η in 2010 *PbPb* collision data (black dots) and MC (yellow histogram)

3.3 Muon Reconstruction

In ATLAS different types of muon reconstruction [59] strategies are used, each optimized for different needs. These can be separated in four categories:

- *Stand-Alone Muons*: Stand-Alone (SA) muons are reconstructed using only the muon spectrometer information. The segments found in the three muon stations are fitted together to form a full track. The track is then back-extrapolated to the beam line, taking into account both multiple scattering effects and the energy loss in the calorimeter.

  SA muons are reconstructed in a larger η region, up to $\eta \sim 2.7$, but suffer from the spectrometer inefficient regions at $\eta \sim 0$ and at $\eta \sim 1.2$. SA reconstruction also is more prone to accept muons produced in the calorimeters, from π and K decays, that are a background for most physics analysis.

- *Combined Muons*: Combined (CB) muons are built matching in η, ϕ and p_T

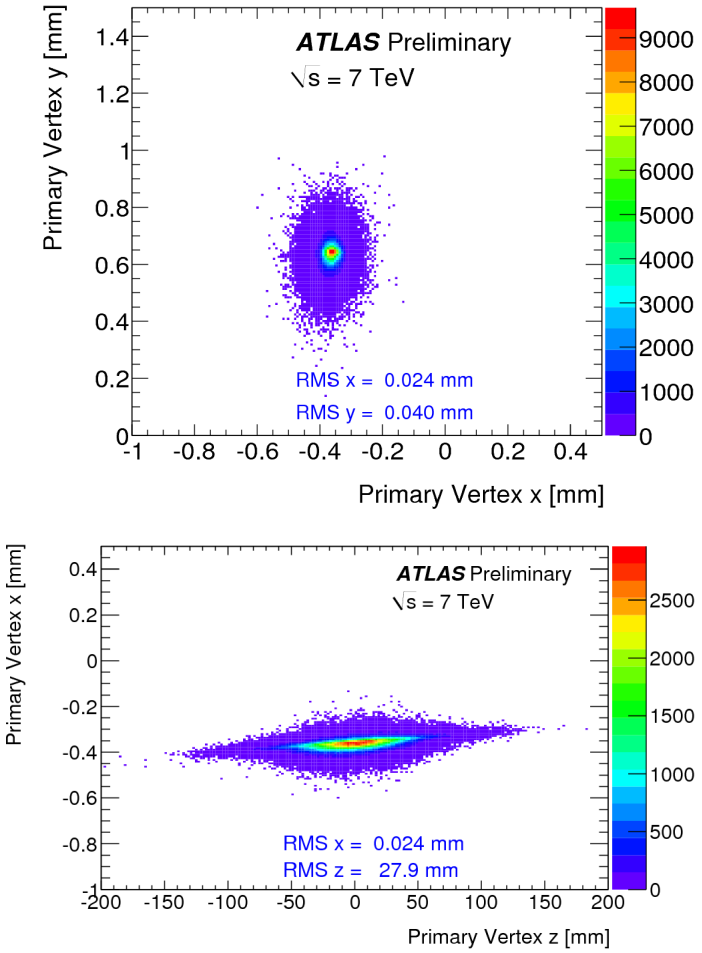

Figure 3.4. Two-dimensional distribution of reconstructed primary vertices in 7 TeV data in the $x - y$ plane (top) and in the $x - z$ plane (bottom).

the stand-alone ones with ID tracks. The CB muons have a better resolution on the muon parameters, in particular a more precise measurement of the p_T is performed thanks to the longer lever arm and to the two independent measurements. They also have high precision vertex parameters, provided by the ID track. The rejection from fake muons coming from decays-in-flight is introduced by the combination process.

- *Tagged Muons*: SA and CB algorithms have a lower reconstruction efficiency for low momentum muons, as these might not penetrate the outermost calorimeter layers, or might be deflected by the toroids magnetic field and not reach the spectrometer middle stations. The tagging algorithms provide a more efficient measurement in that momentum range and in the cracks of the muon spectrometer, using an inside-out strategy. The algorithms extrapolate the ID tracks to the entrance of the muon chambers, and search for nearby hits in the spectrometer.

- *Calorimeter Muons*: Calorimeter muons' algorithms also use an inside-out

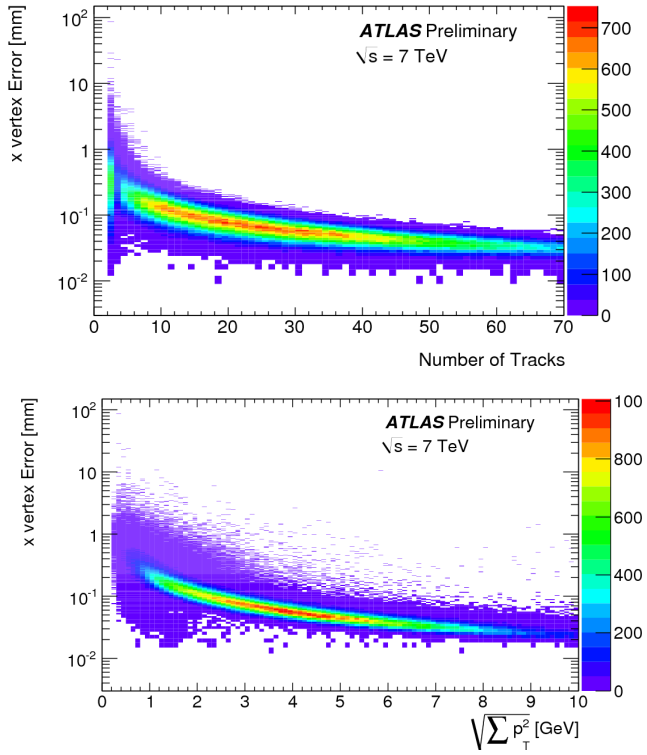

Figure 3.5. Two-dimensional distribution of reconstructed vertex errors in 7 TeV data as a function of the number of tracks (top) and of the square-root of the sum of square transverse momenta of the tracks ($\sqrt{\sum_{trk} p_T^2}$ (bottom).

strategy, where ID tracks are matched to calorimetric deposits compatible with a muon signature.

In ATLAS muon reconstruction is performed by two families of algorithms, Muid [60] and Staco [61], and each family includes one algorithm per reconstruction strategy. The two families have proven to have very similar performances, both in simulation and in data studies. Staco is the default for physics studies.

Reconstruction Efficiency Performances

The efficiency obtained with the ATLAS muon reconstruction was studied on 2010 data using the tag and probe method on muons coming from J/ψ [62] and Z [63, 64] decays. In this method muon pairs are selected by requiring a well reconstructed muon, the *tag*, and an ID track, the *probe*, consistent with coming from a $J/\psi \to \mu^+\mu^-$ decay. This way, the probes are selected independently of the muon spectrometer and can thus be used to measure the efficiency for reconstructing a muon based on the MS. As we are mostly interested in the low p_T region for our studies, the former will be discussed. In Figure 3.6, the muon efficiencies obtained studying the $J/\psi \to \mu\mu$ events in a 2010 data sample of $\sim 3.1\ pb^{-1}$ are shown as a function of the muon p_T (top) and $q \times \eta$ (bottom). Here q is the muon charge, and it is multiplied by the muon pseudo-rapidity to compensate for a mild asymmetry in η for differently charged muons.

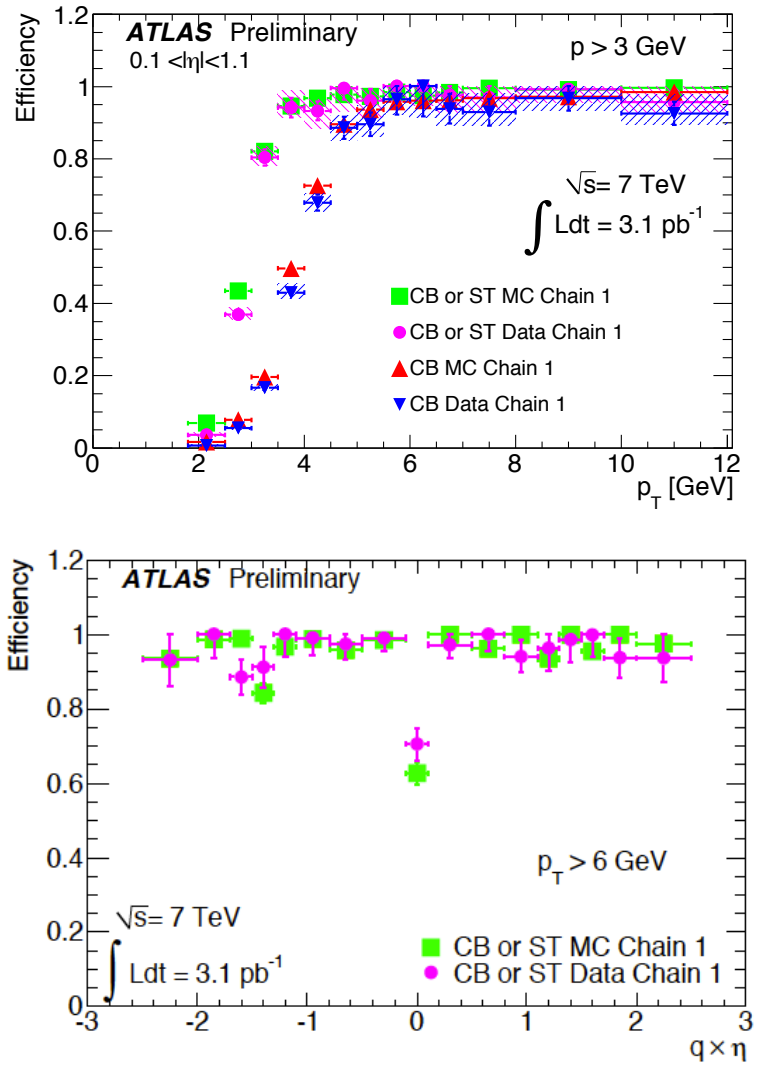

Figure 3.6. Top: efficiencies of Staco (Chain 1) combined (CB) and combined and tagged (CB or ST) muons in 2010 $J/\psi \to \mu\mu$ data and MC as a function of the reconstructed muon p_T. Bottom: efficiencies of Staco (Chain 1) combined and tagged (CB or ST) muons in 2010 $J/\psi \to \mu\mu$ data (pink dots) and MC (green squares) as a function of the reconstructed muon η times its charge.

In the top plot, the efficiencies as a function of the muon p_T, when using only combined muons (blue triangles) or combined and tagged muons (pink dots) in data and superimposed the same distributions as found in MC (respectively red triangles and green squares). The agreement between data and MC is rather good over the whole range. As said before the use of tagged muons improves the efficiency in the low p_T region. In the bottom plot the efficiencies obtained on the same sample as a function of the muon pseudo-rapidity using both combined and tagged muons in data (pink dots) and MC (green squares). Here as well the agreement is very good.

Momentum Measurement Performances

In Figure 3.7 the resolution on the transverse momentum measurement performed by the MS algorithms is shown, extracted using the combined fitting technique described in [65]. The momentum resolution is estimated on the full 2010 data sample, of ~ 40 pb^{-1}, and provided as a function of the muon p_T for muons falling inside the spectrometer barrel region. The resolution curves for experimental data are compared to those from the uncorrected parameters obtained for the simulation. The results on collision data are also compared with the resolution curves obtained from analysis of cosmic ray muons. These results, which are improving fast with the detectors alignment and calibration, where already at a good level during the 2010 data taking period.

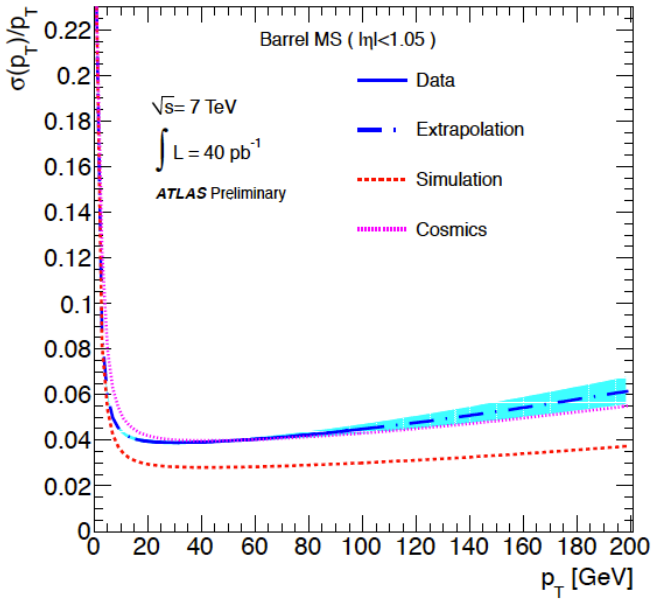

Figure 3.7. MS resolution p_T curve for muons within the barrel region. The solid blue line shows determinations based on data and is continued as dashed line for the extrapolation to p_T ranges not yet accessible. The shaded band represents the sum in quadrature of the statistical and systematic uncertainties. Also, the curve obtained using cosmic ray data (purple dotted line) is overlaid for comparison.

3.4 J/ψ Reconstruction

Reconstruction of the J/ψ resonance in di-muon decays makes use of the high quality track, vertex and muon reconstruction performed at ATLAS and briefly described in sections 3.1, 3.2 and 3.3, and is a useful tool on its own, for the detector, trigger and reconstruction algorithms commissioning. It also represents a starting point for many physics analyses, some of which will be presented in the next chapters of this thesis.

At ATLAS, for J/ψ reconstruction, only muons associated to ID tracks, i.e. combined or tagged muons, are used. This is because, in order to build the J/ψ

candidate's secondary vertex, a precise estimate of the tracks' vertices coordinates is needed. The quality requirement applied on the two muons varies depending on the analysis' needs. In general, though, the candidates pairs with muon tracks associated to two different reconstructed primary vertices are rejected, in order to reduce the combinatorial background due to pile-up events. The fraction of dimuon candidates passing the selection that have the two muons coming from different vertices is very small, less than one percent.

The ID tracks associated to the two muons forming a dimuon candidate, passing some quality selection, are then fitted to a common vertex using the ATLAS offline vertexing tools based on the Kalman filtering method [66]. For low momentum muons, the helix parameters are completely dominated by the ID measurement, hence, in the J/ψ analyses presented, only ID track parameters are used. No constraints on the mass or pointing to the primary vertex are applied to the fit, and only a loose requirement on the secondary vertex χ^2 is by default applied ($\chi^2 < 200$). Those pairs that successfully form a common vertex are considered as J/ψ candidates. Whenever more than on candidate is found that passes the analysis selection, all of the candidates are included in the studies.

The invariant mass distribution of the J/ψ candidates selected in the whole 2010 data sample is shown in Figure 3.8 (black dots). This distribution is fitted using a Gaussian function to describe the signal, and a third order polynomial to describe the combinatorial background. A second peak at higher mass, fitted with a second Gaussian function, corresponds to the $\psi(2S)$ resonance. The mass fit projection is represented as a red continuous line, whereas the background component of the fit is a dashed blue line.

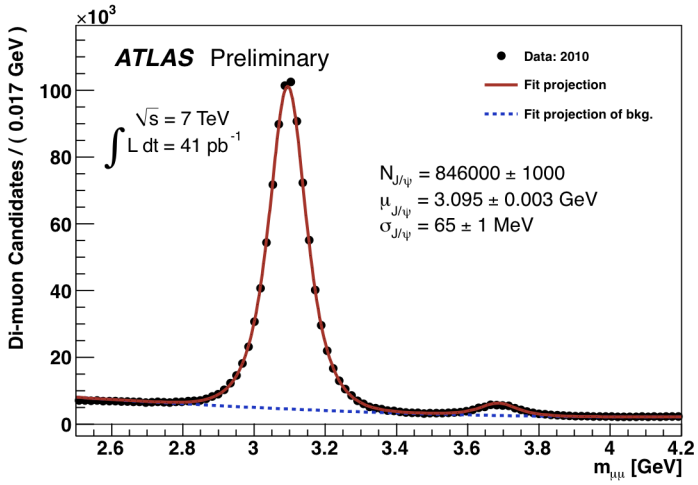

Figure 3.8. $J/\psi \to \mu\mu$ candidates invariant mass distribution found in the 41 pb^{-1} of 7 TeV pp data collected by ATLAS in 2010. Superimposed, the fit projections: the full mass PDF (red continuous line) and the background component (blue dashed line).

From the fit, the main parameters of the J/ψ resonance as measured at ATLAS are extracted. The resonance mass is found to be equal to $m_{J/\psi} = 3.095 \pm 0.003$ GeV, in good agreement with the Particle Data Group (PDG) [67] world average. Moreover the peak width, dominated by the detector resolution, is $\sigma_{J/\psi} = 65 \pm 1$ MeV, as

expected from the MC simulation. These results tell us that after only a year of data taking, the muon and tracking systems and reconstruction provide reliable measurements, thanks to a very successfull initial commissioning phase.

Chapter 4

Inclusive J/ψ Production Cross-Section and Non-prompt to Prompt Fraction Measurements

4.1 Introduction

Despite being among the most studied of the bound–quark systems, there is still no clear understanding of the mechanisms in the production of quarkonium states like the J/ψ that can consistently explain both the production cross-section and spin-alignment measurements in e^+e^-, heavy-ion and hadron-hadron collisions (see review articles [68] and references therein).

Data obtained by the LHC collaborations can help to test existing theoretical models of both quarkonium production and b-production in a new energy regime, at higher transverse momenta and in wider rapidity ranges with respect to previous studies. Furthermore, quarkonium production in pp collisions plays a key role as a reference point to understand heavy ion collisions and to understand the interplay between production and suppression mechanisms in such collisions (see Chapter 6).

In this chapter a measurement of the inclusive J/ψ production cross-section (see Section 4.4) and of the production fraction f_B (see Section 4.5), hereafter referred to as the *non-prompt fraction*, of non-prompt J/ψ to inclusively-produced J/ψ:

$$f_B \equiv \frac{\sigma(pp \to B + X \to J/\psi X')}{\sigma(pp \xrightarrow{\text{Inclusive}} J/\psi X'')} \tag{4.1}$$

are presented. The non-prompt fraction measurement, fundamental in order to compute the J/ψ prompt and non-prompt production cross-sections starting from the inclusive one, performed at ATLAS has been under my supervision, more emphasis will thus be dedicated to it. Both measurements are performed in the decay channel $J/\psi \to \mu^+\mu^-$ as a function of both J/ψ transverse momentum and rapidity, with an integrated luminosity of up to 2.3 pb^{-1}.

The inclusive cross-section and non-prompt fraction measurement results are presented in sections 4.4.4 and 4.5.5 respectively, and compared to the results

obtained by the CMS Collaboration [69] with 314 nb^{-1} of integrated luminosity and those from the CDF Collaboration [70] where appropriate. The J/ψ prompt and non-prompt production cross-sections obtained combining these two measurements are shown in Section 4.6, where they are also compared to corresponding predictions made by the Colour Evaporation Model [71], Fixed-Order Next-to-Leading Log (FONLL) [72] and Colour Singlet NNLO* calculations [73, 74]. The publication relative to the presented results can be found in [1].

4.2 Data and Monte Carlo Samples

The data collected in 2010 by ATLAS in the late Spring and Summer of 2010 with a centre-of-mass energy of 7 TeV is included in this analysis. Of this sample, only the fraction taken during stable beam LHC running, and in a period when the MS, ID and magnet systems were collecting data of a sufficiently high quality to be suitable for physics analysis is used.

This data sample was collected during a period of LHC commissioning, when the instantaneous luminosity provided by the machine was rising from run to run, thus the ATLAS trigger configuration during that period has been changing accordingly. For the inclusive cross-section, for data from the initial running with lower instantaneous luminosity, the L1 muon trigger is used, whereas, during later periods with higher instantaneous luminosity, a more selective EF muon trigger with a 4 GeV p_T threshold is required, and eventually, this is increased to a 6 GeV p_T threshold. The sample collected by these triggers and passing the data quality selections corresponds to an integrated luminosity of 2.2 pb^{-1} and contains approximately 16.6 million events. A detailed description of the ATLAS muon triggers can be found in Section 2.6.2.

In the case of the non-prompt fraction, since a trigger efficiency estimate is not needed for this measurement, a more complicated trigger strategy is used to maximize the available data sample. Therefore, from the initial period, events triggering either the L1 minimum bias trigger with a confirmation that at least one muon has been reconstructed at the EF or the L1 muon trigger are used (whereas only the L1 muon trigger is used for the cross-section). For intermediate instantaneous luminosities the L1 muon trigger is used alone since the minimum bias trigger is highly prescaled at this stage. For the highest instantaneous luminosities, events are accepted which pass any of the EF muon triggers with p_T thresholds of 4, 6 or 10 GeV. This selection leads to a slightly higher integrated luminosity of 2.3 pb^{-1}, approximately 27.8 million events.

In these analyses, Monte Carlo (MC) samples are used in order to characterise the acceptance and efficiencies of the detector and reconstruction, needed for the cross-section measurement. It is therefore important that the kinematic properties of the J/ψ decays are well modelled.

MC samples were generated using Pythia6 [75] tuned with the ATLAS MC09 tune [76] and MRST LO* [77] parton distribution functions. The generated samples were then simulated through the detector using Geant4 [78] and fully reconstructed with the same software that was used to process real data.

For the signal J/ψ MC sample (used for derivation of the kinematic acceptance corrections), the Pythia implementation of prompt J/ψ production subprocesses in the NRQCD Colour Octet Mechanism framework [79] is used. Two samples of

prompt $J/\psi \to \mu\mu$ were produced; the first without any generator level cuts on the muons, and the second with cuts of $p_{T\mu 1,2} > 2.5$ GeV on the muons.

All samples were generated without polar or azimuthal anisotropy in the decay of the J/ψ (the default in PYTHIA), and reweighted at the particle-level to describe a number of different spin-alignment scenarios according to their respective angular dependencies, and these are then used to provide an uncertainty band on the final results, reflecting the theoretical uncertainty on the acceptance due to spin-alignment effects.

4.3 Analysis Selection

After requiring that the events pass the trigger described in the previous section, an additional selection is applied offline on the events and dimuon candidates. In general, to veto cosmic rays, events passing the trigger selection are required to have at least three tracks associated with the same reconstructed primary vertex. The three tracks must each have at least one hit in the pixel system and at least six hits in the SCT.

In each surviving event, pairs of reconstructed muons are sought. Only muons associated with ID tracks that have at least one hit in the pixels and six in the SCT are accepted. J/ψ candidates can be constructed from any combination of tagged and combined muons fitted to a common vertex, as described in section 3.4. Those pairs which successfully form a vertex, and which have an invariant mass (based on the refitted track parameters after vertexing) of between 2 GeV and 4 GeV, are regarded as $J/\psi \to \mu\mu$ candidates. No further cuts are applied to the candidates.

The distribution of reconstructed J/ψ candidates over the candidate $p_T - y$ plane is shown in Figure 4.1. The majority of J/ψ candidates are reconstructed in intermediate-p_T, high-y areas. The number of lower p_T J/ψ is limited by the acceptance of the muon system: the ATLAS muon reconstruction cannot measure a transverse momentum below ~ 4 GeV in the barrel and ~ 3 GeV in the end-cap regions because of the spectrometer geometry and of the strong field provided by the toroidal magnets.

4.4 Inclusive $J/\psi \to \mu^+\mu^-$ Differential Production Cross-Section

The inclusive differential cross-section is defined as

$$\frac{d^2\sigma(J/\psi)}{dp_T dy} Br(J/\psi \to \mu^+\mu^-) = \frac{N_{corr}^{J/\psi}}{\mathcal{L} \cdot \Delta p_T \Delta y} \tag{4.2}$$

where $N_{corr}^{J/\psi}$ is the total number of J/ψ produced in the data sample, $\mathcal{L}$ is the integrated luminosity of the data sample and Δp_T and Δy are the transverse momentum and rapidity bin widths.

In order to recover the J/ψ yield, $N_{corr}^{J/\psi}$, one performs a fit of the weighted, candidate per candidate, muon pairs invariant mass distribution with a correction factor (w). The correction factor accounts for detector efficiency and acceptance

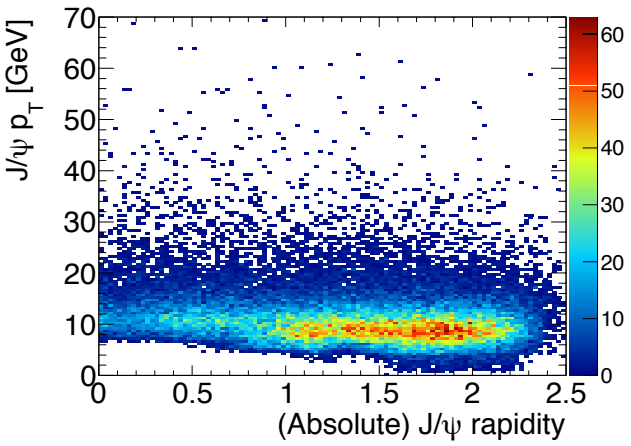

Figure 4.1. Distribution of reconstructed J/ψ candidates (in the invariant mass interval $2.7 < m_{J/\psi} < 3.5$ GeV) as a function of J/ψ p_T and rapidity.

effects, and p_T–y bin migration, and is calculated as follows:

$$w = \frac{1}{\mathcal{A} \cdot \mathcal{M} \cdot \mathcal{E}_{\text{trk}}^2 \cdot \mathcal{E}^+{}_{\mu}(p_T^+, \eta^+) \cdot \mathcal{E}^-{}_{\mu}(p_T^-, \eta^-) \cdot \mathcal{E}_{\text{trig}}} \tag{4.3}$$

where $\mathcal{A}$ is the kinematic acceptance (discussed in the next Section), $\mathcal{M}$ is a correction factor for bin migrations due to finite detector resolution, $\mathcal{E}_{\text{trk}}$ is the ID tracking efficiency and $\mathcal{E}_{\mu}$ is the single-muon offline reconstruction efficiency. Here $p_T^{\pm}$ and $\eta^{\pm}$ are the transverse momenta and pseudo-rapidities of the positive and negative muons from the J/ψ decay. The trigger efficiency $\mathcal{E}_{\text{trig}}$ for a given J/ψ candidate is calculated from single-muon trigger efficiencies $\mathcal{E}_{\text{trig}}^{\pm}(p_T^{\pm}, \eta^{\pm})$ as follows:

$$\mathcal{E}_{\text{trig}} = 1 - \left(1 - \mathcal{E}_{\text{trig}}^{+}(p_T^{+}, \eta^{+})\right) \cdot \left(1 - \mathcal{E}_{\text{trig}}^{-}(p_T^{-}, \eta^{-})\right). \tag{4.4}$$

The approach used to compute w is described in Section 4.4.1. It is important to observe that the acceptance of the muon spectrometer is limiting the measurement at low p_T of the muons, especially in the central region of the detector, whereas for high p_T J/ψan additional loss of efficiency is due to the difficulty of reconstructing the two boosted muons, very near in ΔR, that are produced in the decay. The invariant mass peak, weighted as described, is then fitted, as described in Section 4.4.2, to extract the number of J/ψ produced in the interaction.

4.4.1 Correction Factors

Detector Acceptance

The kinematic acceptance $\mathcal{A}(p_T, y)$ is the probability that the muons from a J/ψ with transverse momentum p_T and rapidity y fall into the fiducial volume of the detector. This is calculated using generator-level MC, applying cuts on the momenta and pseudo-rapidities of the muons to emulate the detector geometry. Global cuts of $|\vec{p}_+|, |\vec{p}_-| > 3$ GeV for $|\eta_+|, |\eta_-| < 2.5$ are supplemented by finer p_T thresholds in slices of η to ensure that regions of the detector where the values of offline and

trigger efficiencies are so low as to be compatible with zero within the uncertainties (approximately 10%) are excluded from the analysis.

The acceptance also depends on the spin-alignment of the J/ψ, which is not known. The central value for the cross-section measurement is obtained under the hypothesis that the decay follows an isotropic angular distribution. The measurement is then repeated using the other most probable scenarios, discussed in Appendix .1, to provide an envelope of maximum variation, which is stated as a separate systematic uncertainty.

Muon Trigger and Reconstruction Efficiency

The offline single muon reconstruction efficiencies are obtained from data using a tag and probe method [80], where muons are paired with ID tracks ("probes") of opposite charge. The pairs are divided into two categories: those in which the probe is reconstructed as a muon ("matched") and those in which it is not ("unmatched"). Both sets of pairs are organized in bins according to the p_T and η of the probe. In each of these bins, the muon identification efficiency is obtained as the ratio of the number of J/ψ candidates in the peak of the distribution of matched candidates to the total number of candidates in the two mass distributions (matched and unmatched). The efficiency is extracted as a parameter of a simultaneous fit to both distributions. This procedure is repeated separately for combined and tagged muons. At higher p_T (for muons with p_T above 6 GeV), the efficiency determination is supported by additional tag and probe $Z \to \mu^+\mu^-$ data [81] for improved precision in the efficiency plateau region. The muons forming a pair are found to be quite uncorrelated at the reconstruction level.

A hybrid MC and data-derived (tag and probe) scheme is used to provide trigger efficiencies for the analysis. The data sample available is not sufficient to build maps binned in p_T, y and charge of the muon with a binning finer than the one used in the analysis. This fine binning is necessary to avoid significant biases that would otherwise appear in the analysis with coarsely binned efficiencies across rapidly-changing $(turn-on)$ efficiency regions.

Due to significant charge dependence at low p_T and high pseudo-rapidity, separate trigger efficiency maps, shown in Figure 4.2, are produced for positive and negative muons. Mainly because only single muon triggers are used in this analysis, no correlation is found, after separating the charges, between the muons. Fully simulated samples of prompt $pp \to J/\psi\,(\mu^+\mu^-)\,X$ decays are used to populate the J/ψ $p_T - y$ plane, using a fine binning. For each bin, the probability of a muon activating the trigger is determined. The derived efficiencies are then reweighted to match the data efficiencies in the reconstructed bins in cases where discrepancies exist between the data and MC, and uncertainties from data are assigned.

Muon reconstruction efficiencies have been determined relative to reconstructed ID tracks using a data sample of $J/\psi \to \mu\mu$ for the lower p_T range and $Z \to \mu\mu$ for the higher p_T range. Inner Detector tracks associated to muons and passing the selection cuts used in this analysis have a reconstruction efficiency $\mathcal{E}_{\text{trk}}$ of $99.5\% \pm 0.5\%$ per track (with no significant pseudo-rapidity or p_T dependence observed within the phase space probed with this analysis) estimated using the tag and probe method. This efficiency is applied as an additional correction to the J/ψ yield.

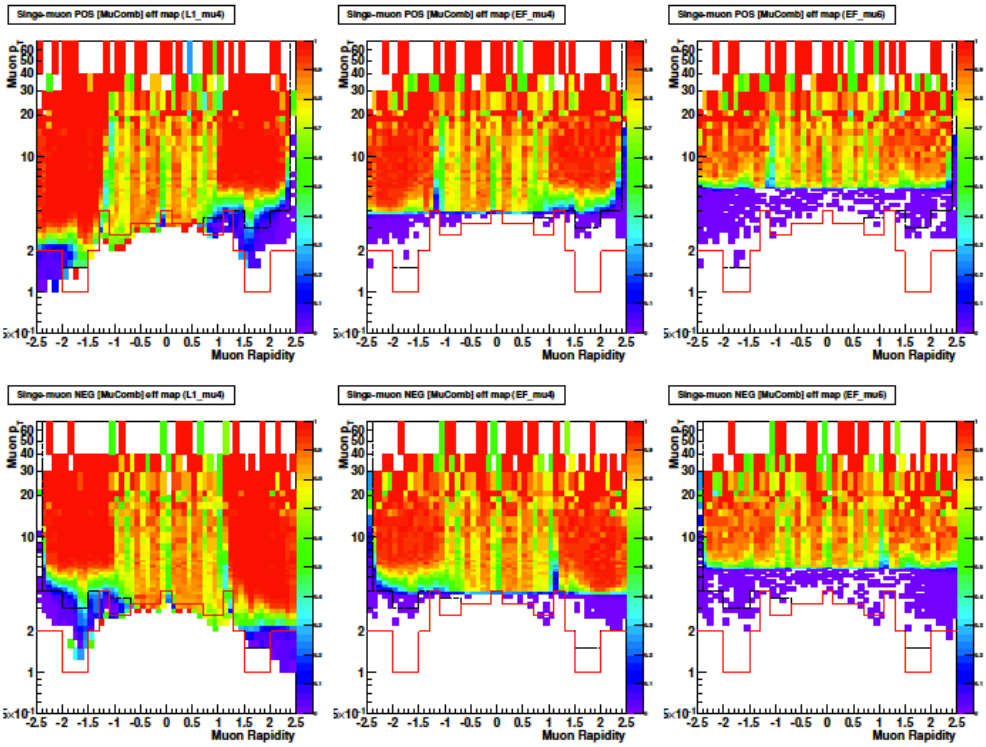

Figure 4.2. Single muon trigger efficiency maps obtained using combined single muons in MC. Maps relative to positively (top) and negatively (bottom) charged muons are shown separately. The red and black lines show the binning in J/ψ p_T and rapidity used in the analysis for positively and negatively charged muons.

Bin migration corrections

The measured efficiency and acceptance corrected J/ψ p_T distribution is parameterised in each rapidity slice by a smooth analytic function smeared with a Gaussian distribution, with resolution derived from the data. This function is integrated numerically over each analysis bin, both with and without smearing applied, and the ratio of the two integrals is assigned as the correction factor. The effects of this correction are minimal at low p_T and at low rapidities (around 0.1%) but increase at higher p_T and at higher rapidities (reflecting the decreasing momentum resolution) to a maximum of approximately 3%.

4.4.2 J/ψ Yield Extraction

The inclusive J/ψ production cross-section is determined in four slices of J/ψ rapidity: $|y| < 0.75, 0.75 < |y| < 1.5, 1.5 < |y| < 2.0$ and $2.0 < |y| < 2.4$. In Figure 4.3, the invariant mass distributions for all oppositely charged muon pairs passing the selection for the differential cross-section measurement are shown, before acceptance and efficiency corrections, for the four rapidity slices. Table 4.1 presents the results of the combined signal and background fits. In these fits the J/ψ and $\psi(2S)$ peaks are represented by Gaussians, while the background is described by a quadratic polynomial.

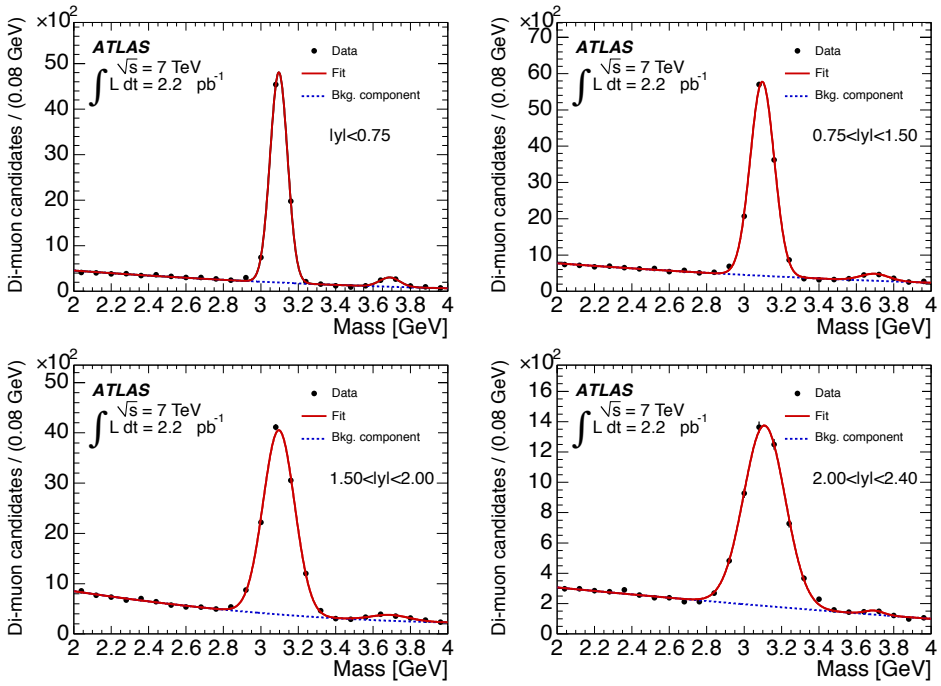

Figure 4.3. Invariant mass distributions of reconstructed $J/\psi \to \mu\mu$ candidates used in the cross-section analysis, corresponding to an integrated luminosity of 2.2 pb^{-1}. The points are data, and the uncertainties indicated are poissonian. The solid lines are the result of the fit described in the text.

Table 4.1. Fitted mass, resolution and yields of J/ψ candidates reconstructed in four J/ψ rapidity bins. All uncertainties quoted are statistical only. The shift in mass away from the world average in the highest rapidity bin reflects the few-per-mille uncertainty in the tracking p_T scale at the extreme ends of the detector.

	J/ψ rapidity range			
	$\lvert y\rvert < 0.75$	$0.75 < \lvert y\rvert < 1.5$	$1.5 < \lvert y\rvert < 2.0$	$2.0 < \lvert y\rvert < 2.4$
Signal yield	6710 ± 90	10710 ± 120	9630 ± 130	4130 ± 90
Fitted mass [GeV]	3.096 ± 0.001	3.097 ± 0.001	3.097 ± 0.001	3.109 ± 0.002
Fitted resolution [MeV]	46 ± 1	64 ± 1	84 ± 1	111 ± 2

The invariant mass distribution of $J/\psi \to \mu^+\mu^-$ candidates in each $p_T - y$ bin is fitted using a binned minimum-χ^2 method. The J/ψ and $\psi(2S)$ signals are described by single Gaussians, while the background is treated as a straight line.

For the differential cross-section measurement, the correction weight w defined in Equation 4.3 is applied to each candidate, and a new binned minimum-χ^2 fit is performed in each bin. The yields of J/ψ determined from these fits, divided by the integrated luminosity, give the inclusive production cross-section for a given bin. Representative invariant mass distributions are shown in Figure 4.4. The χ^2 probability distribution of the weighted fits across all bins is found to be consistent with the statistical expectation.

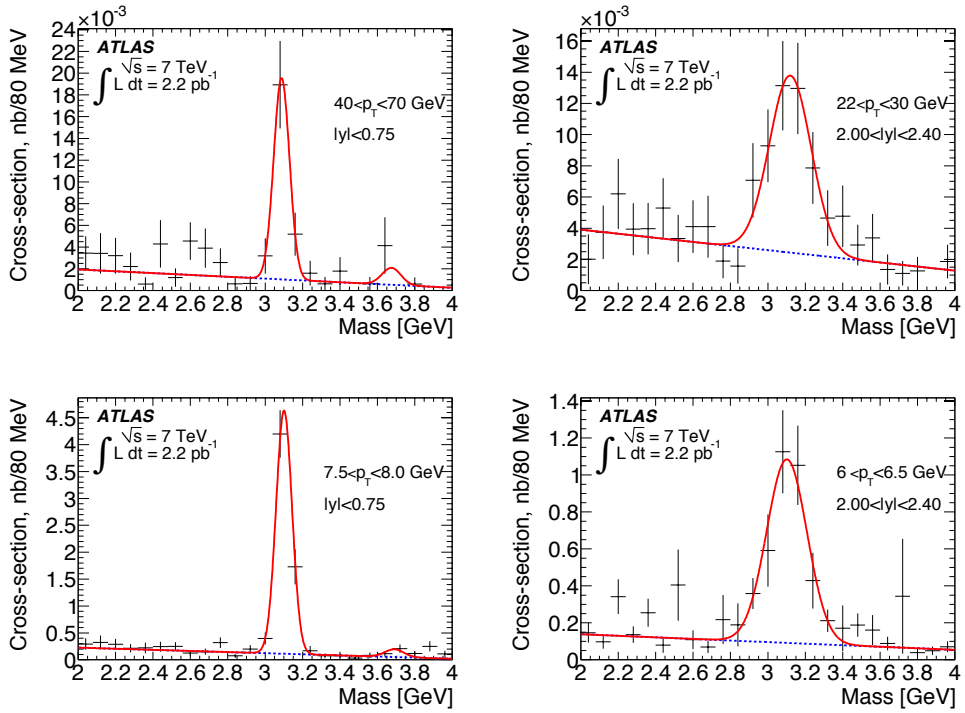

Figure 4.4. Acceptance and efficiency-corrected invariant di-muon mass distributions scaled by integrated luminosity for selected bins in J/ψ rapidity and transverse momentum. Low- and high- p_T bins are shown here for the central and forward rapidity ranges, to represent the complete sample. Statistical uncertainties and systematic uncertainties due to efficiency and acceptance corrections are shown, combined in quadrature.

The cross-sections obtained for each bin are listed in Table .1, the systematic uncertainties considered are displayed in Figure 4.5 and the cross-section results are presented in Figure 4.6. The measurement in each $p_T - y$ analysis bin is positioned at the average p_T for J/ψ candidates in that bin. Various tests of the method described above are performed using simulated samples of known composition, and the number of J/ψ in each analysis bin is successfully recovered within expectations in all cases.

4.4.3 Systematic Uncertainties

Studies are performed to assess all relevant sources of systematic uncertainty on the measurement of the J/ψ inclusive production cross-section. Sources of uncertainty are listed below, ordered according to the approximate size of their contribution (starting with the largest).

1. **Spin-alignment:** Kinematic acceptance depends on the spin-alignment state of the J/ψ and hence affects the corrected yield. Five spin-alignment scenarios are considered, which correspond to the extreme cases for the acceptance corrections within the kinematics accessible in ATLAS. In each bin, the maximal deviations in either direction are assigned as the systematic uncertainty due

to the unknown spin-alignment of the J/ψ. These uncertainties are regarded as theoretical rather than experimental, and are quoted independently of the statistical and experimental systematic uncertainties.

2. **Muon reconstruction:** The single muon efficiency maps are obtained from the data using the tag and probe method, in bins of muon transverse momentum and pseudo-rapidity. Each efficiency has an uncertainty associated with it which is predominantly statistical in nature but has also a systematic component from the tag and probe method. The statistical part is treated as uncorrelated with the statistical uncertainty on the yield extraction, whereas the systematic part as being 100% correlated. In order to obtain an estimate on the effects of uncertainties within these bins, the relative uncertainties (due to systematic and statistical components) on all J/ψ candidates in a bin are averaged. ID tracks originating from muons and having the selection cuts used in this analysis have a reconstruction efficiency of $99.5\% \pm 0.5\%$ per track. The results are corrected for this efficiency, and a systematic uncertainty on the efficiency is assigned for each track, propagated linearly into the cross-section systematic.

3. **Trigger:** The uncertainty on the trigger efficiency has components from the data-derived efficiency determination method (again largely statistical in nature) and from the reweighting of MC maps to the data-driven (tag and probe) efficiency values. These errors are treated similarly to the reconstruction efficiency uncertainties.

4. **Luminosity:** The uncertainty on the integrated luminosity used for this measurement is determined to be 3.4% [82], fully correlated between bins.

5. **Acceptance:**

   - MC statistics: The acceptance maps are obtained from dedicated MC production, in bins of J/ψ transverse momentum and rapidity. The acceptance in each bin has an uncertainty due to MC statistics. The relative error on the acceptance correction for each J/ψ candidate contributing to a particular analysis bin is averaged in quadrature to evaluate the systematic effect of these errors on the cross-section measurement in that bin.
   - Kinematic dependence: The impact of any discrepancies in the underlying kinematic distribution modelling in the MC used to build the maps, or differences in the p_T dependence of the prompt and non-prompt components to the overall inclusive cross-section are studied. A correction to the acceptance maps is made based on the measured non-prompt to prompt fraction to ensure proper correction of the two populations, and an uncertainty is assigned based on the difference in yields from using the corrected and uncorrected maps. This uncertainty is significantly below 1% in most analysis bins, reaching a maximum of 1.5% in some high p_T, low rapidity bins.
   - Bin migration: The changes to the measured cross-section due to the migration of entries between the p_T bins is determined by analytically smearing the efficiency and acceptance corrected p_T spectrum with a

Gaussian resolution function with width based on muon p_T resolutions, taken from data. The correction needed to the central value due to bin migrations is as small as 0.1% at low p_T and low rapidity and rises to $\sim 3\%$ at high p_T and high rapidity. The variation of the bin migration correction within a given analysis bin (due to changing detector resolution and parameterisation of the p_T spectrum) is taken as a systematic.

- Final-State Radiation: The acceptance maps correct the measured cross-section back to the J/ψ kinematics, rather than the final-state muon kinematics, in order to allow proper comparison with theoretical predictions. Emission of QED final-state radiation is known to high accuracy, so the relative uncertainty on the modelling of this correction is determined to be less than 0.1%.

6. **Fit:** Invariant mass distributions for a large number of pseudo-experiments are constructed for each $p_T - y$ bin of the analysis, with the bin contents for each pseudo-experiment being an independently Poisson-fluctuated value with mean equal to the measured data, and uncertainty in the bin determining the variance of the fluctuations. Within these pseudo-experiments, the candidate yields from the central fit procedure and yields from varied fitting models are determined, and the shift per pseudo-experiment calculated. The variation in fitting models include signal and background fitting functions and inclusion/exclusion of the $\psi(2S)$ mass region. The means of the resultant shifts across all pseudo-experiments for each fit model are used to evaluate the systematic uncertainty. The largest mean variation in that bin is assigned as a systematic uncertainty due to the fit procedure.

7. ***J/ψ* vertex-finding efficiency:** The loose vertex quality requirement retains over 99.9% of di-muon candidates used in the analysis, so any correction and systematics associated to the vertexing are neglected.

A summary of the various contributions to the systematic uncertainties on the measurement in each rapidity slice as a function of J/ψ p_T is shown in Figure 4.5. On the y-axis the fractional uncertainty is provided, corresponding to percent of the central value divided by 100. The uncertainty due to the luminosity (3.4%) is not shown, nor is the spin-alignment envelope which represents a full range of variation due to the unknown spin-alignment state.

The muon reconstruction efficiency systematic is dominated by the statistical uncertainties of the finely binned sample used for the reconstruction efficiency measurement. Since both $J/\psi \to \mu^+\mu^-$ and $Z \to \mu^+\mu^-$ samples are used for efficiency determination the systematic uncertainty on muon efficiency does not scale with $J/\psi \to \mu^+\mu^-$ statistics in high-p_{T} bin.

4.4.4 Inclusive J/ψ Cross-Section Results

The results of the inclusive double-differential J/ψ production cross-section measurement are given in Table .1. They are compared to CMS results [69] in Figure 4.6 for cases where the rapidity ranges are close enough to permit comparison. The two sets of results show good agreement within experimental uncertainties and

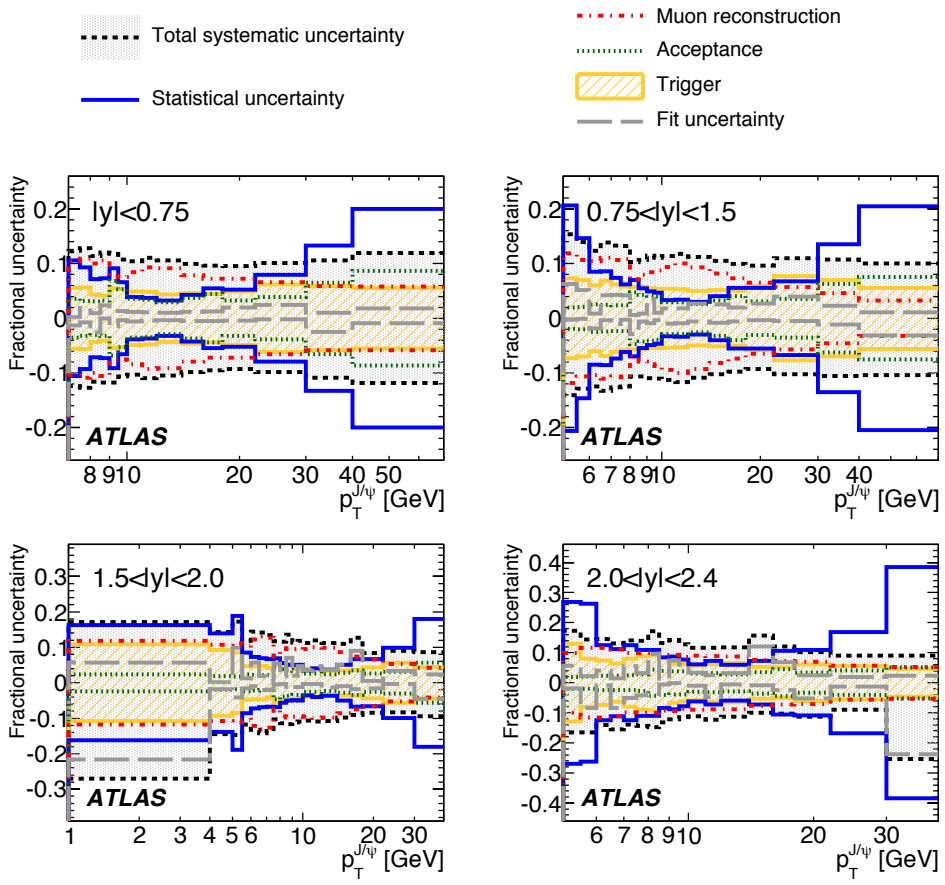

Figure 4.5. Summary of the contributions from various sources to the systematic uncertainty on the inclusive differential cross-section, in the J/ψ p_T and rapidity bins of the analysis. The total systematic and statistical uncertainties are also overlaid. The theoretical uncertainty due to the unknown spin alignment is not included on these plots.

provide complementary measurements at low (CMS) and high (ATLAS) p_T, together providing a measurement over a large kinematic range.

The systematics are dominated by the data-driven muon reconstruction efficiency uncertainties, which are in turn dominated by their statistical uncertainties. There is an additional overall uncertainty of $\pm 3.4\%$ (fully correlated between bins) due to the luminosity measurement uncertainty. The measurement of the differential cross-section is limited by systematic uncertainties, with statistical uncertainties only contributing significantly near the low-p_T thresholds where yields are limited by trigger efficiency, and in the highest transverse momentum bin.

The total cross-section for inclusive $J/\psi \to \mu^+\mu^-$ production, multiplied by the branching fraction into muons and under the isotropic production scenario for the central value, has been measured for J/ψ produced within $|y| < 2.4$ and $p_T > 7$ GeV

to be:

$$Br(J/\psi \to \mu^+\mu^-)\sigma(pp \to J/\psi X; |y_{J/\psi}| < 2.4, p_T^{J/\psi} > 7 \text{ GeV}) \\ = 81 \pm 1 \text{ (stat.)} \pm 10\text{(syst.)} \pm^{25}_{20} \text{ (spin)} \pm 3 \text{ (lumi.) nb}$$

and for J/ψ within $1.5 < |y| < 2$ and $p_T > 1$ GeV to be:

$$Br(J/\psi \to \mu^+\mu^-)\sigma(pp \to J/\psi X; 1.5 < |y_{J/\psi}| < 2, p_T^{J/\psi} > 1 \text{ GeV}) \\ = 510 \pm 70 \text{ (stat.)} \pm^{80}_{120} \text{ (syst.)} \pm^{920}_{130} \text{ (spin)} \pm 20 \text{ (lumi.) nb.}$$

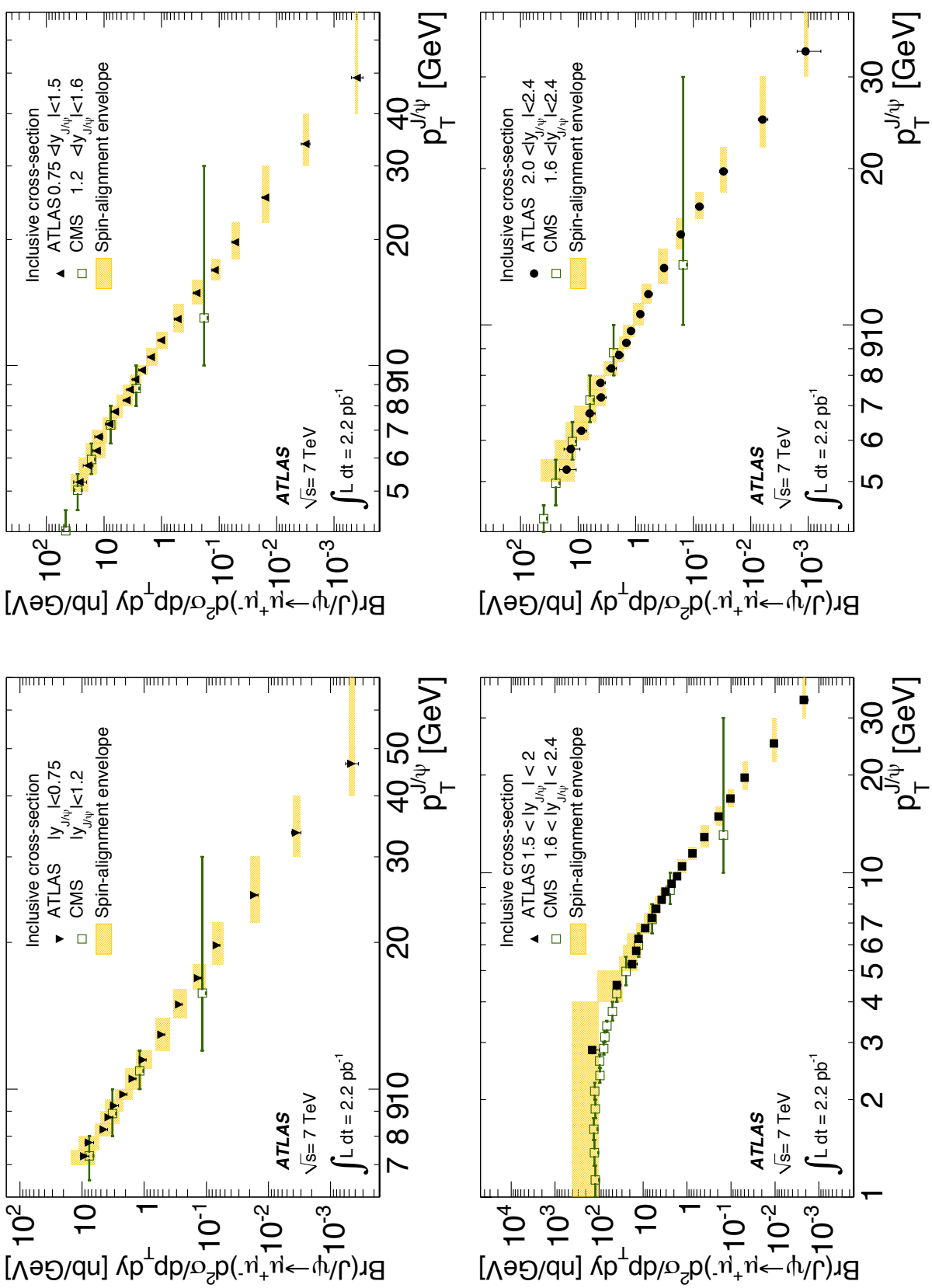

Figure 4.6. Inclusive J/ψ production cross-section as a function of J/ψ transverse momentum in the four rapidity bins. Overlaid is a band representing the variation of the result under various spin-alignment scenarios (see text) representing a theoretical uncertainty. The equivalent results from CMS [69] are overlaid. The luminosity uncertainty (3.4%) is not shown.

4.5 Measurement of the Non-Prompt to Prompt J/ψ Cross-Section Fraction

Experimentally, it is possible to distinguish J/ψ from prompt and non-prompt production, since the former decay very close to the primary vertex of the parent proton-proton collision, while the J/ψ mesons produced in B-hadron decays will have a measurably displaced decay point due to the long lifetime of their B-hadron parent. From the measured distances between the primary vertex and corresponding J/ψ decay vertices the fraction of J/ψ that originate from non-prompt sources (f_B), as defined in Equation 4.1, can be inferred. An unbinned maximum likelihood fit is used to extract this fraction from the data.

4.5.1 Pseudo-Proper Time and J/ψ Non-Prompt to Prompt Separation

The signed projection of the J/ψ flight distance, $\vec{L}$, onto its transverse momentum, $\vec{p}_T^{J/\psi}$, is constructed according to the following formula

$$L_{xy} \equiv \frac{\vec{L} \cdot \vec{p}_T^{J/\psi}}{|\vec{p}_T^{J/\psi}|}, \tag{4.5}$$

where $\vec{L}$ is the vector from the primary vertex to the J/ψ decay vertex and $\vec{p}_T^{J/\psi}$ is the transverse momentum vector of the J/ψ. L_{xy} measures the displacement of the J/ψ vertex in the transverse plane.

The probability for the B-hadron to decay as a function of its proper decay time (t) follows an exponential distribution

$$p(t) = \frac{1}{\tau_B} \exp(-t/\tau_B), \tag{4.6}$$

where τ_B is the lifetime of the B-hadron. For each decay the proper decay time can be calculated as

$$t = \frac{L}{\beta\gamma}, \tag{4.7}$$

where L is the distance between the B-hadron production and decay point and $\beta\gamma$ is the Lorentz factor. Taking the projection of the decay length and momentum on the transverse plane for B-hadrons, one obtains

$$t = \frac{L_{xy}\, m_B}{p_T^B}. \tag{4.8}$$

This measurement is performed in the transverse plane because of the poor resolution associated to the z component of the reconstructed vertices (see section 3.2). In general L_{xy} is measured between the position of the reconstructed J/ψ decay vertex and of the primary vertex. We consider as being the primary vertex of the event the one that has the highest sum of the p_T of the tracks associated to it, according to the ATLAS standard reconstruction definition. In order to build L_{xy} avoiding a bias towards the J/ψ decay vertex position, the primary vertex is then refitted excluding the two muon tracks. In a small number of cases (fewer than 0.2%) the

two tracks forming the J/ψ candidate are included in the reconstruction of different vertices. These candidates are discarded. The uncertainty on L_{xy} is calculated from the covariance matrices of the primary and the secondary vertices.

Since the B-hadron is not reconstructed completely, one does not know its transverse momentum. Instead the J/ψ momentum is used to construct a variable, that will be called *pseudo-proper time*

$$\tau = \frac{L_{xy}\, m_{\mathrm{PDG}}^{J/\psi}}{p_T^{J/\psi}}. \tag{4.9}$$

Here, $m_{\mathrm{PDG}}^{J/\psi}$ is the world average value of the J/ψ. At large $p_T^{J/\psi}$, where most of the B-hadron transverse momentum is carried by the J/ψ, the distribution of τ is approximately exponential, with the B-hadron lifetime as a parameter.

4.5.2 Fitting Procedure

The data sample is divided into bins of p_T and rapidity of the J/ψ candidates. In each bin, in order to determine the fraction of the non-prompt to inclusive J/ψ production cross-sections in that particular bin, a maximum likelihood fit is performed simultaneously on the invariant mass and pseudo-proper time of the J/ψ candidates in the mass region from 2.5 GeV to 3.5 GeV.

In order to do so, the likelihood function:

$$\begin{aligned}\mathcal{L} = \prod_{i=1}^{N} \Big[&(1 - f_{bkg}) P_{sig}(\tau \,|\, \delta\tau) E_{sig}(\delta\tau) \cdot F_{sig}(m_{\mu\mu} \,|\, \delta m) E^m_{sig}(\delta m) + \\ &f_{bkg} P_{bkg}(\tau \,|\, \delta\tau) E_{bkg}(\delta\tau) \cdot F_{bkg}(m_{\mu\mu} \,|\, \delta m) E^m_{bkg}(\delta m) \Big],\end{aligned} \tag{4.10}$$

is defined, where N is the total number of candidates in the mass region considered and f_{bkg} is the fraction of background candidates in the same region. The input variables to the maximum likelihood fit to determine the production ratio are the pseudo-proper time τ, its per candidate uncertainty $\delta\tau$, the dimuon mass $m_{\mu\mu}$ and its per candidate uncertainty δm. P_{sig} and P_{bkg} are the pseudo-proper time conditional Probability Density Functions (PDFs) for respectively signal and background candidates, functions of τ and $\delta\tau$, multiplied by the pseudo-proper time per candidate error distributions, E_{sig} and E_{bkg}. In the same way, F_{sig} and F_{bkg} are the invariant mass conditional PDFs for signal and background candidates, functions of $m_{\mu\mu}$ and δm, multiplied by the per candidate mass error distributions, E^m_{sig} and E^m_{bkg}.

The error distributions of both mass and pseudo-proper time are assumed to be identical in this analysis for signal and background: $E_{sig} = E_{bkg}$ and $E^m_{sig} = E^m_{bkg}$. Although it is not exactly the case, since dimuons from combinatorial background are in general reconstructed worse than real J/ψmesons,it has been verified that these approximations are reasonable, and that the effect on the measurement is negligible. Equation 4.10 then simplifies to:

$$L = \prod_{i=1}^{N} \left[(1 - f_{bkg}) P_{\mathrm{sig}}(\tau, \delta\tau) F_{\mathrm{sig}}(m_{\mu\mu}, \delta m) + f_{\mathrm{bkg}} P_{\mathrm{bkg}}(\tau, \delta\tau) F_{\mathrm{bkg}}(m_{\mu\mu}) \right] \tag{4.11}$$

Below a detailed description of the PDFs composing the likelihood function will be provided.

Invariant Mass Model

The invariant mass PDFs of the likelihood function are used for separating the real J/ψ candidates from the combinatorial background. The mass signal component is modelled using a Gaussian distribution:

$$F_{\text{sig}}(m_{\mu\mu}, \delta m) \equiv \frac{1}{\sqrt{2\pi}\ S_m \cdot \delta m} e^{\frac{-(m_{\mu\mu}-m_{J/\psi})^2}{2(S_m\cdot\delta m)^2}}. \tag{4.12}$$

Here the mean value $m_{J/\psi}$ is the J/ψ mass, free parameter of the fit, and the width is given by the product $S_m \cdot \delta m$, where δm is the measured mass error calculated for each muon pair from the covariance matrix of the vertex reconstruction. S_m is a global scale factor taking into account eventual discrepancies between the per candidate mass resolution from the J/ψ vertex fit, δm, and the true mass resolution obtained from the mass fit.

The mass background component is assumed to follow a second-order polynomial function:

$$F_{bkg}(m_{\mu\mu}) = \mathcal{C}_1 \cdot m_{\mu\mu} + \mathcal{C}_2 \cdot m_{\mu\mu}^2, \tag{4.13}$$

where $\mathcal{C}_1$ and $\mathcal{C}_2$ are the two independent free parameters.

Pseudo-Proper Time Model

The pseudo-proper time PDF for signal candidates, P_{sig}, consists of two terms. One term describes the J/ψ from B-hadron decays (P_B), and the other describes the J/ψ from prompt decays (P_P):

$$P_{\text{sig}}(\tau, \delta\tau) = f_B P_B(\tau, \delta\tau) + (1 - f_B) P_P(\tau, \delta\tau), \tag{4.14}$$

where f_B is the fraction of J/ψ from B-hadron decays as defined in Equation 4.1.

The pseudo-proper time distribution of the J/ψ mesons from B-hadron decays $P_B(\tau, \delta\tau)$ is an exponential function $E(\tau) = \exp(-\tau/\tau_{\text{eff}})$ with a pseudo-proper time slope τ_{eff}, convolved with the pseudo-proper time resolution function $R(\tau' - \tau, \delta\tau)$:

$$P_B(\tau, \delta\tau) = R(\tau' - \tau, \delta\tau) \otimes E(\tau'). \tag{4.15}$$

Promptly produced J/ψ particles decay at the primary vertex, and their pseudo-proper time distribution is thus given by the resolution function itself:

$$P_P(\tau, \delta_\tau) = R(\tau' - \tau, \delta\tau) \otimes \delta(\tau') = R'(\tau, \delta\tau). \tag{4.16}$$

The resolution function R is a Gaussian distribution centred at $\tau = 0$ with a width $S_t \cdot \delta\tau$, where S_t is a scale factor (a parameter of the fit) and $\delta\tau$ is the per candidate uncertainty on τ, the measured pseudo-proper lifetime determined from the covariant error matrix of the tracks.

The pseudo-proper time PDF for the background candidates P_{bkg} has to take into account a prompt component, describing combinatorial background from decays-in-flight of pions and kaons, and a non-prompt component, composed of muons from b and c-quark decays.

In analogy with the signal PDF, the background component is described as the sum of a Dirac δ function, a positive exponential and a symmetric double exponential

(both positive and negative) to describe non-Gaussian tails in the background resolution. All components are convolved with the background resolution function $R_{\text{bkg}}(\tau' - \tau \,|\, \delta\tau)$. This gives:

$$P_{\text{bkg}}(\tau \,|\, \delta\tau) = (1 - f_{B,bkg}) R_{\text{bkg}}(\tau \,|\, \delta\tau) + f_{B,bkg} \left[b_1 \exp\left(\frac{-\tau'}{\tau_{\text{eff1}}}\right) + (1 - b_1) \exp\left(\frac{-|\tau'|}{\tau_{\text{eff2}}}\right) \right] \otimes R_{\text{bkg}}(\tau \,|\, \delta\tau), \tag{4.17}$$

where the parameters τ_{eff1} and τ_{eff2} are the pseudo-proper time slopes of the two exponential components of the background and $\frac{b_1}{1-b_1}$ is their ratio. In the same way, $\frac{f_{B,bkg}}{1-f_{B,bkg}}$ is the ratio between the prompt (Dirac δ function) and the non-prompt (exponential functions) components.

In this formula, the background $R_{\text{bkg}}(\tau \,|\, \delta\tau)$ function is given by a convolution between the resolution function and a Dirac δ function:

$$R'_{\text{bkg}}(\tau \,|\, \delta\tau) = R_{\text{bkg}}(\tau' - \tau \,|\, \delta\tau) \otimes \delta(\tau'), \tag{4.18}$$

which is a Gaussian distribution centered at $\tau = 0$ with width $S_{\text{bkg}} \cdot \delta\tau$. S_{bkg} is a separate scale factor which is a free parameter of the fit.

The τ background functional form has been optimized on the shape of the dimuons contained in the sideband regions of the invariant mass distribution, defined as $[m_{J/\psi} - 10\sigma, m_{J/\psi} - 6\sigma] \cup [m_{J/\psi} + 6\sigma, m_{J/\psi} + 10\sigma]$.

Summary of Free Parameters

All of the parameters used in the fit are listed in Table 4.2.

Table 4.2. List of the parameters involved in the mass and lifetime simultaneous fit.

Parameter	Description
$m_{\mu\mu}$ Signal PDF	
$m_{J/\psi}$	Gaussian function mean value
S_m	Gaussian function resolution scale factor
$m_{\mu\mu}$ Background PDF	
f_{bkg}	background fraction
C_1	Chebychev polynomial 1st order parameter
C_2	Chebychev polynomial 2nd order parameter
τ Signal PDF	
f_B	fraction of J/ψ from B-hadron decays
S_t	resolution scale factor of prompt and non-prompt J/ψ candidates
τ_{eff}	pseudo-proper time slope
τ Background PDF	
$f_{B,bkg}$	fraction of non-prompt background candidates
S_{bkg}	resolution scale factor of background candidates
b_1, b_2	normalization fractions of different components
$\tau_{eff\,1}$	slope of the positive exponential
$\tau_{eff\,2}$	slope of the symmetric exponential

Test of the Fitting Technique

The reliability of the fitting technique is verified using simplified MC trial experiment samples (*toy* MC). The simultaneous mass and pseudo-proper time fit model is used to generate 100 toy MC experiments for each p_T and y bin. The number of events generated is approximately the same as the number of data events in the corresponding bin. The invariant mass and pseudo-proper time values are generated randomly from the total PDF, while the per candidate error on invariant mass and pseudo-proper time are sampled from the corresponding experimental data distributions.

For each experiment, a fit of the total PDF on the toy MC sample is performed. The pull, Δ, defined as

$$\Delta = \frac{(f_B^{\text{generated}} - f_B^{\text{extracted}})}{\sigma(f_B^{\text{extracted}})},$$

is computed for each MC experiment. Here $f_B^{\text{generated}}$ is the non-prompt fraction for the signal component according to which the MC samples are generated (i.e. the result of the fit of the global model to the experimental data), while $f_B^{\text{extracted}}$ and $\sigma(f_B^{\text{extracted}})$ are the value and uncertainty obtained from the fit. The results of this study in each p_T and y bin are shown in Appendix .2; the Gaussian mean value and width are statistically compatible respectively with zero and unity in all the bins, indicating that no bias or improper uncertainty estimate is introduced by the fit.

4.5.3 Results of the likelihood fit

The results of the likelihood fit to the pseudo-proper time distributions in a representative $p_T^{J/\psi}$ bin are shown in Figure 4.7. The Figure shows the result of the unbinned maximum likelihood fit for the signal and background components projected onto the lifetime and invariant mass distributions.

From the results of the fit, it is possible to derive the non-prompt to inclusive production fraction as a function of $p_T^{J/\psi}$. The χ^2 probabilities and Kolmogorov-Smirnov test results, computed as described in appendix .3, for the fits across all analysis bins are found to be consistent with statistical expectations, with the lowest fit probability out of over 70 fits being 1%.

The results of all the fits in the 70 p_T and y bins can be found in Appendix .4. In particular in section .4.1 all of the mass and pseudo-proper time plots are shown, whereas in section .4.2 the non-prompt to prompt ratios measured and the output of the fit quality tests are provided.

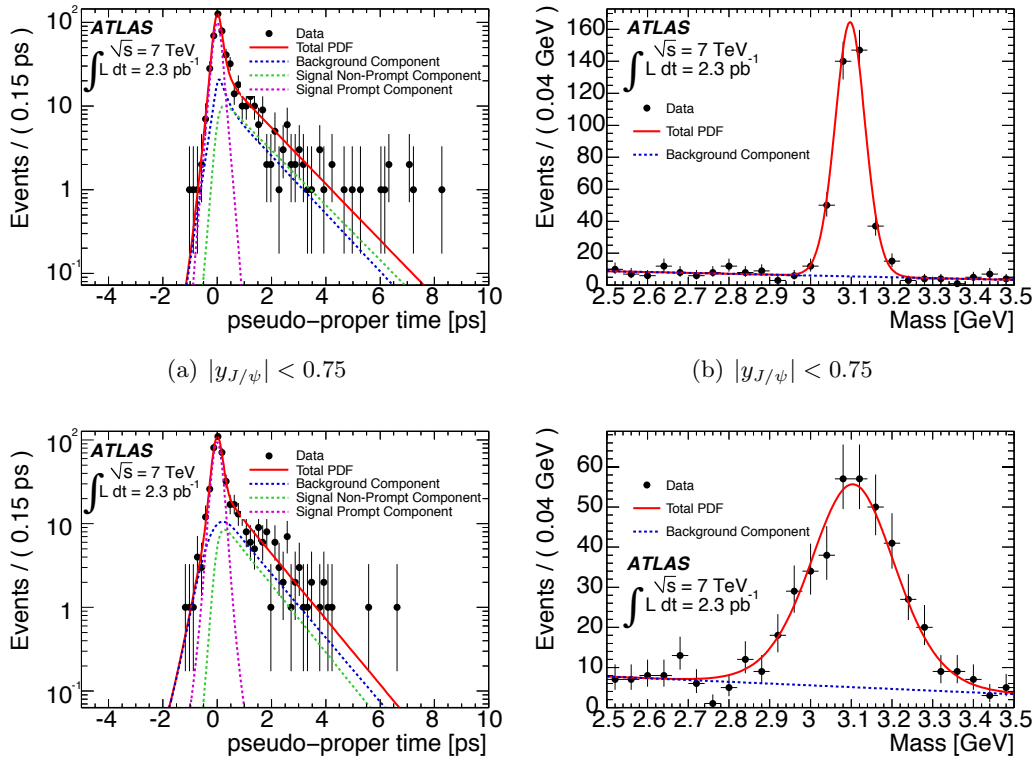

(a) $|y_{J/\psi}| < 0.75$

(b) $|y_{J/\psi}| < 0.75$

(c) $2.0 < |y_{J/\psi}| < 2.4$

(d) $2.0 < |y_{J/\psi}| < 2.4$

Figure 4.7. Pseudo-proper time distributions (left) of $J/\psi \to \mu^+\mu^-$ candidates in the signal region, for a selected p_T bin $9.5 < p_T < 10.0$ GeV in the most central and most forward rapidity regions. The points with error bars are data. The solid line is the result of the maximum likelihood unbinned fit to all dimuon pairs in the $2.5 - 3.5$ GeV mass region projected on the narrow mass window $2.9 - 3.3$ GeV. The invariant mass distributions which are simultaneously fitted with the pseudo-proper time are shown on the right for the same bins.

4.5.4 Checks and Systematic Uncertainties

Several studies have been performed to assess all relevant sources of systematic uncertainties on the measured fraction of non-prompt to inclusive J/ψ decays. In this section a brief account of it is provided.

Spin-Alignment

In general, spin-alignment may be different for prompt and non-prompt J/ψ, which may result in different acceptances in the two cases. The central value of the ratio measurement assumes they are the same (isotropic distribution in both angles, as for the inclusive cross-section central result), but four additional scenarios for the prompt component are also considered, as discussed in Appendix .1. The largest variations within the four models from the isotropic assumption is calculated for each bin in turn and assigned as an uncertainty envelope on prompt production.

The possible variation of spin-alignment in $B \to J/\psi X$ decays is expected to be much smaller than for prompt J/ψ due to the averaging effect caused by the admixture of various exclusive $B \to J/\psi X$ decays. We assign an additional uncertainty on the non-prompt fraction (and non-prompt cross-section) for the difference in final result when using either an isotropic spin-alignment assumption for non-prompt decays or maps reweighted to the CDF result [83] for $B \to J/\psi$ spin-alignment. This contributes up to an additional 0.4% uncertainty on the overall (prompt and non-prompt) systematic due to spin-alignment on the fraction.

PDFs Modelling

A number of changes are applied to the fitting procedure, and the fit is repeated in order to gauge the sensitivity of the fraction f_B to the assumptions made to build the likelihood function. Three possible sources of systematics due to the choice of PDFs are investigated:

- **Pseudo-Proper Time Resolution Modelling:** The per-candidate resolution function, a single Gaussian in the default fitting model, is changed to a per-candidate double Gaussian function. The use of two different scale factors, one for each Gaussian, to be determined in the fit accounts for differences between the resolution returned by the tracking reconstruction algorithm and the resolution measured in the fit. Differences in the measured non-prompt fraction from the main fit, are assigned as a systematic uncertainty.

- **Pseudo-Proper Time Background Modelling:** The measurement assumes a background model for the pseudo-proper time distribution of the background that includes one exponential function with a negative slope and a symmetric double exponential term with the same absolute value, τ_{eff2}, for the negative and positive slopes.

  To test the robustness of the result obtained, this model is changed in two different ways:

  - the symmetric term is no longer required to be symmetric, i.e. different values of the negative and positive slopes are allowed;

  - the sum of two asymmetric double exponentials is used (instead of only one), having the same negative decay constant but differing positive decay constants.

  The maximum deviation from the central value is taken as a systematic uncertainty.

- **Invariant Mass Background Modelling:** The main measurement uses a second order polynomial in the mass fit to describe the background distribution. To test the sensitivity to this choice, the fits are repeated using instead polynomials of order one and three. Differences from the main fit are assigned as a systematic.

- **Kinematic Dependence:** Differences in the acceptance of prompt and non-prompt J/ψ due to their different momentum spectra, averaged across an analysis bin, can bias the fraction measurement. A correction factor is calculated based on the MC simulation acceptance maps with and without momentum reweighting to account for the differences between prompt and non-prompt J/ψ and this correction assigned as a systematic uncertainty.

A number of additional checks have been performed, that lead to negligible systematic effects on the measurement. The most relevant studies are briefly outlined below.

- **Invariant Mass Fit Range:** The central result takes J/ψ candidates in a narrow mass range from 2.5 to 3.5 GeV, so that the mass region of the $\psi(2S)$ is excluded from the analysis. In order to test the stability of the result and to increase the statistics in the sideband regions, the analysis is repeated with a mass range from 2 to 4 GeV, but excluding the region from 3.5 to 3.8 GeV. The result is compatible with the expected statistical fluctuations, hence no systematic uncertainty is assigned for this source.

- **Reconstruction Efficiencies:** The central result for the fraction assumes that the reconstruction efficiencies are the same for non-prompt and prompt J/ψ mesons and hence cancel in extracting the fraction. This assumption is tested on Monte Carlo samples described in Section 5.2, and no statistically significant shift is observed. Thus, no systematic uncertainty is assigned.

4.5.5 Fraction of Non-Prompt J/ψ as a Function of J/ψ Transverse Momentum and Rapidity

Figure 4.8 and Tables .2 to .5 show the results of the differential non-prompt fraction measurement as a function of average $p_T^{J/\psi}$, in each of the four rapidity bins. The uncertainty envelopes due to the unknown spin-alignment are overlaid as solid bands.

The measurements are compared with those of CMS [69] and CDF [70] and build upon those results, with a finer rapidity binning, a much extended rapidity coverage relative to CDF and significantly increased p_T reach relative to both experiments. Strong p_T dependence of the fraction is observed: $\sim 90\%$ of J/ψ are produced promptly at low p_T, but the fraction of non-prompt J/ψ rapidly increases at mid-p_T from $\sim 15\%$ at 7 GeV to $\sim 70\%$ at the highest accessible p_T values. No significant

rapidity dependence is seen. The ATLAS results exhibit good agreement with CMS results where they overlap, and also with the CDF measurements, indicating that there is no strong dependence of the fraction on collision energies.

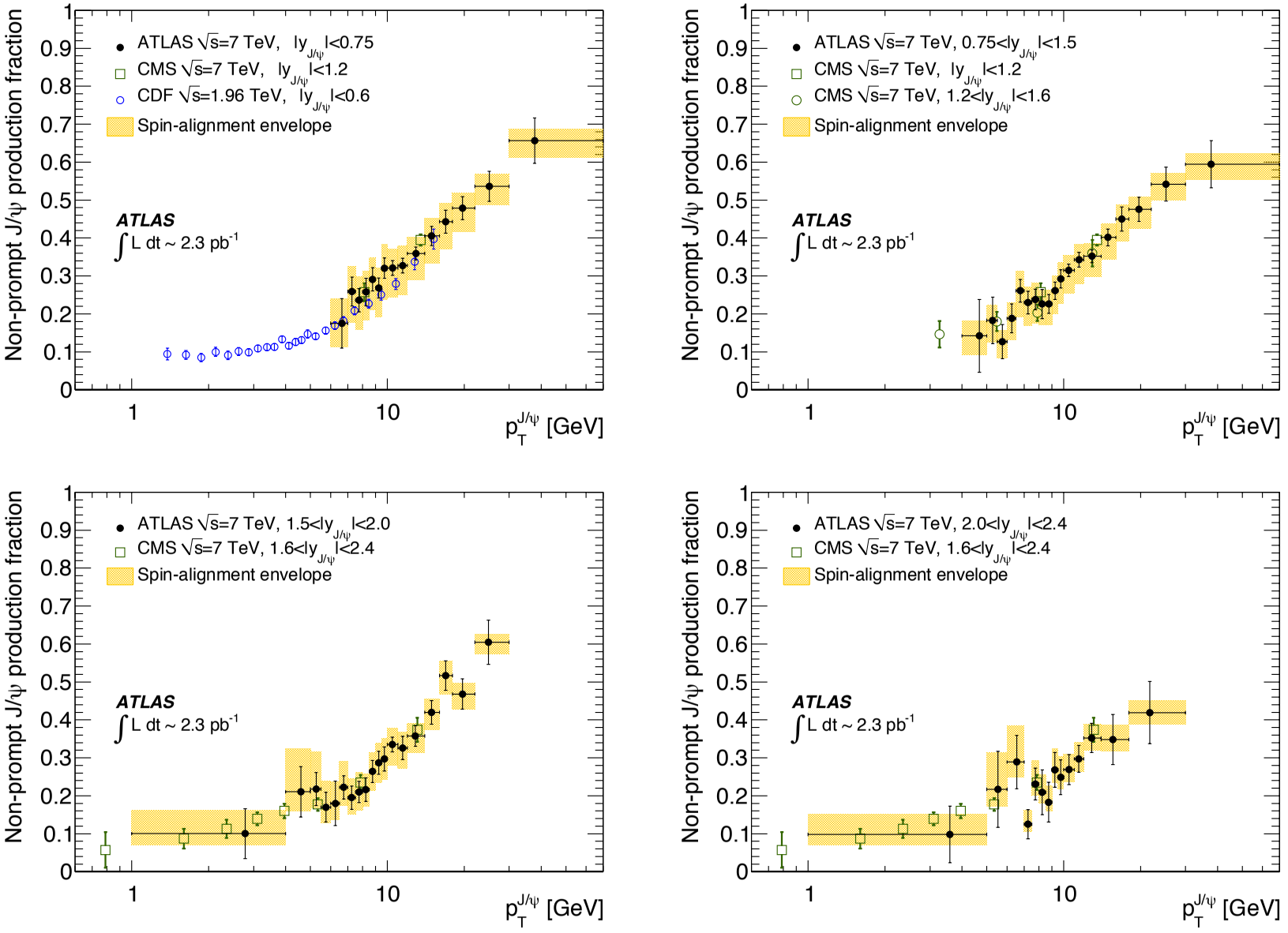

Figure 4.8. J/ψ non-prompt to inclusive fractions as a function of J/ψ transverse momentum. Overlaid is a band representing the variation of the result under various spin-alignment scenarios (see text) representing a theoretical uncertainty on the prompt and non-prompt J/ψ components. The equivalent results from CMS [69] and CDF [70] are included.

4.6 Prompt and Non-Prompt Differential Production Cross-Sections

The prompt and non-prompt J/ψ production cross-sections can be derived from the inclusive production cross-section and the non-prompt fraction. Where necessary, p_T bins in the inclusive cross-section are merged to align bins in the prompt/non-prompt cross-section result with those in the non-prompt fraction measurement. The relative systematic uncertainties in each of the fraction and inclusive cross-section measurement bins (merged where appropriate) are taken to be uncorrelated, while the statistical uncertainties are combined taking correlations into account. The spin–alignment uncertainties are quoted independently of the experimental uncertainties. The result is already dominated by systematic effects, although only a small fraction of the LHC available statistics has been analyzed. The biggest uncertainty associated to the measurement depends on the unknown spin–alignment of the J/ψ, which will be measured next year, when the inclusive $J/\psi \rightarrow \mu^+\mu^-$ data sample will be large enough.

4.6.1 Non-prompt Differential Production Cross-Sections

In this measurement we assume the spin-alignment of a J/ψ meson from a $B \rightarrow J/\psi X$ decay has no net polar or azimuthal anisotropy for the central result. Experimentally, the spin-alignment of J/ψ from B-meson decays has been measured at CDF [83] and found to be close to zero, and equal to zero within uncertainties. From the theoretical point of view, although no rigourous prediction has been made, the spin-alignment in $B \rightarrow J/\psi X$ decays is expected to be much smaller than for prompt J/ψ due to the averaging effect caused by the admixture of various exclusive $B \rightarrow J/\psi X$ decays. In order to get a significant non-zero polarisation you would have to have a dominant decay channel with a specific reason for being polarised in one way. We assign a spin-alignment uncertainty on the non-prompt cross-section for the difference in the final result when using either an isotropic spin-alignment assumption for non-prompt decays or maps reweighted to the CDF result [83] for $B \rightarrow J/\psi$ spin-alignment.

The total integrated cross-section for non-prompt J/ψ, multiplied by the branching fraction into muons and under the isotropic production scenario, has been measured for J/ψ mesons produced within $|y| < 2.4$ and $p_T > 7$ GeV to be:

$$Br(J/\psi \rightarrow \mu^+\mu^-)\sigma(pp \rightarrow B + X \rightarrow J/\psi X; |y_{J/\psi}| < 2.4, p_T^{J/\psi} > 7 \text{ GeV}) = 23.0 \pm 0.6 \text{ (stat.)} \pm 2.8\text{(syst.)} \pm 0.2 \text{ (spin)} \pm 0.8 \text{ (lumi.) nb}$$

and for J/ψ mesons produced with $1.5 < |y| < 2$ and $p_T > 1$ GeV to be:

$$Br(J/\psi \rightarrow \mu^+\mu^-)\sigma(pp \rightarrow B + X \rightarrow J/\psi X; 1.5 < |y_{J/\psi}| < 2, p_T^{J/\psi} > 1 \text{ GeV}) = 61 \pm 24 \text{ (stat.)} \pm 19 \text{ (syst.)} \pm 1 \text{ (spin)} \pm 2 \text{ (lumi.) nb.}$$

ATLAS non-prompt J/ψ production cross-section measurements are compared to Fixed Order Next-to-Leading Logarithm (FONLL) calculations [72] in Tables .6 and .9 and in Figure 4.9. FONLL v1.3.2 is used for these predictions, using the CTEQ6.6 [84] parton density function set. FONLL predictions use a $B \rightarrow J/\psi X$ branching fraction of $Br(B \rightarrow J/\psi) = 0.0116$. Uncertainty bands associated with

the predictions come from the input b-quark mass, varied within 4.75 ± 0.25 GeV, renormalisation (μ_R) and factorisation (μ_F) scales (independently) varied within $0.5 < \mu_{R,F}/m < 2$ (with the additional constraint that $0.5 < \mu_R/\mu_F < 2$) and parton density function uncertainties. Good agreement is seen between the experimental data and the theoretical prediction across the full range of rapidity and transverse momentum considered.

4.6.2 Prompt Differential Production Cross-Sections

The prompt production cross-section is of direct interest for the study of quarkonium production in QCD. The spin-alignment state and p_T dependence of the spin-alignment of promptly produced J/ψ particles are thought to be non-trivial, so the spin-alignment uncertainty envelope on the inclusive cross-section measurement is propagated into the prompt cross-section measurement. The prompt production cross-sections are presented in Tables .10 to .13.

The total cross-section for prompt J/ψ (times branching fraction into muons) under the flat production scenario has been measured for J/ψ produced within $|y| < 2.4$ and $p_T > 7$ GeV to be:

$$\begin{aligned} Br(J/\psi \to \mu^+\mu^-)\sigma(pp \to \text{prompt } J/\psi X; |y| < 2.4, p_T > 7 \text{ GeV}) \\ = 59 \pm 1 \text{ (stat.)} \pm 8\text{(syst.)} \pm {}^{9}_{6} \text{ (spin)} \pm 2 \text{ (lumi.) nb} \end{aligned}$$

and for J/ψ within $1.5 < |y| < 2$ and $p_T > 1$ GeV to be:

$$\begin{aligned} Br(J/\psi \to \mu^+\mu^-)\sigma(pp \to \text{prompt } J/\psi X; 1.5 < |y| < 2, p_T > 1 \text{ GeV}) \\ = 450 \pm 70 \text{ (stat.)} \pm {}^{90}_{110} \text{ (syst.)} \pm {}^{740}_{110} \text{ (spin)} \pm 20 \text{ (lumi.) nb.} \end{aligned}$$

In Figure 4.10 the prompt production data are compared to the predictions of the Colour Evaporation Model [71, 85] for prompt J/ψ production (with no uncertainties defined) and a calculation of the direct J/ψ production cross-section in the Colour Singlet Model [86, 87] at NLO and a partial NNLO* calculation.

The CEM predictions are produced using the CTEQ6M parton density functions, a charm quark mass of 1.2 GeV and the renormalisation and factorisation scales set to $\mu_0 = 2\sqrt{p_T^2 + m_Q^2 + k_T^2}$ (where p_T is the transverse momentum of the J/ψ and m_Q is the quark mass and k_T is a phenomenological fit parameter set to 1.5 GeV^2). The CEM predictions include contributions from χ_c and ψ(2S) feed-down and can be directly compared with the prompt J/ψ data. The normalisation of the CEM prediction is generally lower than in data and strongly diverges in shape from measured data, showing significant disagreement in the extended p_T range probed by the measurement described in this paper.

The Colour Singlet NLO and NNLO* predictions[1] for direct J/ψ production use a charm quark mass of 1.5 GeV, the CTEQ6M parton density function set, and factorisation and renormalisation scales set to $\mu_0 = \sqrt{p_T^2 + m_Q^2}$ (varied up and down by a factor of two to determine scale uncertainties). As the calculation is for direct

[1] The NNLO* calculation is not a *full* next-to-next-to-leading order prediction, as it does not include all loop corrections to $pp \to Q + jjj$ (where j is a light parton) up to order α_s^5. This limits the applicability of the calculation to values above a particular J/ψ p_T threshold (due to soft and collinear divergences).

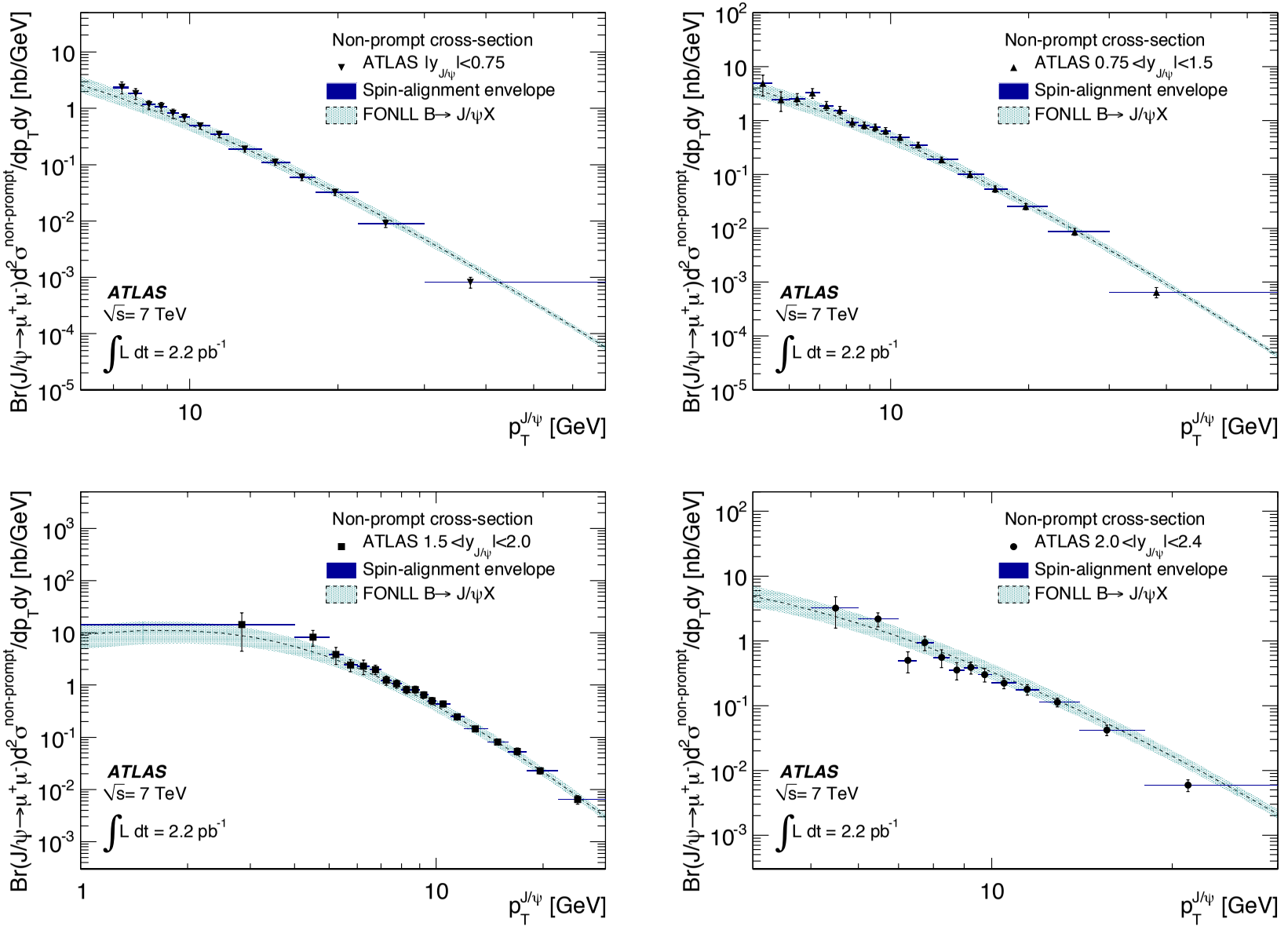

Figure 4.9. Non-prompt J/ψ production cross-section as a function of J/ψ transverse momentum, compared to predictions from FONLL theory. Overlaid is a band representing the variation of the result under spin-alignment variation on the non-prompt J/ψ component as described in the text. The central value assumes an isotropic polarisation for both prompt and non-prompt components. The luminosity uncertainty (3.4%) is not shown.

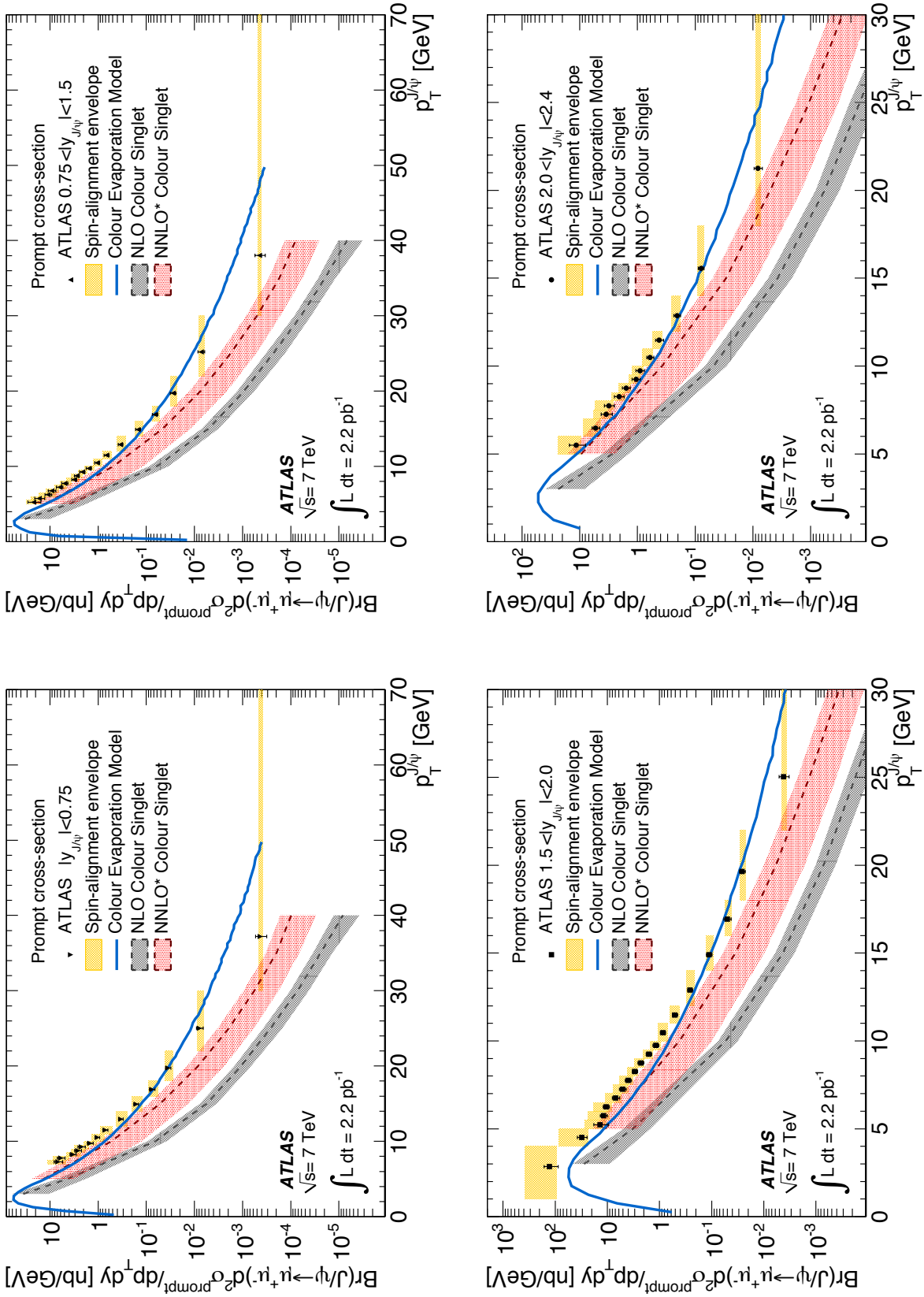

Figure 4.10. Prompt J/ψ production cross-section as a function of J/ψ transverse momentum in the four rapidity bins. Overlaid is a band representing the variation of the result under various spin-alignment scenarios (see text) representing a theoretical uncertainty on the prompt component. Predictions from NLO and NNLO* calculations, and the Colour Evaporation Model are overlaid. The luminosity uncertainty (3.4%) is not shown.

production, corrections must be applied for χ_c and $\psi(2S)$ feed-down to bring the calculations in direct comparison with data. To correct for feed-down, a flat 10% correction is applied to account for the contribution of $\psi(2S) \to J/\psi\pi\pi$ and a 40% correction is added to account for radiative χ_c decays. This yields a total correction of 50%. The correction factor is not well-determined from theory or experiment so is assigned a 100% uncertainty. This uncertainty is not included in the CSM theoretical uncertainty.

The NLO and NNLO* predictions are overlaid with the ATLAS measurements in Figure 4.10 for each rapidity region. The dashed lines represent the central NLO and NNLO* predictions while the shaded areas show the range of the prediction due to factorisation and renormalisation scale variation (although the upper band of this uncertainty may not encapsulate the full range of infrared uncertainties [73]).

The CSM predictions at NNLO* show significant improvement in describing the p_T dependence and normalisation of prompt J/ψ production over NLO, and vast improvement over earlier LO predictions that are compared to Tevatron data, although it is clear that these predictions still fall short of fully describing the production mechanisms of prompt J/ψ, particularly at the highest transverse momenta explored in this analysis. The overall scale of the central prediction is somewhat low, but these discrepancies are similar in nature to those seen between NNLO* calculations and $\psi(2S)$ production as measured by CDF [87, 88] at lower p_T and centre-of-mass energy and may be attributed to higher order corrections beyond NNLO* that are still expected to be relatively significant for hidden charm production.

Chapter 5

Average B Lifetime Measurement

5.1 Introduction

Building on the tools ad methods developed for the separation of prompt and non-prompt components in J/ψ production, we perform a measurement of the average B lifetime. With the goal of preparing the way to precision measurements of B-hadron lifetimes, early LHC data can be helpful to understand detector resolution, alignment and calibration using high statistics samples of inclusive leptons or, as in the present work, of inclusive $B \rightarrow J/\psi X \rightarrow \mu^+\mu^- X$ decays. With orders of magnitude higher statistics than for fully reconstructed exclusive B-meson or B-baryon candidates, the inclusive $B \rightarrow J/\psi X$ sample makes possible a detailed investigation of the decay lenght resolution and the impact of residual misalignment of the tracking system.

A lifetime measurement in inclusive $B \rightarrow J/\psi X \rightarrow \mu^+\mu^- X$ decays, $< \tau_b >$, measures the average lifetime of the admixture of B-hadrons produced in LHC proton–proton collisions and decaying to final states including a J/ψ meson. The measurement performed with the ATLAS detector using the entire 2010 data (see Sections 5.2 and 5.3) is presented here. In Section 5.4 the technique used to extract the average B lifetime from the data sample is described, and in Section 5.5 studies on systematic uncertainties are presented. The results of the measurement are shown in Section 5.6, where a comparison with results of previous measurements performed at LEP [22–25, 27, 28] and at the Tevatron [29] is provided.

5.2 Data and Monte Carlo Samples

For this analysis, the full proton-proton collision data sample collected by ATLAS in 2010 at centre-of-mass energy of 7 TeV was used. Data was only included in this analysis if taken during the LHC stable beams periods, and when the muon spectrometer, inner detector and both the magnet systems were operational. In addition, it is required that the events pass the single RoI seeded dimuon trigger, described in Section 2.6.3. After applying these requirements, the data sample corresponds to an integrated luminosity of about 35 pb^{-1}.

Three Monte Carlo (MC) samples are used:

- J/ψ coming from B-hadrons and decaying in two muons;
- promptly produced J/ψ (including contributions from hard processes and from feed-down to J/ψ from higher states such as χ_c);
- generic $b\bar{b}$ production with two muons in the final state.

All three samples are generated using PYTHIA6 and tuned using the ATLAS MC10 tune [89] and MRST LO* parton distribution functions, simulated with GEANT4 and fully reconstructed with the same software that is used to process real data. The samples include underlying events in the physics event generation process, and pile-up corresponding to 2.2 collisions per bunch crossing. Generator level cuts of 2.5 GeV are applied on the transverse momenta of the two muons in the final state.

To the purpose of this analysis, it is important to observe that PYTHIA simulation uses a Lund symmetric fragmentation function, for heavy endpoint quarks, modified according to the Bowler (Artru-Mennessier, Morris) space-time picture of string evolution [75]. This parametrization is known to be able to reproduce the LEP data on fragmentation fractions. For B-hadron decays the standard tables of the ATLAS tune are used. In these samples, the B-hadrons production fractions are as follows: $B^+ : B^0 : B_s : B-\text{baryons} = 0.42 : 0.42 : 0.09 : 0.07$. These fractions agree within uncertainties with the PDG averages.

5.3 Analysis Selection

Only events passing the single RoI seeded dimuon trigger, described in section 2.6.3, are considered in the analysis. Furthermore, in order to veto cosmic rays, events passing the trigger selection are required to have at least three tracks associated to the same reconstructed primary vertex. The three tracks must each have at least one hit in the pixel system and at least six hits in the SCT.

In each surviving event, pairs of reconstructed opposite charge muons are sought, as described in section 3.4. It is required that at least one of the two muons is combined, i.e. tagged-tagged combinations are excluded. The ID tracks associated to the muons must have at least two hits in the pixels of which one B-layer hit and six in the SCT. In addition only pairs where both muons have transverse momentum greater than 6 GeV and which are measured in the barrel region of the detector, hence within $|\eta_{1,2}| < 1.05$, are selected due to better mass and pseudo-proper time resolution. This improves the signal-to-background ratio and the systematic uncertainties, and still provides a sufficiently large statistical sample.

The two inner detector tracks associated to the pair of muons passing these selections are then fitted in the three dimensional space to a common vertex (see section 3.4). Those pairs which successfully form a vertex and which have an invariant mass (based on the refitted track parameters after vertexing) between 2.6 and 3.52 GeV, are regarded as $J/\psi \to \mu\mu$ candidates. These pairs are approximately 34000 in our data sample.

5.4 Lifetime Fitting Technique

5.4.1 Pseudo-Proper Time and F-Factor Definition

At the LHC, B-hadrons that may decay to J/ψ are B^0, $B^{\pm}$, B_s, B_c and B-baryons (mainly Λ_B). Each of these B-hadrons has a non-zero lifetime, and an average of the lifetimes can be measured with a partial reconstruction of their decay, using the J/ψ vertex. Reconstruction of J/ψ mesons is performed here when they decay to two muons.

Since the B-hadrons average lifetime measurement is performed in inclusive $B \to J/\psi\ X$ decay channels, the momentum of the B-hadron is never reconstructed, hence the B proper decay time, defined in Equation 4.5.1, cannot be measured. Instead, as described in Section 4.5.1, it is possible to approximate it using the J/ψ pseudo-proper time observable τ, defined in Equation 4.5.1, where the B-hadron p_T is replaced by the J/ψ one.

A correction of the smearing introduced by the use of the J/ψ pseudo-proper decay time is needed to measure the B lifetime. This correction can be performed introducing a factor, that will be called in the following the F-factor, defined as:

$$F = \frac{(\beta\gamma)_T^B}{(\beta\gamma)_T^{J/\psi}} = \frac{m_{PDG}^B \cdot p_T^{J/\psi}}{p_T^B \cdot m_{PDG}^{J/\psi}} \cdot \frac{1}{\cos\left(\Delta\phi(J/\psi\ - B)\right)}, \tag{5.1}$$

where $\Delta\phi(J/\psi\ - B)$ is the angle between the direction of flight of the J/ψ and the B-hadron, m_{PDG}^B and $m_{PDG}^{J/\psi}$ are the PDG masses of the B-hadron and the J/ψ meson respectively, and p_T^B and $p_T^{J/\psi}$ are their transverse momenta. The F-factor is extracted from the Pythia $b\bar{b} \to J/\psi\ X$ MC, as described in the following section.

5.4.2 Inclusive J/ψ Modelling in Monte Carlo

The correction factor F in Equation 5.1 cannot be extracted from data, since the B-hadron decays are not fully reconstructed in this measurement. Therefore, the transverse momentum of the B-hadron is unknown, and one has to rely on MC simulation.

As the F-factor is extracted from a MC sample, and since it depends on the momenta of the J/ψ and B in the sample, it is crucial that the inclusive J/ψ spectrum in B-hadron decays is correctly described by the simulation. It is known that there are difficulties in simulating correctly the inclusive J/ψ spectrum using a limited number of measured decay modes, as in the standard ATLAS simulation, and also from the theoretical point of view [90]. In order to quantify the discrepancy, the truth spectra of the $b\bar{b} \to J/\psi\ X$ ATLAS Pythia MC sample described in Section 5.2 is compared to the measurements of the BaBar experiment at SLAC in data recorded at the $\Upsilon(4S)$ resonance.

At SLAC, the $B_{u,d}$ mesons were produced via two body decays of $\Upsilon(4S)$. Hence a comparison of the MC simulation with the BaBar results should only include $B^{\pm}$ and B^0 hadrons. The uncertainty on the fractions and spectra of the additional B-hadrons produced at the LHC, such as B_s and Λ_b, have been included as a source of systematic uncertainty, as described in Section 5.5.1.

BaBar data are presented in Figure 5.1, taken from reference [91]. The data points represent the momentum spectrum, corrected for detector acceptance, of the

J/ψ in the $\Upsilon(4S)$ rest frame ($p^\star$) and can be compared to truth information in MC simulation.

Although in the MC sample the B-hadrons are not produced in a $\Upsilon(4S)$ decay, it is straightforward to apply the correct boost to the J/ψ mesons. Since the $\Upsilon(4S)$ is a two body decay, the momenta of the two B-mesons daughters in its rest frame are fixed to $p^\star(B^\pm) = 0.334\,\text{GeV}$ and $p^\star(B^0) = 0.328\,\text{GeV}$. This allows a Lorentz transform of the J/ψ parameters in the rest frame of the $\Upsilon(4S)$ in the MC simulation to be performed, even though there is no $\Upsilon(4S)$ in the actual decay.

The two $p^\star$ distributions, one from BaBar and the other from MC simulation, shown in Figure 5.1 (top), present a discrepancy both in shape and in mean value. In particular, a relative shift in the average $p^\star$ of 5% is observed, and a similar bias in lifetime could be expected from this mismatch. This highlights the need to improve the MC modelling, the main shortcoming of which is most likely due, as said before, to the fact that not all of the inclusive B-meson decays are simulated. In order to have a more reliable estimate of the needed correction factor, and to reduce the shift in average $p^\star$, an empirical re-weighting of the MC sample is performed modifying decay branching ratios, in analogy with earlier measurements at CDF [29, 92].

To do so a number of decay channels are chosen to which the weights are assigned. The suitable decay channels need to correspond to a combination of kinematic ranges that span the whole $p^\star$ space. The choice of these decay channels is arbitrary since only the reproduction of the expected spectra matters here. Three suitable decay channels are found: $B \to \psi(2S)K\pi\pi$, $B \to J/\psi K_1(1270)$ and $B \to J/\psi K$. The remaining decays are assigned a weight equal to 1.

To optimize the combination of weights associated to the three chosen decay channels, a χ^2 variable is minimized. The J/ψ $p^\star$ distribution in the MC sample after the re-weighting procedure has been applied is shown on the bottom plot of Figure 5.1. A drop in the difference between the mean values of the two distributions from 0.076 GeV to 0.003 GeV is observed, and a reasonable agreement in shape is obtained. The F-factor distribution, before and after the re-weighting procedure has been applied to the MC sample, is shown in Figure 5.2.

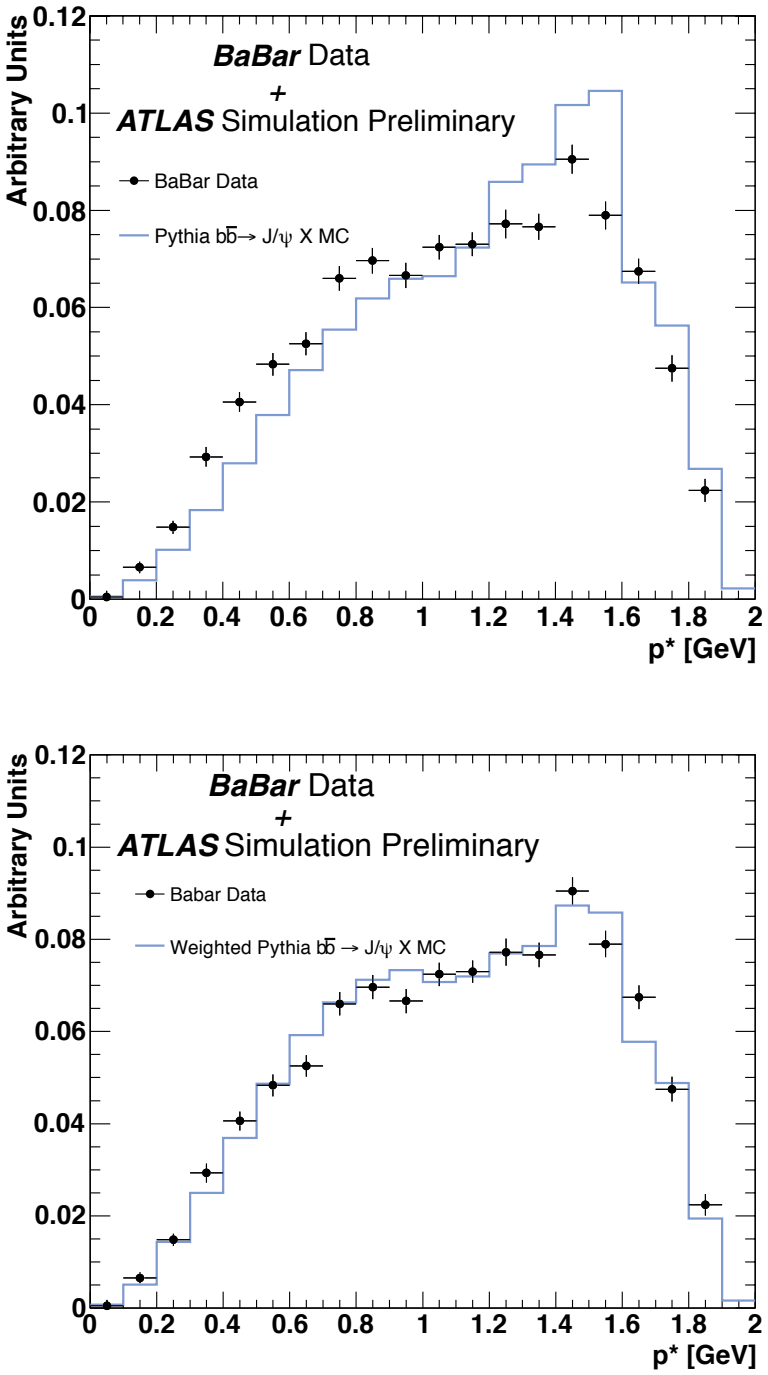

Figure 5.1. Distributions of $p^{\star}$, the momentum of the J/ψ from B-hadron decays in the system of reference of the centre-of-mass of the $\Upsilon(4S)$, mother of the B. Top: black points correspond to the BaBar data distribution, deconvolved for all detector effects, and the blue histogram represents the same distribution at the truth level of the ATLAS PYTHIA $b\bar{b} \rightarrow J/\psi\ X$ MC sample for $B^{\pm}$ and B^{0} hadrons (as defined in the text). Bottom: same comparison after re-weighting of the MC simulation.

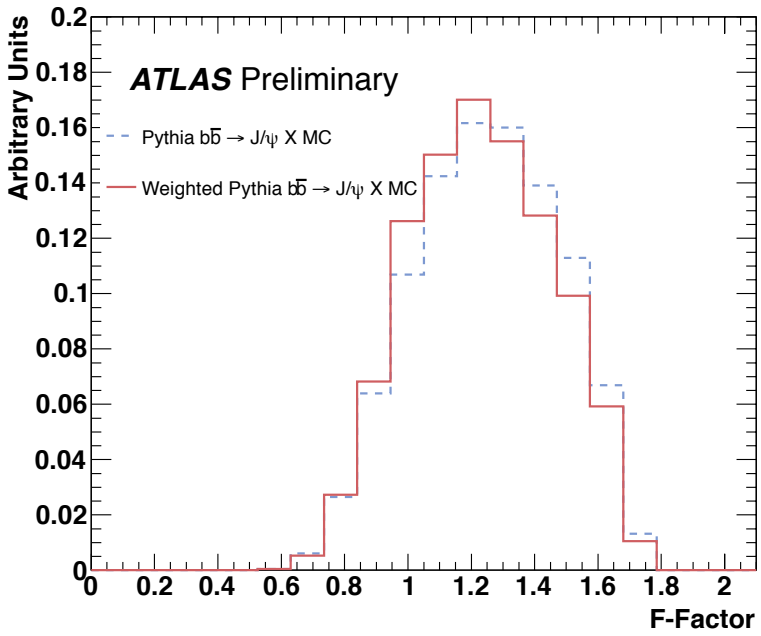

Figure 5.2. The F-factor PDF before (blue dashed line) and after (red solid line) re-weighting has been applied to the MC simulation.

5.4.3 Fitting Procedure

The average B lifetime can be extracted from data performing an unbinned maximum likelihood fit simultaneously on the J/ψ invariant mass ($m_{\mu\mu}$), in a range of $\pm 10\,\sigma$ around the peak, and pseudo-proper time (τ), in analogy with what described in Section 4.5.1. For this purpose the likelihood function defined in Equation 4.10 is used.

Here, the mass error distributions, E^m_{sig} and E^m_{bkg}, are assumed to be identical in this analysis for signal and background. This is a reasonable approximation since the two distributions are similar, and the effect of the approximation on the measured lifetime has been verified to be negligible. On the other hand, we do not use the same approximation for the pseudo-proper time per candidate errors, since this might, in this case, introduce a bias on the measurement. Equation 4.10 can thus be simplified, and we obtain:

$$\mathcal{L} = \prod_{i=1}^{N} \Big[(1-f_{bkg}) P_{sig}(\tau \,|\, \delta\tau) E_{sig}(\delta\tau) F_{sig}(m_{\mu\mu}, \delta m) + f_{bkg} P_{bkg}(\tau \,|\, \delta\tau) E_{bkg}(\delta\tau) F_{bkg}(m_{\mu\mu}) \Big]. \tag{5.2}$$

In the following sections a complete description of the PDFs and a brief account of the tests performed to validate the fitting technique is provided.

Invariant Mass Model

The higher statistics available for this measurement, with respect to the measurement presented in section 4.5, justifies the appearence of a radiative tail in the signal invariant mass distribution. The prompt and non-prompt J/ψ invariant mass distribution is hence modelled using a Crystal-Ball function:

$$F_{sig} = \begin{cases} \exp\left(-\frac{(m_{\mu\mu}-m_{J/\psi})^2}{2(S_m\delta m)^2}\right) & for \quad \frac{m_{\mu\mu}-m_{J/\psi}}{(S_m\delta m)} > -\alpha, \\ A\cdot\left(B-\frac{m_{\mu\mu}-m_{J/\psi}}{(S_m\delta m)}\right)^{-n} & for \quad \frac{m_{\mu\mu}-m_{J/\psi}}{(S_m\delta m)} \leq -\alpha, \end{cases} \tag{5.3}$$

where

$$A = \left(\frac{n}{|\alpha|}\right)^n \exp\left(-\frac{|\alpha|^2}{2}\right), \quad B = \frac{n}{|\alpha|} - |\alpha|. \tag{5.4}$$

Here n and α are free parameters of the fit, $m_{J/\psi}$, δm and S_m are defined in analogy with what was done in Section 4.5.2.

For the background component a Chebychev first order polynomial function is used:

$$F_{bkg}(m_{\mu\mu}) = \mathcal{C}_1 \cdot m_{\mu\mu}. \tag{5.5}$$

Pseudo-proper Time Model

In the following section the pseudo-proper time fitting model, composed by the signal and background PDFs and the two per candidate error PDFs, will be described.

- **Signal Model:** the pseudo-proper time PDF for the signal, P_{sig}, is composed by two terms: one describes the J/ψ coming from B-hadron decays and the other one the prompt J/ψ, as defined in Equation 4.14. The prompt component $P_P(\tau, \delta\tau)$, has been defined in Equation 4.16 as a Dirac's δ function convolved with the resolution function $R(\tau' - \tau, \delta\tau)$.

  On the other hand, since we need to extract the B-hadrons lifetime from this fit, a correction needs to be applied to the non-prompt signal PDF, $P_B(\tau, \delta\tau)$, described in Equation 4.15, so that $\tau_{eff} = \tau_B$. This is done, convolving it with the F-factor PDF ($H(F)$), shown in Figure 5.2, as in:

$$P_B(\tau \,|\, \delta\tau) = \int dF\, H(F)\, F\, \exp\left(\frac{-\tau\cdot F}{\tau_B}\right) \otimes R(\tau \,|\, \delta\tau). \tag{5.6}$$

  This convolution makes the fit procedure very time consuming, but the CPU time can be very much reduced discretizing the integral:

$$P_B(\tau \,|\, \delta\tau) \simeq \sum_{i=0}^{N} \Delta F_i\, H(F_i)\, F_i\, \exp\left(\frac{-\tau\cdot F_i}{\tau_B}\right) \otimes R(\tau \,|\, \delta\tau), \tag{5.7}$$

  where the F-factor PDF is not a continuous function but a histogram with $N = 20$ bins. This procedure has been tested on MC and it has been verified that the impact of the F-factor PDF binning on the lifetime measurement is negligible.

- **Background Model:** the pseudo-proper time PDF for the background candidates P_{bkg} is the same as the one used for the non-prompt fraction measurement, and is defined in Equation 4.17.

- **Signal and Background Pseudo-proper Time Error Models:** using the per candidate error in the pseudo-proper time resolution, the prior probabilities of the errors for both signal and background, respectively E_{sig} and E_{bkg}, need to be included in the likelihood function. These PDFs are directly extracted from data, using a template to describe each one of them.

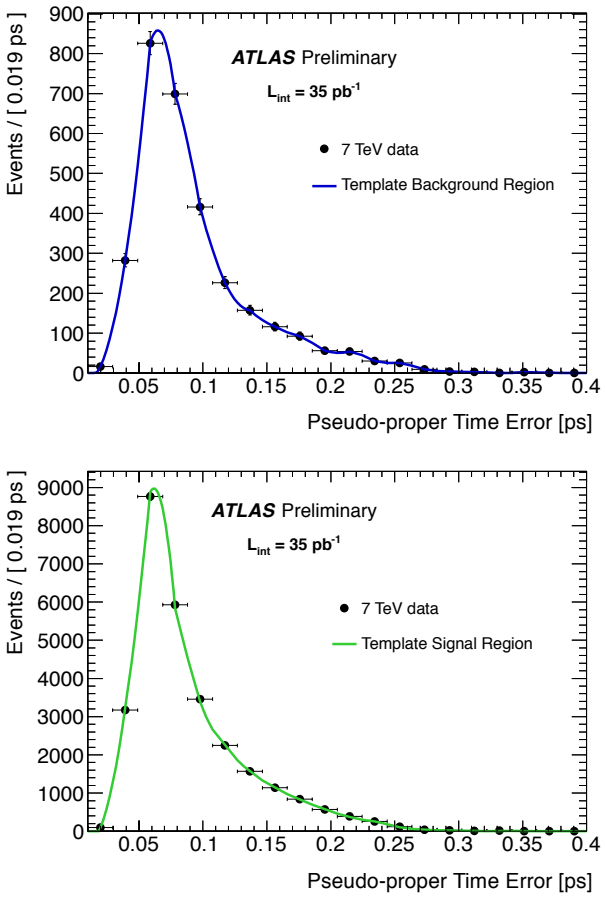

Figure 5.3. The background (top) and signal (bottom) τ error templates used in the simultaneous fit are shown. Superimposed, the data points of respectively the sideband candidates and the sideband subtracted signal region ones.

To build the background error distribution template, the candidates contained in the sideband regions, defined in a invariant mass range of $[m_{J/\psi} - 10\sigma, m_{J/\psi} - 6\sigma]$ and $[m_{J/\psi} + 6\sigma, m_{J/\psi} + 10\sigma]$, are considered. For the signal error distribution only the candidates contained in the signal region, defined in an invariant mass range of $\pm 5\,\sigma$ around the peak, are included, after performing a sideband subtraction on the distribution. The extracted templates are shown as solid lines in Figure 5.3, superimposed on the data distributions they've

been extracted from (black dots).

Summary of Free Parameters

The parameters used in the fit are listed in Table 5.1

Table 5.1. List of the parameters involved in the simultaneous fit.

Parameter	Description
$m_{\mu\mu}$ Signal PDF	
$m_{J/\psi}$	Crystal-Ball function mean value
S_m	Crystal-Ball function resolution scale factor
α	Crystal-Ball function α parameter
n	Crystal-Ball function n parameter
$m_{\mu\mu}$ Background PDF	
C_1	Chebychev polynomial parameter
$f_{\rm bkg}$	background fraction
τ Signal PDF	
f_B	fraction of non-prompt signal candidates
S_t	resolution scale factor of J/ψ candidates
τ_B	average B lifetime
τ Background PDF	
$f_{B,bkg}$	fraction of non-prompt background candidates
$S_{\rm bkg}$	resolution scale factor of background candidates
b_1	normalization fraction of positive and symmetric exponential
$\tau_{\rm eff\,1}$	slope of the positive exponential
$\tau_{\rm eff\,2}$	slope of the symmetric exponential

5.4.4 Test of the Fitting Technique

Both the fitting technique and the F-factor convolution procedure have been validated using respectively toy MC experiments and fully simulated MC data.

Fitter Validation Using Toy MC Experiments

The simultaneous mass and pseudo-proper time fit model is used to generate 1000 toy MC experiments, using the method described in Section 4.5.2.

For each experiment, a fit of the total PDF on the toy MC sample is performed. The pull, Δ, defined as:

$$\Delta = \frac{(\tau_B^{\rm generated} - \tau_B^{\rm extracted})}{\sigma^{\rm extracted}(\tau_B)},$$

is computed for each toy MC experiment. Here $\tau_B^{\rm generated}$ is the B lifetime according to which the toy MC samples are generated (i.e. the result of the fit of the global model to the experimental data), while $\tau_B^{\rm extracted}$ and $\sigma^{\rm extracted}(\tau_B)$ are respectively the value and error obtained from the fit. The pull distribution, shown in Figure 5.4, is then fitted with a Gaussian. The Gaussian mean value and width are: mean = -0.013 $\pm$ 0.032, σ = 1.00 $\pm$ 0.02. These values are statistically compatible respectively

with zero and one, indicating that no bias or improper error estimate is introduced by the fit.

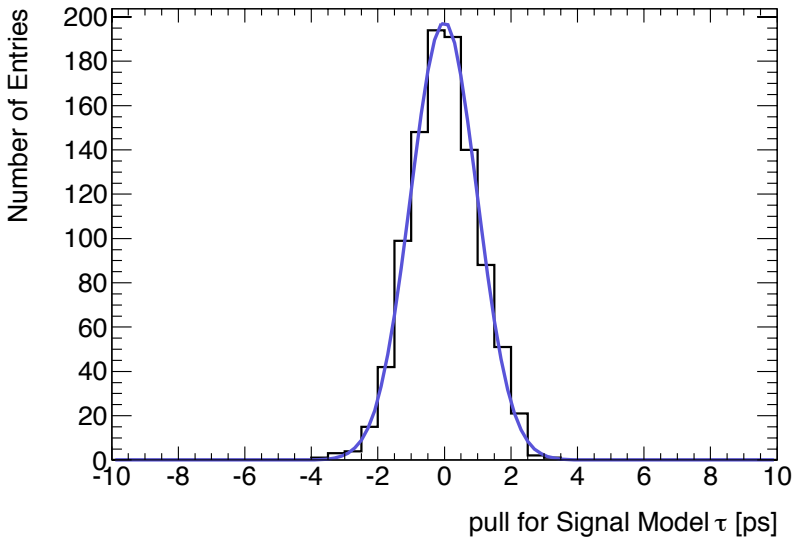

Figure 5.4. Average B lifetime pull distribution with the Gaussian fit superimposed.

Fitting Technique Validation Using Pythia Monte Carlo

A test of the fitting procedure has been performed on fully simulated MC samples to verify whether the convolution of the F-factor distribution with the non-prompt signal τ PDF corrects as expected the J/ψ pseudo-proper time observable, and that the whole fitting procedure does not introduce any bias on the extracted average B lifetime.

First a test is performed on the MC $b\bar{b} \rightarrow J/\psi\ X$ selecting only one lifetime component. This test checks that the F-factor correction is working as expected, providing a value of the measured lifetime compatible with the true value in the MC. To achieve this only reconstructed candidates matched to a true J/ψ coming from B^0 decays are selected. The pseudo-proper time fit is performed using only the P_B component of the PDF, obtaining the distribution in Figure 5.5 (top). The B^0 lifetime is estimated using the fit: $\tau_{B^0}^{\mathrm{FIT}} = 1.56 \pm 0.03$ ps. This result is in agreement with the true input lifetime of the MC sample: $\tau_{B^0}^{\mathrm{TRUTH}} = 1.56$ ps.

An intrinsic problematic of this measurement is given by the fact that one has to perform the fit using a single exponential function to reproduce a distribution given by the combination of several exponentials, each corresponding to a different lifetime. It has been shown that this should not affect the outcome of the fit, which converges to the average lifetime value [93], provided that no bias is introduced in the pseudo-proper time measurement, and that the resolution description is good. In order to verify this, a second test is performed fitting the full $b\bar{b} \rightarrow J/\psi\ X$ simulated sample. The resulting distribution from the fit is shown in Figure 5.5 (bottom), and the average lifetime obtained from the fit is $\tau_B^{\mathrm{FIT}} = 1.530 \pm 0.020$ ps. The fitted inclusive lifetime is compared to the average of the true lifetimes of the B-hadrons

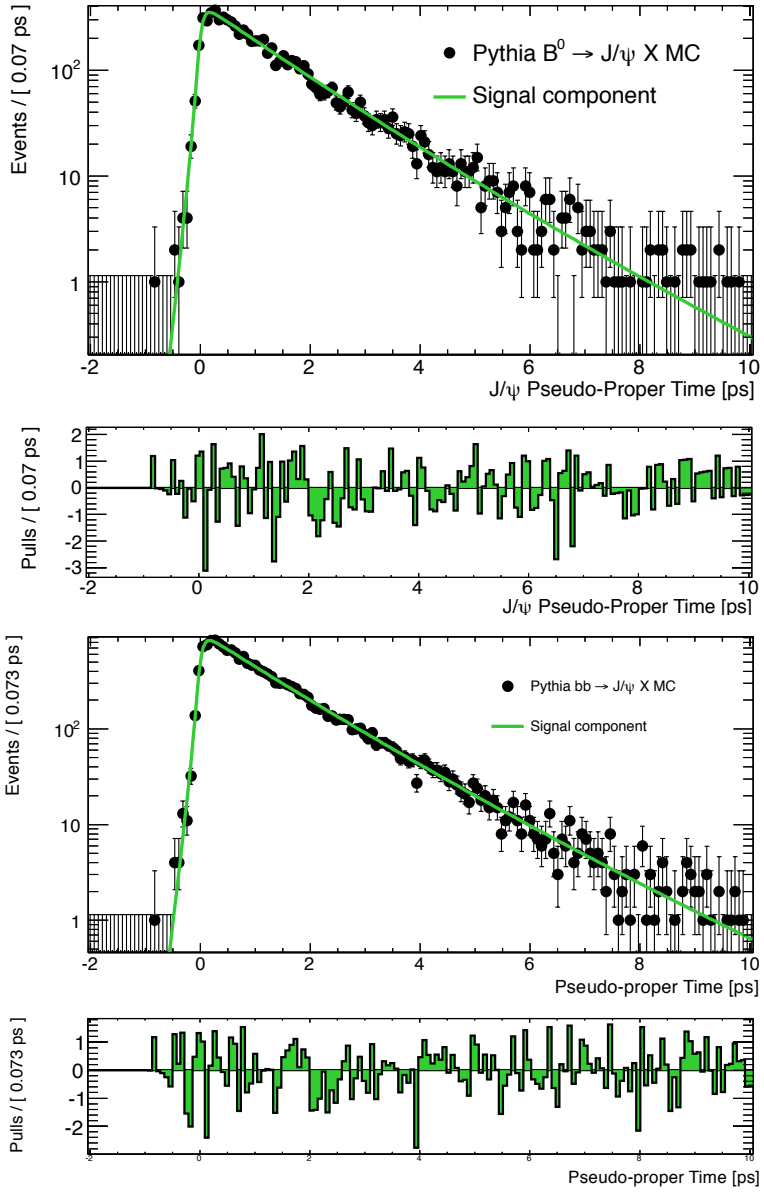

Figure 5.5. Pseudo-proper time fit of the signal non-prompt component obtained on $B^0 \rightarrow J/\psi\ X$ (top) and inclusive B to J/ψ (bottom) simulated events.

contained in the MC sample, $\tau_B^{\mathrm{TRUTH}} = 1.53$ ps. Also in this case the result of the fit on the MC sample is as expected.

A fit is then performed on a sample with both prompt and non-prompt J/ψ and, as a background, a $b\bar{b} \to \mu\mu X$ MC. Although the source of the background dimuon candidates in the data sample is not limited to muons from b-quark decays, this represents a useful cross-check to verify that the simultaneous fit gives the expected result also in presence of a background. As the used MC does not include the simulation of radiative decays of the J/ψ , in this fit the Crystal-Ball function described in section 5.4.3 is replaced by a per candidate error Gaussian function. The measured lifetime, $\tau_B^{\mathrm{FIT}} = 1.536 \pm 0.012$ ps, is in good agreement with the true expected value.

The fitted distributions are shown in Figure 5.6, on the bottom of the plot, the residuals of the pseudo-proper time projection of the fit normalized on their errors are shown. Results of these tests are summarized in Table 5.2.

Table 5.2. Results of the test of the fitting technique performed on PYTHIA MC samples.

MC sample	τ^{truth} [ps]	τ^{fit} [ps]
$B^0 \to J/\psi\ X$	1.56	1.560 ± 0.030
$b\bar{b} \to J/\psi\ X$	1.53	1.530 ± 0.020
full sample	1.53	1.536 ± 0.012

Finally, in order to test the robustness of the fitter used, a test on different lifetime values is performed. Since the dominating lifetime components in the MC sample have very similar lifetimes, this test involves a reweighting procedure of the lifetime in the $B^0 \to J/\psi\ X$ sample, obtaining lifetimes of 1.2 and 2 ps. The fits performed on those two reweighted samples give the following results: $\tau = 1.205 \pm 0.014$ ps and 2.009 ± 0.024 ps respectively, showing that the response of the fitting procedure is linear with increasing lifetimes as expected.

5.4.5 Fit Results

The results of the simultaneous invariant mass and pseudo-proper time fit are presented in this section. The simultaneous fit provides an estimate of the B average lifetime of $\tau_B = 1.489 \pm 0.016$ ps, where the uncertainty is purely statistical. Table 5.3 contains the list of all fitted parameters, with their statistical uncertainty, and the quality of the fit computed as described in Appendix .3. In Table .22 in Appendix .6 the complete covariance matrix is provided.

In figure 5.7 the invariant mass and pseudo-proper time projections of the fit are shown, with the respective pulls distributions. In figure 5.8, on top, the background component of the pseudo-proper time PDF is projected onto the J/ψ candidates from the invariant mass sidebands regions. This is done in order to check the quality of the background estimate in the simultaneous fit. On the bottom plot in figure 5.8 the total pseudo-proper time PDF is projected onto the signal region candidates.

The χ^2 contribution of high pseudo-proper time bins justifies the p-value obtained (7%). This is an intrinsic side-effect of fitting with a single exponential the combination of several exponentials corresponding to different lifetimes, as discussed

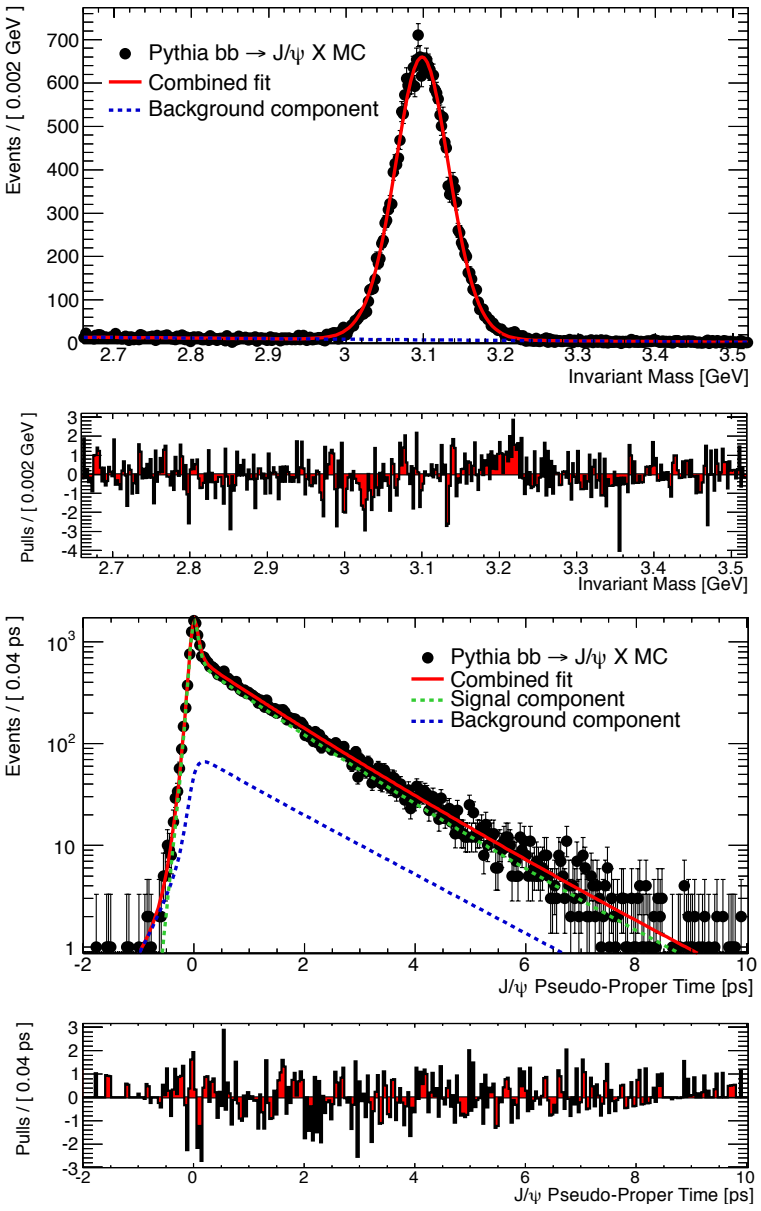

Figure 5.6. Results of a simultaneous fit of mass and lifetime performed on a full MC sample, as a background a $b\bar{b} \rightarrow \mu\mu X$ sample is used. On the top, invariant mass projection, on the bottom pseudo-proper time projection.

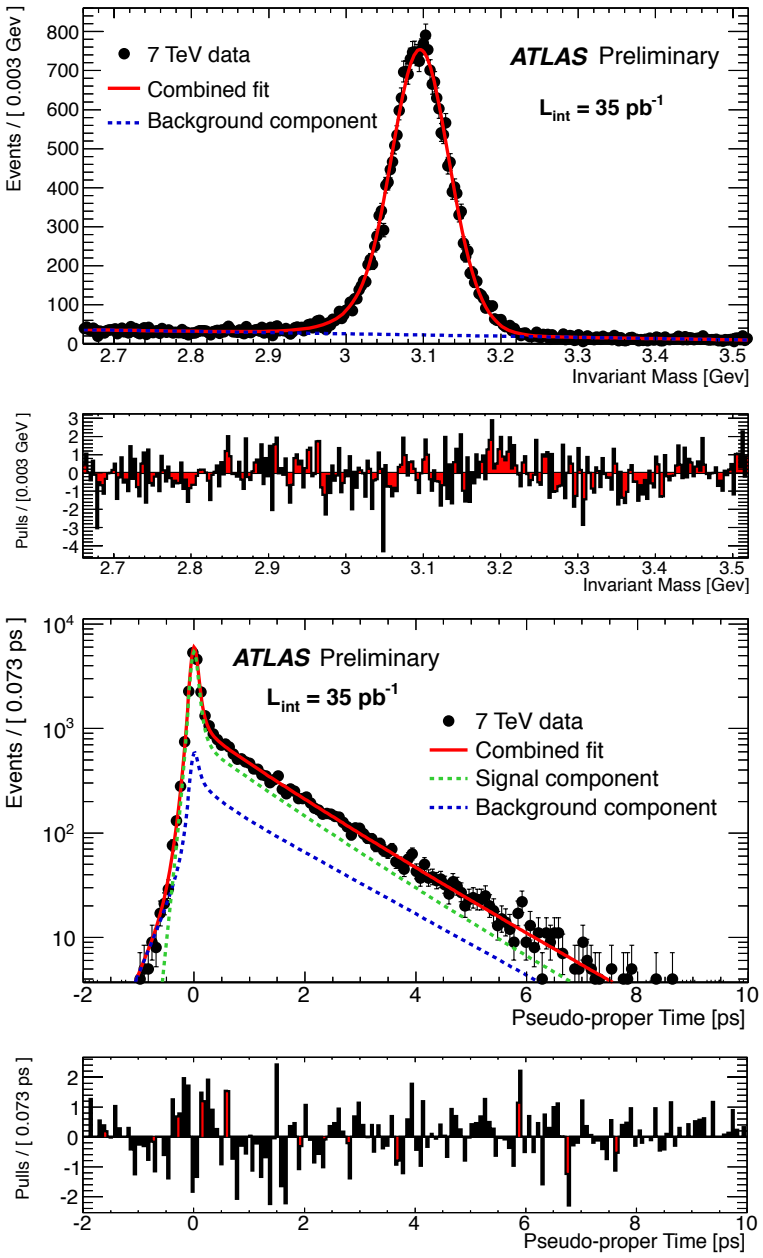

Figure 5.7. Invariant mass (top) and pseudo-proper time (bottom) projections of the simultaneous fit PDF with their pull distributions.

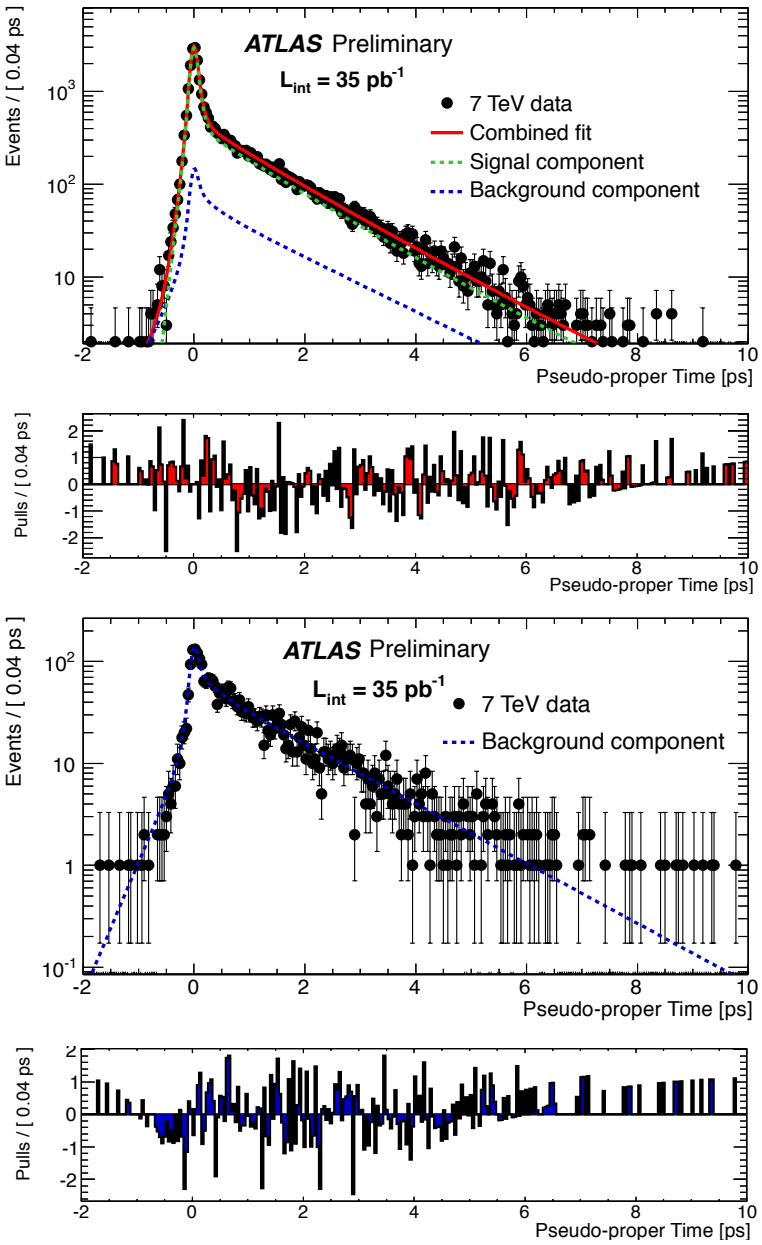

Figure 5.8. Top: total PDF projected onto pseudo-proper time observable in the signal invariant mass region, and respective pulls. Bottom: background PDF projected onto pseudo-proper time observable for candidates in the sideband invariant mass region, and respective pulls.

Table 5.3. Quality of the fit and parameters obtained with the simultaneous mass-lifetime fit and their statistical uncertainties.

Parameters	Fit Results
χ^2/NDoF	224/193
χ^2 p-value	0.07
Kolmogorov test	0.18
$m_{\mu\mu}$ Signal PDF	
$m_{J/\psi}$	3.09553 ± 0.00031
S_m	1.187 ± 0.008
α	1.654 ± 0.093
n	7.9 ± 3.7
$m_{\mu\mu}$ Background PDF	
C_1	-0.578 ± 0.019
f_{bkg}	0.213 ± 0.003
τ Signal PDF	
f_B	0.496 ± 0.004
S_t	1.018 ± 0.008
τ_B	**1.489 ± 0.016**
τ Background PDF	
$f_{B,bkg}$	0.848 ± 0.010
S_{bkg}	1.026 ± 0.058
b_1	0.129 ± 0.011
$\tau_{eff\,1}$	1.478 ± 0.026
$\tau_{eff\,2}$	0.338 ± 0.024

in section 5.4.4.

5.5 Checks and Systematics

The studies performed to assess the relevant sources of systematic uncertainties on the measured average B lifetime are outlined below.

5.5.1 F-Factor Extraction Systematics

The F-factor correction, extracted from MC, relies on the assumption that the simulated sample reproduces data well. An assessment of the systematic uncertainties introduced in the B lifetime measurement by this assumption has been made, and is presented here.

MC Reweighting Procedure

In order to reduce the systematic effect due to a poor description of the spectra of J/ψ from $B^{\pm}$ and B^0 mesons, an empirical reweighting has been applied on the MC samples before extracting the F-factor PDF, as described in section 5.4.2. The

impact of the choice of the weights on the measurement has been studied varying them within one standard deviation and comparing the obtained τ_B values with the central one. The $p^\star$ distributions obtained with each of the weights configuration are shown in Figure 5.9. The largest deviation from the central value was found to be $\Delta\tau_B = 0.003$ ps, and taken as a systematic uncertainty on the measurement.

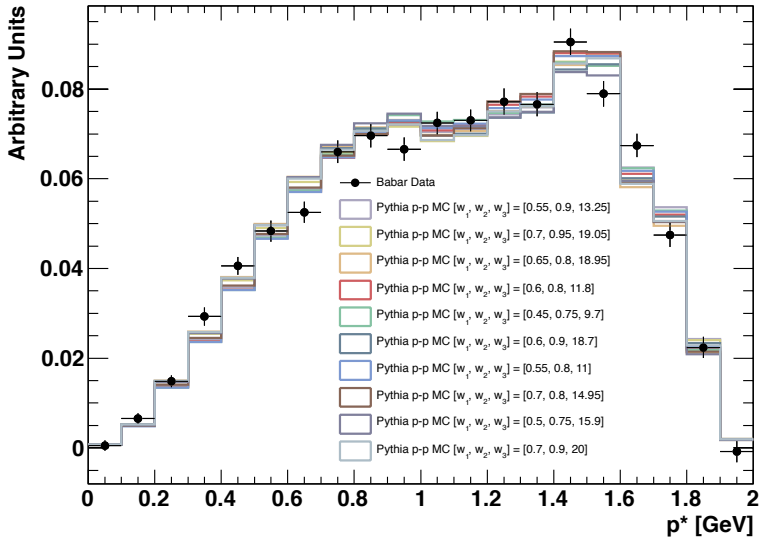

Figure 5.9. J/ψ $p^\star$ distributions, as defined in Section 5.4.2. The black dots are the BaBar distribution, which is compared here with the ten $p^\star$ distributions obtained varying the weights applied on the MC sample as described in Section 5.4.2.

Uncertainties on B_s and B-baryons Fractions

The BaBar data does not include B_s and B-baryons, an uncertainty must then be associated to the contribution of these B-hadrons in the F-factor. In order to estimate this uncertainty, the fractions of B_s and B-baryons decaying to J/ψ have been varied. The largest deviations obtained with respect to the central value of the lifetime have been taken as systematic uncertainties on the measurement. The fraction of B_s mesons in the sample has been varied by 20% around its central value of ~ 0.009, and a deviation of 0.001 ps from the lifetime central value has been assessed. The B-baryons, when studying inclusive decays in J/ψ mesons, are dominated in numbers by the Λ_B baryon. The Λ_B decays are removed from the MC sample and a shift of 0.002 ps is measured on the lifetime. The other B-baryons in the sample were found to have a negligible effect on the lifetime estimate.

F-Factor Dependence on the J/ψ p_T

A mild dependence of the F-factor on the J/ψ meson's p_T is observed in the kinematic range studied. The data and MC non-prompt J/ψ spectra are compared and found in very good agreement, as shown in figure 5.10, where J/ψ are shown after a cut of

$\tau > 0.3$ mm (to select those coming from B decays) and a background subtraction have been applied. In order to test the B lifetime measurement sensitivity to the J/ψ spectrum description in MC, a set of weights (bottom in figure 5.10), computed as the ratio of the two normalized p_T distributions, was used to rescale the MC sample. The related systematic effect observed was found to be negligible.

5.5.2 Fitting Models

A number of changes are applied to the fitting procedure, and the fit is repeated in order to gauge the sensitivity of the B lifetime to the details of the fits:

Pseudo-proper Time Resolution Modelling

One thousand toy MC experiments are generated using a per candidate double Gaussian resolution function, with two different scale factors to account for differences between the pseudo-proper time resolution returned by the tracking algorithm and the measured one. Each experiment is then fitted using the default PDF, with a per candidate single Gaussian resolution function, and the B lifetime pull distribution is produced. The shift in the pull distribution ($\sim 0.03\%$) can be neglected with respect to the other systematic uncertainties in play. No relevant improvement in the normalized residuals distributions of the pseudo-proper time fit projections is observed when adding a second Gaussian to the resolution model.

Mass Background Modelling

The main result uses a first-order Chebychev polynomial in the mass fit to describe the background. To test the sensitivity to this choice, 1000 toy MC experiments are generated using the default model and fitted instead with polynomials of second-order. The shift on the lifetime measured is of the order of 0.03% and can thus be neglected.

Pseudo-proper Time Background Modelling

The central value of the average B lifetime measurement uses a parametric model for the pseudo-proper time background description. To assess the systematic related to the choice of the model, a pseudo-proper time fit is performed in a region of $\pm 5\,\sigma$ around the J/ψ peak using templates to describe the background τ component. The systematic obtained is rather conservative since we are comparing two completely opposite approaches: one where all of the background model parameters are free in the fit, the other where they are all fixed using the sidebands J/ψ candidates.

The first step in this procedure is an invariant mass fit, which is used to estimate the background fraction of the data sample f_B in the signal region, defined as $\pm 5\,\sigma$ around the J/ψ mass peak. Then the templates for the background component are built: two different templates are extracted from data, one for the left sideband, defined between $-10\,\sigma$ and $-6\,\sigma$ from the mass peak, and the second one for the right sideband, defined between $6\,\sigma$ and $10\,\sigma$ from the peak. The two templates are shown in figure 5.11, superimposed on the left or right sideband data points. When extracting the templates PDF, one hundred bins are used in the τ histograms relative to the two sideband regions. It was found that changing from 40 to 100 bins,

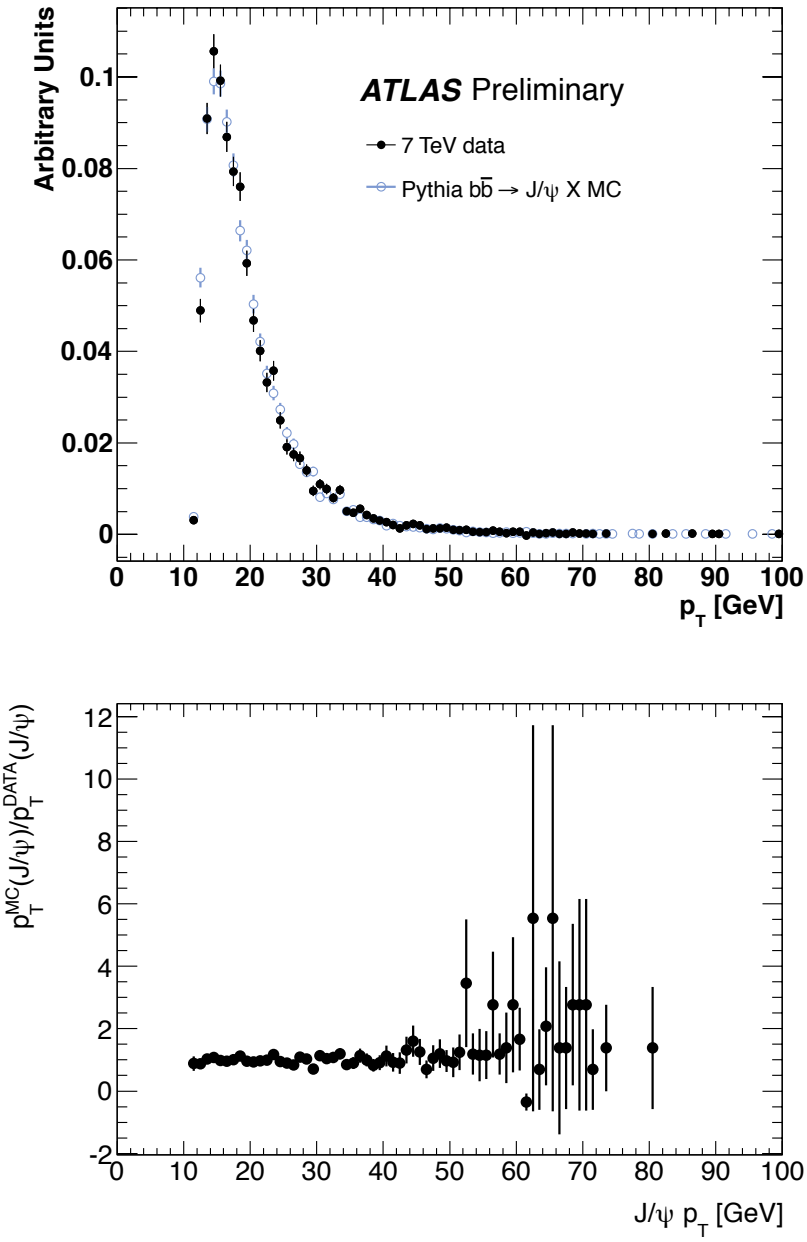

Figure 5.10. Top: p_T spectrum of the J/ψ candidates in data (full black points) and in MC simulation (empty blue points). A sideband subtraction is performed on the distribution, and a $\tau > 0.3$ mm cut is applied. Bottom: weights, computed as the ratio between data and MC p_T distributions, are shown.

an oscillation of only 0.3% on τ_B is observed. This effect can thus be neglected in the systematic estimate.

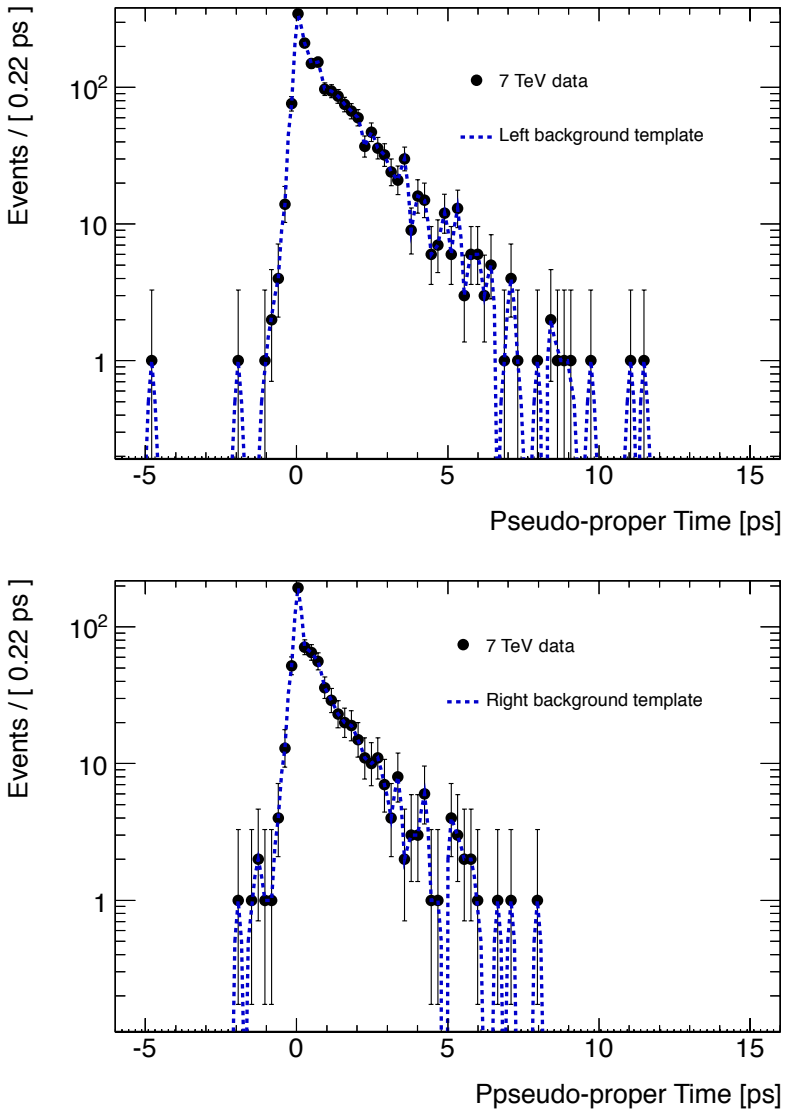

Figure 5.11. On the top and bottom plots respectively the left and right sideband candidates are represented as the black points, and, superimposed are the templates used in the τ background model template building procedure.

The left and right τ distributions are quite different, as expected, since the background events mixture changes with the invariant mass of the candidate. In particular a higher combinatorial background from b and c-quark semi-leptonic decays is expected in the left sideband region, justifying the more pronounced long-lived tail of the left sideband distribution, whereas on the right sideband region most of the background should be given by muons from pions and kaons decays-in-flight. It is therefore important to correctly mix the two templates in order to describe the background candidates under the invariant mass peak in the signal region. This is

done according to the fraction $f_{\frac{right}{left+right}}$ defined as:

$$f_{\frac{right}{left+right}} = \frac{\mathcal{A}_{bkg}(m_{J/\psi}\ , m_{J/\psi}\ + 5\,\sigma)}{\mathcal{A}_{bkg}(m_{J/\psi}\ - 5\,\sigma, m_{J/\psi}\ + 5\,\sigma)} \simeq 0.43 \tag{5.8}$$

where $\mathcal{A}_{bkg}$ represents the integral of the mass background model in the mass range defined within the parenthesis.

The pseudo-proper time fit is then performed on the candidates contained in the invariant mass signal region, where both $f_{\frac{right}{left+right}}$ and f_B are fixed, and only the signal scale factor, non-prompt fraction and average B lifetime parameters are let free. The results of this fit are shown in table 5.4 and the fitted pseudo-proper time distribution is shown in figure 5.12 with the corresponding pulls distribution. The difference between this result and the central value of the measurement, $\Delta\tau_B \simeq 0.024$ ps, is accounted for as one of the dominant systematic effects on the lifetime estimate.

Table 5.4. Results of the fit performed using templates to describe the background τ component of the PDF.

parameters	fit results
χ^2/NDoF	167/105
χ^2 p-value	0.0001
Kolmogorov test	0.68
f_{bkg}	0.213 (fixed)
$f_{\frac{right}{left+right}}$	0.43 (fixed)
f_B	0.492 ± 0.004
S_t	1.061 ± 0.009
τ_B	**1.513 ± 0.017**

5.5.3 Alignment of the ID Tracker

The study of the impact of residual misalignments of the ATLAS ID on the average B lifetime measurement is presented. Two different residual misalignments are studied, which are considered to have the largest impact on the alignment: a sagitta distortion and a radial misplacement of the individual sensors. The impact on the lifetime measurement is estimated by reconstructing $b\bar{b} \to J/\psi\ X$ simulated events with a distorted geometry. The lifetime measured on a set using perfect geometry reproduces the true lifetime used as input of the simulation, thus the difference between the lifetime measured using simulated events with distorted geometry and perfect geometry is taken as a systematic uncertainty.It is also important to stress that the lifetime shift measured using a signal plus background sample is consistent with what found on the signal sample only.

The largest impact on the measured pseudo-proper time is expected to be due to the residual misalignments of the first pixel layer, the one nearest to the beam-line, while a residual misalignment of the more external layers will have an impact on the

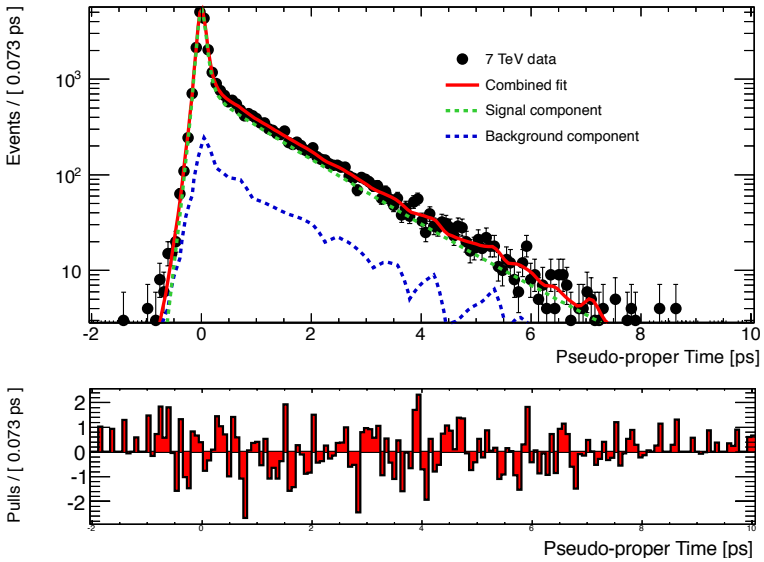

Figure 5.12. The pseudo-proper time distribution of the candidates contained in the invariant mass region between $\pm 5\,\sigma$ around the J/ψ peak is shown. Superimposed the PDF used to fit the distribution. On the bottom plot the pulls distribution.

overall momentum scale. The procedure used to align the ID forces the tracks to originate from the beam-line and for this reason only a small impact due to residual misalignments is expected.

Sagitta Misalignment

In the sagitta distorted sample the centers of the pixel and SCT barrel layers, located in the perfect geometry case at the beam-line, are shifted. The center of the barrel layer has a shift in the ATLAS global x coordinate which increases linearly with the barrel radius. The maximal shift corresponds to 200 μm on the most external SCT layer. The size of the shift is chosen to extract a conservative, but still realistic, estimate of the sagitta misalignment in the 2010 reconstructed data.

The ID alignment procedure is then performed on this distorted geometry, following closely the procedure used on real data. The distortion on the most external SCT barrel layer is reduced by the alignment procedure by a factor of two, to about 100 μm.

Radial Misalignment

A second set is used to estimate the impact of a possible radial distortion. Here the barrel modules are moved along the out-of-plane direction, i.e. the radial ATLAS coordinate. The alignment procedure applied on the sagitta misaligned sample is not optimized for out-of-plane corrections, and the initial misalignment is hardly removed. For this reason the estimate of the residual out-of-plane distortions has been extracted from data.

Possible out-of-plane distortions can be estimated using tracks passing through

the overlap region of two modules adjacent in ϕ. Overlap residuals are defined as the difference between the residual measured in one layer and the residual measured in the adjacent layer: $\text{Overlap Residual} = \text{Res}_{\phi=n} - \text{Res}_{\phi=n\pm1}$. To the first order, for a full circumference of overlapping modules, the overlap residuals are proportional to distortions in the radial direction:

$$2\pi\Delta R = \#(\text{Overlap Regions}) \cdot \text{Mean}(\text{Overlap Residuals}).$$

For the most internal pixel layer an overall shift of 15 μm in the radial direction corresponds to a shift of 5 μm of the overlap residuals distribution.

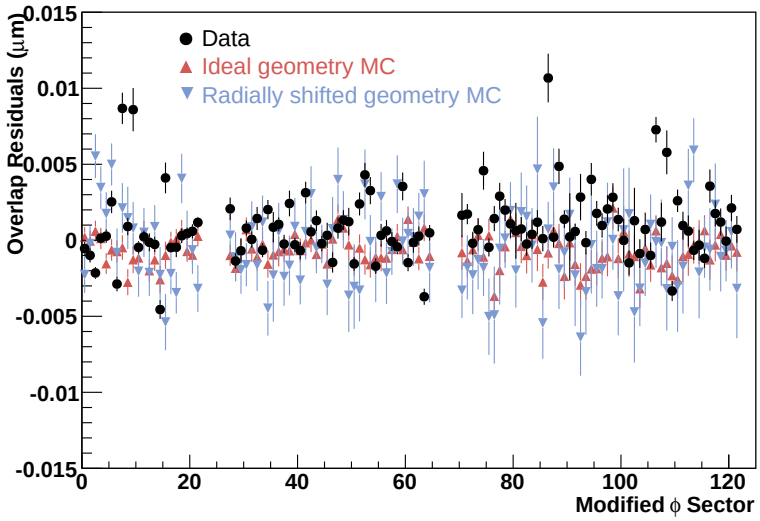

Figure 5.13. Overlap residuals distribution measured on data (black dots), ideal geometry MC (red triangles) and radially distorted geometry MC (blue triangles). The three pixel layers are shown, artificially separated by intervals on the x axis.

Figure 5.13 shows the measured overlap residuals as a function of ϕ for the three pixel barrel layers in data (black dots), perfect geometry MC (red triangles) and radially distorted geometry MC (blue triangles).

The random distortion is generated using a Gaussian distribution with a width of 15 μm. The overlap residuals distribution of the MC events with distorted geometry shows a random spread around zero, as expected, whereas the data one corresponds more to a systematic behavior with some peaks. However, the scatter of the overlap residuals distribution is well reproduced by the simulated events, for this reason we use it to estimate the related systematic uncertainty.

Systematic Uncertainty Estimate Procedure

A fit on the pseudo-proper time distribution of the different $b\bar{b} \to J/\psi$ MC samples is performed. The generated events are the same in all alignment configurations, so the systematic on the lifetime measurement can be extracted directly from the differences between the parameters central values.

The fits results are shown in Table 5.5. The biggest distortion is given, as expected, by the radial expansion of the ID sub-detectors, as the lifetime measurement is a distance measurement on the detector transverse plane. The systematic uncertainties associated to the sagitta and radial distortions are respectively $\Delta\tau_B^{\text{sagitta}} = 0.012$ ps and $\Delta\tau_B^{\text{radial}} = 0.033$ ps. In order to make a conservative estimate of the systematic uncertainty related to residual misalignment effects, the two distortions are assumed to be completely uncorrelated, and are therefore added in quadrature to obtain a total systematic uncertainty of $\Delta\tau_B^{\text{alignment}} = 0.035$ ps.

Table 5.5. Results of the pseudo-proper time fits performed on the MC samples, simulated with differently aligned ID.

MC Sample	τ_B [ps]	scale factor
Ideal Alignment	1.540 ± 0.016	1.064 ± 0.036
Sagitta Distortion	1.528 ± 0.018	1.069 ± 0.042
Radial Expansion	1.573 ± 0.019	1.045 ± 0.042

5.5.4 Track Quality Selection

A check has been performed to verify if the quality selection applied on the J/ψ candidates' tracks introduces a bias on the lifetime measurement. This could in principle be the case if a correlation is found between the J/ψ coming from a long-lived mother and the quality of the track, i.e. the number of silicon or TRT hits on the track, the presence of a B-layer hit, etc... A tighter tracking selection is applied on the muon candidates with respect to the one described in section **??**, and the full analysis is repeated on this sub-sample. A deviation of 0.007 ps is found, and assigned as a systematic to the lifetime measurement.

Additional stability checks were performed. No significant trends have been observed in the fitted lifetime as a function of the primary vertex selection, kinematic properties of the J/ψ, data taking period.

5.6 Summary

The average B lifetime is measured as

$$<\tau_b> = 1.489 \pm 0.016\,(\text{stat}) \pm 0.043\,(\text{syst})\ \text{ps}.$$

Although only a limited fraction of the data available at the LHC is used, systematic uncertainties already dominate over statistical ones. The main systematic uncertainties on the measurement are listed in table 5.6. The different sources are assumed to be uncorrelated, therefore all of the terms are added in quadrature to obtain a total systematic uncertainty on the measurement of 0.043 ps.

The most recent measurement using inclusive $J/\psi \to \mu^+\mu^-$ decays is from CDF in Run I [29], $<\tau_b> = 1.533 \pm 0.015\ ^{+0.035}_{-0.031}$ps. The Particle Data Group (PDG) [67] world average is instead dominated by a measurement from the Delphi collaboration at LEP [23], which refers to a specific mixture of B-hadrons that is not predicted by generic b-quark hadronization models. Moreover, the measurement is performed by

Table 5.6. List of the systematic contributions taken into account in this measurement. The total systematic is computed adding all the contributions in quadrature, assuming they're all uncorrelated with one another.

systematic source	$\Delta\tau_B$ [ps]
τ Background Model	0.024
F-Factor: Reweighting Procedure	0.003
F-Factor: J/ψ p_T Description in MC	0.002
F-Factor: B_s Fraction	0.001
F-Factor: Λ_B Fraction	0.001
Sagitta ID alignment	0.012
Radial ID alignment	0.033
ID Tracks Selection	0.007
Total Systematic	0.043

fitting only candidates with a decay time greater that 1 ps, whereas, in the presence of different lifetime components, a single exponential fit will converge to the average lifetime of the sample only if the fit is performed in all the decay time range. A comparison with past average B lifetime measurement is shown in Figure 5.14.

It is also possible to compare the obtained result with the expected average lifetime computed using PDG values for the different B-hadron species:

$$<\tau_b^{exp}>= f_u\tau_u + f_d\tau_d + f_s\tau_s + f_d\tau_\Lambda = 1.544 \pm 0.014 \text{ ps}, \tag{5.9}$$

where equal inclusive decay rates into J/ψ for all B-hadron species are assumed, and correlations between the fragmentation fractions quoted in the PDG have been used. In the above calculation, the average lifetime of B_s^0 mesons in the $J/\psi\phi$ final states is used. This should be a reasonable approximation since inclusive B_s^0 decays in J/ψ mesons are dominated by $b\to c\bar{c}s$ transitions, which should produce CP-even and CP-odd final states in a similar proportion to $B_s^0\to J/\psi\phi$ decays. Additional uncertainties in the above estimate may be evaluated using the average B_s lifetime or using the recent LHCb measurement [94, 95] f_s/f_d ratio (~ 0.02 ps).

The average B-lifetime $<\tau_b^{exp}>$ in Equation 5.9 assumes equal branching ratio of all B-hadrons into J/ψ, which is not experimentally verified with great precision nor is expected if one considers also B_c mesons. In the latter case, the inclusive branching ratio into J/ψ can be as high as 10% due to the spectator c-quark. Thus, despite B_c being produced at a negligible rate overall, the fraction of B_c decays in the inclusive J/ψ sample might not be so small, and an estimate of order 5% is realistic. Since B_c lifetime (0.453 ps) is smaller than other B-hadrons we can expect $<\tau_b^{exp}>$ to be lower than the value in Equation 5.9 by up to a few percent.

The presented average B lifetime measurement is in agreement within the errors both with the Tevatron one and with the Equation 5.9 average lifetime. This result highlights that the B-hadron admixture produced at colliders should be very similar at the two very different centre-of-mass energies of LHC and the Tevatron. It also shows, with a large statistical sample, that the ATLAS experiment is already suitable to perform B exclusive lifetime measurements, and that the systematic effects related to the measurement technique here presented are under control.

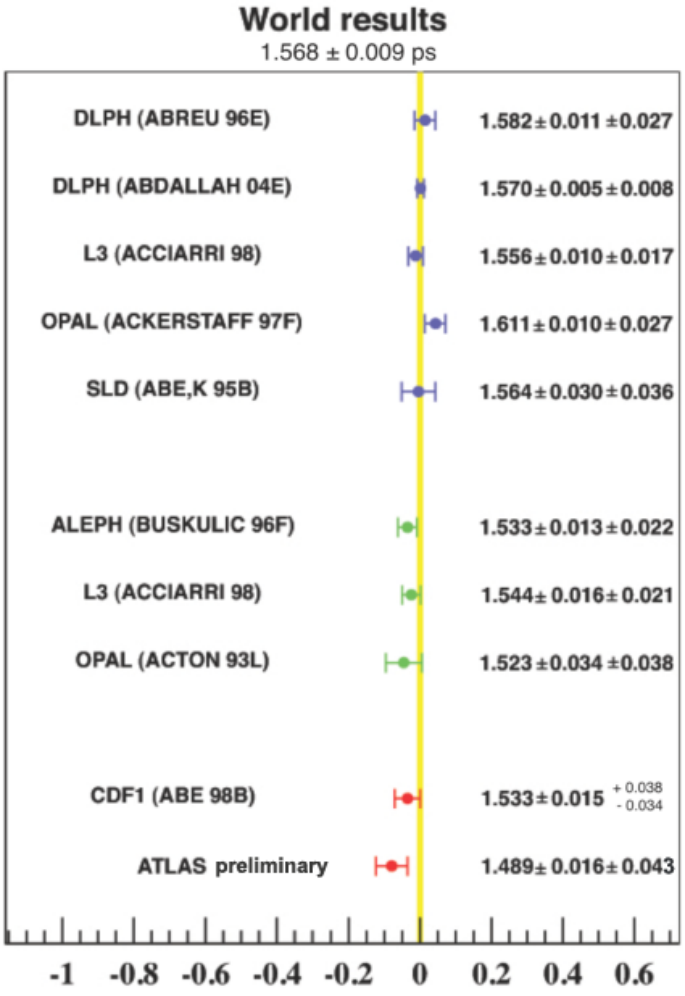

Figure 5.14. Comparison of the average B lifetime obtained at ATLAS on an inclusive $B \to J/\psi\, X \to \mu^+\mu^-$ sample with the results of past LEP, Tevatron and SLD results.

Chapter 6

J/ψ Studies in Lead-Lead Collisions

6.1 Introduction

The measurement of quarkonia production in ultra-relativistic heavy ion collisions provides a potentially powerful tool for studying the properties of hot and dense matter created in these collisions. If deconfined matter is indeed formed, then colour screening is expected to prevent the formation of quarkonium states when the screening length becomes shorter than the quarkonium size [96]. Since this length is directly related to the temperature, a measurement of a suppressed quarkonium yield may provide direct experimental sensitivity to the temperature of the medium created in high energy nuclear collisions [97].

The LHC heavy ion program, which commenced in November 2010, offers an opportunity to measure J/ψ and, for the first time, Z production in nuclear collisions at the highest energies ever achieved. The ATLAS detector provides excellent muon detection capabilities down to momenta of about 3 GeV, and J/ψ mesons and Z bosons can be readily detected via their decays to $\mu^+\mu^-$ final states.

In this Chapter the first measurements of the relative yields of J/ψ meson and Z boson decays in lead-lead collisions produced by the LHC in 2010 at a centre-of-mass energy of $\sqrt{s_{NN}} = 2.76$ TeV per nucleon are presented. The yields are measured in four bins of collision centrality (see definition in Section 6.2). In Section 6.5 the J/ψ yield extraction is presented, in Section 6.5.5 the variation of the yields with centrality is compared to the dependence expected if hard scattering processes scale according to expectations from nuclear geometry. The first observation of Z boson production in $PbPb$ collisions is presented in Section 6.6, and the yield variation as a function of centrality is measured in analogy with what done for J/ψ mesons.

6.2 Centrality Definition and N_{coll} Estimate

$PbPb$ collisions are not point-like as pp collisions, since they consist of interactions between two lead nuclei each consisting of more than 200 nucleons. In each nuclei collision there are N_{coll} one-to-one (*binary*) collisions between N_{part} nucleons. This means that any yield measurement performed on events produced in heavy ion collisions must be normalized on N_{coll}. Since this number depends on the dynamic

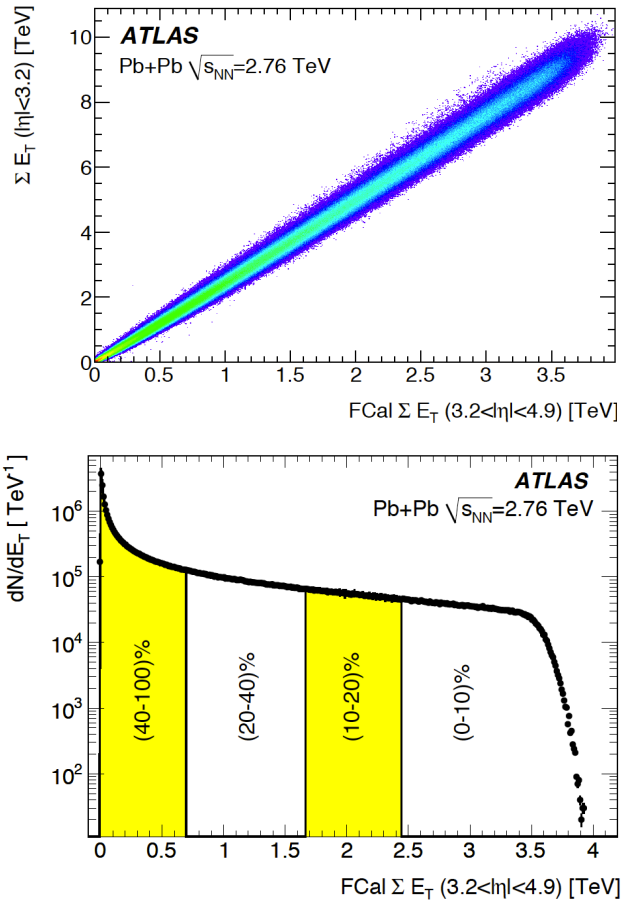

Figure 6.1. Top: Correlation of uncorrected E_T in $|\eta| < 3.2$ with that measured in the FCal ($3.2 < |\eta| < 4.9$). Bottom: Distribution of uncorrected E_T in the ATLAS FCal. Centrality bins are indicated by the alternating bands (see text for details) and labeled according to increasing fraction of *PbPb* total cross-section starting from the largest measured E_T.

of the given interaction, and notably on the impact parameter of the two nuclei, it cannot be measured directly from data.

It is on the other hand verified that the activity in the ATLAS detector in an event of *PbPb* collisions increases monotonically as the impact parameter between the two nuclei decreases. The level of activity can be characterized using the total transverse energy deposited in the ATLAS FCal ($3.2 < |\eta| < 4.9$), since it has been verified that this distribution is linearly correlated to the transverse energy deposited in the mid-rapidity region of the calorimeters ($|\eta| < 3.2$) (see Figure 6.2, top plot). Bins of centrality can then be defined according to fractions of the total *PbPb* cross-section selected by the trigger, and are expressed in terms of percentiles, as shown in Figure 6.2 (bottom), in analogy with the definition used in [98].

The full data sample is therefore divided into four bins of collision centrality, 40-80% (corresponding to the most peripheral events), 20-40%, 10-20%, and 0-10% (corresponding to the most central events). In each centrality bin (denoted with the subscript "c"), the mean number of binary nucleon-nucleon collisions, $N_{c,\,\mathrm{coll}}$, can

then be calculated as explained in Section 6.5.3. The most peripheral 20% of collisions in Figure 6.2 (bottom) are excluded from this analysis due to larger systematic uncertainties in estimating the number of binary nucleon-nucleon collisions in these events.

6.3 Data and Monte Carlo Samples

The data sample consists of approximately 5 μb^{-1} of the total 9.17 μb^{-1} *PbPb* collisions recorded at ATLAS in 2010.

In order to determine the $J/\psi \to \mu^+\mu^-$ reconstruction efficiency, MC samples have been produced superimposing $J/\psi \to \mu^+\mu^-$ and $Z \to \mu^+\mu^-$ events from Pythia6 [75] onto simulated *PbPb* events generated with the Hijing [99] event generator. Hijing was run in a mode with effects from jet quenching turned off, since they have not been adjusted to agree with existing experimental data. Elliptic flow was imposed on the events subsequent to generation, with a magnitude and p_T dependence derived from RHIC data. The detector response to the complete Pythia and Hijing event is then simulated through the ATLAS detector using Geant4 [78].

6.4 Analysis Selection

No muon-specific triggers were used to select the data presented here. The MBTS trigger was configured to require at least one hit above threshold from each side of the detector. A L2 timing requirement on a coincidence of signals from the MBTS was then imposed to remove beam backgrounds. The trigger selection is measured to be $\sim 100\%$ efficient for all considered centralities.

In the offline analysis, minimum–bias triggered events are required to have a reconstructed primary vertex, at least one hit in each set of MBTS counters, and a time difference between the sides of less than 3 ns to reject beam-halo and other beam-related background events.

For this analysis, dimuon candidates are required to be built from two combined muons. ID tracks associated to these muons must have at least nine silicon hits, with no missing pixel hits and not more than one missing SCT hit, in both cases where such hits are expected. The tighter selection with respect to the one used for *pp* studies, both in terms of track quality and of muon quality, is needed because of the very high hit occupancy level given, in the ID, by heavy ion collisions.

The relative momentum resolution on the muon ranges from about 2% at low momentum up to about 3% at $p_T \sim 50$ GeV. For this analysis, oppositely charged muons are selected with a minimum p_T of 3 GeV each and within the region $|\eta| < 2.5$. These boundaries are determined by the detector acceptance for combined muons. No vertex constraints are applied on the dimuon candidates.

6.5 J/ψ Production as a Function of Centrality

The reconstructed $J/\psi \to \mu^+\mu^-$ yield in *PbPb* collisions in each centrality bin (N_c^{meas}) is extracted from data. In order to recover the real number of J/ψ produced

during the interaction (N_c^{corr}), this yield needs to be corrected by the J/ψ reconstruction efficiency in the centrality bin (ϵ_c) and the width of the centrality bin (W_c), which represents a well-defined fraction of the minimum bias events. The corrected yield of J/ψ mesons is therefore given by:

$$N_c^{\text{corr}}(J/\psi \to \mu^+\mu^-) = \frac{N_c^{\text{meas}}(J/\psi \to \mu^+\mu^-)}{\epsilon(J/\psi)_c \cdot W_c}. \tag{6.1}$$

The corrected yield in the given centrality bin is then normalized on the corrected yield in the most peripheral one, so that all of the detector and reconstruction effects independent of centrality cancel out, considerably simplifying the systematic uncertainties assessment procedure.

Finally, in heavy ion collisions, the yield has to be normalized on the number of binary collisions in the given centrality bin ($N_{c,\,\text{coll}}$), as explained in Section 6.2. The "normalized yield" is thus defined as follows:

$$R_c = \frac{N_c^{\text{corr}}(J/\psi \to \mu^+\mu^-)}{N_{40-80\%}^{\text{corr}}(J/\psi \to \mu^+\mu^-)} \cdot \frac{1}{R_{\text{coll}}} \tag{6.2}$$

where R_{coll} is the ratio between the number of binary collisions in the given centrality bin and the same number in the most peripheral bin, defined as:

$$R_{\text{coll}} = \frac{N_{c,\,\text{coll}}}{N_{40-80\%,\,\text{coll}}}. \tag{6.3}$$

Note that the uncertainties in the 40-80% bin are not propagated into this ratio to the more central bins.

In this measurement we aim to estimate the normalized J/ψ yield defined in Equation 6.2 in each of the four centrality bins (defined in Section 6.2). Below, a discussion on how the main ingredients of Equation 6.2 are obtained is provided.

6.5.1 J/ψ Yield Extraction in Centrality Bins

The oppositely-charged dimuon candidates invariant mass spectra after the selection are shown in Figure 6.2. The number of $J/\psi \to \mu^+\mu^-$ reconstructed decays is found by a simple sideband subtraction and counting technique.

The signal mass window is defined by the range 2.95–3.25 GeV. The background under the mass peak is subtracted, under linear hypothesis, using the candidates in the mass sideband regions, defined as 2.4–2.8 GeV and 3.4–3.8 GeV. To determine the uncertainties related to the signal extraction, an alternative method based on an unbinned maximum likelihood fit with the mass resolution left as a free parameter is used, as explained in section 6.5.4.

The number of J/ψ decays after background subtraction, but before any other correction, in each centrality bin is listed in the first column of Table 6.1. With the chosen transverse momentum cuts on the decay muons, 80% of the reconstructed J/ψ have $p_T > 6.5$ GeV.

6.5.2 J/ψ Reconstruction Efficiency

The $J/\psi \to \mu^+\mu^-$ reconstruction efficiency is obtained from the MC sample described in Section 6.3. The overall value of the efficiency is not relevant to this measurement,

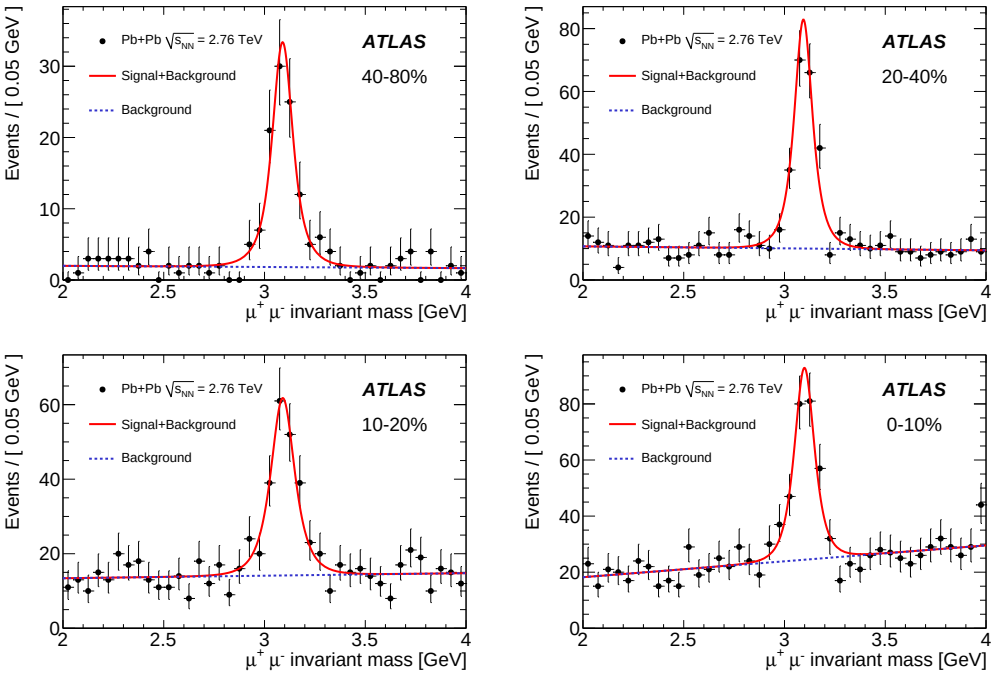

Figure 6.2. Oppositely-charged dimuon invariant mass spectra in the four considered centrality bins from most peripheral (40-80%) to most central (0-10%). The J/ψ yields in each centrality bin are obtained using a sideband technique. The fits shown here are used as a cross check.

as in Equation 6.2 the J/ψ yield is normalized on the 40–80% centrality bin. What really matters in this case is its dependence with respect to centrality.

The centrality dependence here is parameterized as a function of the total number of hits per unit of pseudorapidity detected in the first pixel layer. This is strongly correlated to $\Sigma E_{\mathrm{T}}^{\mathrm{FCal}}$, but gives a more direct measure of the ID occupancy and is thus more suited for the tracking efficiency studies.

In Figure 6.3 the reconstruction efficiency of ID tracks (green points), stand-alone muons (blue points), and combined muons (red points) as a function of centrality is shown. The ID tracks reconstruction efficiency gradually decreases from peripheral to central collisions: the overall effect is smaller than a 3–4% drop as shown in Table 6.1. This is a foreseeable behaviour, due primarily to an inefficiency in the ID tracking induced by the heavy ion collisions occupancy in the tracking detector, particularly elevated for highly central events. On the other hand, stand-alone muon efficiency does not show any trend, since the MS does not suffer from occupancy problems as most of the tracks produced in the collision stop before reaching the spectrometer. Thus combined muons show a drop similar to the one observed for ID tracks, which is included as a correction to the yield ratio measurement.

6.5.3 R_{coll} Computation

In each centrality bin, the mean number of binary nucleon-nucleon collisions can be calculated with a Glauber MC package, that has been used extensively at RHIC

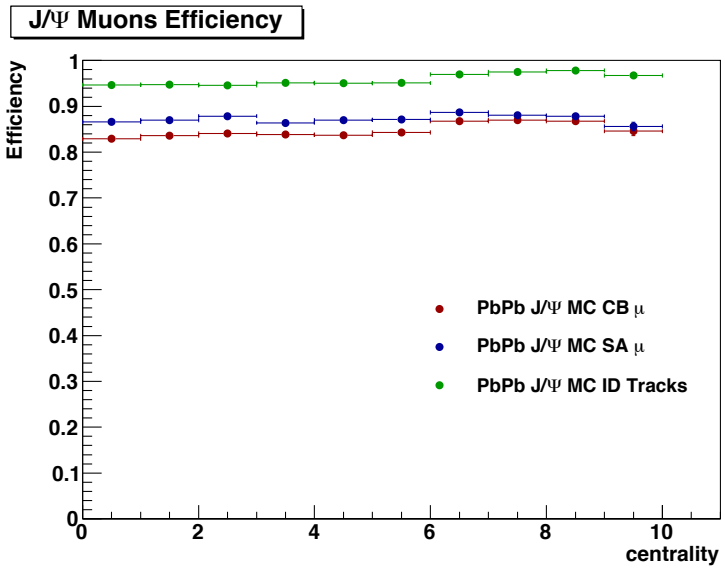

Figure 6.3. ID tracks (green points), stand-alone muons (blue points) and combined muons (red points) reconstruction efficiency extracted from MC as a function of the event centrality.

energies [100, 101].

In the Glauber MC simulation, the impact parameter of the interaction is selected randomly event by event, and both the number of participating nucleons which undergo at least one inelastic collision and the number of binary collisions are calculated for each event. The primary experimental inputs to the Glauber calculation are the radius (R) and skin depth (a) parameters of the Wood-Saxon parameterization of the nuclear density ($\rho(r) = \rho_0/[1 + \exp((r - R)/a)]$), $R = 6.62 \pm 0.06$ fm and $a = 0.546 \pm 0.010$ fm, respectively [102], and the nucleon-nucleon inelastic cross-section, assumed to be $\sigma_{\text{inel}} = 64 \pm 6$ mb from an extrapolation of lower energy data. Using these parameters, the Glauber calculations give a total inelastic cross-section of 7.6 b.

The values of R_{coll} extracted using the presented method are shown in the first column of Table 6.2. A discussion of the associated systematic uncertainties is provided in Section 6.5.4.

6.5.4 Systematic Uncertainties

Several systematic effects are considered. These are grouped into those affecting the J/ψ reconstruction efficiency, those coming from the extraction of the number of signal events from the dimuon mass spectra and those related to the R_{coll} computation. Since this measurement only determines the relative yields as a function of centrality, only the centrality dependence of these effects is relevant, whereas any uncertainty on the absolute value cancels out in the ratio.

Reconstruction Efficiency Extraction

The variation of the J/ψ reconstruction efficiency with centrality observed in simulation is mainly due to the larger occupancy in the ID for highly central events. Because of the low occupancy in the MS by the primarily-soft tracks produced in heavy ion collisions, the fraction of muons from J/ψ decays with a reconstructed track in the MS is independent of centrality within the MC statistical uncertainty. On the other hand, to improve the reliability of the ID track reconstruction in the dense environment, rather stringent track quality requirements are made, relative to those defined for pp collisions [103].

In order to evaluate systematic uncertainties, comparisons have been made between the distributions of hits associated with tracks and missing hits between data and MC as a function of centrality. The difference between the fraction of tracks with a number of associated or missing hits close to the track selection cuts have been used to derive the systematic uncertainties on the ID track reconstruction, ranging between 1 and 3% as a function of the centrality. These uncertainties are fully correlated for both muons from the J/ψ decay, resulting in a systematic uncertainty up to about 7% on the J/ψ reconstruction efficiency. An example of the very good agreement between data and MC in different centrality bins is presented in Figure 6.4, which shows the numbers of Pixel and SCT hits associated to tracks selected with a looser $p_{\mathrm{T}} > 0.5$ GeV cut than that for the J/ψ. The figure shows results for data and MC at two different centralities (0–10% and 40–80%). The distributions of the number of hits averaged over η and the average number of hits as a function of η are shown. The slight decrease of the number of SCT hits on track as a function of centrality is well reproduced by the simulation, demonstrating that the dense environment of the most central collisions is reasonably well modelled.

As an additional cross-check, the ID reconstruction was run with looser cuts on the number of missing pixel and SCT hits, in order to study directly the number of tracks lost because of the cuts on these quantities. The resulting track losses, as a function of centrality in data and simulation, were compatible with the systematic uncertainties derived with the hit comparison method described above.

Further cross-checks have been made by studying the matching between the MS and ID momentum measurements, and by examining variables such as the track multiplicity distribution in a cone of $\Delta R < 0.1$ (where $\Delta R^2 = \Delta\phi^2 + \Delta\eta^2$) around muon candidates, and by evaluating the relative momentum difference between the two independent measurements of the same muon candidate. The fraction of muons measured in the MS but not matched to any ID track has also been compared in data and MC as a function of centrality. All of these studies show that the MC reproduces well the behaviour of the data as a function of centrality. The relative statistical uncertainty on the MC efficiency corrections ranges between 1.6 and 3.2% and this is combined in quadrature with the other uncertainties.

J/ψ Yield Extraction

To address the uncertainties associated with the J/ψ signal extraction, an independent method based on an unbinned maximum likelihood fit is used to evaluate the number of signal events from the dimuon mass spectra. An overall scale factor on the event-by-event mass resolution is a free parameter of the fit, allowing for possible

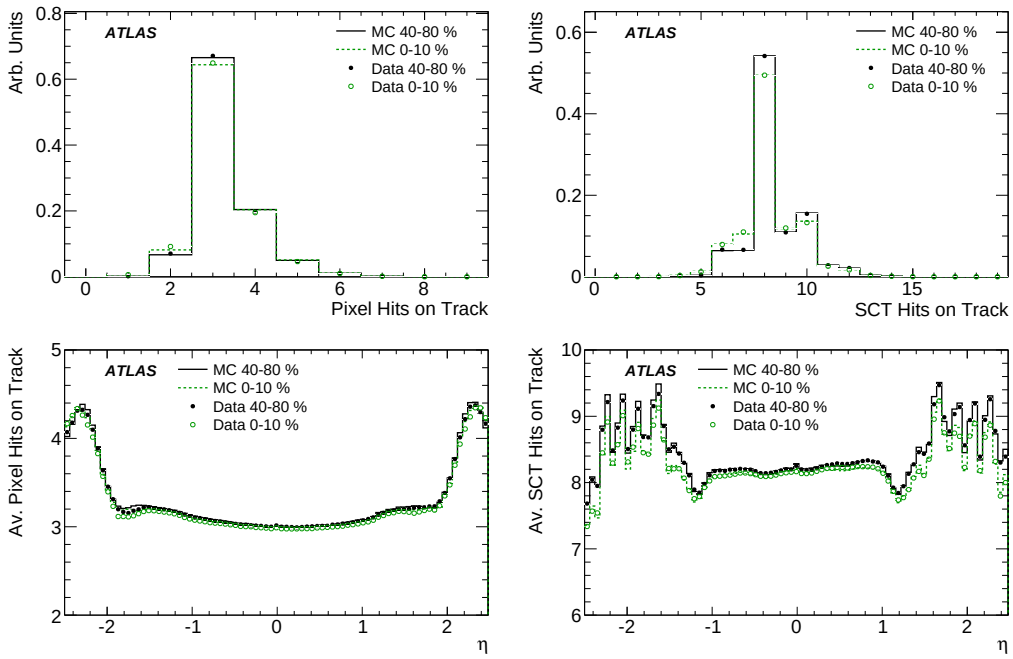

Figure 6.4. (top row) The number of Pixel (left) and SCT (right) hits on tracks for data (points with errors) and MC (histogram) for two different centrality bins: 0-10% (open/dotted) and 40-80% (closed/solid). (bottom row) The average number of Pixel (left) and SCT (right) hits as a function of η for MC and data in the same two centrality bins.

variations of resolution with centrality. Two different background parameterizations are used, with either a first or second order polynomial. The maximum deviation of the fitted yield compared to the sideband subtraction method is taken as the systematic uncertainty on the signal extraction. Fit curves are shown, superimposed on the data invariant mass distribution, in Figure 6.2.

The systematic uncertainties from the different sources are listed in Table 6.1.

R_{coll} Computation

Systematic uncertainties on the R_{coll} values are estimated by separately varying R, a and σ_{inel} in the Glauber MC simulation by one standard deviation. The variations of R and a are found to give results of the same magnitude but opposite sign, indicating that the uncertainties on the two parameters are correlated. However, they are conservatively treated as uncorrelated for the error analysis used in these studies.

Any possible variation in the fraction of the geometric cross section selected by the combination of trigger and event selection criteria, $\varepsilon_{\mathrm{mb}}$, as a function of centrality must also be considered in evaluating systematic uncertainties on the $PbPb$ collision geometry, so that the centrality percentiles correspond to the correct fractions of the efficiency-corrected geometric cross section. The uncertainty is estimated by examining the distribution of $\Sigma E_{\mathrm{T}}^{\mathrm{FCal}}$ in the independent data sample selected by a random trigger and filtered by requiring a minimal amount of Inner Detector activity. The event selection criteria described above are also applied, with an additional

Centrality	$N^{\text{meas}}(J/\psi)$	$\epsilon(J/\psi)_c/$ $\epsilon(J/\psi)_{40-80}$	Systematic Uncertainty		
			Reco. eff.	Sig. extr.	Total
0-10%	190 ± 20	0.93 ± 0.01	6.8 %	5.2 %	8.6 %
10-20%	152 ± 16	0.91 ± 0.02	5.3 %	6.5 %	8.4 %
20-40%	180 ± 16	0.97 ± 0.01	3.3 %	6.8 %	7.5 %
40-80%	91 ± 10	1	2.3 %	5.6 %	6.1 %

Table 6.1. The measured numbers of J/ψ signal events per centrality bin before any correction, with their statistical errors, are listed in the second column. The relative efficiency corrections derived from the simulation are also shown, with the MC statistical error. The last columns give the experimental systematic uncertainties on the reconstruction efficiency and signal extraction, as well as the total uncertainty.

requirement that both ZDCs see energies consistent with the presence of at least one neutron. This combination of vertex, MBTS and ZDC selections efficiently rejects photonuclear interactions [104]. The total selected fraction of the geometric cross section is estimated using a fit to the resulting $\Sigma E_{\text{T}}^{\text{FCal}}$ distribution, assuming the transverse energy in each event results from a superposition of participating nucleons and binary collisions (a similar assumption to that used in Ref. [105]):

$$\Sigma E_{\text{T}}^{\text{FCal}} = E_{\text{T}}^{pp} \left\{ (1-x)\frac{N_{\text{part}}}{2} + xN_{\text{coll}} \right\}. \tag{6.4}$$

In this formula, E_{T}^{pp} is the value of $\Sigma E_{\text{T}}^{\text{FCal}}$ when $N_{\text{part}} = 2$ and $N_{\text{coll}} = 1$ (the values for a single pp collision) and x controls the relative contribution of participants and binary collisions in $PbPb$ events. An additional constant noise term is also included to account for the low energy part of the distribution. Distributions of $\Sigma E_{\text{T}}^{\text{FCal}}$ are generated for 500k MC events and fitted to the data for a range of values of x (from 0.09 to 0.15), and also varying E_{T}^{pp} and the noise term. For all cases, the integral of the observed distribution in data accounts for around 98% of the best fit to the simulated distribution, with a variation of around 1%. This provides an estimate of the total event selection efficiency ε_{mb} relative to the geometric cross section. An absolute systematic error of ±2% is assigned to ε_{mb} with the positive range also accounting for the possible leakage of photonuclear events into the event sample used to obtain the ΣE_T^{FCal} distribution.

Centrality	R_{coll}	Uncertainty
0-10%	19.5	5.3 %
10-20%	11.9	4.7 %
20-40%	5.7	3.2 %
40-80%	1.0	–

Table 6.2. The correction factors R_{coll}, together with the relative systematic uncertainty, stated as a 1σ value.

The total systematic uncertainties on the ratios R_{coll} are evaluated by combining the variations with R, a, σ_{inel} and ε_{mb}, in quadrature. The values of the systematic uncertainties obtained are reported in Table 6.2. It should be noted that the

estimate of $\varepsilon_{\mathrm{mb}}$ leads to correlations between the extracted values of N_{coll}, and thus the uncertainties on R_{coll} are also correlated bin-to-bin.

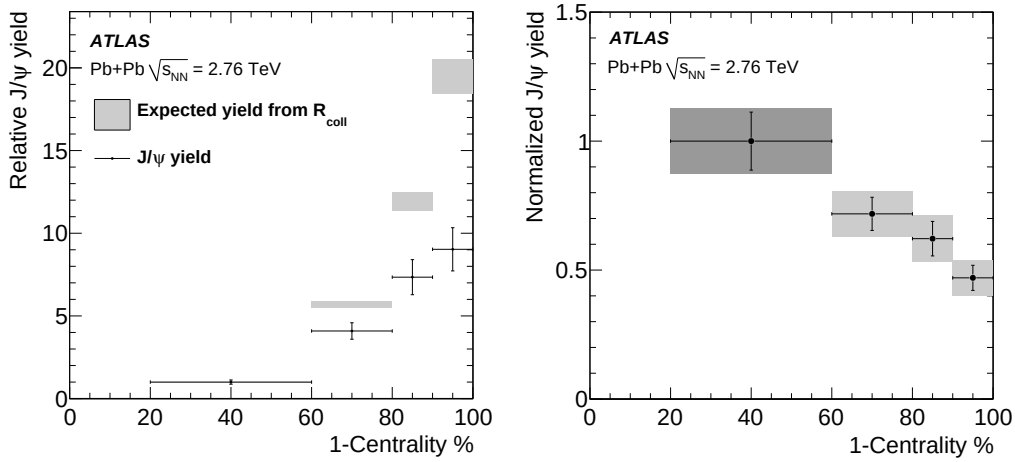

Figure 6.5. (left) Relative J/ψ yield as a function of centrality normalized to the most peripheral bin (black dots with errors). The expected relative yields from the (normalized) number of binary collisions (R_{coll}) are also shown (boxes, reflecting 1σ systematic uncertainties). (right) Value of R_{cp}, as described in the text, as a function of centrality. The statistical errors are shown as vertical bars while the grey boxes also include the combined systematic errors. The darker box indicates that the 40-80% bin is used to set the scale for all bins, but the uncertainties in this bin are not propagated into the more central ones.

6.5.5 Measurement Results

The relative J/ψ yields after normalization and efficiency corrections as in equation 6.1, R_c, are compared to the expected R_{coll} values in the left panel of Figure 6.5. The yield errors are computed by adding the statistical and systematic uncertainties in quadrature. A clear difference is observed as a function of centrality between the measured relative J/ψ yield and the prediction based on R_{coll}, indicating a deviation from the simplest expectation based on QCD factorization. The ratio of these two values, R_{cp}, is shown as a function of centrality in the right panel of Figure 6.5. The data points are not consistent with their average, giving a $P(\chi^2, N_{\mathrm{DOF}})$ value of 0.11% with three degrees of freedom, computed conservatively ignoring any correlations among the systematic uncertainties. Instead, a significant decrease of R_{cp} as a function of centrality is observed.

Centrality	N(Z)	$\epsilon(Z)_c/\epsilon(Z)_{40-80}$
0-10%	19	0.99 ± 0.01
10-20%	5	0.97 ± 0.01
20-40%	10	0.98 ± 0.01
40-80%	4	1

Table 6.3. The number of Z events per centrality bin and the relative efficiency corrections derived from the simulation.

6.6 Z Production as a Function of Centrality

Z candidates are selected by requiring a pair of oppositely charged muons with $p_{\mathrm{T}} > 20$ GeV and $|\eta| < 2.5$ [106]. An additional cosmic ray rejection cut on the sum of the pseudorapidities of the two muons, $|\eta_1 + \eta_2| > 0.01$, is also applied. The invariant mass distribution of the selected pairs is shown in the left panel of Figure 6.6. With this selection, 38 Z candidates are retained in the signal mass window of 66 to 116 GeV. The background after this selection is expected to be below 2%, and is not corrected for in the result. The number of Z events in each centrality bin is given in Table 6.3.

The R_{cp} variable for the Z candidates is computed in the same way as for the J/ψ sample. The relative efficiency corrections determined from dedicated MC samples are given in Table 6.3. For high transverse momentum tracks, the reconstruction is expected to perform as well as or better than in the low p_{T} regime characteristic of the J/ψ study. For this reason, the same systematic uncertainties as for the J/ψ results have been applied to the Z relative yield measurements. Several cross-checks have been performed to support this assumption. In addition to the tracks reconstructed with the combined ID and MS information, tracks reconstructed by the MS alone have been checked, and only one additional candidate was found. This candidate has been inspected and an ID track was in fact found but with too few hits to pass the stringent reconstruction requirements. The Z selection was also applied to same charge muon pairs, and no candidates were selected within the 66–116 GeV mass window. To control the residual background from cosmic rays, the distribution of the difference of the transverse impact parameters of the two muons from Z candidates was examined and found to be compatible with that expected for collision muons.

The measured Z yields are displayed in the right panel of Figure 6.6, normalized to the yield in the most peripheral bin and to the number of binary collisions (R_{cp}). Although, within the large statistical uncertainty, they appear to be compatible with a linear scaling with the number of binary collisions, the low statistics preclude drawing any conclusion.

6.7 Summary

The first results on J/ψ and Z relative yields, when decaying to a $\mu^+\mu^-$ pair, measured in $PbPb$ collisions with the ATLAS detector at the LHC have been presented. In a sample of events with oppositely charged muon pairs with a transverse momentum above 3 GeV and with $|\eta| < 2.5$, a centrality dependent suppression

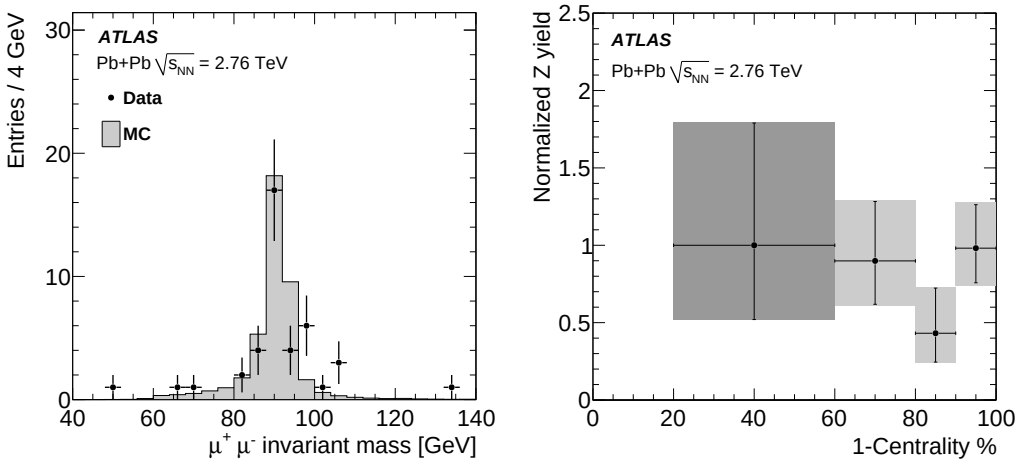

Figure 6.6. The dimuon invariant mass (left) after the selection described in the text. The value of R_{cp} (right) computed with the 38 selected Z candidates. The statistical errors are shown as vertical bars while the grey boxes also include the combined systematic errors. The darker box indicates that the 40-80% bin is used to set the scale for all bins, but the uncertainties in this bin are not propagated into the more central ones.

is observed in the normalized J/ψ yield. The relative yields of the 38 observed Z candidates as a function of centrality are also presented, although no conclusion can be inferred about their scaling with the number of binary collisions due to the limited statistics available. Both measurement are dominated by statistical uncertainties. A *PbPb* collision run at higher luminosity is foreseen for the end of 2011, the data collected then will allow to perform higher precision studies on quarkonia production in matter, and to provide the first significant results on vector boson production in matter at ATLAS.

Chapter 7

Conclusions

In the present thesis, three physics measurements performed, using $J/\psi \to \mu^+\mu^-$ events, in the first two years of data taking at the ATLAS experiment have been described.

The first ATLAS measurement of the non-prompt to prompt J/ψ cross-section fraction f_B on 2.3 pb^{-1} of integrated luminosity has been performed using an unbinned maximum likelihood simultaneous fit on the dimuon candidates invariant mass and pseudo-proper time. Only $\sim 10\%$ of the J/ψ are found to be produced in B-hadron decays at low p_T, but the fraction quickly increases at mid and high p_T, starting from $\sim 15\%$ at 7 GeV and reaches $\sim 70\%$ at the highest p_T values measured, showing a strong dependence of the fraction as a function of the transverse momentum of the J/ψ. The measured non-prompt fraction can be combined with the J/ψ inclusive cross-section to obtain the prompt and non-prompt J/ψ production cross-sections. For J/ψ mesons in the kinematic range $|y| < 2.4$ and $p_T > 7$ GeV, the total cross-section for prompt production has been found to be:

$$Br(J/\psi \to \mu^+\mu^-)\sigma(pp \to (\text{prompt})\, J/\psi\, X; |y^{J/\psi}| < 2.4,\, p_T^{J/\psi} > 7\,\text{GeV})$$
$$= 59 \pm 1(\text{stat.}) \pm 8(\text{syst.})\, {}^{+9}_{-6}(\text{spin}) \pm 2(\text{lumi.})\,\text{nb},$$

and for J/ψ within $1.5 < |y| < 2$ and $p_T > 1$ GeV:

$$Br(J/\psi \to \mu^+\mu^-)\sigma(pp \to (\text{prompt})\, J/\psi\, X; 1.5 < |y^{J/\psi}| < 2,\, p_T^{J/\psi} > 1\,\text{GeV})$$
$$= 450 \pm 70(\text{stat.})\, {}^{+90}_{-110}(\text{syst.})\, {}^{+740}_{-110}(\text{spin}) \pm 20(\text{lumi.})\,\text{nb}$$

is found. The differential cross-section distribution as a function of the p_T and in the rapidity bins is compared to different theoretical predictions. The comparison with the CEM predictions is not very successful, both in shape and in terms of normalization. The CSM predictions, on the other hand, improve when going to higher order of approximation, although the prediction still does not match the data, especially for high p_T J/ψ. Moreover, for J/ψ from B-hadron decays in a kinematic range of $|y| < 2.4$ and $p_T > 7$ GeV, the total production cross-section has been found to be:

$$Br(J/\psi \to \mu^+\mu^-)\sigma(pp \to B + X \to (\text{prompt})\, J/\psi\, X; |y^{J/\psi}| < 2.4,\, p_T^{J/\psi} > 7\,\text{GeV})$$
$$= 23.0 \pm 0.6(\text{stat.}) \pm 2.8(\text{syst.}) \pm 0.2(\text{spin}) \pm 0.8(\text{lumi.})\,\text{nb},$$

and for J/ψ within $1.5 < |y| < 2$ and $p_T > 1$ GeV:

$$Br(J/\psi \rightarrow \mu^+\mu^-)\sigma(pp \rightarrow B{+}X \rightarrow (\text{prompt})\, J/\psi\, X; 1.5 < |y^{J/\psi}| < 2,\, p_T^{J/\psi} > 1\,\text{GeV})$$
$$= 61 \pm 24(\text{stat.}) \pm 19(\text{syst.}) \pm 1(\text{spin}) \pm 2(\text{lumi.})\,\text{nb}.$$

A good agreement is found between the measured non-prompt differential cross-section, as a function of the p_T and in all of the rapidity bins with the theoretical predictions provided by the FONLL calculations. These measurements, covering wider kinematic ranges than previous measurements, especially at high p_T, provide new experimental input for the development of the theory describing both quarkonia production and single heavy quark (b-quark in particular) production. Although these measurements are performed on a small fraction of the data LHC has collected today, systematic uncertainties already dominate over the statistical one, and it is foreseen that the uncertainty on the measurement will be much reduced once one of the dominating factors, the spin-alignment of the J/ψ, will be assessed experimentally.

With the same technique used to separate prompt and non-prompt J/ψ and measure the non-prompt fraction, the first measurement of the average B-hadron lifetime at the LHC has been presented. It has been performed using a sample of inclusive $B \rightarrow J/\psi\, X \rightarrow \mu^+\mu^-\, X$ events of about 35 pb^{-1}. An average lifetime of

$$< \tau_B >= 1.489 \pm 0.016(\text{stat.}) \pm 0.043(\text{syst.})\,\text{ps}$$

has been extracted from a simultaneous invariant mass and pseudo-proper time fit on the dimuon candidates distributions. In this measurement as well, systematic uncertainties are already dominant. In particular, the main systematic uncertainties are related to the pseudo-proper time background modelling and the detector residual misalignment. Ongoing improvements to the alignment procedures, and a larger statistical sample to properly constraint background uncertainties, will allow a significant reduction in the systematic uncertainty. The average B lifetime measurement is in agreement with that measured at the Tevatron and with the expected average computed using PDG values for the different B-hadron species, showing the good performances of the ATLAS detector, trigger and reconstruction in the first year of data taking. Moreover, the studies performed for this measurement allow a detailed validation of the proper-time resolution function in ATLAS, and represent the first step towards exclusive lifetime measurements.

J/ψ studies also represent one of the fundamental points in the ATLAS heavy ion physics programme. A J/ψ relative yield measurement was presented, performed using LHC $PbPb$ collision data and taking advantage, for the J/ψ reconstruction and yield extraction, of the experience made on pp collisions. In a sample of events with oppositely charged muon pairs with a p_T above 3 GeV and with $|\eta| < 2.5$ of about 5 μb^{-1}, a centrality dependent suppression is observed in the normalized J/ψ yield. For the first time, we also observed the Z boson invariant mass peak. As a cross-check, the relative yield of the 38 observed Z candidates was measured as a function of centrality: no suppression was observed in this case, although no conclusion can be inferred because of the very high statistical uncertainty associated to the measurement. These measurements are still dominated by the statistical uncertainties, thus the integrated luminosity in $PbPb$ collisions that will be recorded next November is expected to much improve them, increasing the statistical significance and allowing

a finer binning in centrality, a differential measurement in p_T and rapidity of the J/ψ and, if possible, a separation of the non-prompt and prompt components.

Bibliography

[1] ATLAS Collaboration, Nucl. Phys. B 850 (2011) 387-444, arXiv:1104.3038v2 [hep-ex].

[2] ATLAS Collaboration, ATLAS-CONF-2011-145.

[3] ATLAS Collaboration, Phys. Lett. B **697**, 294 (2011), arXiv:1012.5419 [hep-ex].

[4] O. S. Brüning, P. Collier, P. Lebrun, S. Myers, R. Ostojic, J. Poole and P. Proudlock, *LHC Design Report*, CERN, Geneva, 2004.

[5] C. Quigg, arXiv:09083660v2 [hep-ph].

[6] **ATLAS** Collaboration, CERN-LHCC 99-14/15 (1999).

[7] **CMS** Collaboration, CMS-TDR-008-1 (2006); CMS-TDR-008-2 (2006).

[8] **ALICE** Collaboration, CERN-LHCC 2001-021 (2001).

[9] **LHCb** Collaboration, CERN-LHCC-98-004 (1998).

[10] J. J. Aubert *et. al.* [E598 Collaboration], Phys. Rev. Lett. **33** (1974) 1404.

[11] J. E. Augustin *et. al.* [SLAC-SP-017 Collaboration], Phys. Rev. Lett. **33** (1974) 1406.

[12] G. S. Abrams *et al.*, Phys. Rev. Lett. **33**, 1453 (1974).

[13] S. L. Glashow, J. Iliopoulos and L. Maiani, Phys. Rev. **D2** (1970) no. 7, 1285-1292.

[14] N. Brambilla *et. al.* [Quarkonium Working Group Collaboration], [arXiv:hep-ph/0412158].

[15] M. Antonelli *et. al.*, Phys. Rep. **494** (2010) 197-414, arXiv:0907.5386v2 [hep-ph].

[16] G. A. Schuler, [arXiv:hep-ph/9403387v1].

[17] J. C. Collins, D. E. Soper and G. Sterman, Adv. Ser. Direct. High Energy Phys. **5** (1988) 1-91, [arXiv:hep-ph/0409313].

[18] F. Abe *et. al.* [CDF Collaboration], Phys. Rev. Lett. **79** (1997) 572;
F. Abe *et. al.* [CDF Collaboration], Phys. Rev. Lett. **79** (1997) 578.

[19] H. Fritzsch, Phys. Lett. B **67** (1977) 217;

[20] F. Abe *et. al.* [CDF Collaboration], Phys. Rev. Lett. **99** (2007) 132001.
F. Halzen, Phys. Lett. B **69** (1977) 105;
M. Glück, J. F. Owens and E. Reya, Phys. Rev. D **17** (1978) 2324;
V. D. Barger, W. Y. Keung and R. J. Phillips, Phys. Lett. B **91** (1980) 253.

[21] M. Beneke, G. Buchalla, C. Greub, A. Lenz and U. Nierste, Nucl. Phys. B **639**, 389 (2002) [arXiv:hep-ph/0202106v1];
E. Franco, V. Lubicz, F. Mescia and C. Tarantino, Nucl. Phys. B **633**, 212 (2002) [arXiv:hep-ph/0203089v1];
C. Tarantino, Eur. Phys. J. C **33**, S895 (2004) [arXiv:hep-ph/0310241];
A. Lenz and U. Nierste, arXiv:1102.4274v1 [hep-ph].

[22] D. Buskulic *et al.* [ALEPH Collaboration], Phys. Lett. **B314**, 459-470 (1993).

[23] P. Abreu *et al.* [DELPHI Collaboration], Z. Phys. **C63**, 3-16 (1994).
P. Abreu *et al.* [DELPHI Collaboration], Phys. Lett. **B377**, 195-204 (1996).
J. Abdallah *et al.* [DELPHI Collaboration], Eur. Phys. J. C **33**, 307 (2004) [arXiv:hep-ex/0401025].

[24] M. Acciarri *et al.* [L3 Collaboration], Phys. Lett. **B416**, 220-232 (1998).

[25] K. Ackerstaff *et al.* [OPAL Collaboration], Z. Phys. **C73**, 397-408 (1997).

[26] K. Abe *et al.* [SLD Collaboration], Phys. Rev. Lett. **75**, 3624-3628 (1995), [arXiv:hep-ex/9511005].

[27] D. Buskulic *et al.* [ALEPH Collaboration], Phys. Lett. **B369**, 151-162 (1996).

[28] P. D. Acton *et al.* [OPAL Collaboration], Z. Phys. **C60**, 217-228 (1993).

[29] F. Abe *et al.* [CDF Collaboration], Phys. Rev. D **57**, 5382-5401 (1998).

[30] D. Asner *et. al.* [the Heavy Flavor Averaging Group], arXiv:1010.1589v2 [hep-ex].

[31] T. Matsui and H. Satz, Phys. Lett. B **178** (1986) 416.

[32] B. Alessandro *et al.* [NA50 Collaboration], Eur. Phys. J. **C39** (2005) 335-345.

[33] A. Adare *et al.* [PHENIX Collaboration], Phys. Rev. Lett. **98** (2007) 232301.

[34] J. Badier *et al.* [NA3 Collaboration], Z. Phys. C **20** (1983) 101;
M. C. Abreu *et al.* [NA38 Collaboration], Phys. Lett. **B444** (1998) 516;
M. J. Leitch *et al.* [FNAL E866 Collaboration], Phys. Rev. Lett. **84** (2000) 3256;
B. Alessandro *et al.* [NA50 Collaboration], Eur. Phys. J. C **33** (2004) 31;
B. Alessandro *et al.* [NA50 Collaboration], Eur. Phys. J. C **48** (2006) 329;
I. Abt *et al.* [HERA-B Collaboration], Eur. Phys. J. C **60** (2009) 525;
A. Adare *et al.* [PHENIX Collaboration], arXiv:1010.1246 [nucl-ex], submitted to Phys. Rev. Lett.

[35] R. L. Thews and M. L. Mangano, Phys. Rev. **C73** (2006) 014904.

[36] R. Vogt, Phys. Rev. **C64** (2001) 044901.

[37] **ATLAS** Collaboration, *Magnet System Technical Design Report*, CERN/LHCC 97-18 (1997).

[38] **ATLAS** Collaboration, CERN/LHCC 97-21 (1997).

[39] **ATLAS** Collaboration, CERN/LHCC 97-19 (1997).

[40] **ATLAS** Collaboration, CERN/LHCC 97-20 (1997).

[41] **ATLAS** Collaboration, CERN/LHCC 97-16 (1997).

[42] **ATLAS** Collaboration, CERN/LHCC 96-41 (1996).

[43] **ATLAS** Collaboration, CERN/LHCC 96-42 (1996).

[44] **ATLAS** Collaboration, JINST 3 (2008) S08003.

[45] **ATLAS** Collaboration, CERN/LHCC 97-22 (1997).

[46] **ATLAS** Collaboration, ATLAS Trigger Performances, ATL-COM-PHYS-2008-067, CERN (2008).

[47] **ATLAS** Collaboration, CERN/LHCC 98-14 (1998).

[48] **ATLAS** Collaboration, CERN/LHCC 98-16 (1998).

[49] **ATLAS** Collaboration, to be submitted to Eur. Phys, J. C (2011).

[50] **ATLAS** Collaboration, ATLAS Trigger Performances, ATL-COM-PHYS-2008-067, CERN (2008).

[51] **ATLAS** Collaboration, ATLAS Trigger Performances, ATL-COM-PHYS-2008-067, CERN (2008).

[52] **ATLAS** Collaboration, arXiv:0901.0512v4 [hep-ex], CERN (2008).

[53] **ATLAS** Collaboration, arXiv:1005.5254v1 [hep-ex], CERN (2010).

[54] T. Cornelissen and W. Liebig, Nuclear Physics B Proceedings Supplements, 172, (2007).

[55] **ATLAS** Collaboration, accepted by EPJC (2010).

[56] **ATLAS** Collaboration, ATLAS-CONF-2010-072, CERN (2010).

[57] **ATLAS** Collaboration, ATL-CONF-2010-069, (2010).

[58] **ATLAS** Collaboration, ATL-CONF-2010-027, (2010).

[59] **ATLAS** Collaboration, ATL-PHYS-PUB-2009-008, (2010).

[60] D. Adamans et al., ATL-SOFT-2003-007, CERN (2003).

[61] R. Nicolaidou, L. Chevalier, S. Hassani, *et al.*, Journal of Physics: Conference Series 219 (2010) no.3, 032052.

[62] **ATLAS** Collaboration, ATLAS-CONF-2011-021, CERN (2011).

[63] **ATLAS** Collaboration, ATLAS-CONF-2011-008, CERN (2011).

[64] **ATLAS** Collaboration, ATLAS-CONF-2011-063, CERN (2011).

[65] **ATLAS** Collaboration, ATLAS-CONF-2011-046, CERN (2011).

[66] V. Kostyukhin, ATL-PHYS-2003-031, CERN, (2003).

[67] K. Nakamura et al., *Particle Data Group*, J. Phys. G 37, 075021 (2010).

[68] M. Kramer, Prog. Part. Nucl. Phys. **47** (2001) 141 [arXiv:hep-ph/0106120];
J. P. Lansberg, Int. J. Mod. Phys. A **21** (2006) 3857, [arXiv:hep-ph/0602091];
J. P. Lansberg *et al.*, AIP Conf. Proc. **1038** (2008) 15, arXiv:0807.3666 [hep-ph].

[69] CMS Collaboration, arXiv:1011.4193 [hep-ex], CMS-BPH-10-002, CERN-PH-EP-2010-046.

[70] T. Aaltonen et al. [CDF Collaboration], Phys. Rev. **D71** (2005) 032001, arXiv:hep-ex/0412071.

[71] T. Ullrich, A. D. Frawley and R. Vogt, Phys. Rept. **462** (2008) 125, arXiv:0806.1013 [nucl-ex].

[72] M. Cacciari, M. Greco and P. Nason, JHEP **9805** (1998) 007, arXiv:hep-ph/9803400;
M. Cacciari, M. Greco and P. Nason, JHEP **0103** (2001) 006, arXiv:hep-ph/0102134.

[73] P. Artoisenet, J. M. Campbell, J. P. Lansberg, F. Maltoni, and F. Tramontano, Phys. Rev. Lett. **101** (2008) 152001, arXiv:0806.3282 [hep-ph].

[74] N. Brambilla *et al.*, Eur. Phys. J. C **71** (2011) 1534 arXiv:1010.5827 [hep-ph].

[75] T. Sjostrand, S. Mrenna, and P. Z. Skands, JHEP **0605**, 026 (2006), arXiv:hep-ph/0603175.

[76] ATLAS Collaboration, ATL-PHYS-PUB-2010-002, CERN, Geneva, Mar, 2010.

[77] A. Sherstnev and R. S. Thorne, Eur. Phys. J. C **55** 553 (2008), arXiv:0711.2473 [hep-ph].

[78] S. Agostinelli *et al.*, Nucl. Instrum. Meth. A **506**, 250 (2003);
ATLAS Collaboration, Eur. Phys. J. C **70**, 823 (2010), arXiv:1005.4568 [physics.ins-det].

[79] P. Nason *et al.*, Standard Model Physics (and more) at the LHC, 231, Geneva (1999), arXiv:hep-ph/0003142.

[80] ATLAS Collaboration, ATLAS-CONF-2011-021, Mar, 2011., CERN, Geneva.

[81] ATLAS Collaboration, ATLAS-CONF-2011-008, Feb, 2011., CERN, Geneva.

[82] ATLAS Collaboration, accepted by Eur. Phys. J, arXiv:1101.2185 [hep-ex]; ATLAS Collaboration, ATLAS-CONF-2011-011, Mar, 2011., CERN, Geneva.

[83] CDF Collaboration, T. Aaltonen et al., Phys. Rev. Lett. **99** (2007) 132001, arXiv:0704.0638 [hep-ex].

[84] J. Pumplin, D. R. Stump, J. Huston, H. L. Lai, P. M. Nadolsky and W. K. Tung, JHEP **0207**, 012 (2002), arXiv:hep-ph/0201195.

[85] V. D. Barger, W. Y. Keung and R. J. N. Phillips, Phys. Lett. B **91** (1980) 253; V. D. Barger, W. Y. Keung and R. J. N. Phillips, Z. Phys. C **6** (1980) 169.

[86] J. Lansberg, arXiv:1006.2750[hep-ph]; S. J. Brodsky and J. P. Lansberg, Phys. Rev. **D81** (2010) 051502(R).

[87] J. P. Lansberg, Eur. Phys. J. C **61** (2009) 693, arXiv:0811.4005 [hep-ph].

[88] T. Aaltonen et al. [CDF Collaboration], Phys. Rev. **D80** (2009) 031103, arXiv:0905.1982 [hep-ex].

[89] ATLAS Collaboration, New J. Phys. 13, 053033 (2011).

[90] I. Bigi, L. Maiani, F. Piccinini, A. D. Polosa, V. Riquer, Phys. Rev. **D72** (2005) 114016, [hep-ph/0510307]; T. J. Burns, F. Piccinini, A. D. Polosa, V. Prosperi and C. Sabelli, Phys. Rev. D **83** (2011) 114029, arXiv:1104.1781 [hep-ph].

[91] Babar Collaboration, P. R. D. **67** (2003) 032002, [arXiv:hep-ex/0207097v3].

[92] F. Acosta *et al.* [CDF Collaboration], Phys. Rev. **D71**, 032001 (2005).

[93] K. Hartkorn and H. G. Moser, Eur. Phys. J. C **8**, 823 (1999) 381.

[94] LHCb Collaboration, LHCb-CONF-2011-013, 5 April 2011.

[95] LHCb Collaboration, LHCb-CONF-2011-028, 28 June 2011.

[96] T. Matsui and H. Satz, Phys. Lett. **B178** (1986) 416.

[97] A. Mocsy and P. Petreczky, Phys. Rev. Lett. **99** (2007) 211602.

[98] ATLAS Collaboration, Phys. Rev. Lett. **105** (2010) 252303.

[99] X. -N. Wang and M. Gyulassy, Phys. Rev. **D44** (1991) 3501-3516.

[100] B. Alver, M. Baker, C. Loizides *et al.*, arXiv:0805.4411 [nucl-ex].

[101] M. L. Miller, K. Reygers, S. J. Sanders *et al.*, Ann. Rev. Nucl. Part. Sci. **57** (2007) 205-243.

[102] H. De Vries, C. W. De Jager and C. De Vries, Atom. Data Nucl. Data Tabl. **36** (1987) 495-536.

[103] ATLAS Collaboration, Phys. Lett. **B688**, (2010) 21-42.

[104] O. Djuvsland and J. Nystrand, arXiv:1011.4908 [hep-ph].

[105] ALICE Collaboration, arXiv:1012.1657 [nucl-ex].

[106] ATLAS Collaboration, G. Aad *et al.*, arXiv:1010.2130v1 [hep-ex], accepted by JHEP.

[107] P. Faccioli, C. Lourenco, J. Seixas and H. K. Wohri, Eur. Phys. J. C **69** (2010) 657, arXiv:1006.2738 [hep-ph].

Tables of Measured Cross-Sections and B-Fractions

Table .1. Inclusive J/ψ production cross-sections as a function of J/ψ p_T in four rapidity ($|y|$) bins. The first uncertainty is statistical, the second is systematic and the third encapsulates any possible variation due to spin-alignment from the unpolarised ($\lambda_\theta = \lambda_\phi = \lambda_{\theta\phi} = 0$) central value.

		$\frac{d^2\sigma}{dp_T dy}\cdot\mathrm{Br}(J/\psi \to \mu^+\mu^-)$ [pb/GeV]								
p_T	$\langle p_T \rangle$	$2 < \lvert y \rvert < 2.4$				$\langle p_T \rangle$	$1.5 < \lvert y \rvert < 2$			
(GeV)	(GeV)	Value	± (stat.)	± (syst.)	± (spin)	(GeV)	Value	± (stat.)	± (syst.)	± (spin)
1.0-4.0						2.8	143000	±23000	$\pm^{25000}_{39000}$	$\pm^{274000}_{39000}$
4.0-5.0						4.5	39400	±5500	$\pm^{5700}_{5700}$	$\pm^{69300}_{9700}$
5.0-5.5	5.3	15900	±4300	$\pm^{2800}_{2600}$	$\pm^{28800}_{4300}$	5.2	17600	±3300	$\pm^{3000}_{2600}$	$\pm^{17300}_{4100}$
5.5-6.0	5.8	13500	±3600	$\pm^{1900}_{2200}$	$\pm^{11400}_{2700}$	5.7	14300	±1200	$\pm^{1700}_{1700}$	$\pm^{14000}_{3100}$
6.0-6.5	6.3	8800	±1100	$\pm^{1300}_{1200}$	$\pm^{7900}_{2200}$	6.3	12760	±920	$\pm^{1840}_{1690}$	$\pm^{9970}_{2620}$
6.5-7.0	6.8	6290	±700	$\pm^{830}_{980}$	$\pm^{5140}_{1360}$	6.8	8910	±610	$\pm^{1270}_{1270}$	$\pm^{5420}_{1990}$
7.0-7.5	7.3	3990	±500	$\pm^{560}_{550}$	$\pm^{2630}_{690}$	7.2	6350	±430	$\pm^{860}_{860}$	$\pm^{3130}_{1430}$
7.5-8.0	7.7	4070	±450	$\pm^{570}_{580}$	$\pm^{2920}_{650}$	7.7	5040	±350	$\pm^{590}_{520}$	$\pm^{2260}_{900}$
8.0-8.5	8.3	2650	±290	$\pm^{460}_{390}$	$\pm^{910}_{570}$	8.3	3790	±210	$\pm^{440}_{430}$	$\pm^{1490}_{450}$
8.5-9.0	8.7	1930	±160	$\pm^{260}_{260}$	$\pm^{620}_{350}$	8.7	3110	±160	$\pm^{420}_{360}$	$\pm^{980}_{450}$
9.0-9.5	9.2	1450	±130	$\pm^{210}_{180}$	$\pm^{480}_{210}$	9.2	2260	±110	$\pm^{260}_{250}$	$\pm^{640}_{370}$
9.5-10.0	9.7	1208	±94	$\pm^{155}_{138}$	$\pm^{440}_{166}$	9.7	1674	±85	$\pm^{198}_{183}$	$\pm^{450}_{296}$
10.0-11.0	10.5	829	±51	$\pm^{96}_{92}$	$\pm^{286}_{87}$	10.5	1297	±46	$\pm^{146}_{139}$	$\pm^{316}_{241}$
11.0-12.0	11.5	598	±43	$\pm^{69}_{73}$	$\pm^{174}_{71}$	11.5	754	±31	$\pm^{90}_{83}$	$\pm^{168}_{147}$
12.0-14.0	12.9	320	±19	$\pm^{38}_{36}$	$\pm^{79}_{40}$	12.9	404	±15	$\pm^{45}_{43}$	$\pm^{74}_{75}$
14.0-16.0	14.9	164	±12	$\pm^{26}_{16}$	$\pm^{33}_{21}$	14.9	193	±10	$\pm^{21}_{19}$	$\pm^{28}_{32}$
16.0-18.0	16.9	77.8	±8.2	$\pm^{9.4}_{8.0}$	$\pm^{14.1}_{9.9}$	16.9	103.0	±6.9	$\pm^{13.0}_{9.4}$	$\pm^{12.0}_{15.5}$
18.0-22.0	19.7	29.9	±3.3	$\pm^{3.1}_{3.4}$	$\pm^{3.7}_{3.8}$	19.6	48.9	±3.2	$\pm^{4.1}_{4.2}$	$\pm^{4.9}_{6.5}$
22.0-30.0	24.9	6.2	±1.1	$\pm^{0.6}_{0.6}$	$\pm^{0.6}_{0.7}$	25.0	10.6	±1.1	$\pm^{1.0}_{0.9}$	$\pm^{0.8}_{1.2}$
30.0-40.0	33.6	1.12	±0.43	$\pm^{0.10}_{0.28}$	$\pm^{0.06}_{0.10}$	34.1	2.22	±0.40	$\pm^{0.19}_{0.21}$	$\pm^{0.13}_{0.22}$

		$\frac{d^2\sigma}{dp_T dy}\cdot\mathrm{Br}(J/\psi \to \mu^+\mu^-)$ [pb/GeV]								
p_T	$\langle p_T \rangle$	$0.75 < \lvert y \rvert < 1.5$				$\langle p_T \rangle$	$\lvert y \rvert < 0.75$			
(GeV)	(GeV)	Value	± (stat.)	± (syst.)	± (spin)	(GeV)	Value	± (stat.)	± (syst.)	± (spin)
5.0-5.5	5.3	26800	±5600	$\pm^{4100}_{3800}$	$\pm^{10600}_{7900}$					
5.5-6.0	5.8	19200	±2800	$\pm^{2700}_{2500}$	$\pm^{8600}_{5700}$					
6.0-6.5	6.2	13500	±1100	$\pm^{1700}_{1700}$	$\pm^{7100}_{4000}$					
6.5-7.0	6.7	12400	±1100	$\pm^{1700}_{1700}$	$\pm^{3900}_{3600}$					
7.0-7.5	7.2	8190	±610	$\pm^{1090}_{1040}$	$\pm^{2220}_{2300}$	7.3	9220	±980	$\pm^{1140}_{1150}$	$\pm^{5770}_{2960}$
7.5-8.0	7.7	6500	±400	$\pm^{860}_{810}$	$\pm^{1620}_{1770}$	7.8	7780	±720	$\pm^{1000}_{990}$	$\pm^{3540}_{2470}$
8.0-8.5	8.2	4080	±280	$\pm^{420}_{440}$	$\pm^{1870}_{900}$	8.3	4500	±320	$\pm^{510}_{530}$	$\pm^{1730}_{1410}$
8.5-9.0	8.7	3600	±200	$\pm^{390}_{390}$	$\pm^{1040}_{800}$	8.8	3720	±270	$\pm^{450}_{440}$	$\pm^{1310}_{1150}$
9.0-9.5	9.3	2880	±140	$\pm^{330}_{320}$	$\pm^{610}_{640}$	9.2	3040	±280	$\pm^{360}_{360}$	$\pm^{1240}_{840}$
9.5-10.0	9.7	2210	±100	$\pm^{250}_{240}$	$\pm^{420}_{490}$	9.8	2170	±140	$\pm^{230}_{230}$	$\pm^{740}_{600}$
10.0-11.0	10.5	1542	±51	$\pm^{176}_{174}$	$\pm^{283}_{348}$	10.5	1528	±59	$\pm^{160}_{160}$	$\pm^{471}_{430}$
11.0-12.0	11.5	1022	±35	$\pm^{121}_{120}$	$\pm^{187}_{234}$	11.5	1051	±39	$\pm^{116}_{116}$	$\pm^{288}_{293}$
12.0-14.0	12.9	531	±16	$\pm^{60}_{58}$	$\pm^{94}_{118}$	12.9	528	±17	$\pm^{56}_{56}$	$\pm^{127}_{141}$
14.0-16.0	14.9	249	±10	$\pm^{26}_{26}$	$\pm^{40}_{52}$	14.9	274	±12	$\pm^{27}_{27}$	$\pm^{60}_{70}$
16.0-18.0	16.9	119.2	±6.7	$\pm^{11.9}_{11.7}$	$\pm^{17.0}_{23.1}$	16.9	136.2	±7.5	$\pm^{13.1}_{13.1}$	$\pm^{26.5}_{32.1}$
18.0-22.0	19.7	53.3	±3.0	$\pm^{5.2}_{5.0}$	$\pm^{6.7}_{9.6}$	19.7	67.7	±3.6	$\pm^{6.4}_{6.3}$	$\pm^{10.9}_{14.5}$
22.0-30.0	25.2	15.9	±1.1	$\pm^{1.8}_{1.6}$	$\pm^{1.7}_{2.4}$	25.0	16.9	±1.4	$\pm^{1.7}_{1.7}$	$\pm^{2.2}_{3.0}$
30.0-40.0	33.9	3.16	±0.43	$\pm^{0.34}_{0.34}$	$\pm^{0.27}_{0.39}$	33.6	3.60	±0.48	$\pm^{0.38}_{0.39}$	$\pm^{0.43}_{0.52}$
40.0-70.0	48.8	0.407	±0.084	$\pm^{0.041}_{0.043}$	$\pm^{0.022}_{0.017}$	46.6	0.462	±0.093	$\pm^{0.055}_{0.055}$	$\pm^{0.046}_{0.049}$

Table .2. Non-prompt to inclusive production cross-section fraction f_B as a function of J/ψ p_T for $|y|_{J/\psi} < 0.75$ under the assumption that prompt and non-prompt J/ψ production is unpolarised ($\lambda_\theta = 0$). The spin-alignment envelope spans the range of possible prompt cross-sections under various polarisation hypotheses, plus the range of non-prompt cross-sections within $\lambda_\theta = \pm 0.1$. The first uncertainty is statistical, the second uncertainty is systematic, the third number is the uncertainty due to spin-alignment.

		Non-prompt to inclusive production fraction $\lvert y\rvert < 0.75$			
p_T (GeV)	$\langle p_T \rangle$ (GeV)	f_B	± (stat.)	± (syst.)	± (spin)
6.0-7.0	6.6	0.175	±0.057	±0.032	$\pm^{0.064}_{0.062}$
7.0-7.5	7.3	0.259	±0.038	±0.002	$\pm^{0.066}_{0.080}$
7.5-8.0	7.8	0.236	±0.030	±0.007	$\pm^{0.061}_{0.076}$
8.0-8.5	8.3	0.258	±0.032	±0.017	$\pm^{0.054}_{0.074}$
8.5-9.0	8.8	0.291	±0.030	±0.005	$\pm^{0.058}_{0.079}$
9.0-9.5	9.2	0.268	±0.025	±0.008	$\pm^{0.054}_{0.076}$
9.5-10.0	9.8	0.320	±0.026	±0.006	$\pm^{0.062}_{0.083}$
10.0-11.0	10.5	0.321	±0.018	±0.007	$\pm^{0.050}_{0.077}$
11.0-12.0	11.5	0.327	±0.019	±0.003	$\pm^{0.051}_{0.078}$
12.0-14.0	12.9	0.359	±0.017	±0.003	$\pm^{0.044}_{0.069}$
14.0-16.0	14.9	0.405	±0.024	±0.008	$\pm^{0.046}_{0.072}$
16.0-18.0	16.9	0.443	±0.030	±0.005	$\pm^{0.048}_{0.073}$
18.0-22.0	19.7	0.479	±0.030	±0.004	$\pm^{0.040}_{0.063}$
22.0-30.0	25.0	0.536	±0.039	±0.008	$\pm^{0.032}_{0.050}$
30.0-70.0	37.7	0.656	±0.059	±0.008	$\pm^{0.030}_{0.045}$

Table .3. Non-prompt to inclusive production cross-section fraction f_B as a function of J/ψ p_T for $0.75 < |y|_{J/\psi} < 1.5$ under the assumption that prompt and non-prompt J/ψ production is unpolarised ($\lambda_\theta = 0$). The spin-alignment envelope spans the range of possible prompt cross-sections under various polarisation hypotheses, plus the range of non-prompt cross-sections within $\lambda_\theta = \pm 0.1$. The first uncertainty is statistical, the second uncertainty is systematic, the third number is the uncertainty due to spin-alignment.

		Non-prompt to inclusive production fraction			
p_T	$\langle p_T \rangle$	$0.75 < \lvert y \rvert < 1.5$			
(GeV)	(GeV)	f_B	$\pm$ (stat.)	$\pm$ (syst.)	$\pm$ (spin)
4.0-5.0	4.7	0.142	± 0.094	± 0.018	$\pm^{0.039}_{0.049}$
5.0-5.5	5.3	0.183	± 0.049	± 0.036	$\pm^{0.039}_{0.058}$
5.5-6.0	5.8	0.127	± 0.038	± 0.024	$\pm^{0.030}_{0.043}$
6.0-6.5	6.3	0.188	± 0.033	± 0.019	$\pm^{0.042}_{0.057}$
6.5-7.0	6.8	0.261	± 0.029	± 0.007	$\pm^{0.051}_{0.069}$
7.0-7.5	7.2	0.230	± 0.025	± 0.017	$\pm^{0.041}_{0.061}$
7.5-8.0	7.8	0.238	± 0.023	± 0.015	$\pm^{0.043}_{0.062}$
8.0-8.5	8.2	0.226	± 0.022	± 0.032	$\pm^{0.036}_{0.055}$
8.5-9.0	8.8	0.226	± 0.021	± 0.013	$\pm^{0.036}_{0.055}$
9.0-9.5	9.2	0.261	± 0.021	± 0.009	$\pm^{0.040}_{0.060}$
9.5-10.0	9.8	0.292	± 0.023	± 0.008	$\pm^{0.043}_{0.064}$
10.0-11.0	10.5	0.315	± 0.016	± 0.004	$\pm^{0.040}_{0.061}$
11.0-12.0	11.5	0.343	± 0.018	± 0.007	$\pm^{0.041}_{0.064}$
12.0-14.0	12.9	0.352	± 0.016	± 0.005	$\pm^{0.033}_{0.054}$
14.0-16.0	14.9	0.401	± 0.022	± 0.003	$\pm^{0.035}_{0.058}$
16.0-18.0	16.9	0.450	± 0.031	± 0.006	$\pm^{0.036}_{0.058}$
18.0-22.0	19.7	0.476	± 0.031	± 0.006	$\pm^{0.033}_{0.052}$
22.0-30.0	25.1	0.542	± 0.042	± 0.015	$\pm^{0.029}_{0.042}$
30.0-70.0	37.8	0.594	± 0.060	± 0.016	$\pm^{0.029}_{0.040}$

Table .4. Non-prompt to inclusive production cross-section fraction f_B as a function of J/ψ p_T for $1.5 < |y|_{J/\psi} < 2$ under the assumption that prompt and non-prompt J/ψ production is unpolarised ($\lambda_\theta = 0$). The spin-alignment envelope spans the range of possible prompt cross-sections under various polarisation hypotheses, plus the range of non-prompt cross-sections within $\lambda_\theta = \pm 0.1$. The first uncertainty is statistical, the second uncertainty is systematic, the third number is the uncertainty due to spin-alignment.

		Non-prompt to inclusive production fraction $1.5 < \|y\| < 2$			
p_T (GeV)	$\langle p_T \rangle$ (GeV)	f_B	$\pm$ (stat.)	$\pm$ (syst.)	$\pm$ (spin)
1.0-4.0	2.8	0.100	± 0.053	± 0.039	$^{+0.061}_{-0.031}$
4.0-5.0	4.6	0.210	± 0.042	± 0.051	$^{+0.115}_{-0.051}$
5.0-5.5	5.3	0.218	± 0.043	± 0.006	$^{+0.097}_{-0.050}$
5.5-6.0	5.8	0.170	± 0.034	± 0.019	$^{+0.068}_{-0.041}$
6.0-6.5	6.3	0.180	± 0.034	± 0.048	$^{+0.057}_{-0.042}$
6.5-7.0	6.8	0.222	± 0.028	± 0.013	$^{+0.069}_{-0.048}$
7.0-7.5	7.3	0.195	± 0.025	± 0.017	$^{+0.049}_{-0.044}$
7.5-8.0	7.8	0.210	± 0.024	± 0.014	$^{+0.052}_{-0.047}$
8.0-8.5	8.2	0.216	± 0.022	± 0.022	$^{+0.042}_{-0.044}$
8.5-9.0	8.8	0.264	± 0.023	± 0.018	$^{+0.049}_{-0.050}$
9.0-9.5	9.2	0.287	± 0.026	± 0.015	$^{+0.051}_{-0.052}$
9.5-10.0	9.7	0.297	± 0.028	± 0.015	$^{+0.053}_{-0.053}$
10.0-11.0	10.5	0.335	± 0.019	± 0.004	$^{+0.043}_{-0.055}$
11.0-12.0	11.5	0.326	± 0.026	± 0.017	$^{+0.042}_{-0.054}$
12.0-14.0	12.9	0.357	± 0.022	± 0.015	$^{+0.034}_{-0.045}$
14.0-16.0	14.9	0.420	± 0.029	± 0.011	$^{+0.035}_{-0.047}$
16.0-18.0	16.9	0.517	± 0.038	± 0.007	$^{+0.039}_{-0.048}$
18.0-22.0	19.7	0.468	± 0.038	± 0.012	$^{+0.029}_{-0.041}$
22.0-30.0	24.9	0.605	± 0.058	± 0.005	$^{+0.021}_{-0.032}$

Table .5. Non-prompt to inclusive production cross-section fraction f_B as a function of J/ψ p_T for $2 < |y|_{J/\psi} < 2.4$ under the assumption that prompt and non-prompt J/ψ production is unpolarised ($\lambda_\theta = 0$). The spin-alignment envelope spans the range of possible prompt cross-sections under various polarisation hypotheses, plus the range of non-prompt cross-sections within $\lambda_\theta = \pm 0.1$. The first uncertainty is statistical, the second uncertainty is systematic, the third number is the uncertainty due to spin-alignment.

		Non-prompt to inclusive production fraction			
p_T	$\langle p_T \rangle$	$2 < \|y\| < 2.4$			
(GeV)	(GeV)	f_B	± (stat.)	± (syst.)	± (spin)
1.0-5.0	3.6	0.098	±0.065	±0.036	$\pm^{0.053}_{0.027}$
5.0-6.0	5.5	0.217	±0.077	±0.065	$\pm^{0.096}_{0.044}$
6.0-7.0	6.6	0.289	±0.047	±0.052	$\pm^{0.096}_{0.041}$
7.0-7.5	7.2	0.125	±0.035	±0.016	$\pm^{0.037}_{0.019}$
7.5-8.0	7.8	0.231	±0.037	±0.020	$\pm^{0.063}_{0.031}$
8.0-8.5	8.2	0.209	±0.042	±0.042	$\pm^{0.046}_{0.028}$
8.5-9.0	8.7	0.183	±0.041	±0.032	$\pm^{0.042}_{0.024}$
9.0-9.5	9.2	0.268	±0.037	±0.027	$\pm^{0.057}_{0.033}$
9.5-10.0	9.7	0.249	±0.045	±0.008	$\pm^{0.055}_{0.032}$
10.0-11.0	10.5	0.269	±0.037	±0.014	$\pm^{0.040}_{0.033}$
11.0-12.0	11.5	0.297	±0.034	±0.010	$\pm^{0.045}_{0.034}$
12.0-14.0	12.9	0.352	±0.034	±0.018	$\pm^{0.037}_{0.033}$
14.0-18.0	15.6	0.348	±0.044	±0.049	$\pm^{0.038}_{0.032}$
18.0-30.0	21.7	0.419	±0.058	±0.058	$\pm^{0.032}_{0.031}$

Table .6. Non-prompt J/ψ production cross-sections as a function of J/ψ p_T for $|y|_{J/\psi} < 0.75$ under the assumption that prompt and non-prompt J/ψ production is unpolarised ($\lambda_\theta = 0$), and the spin-alignment envelope spans the range of non-prompt cross-sections within $\lambda_\theta = \pm 0.1$. The first uncertainty is statistical, the second uncertainty is systematic. Comparison is made to FONLL predictions.

		$\frac{d^2\sigma^{non-prompt}}{dp_T dy} \cdot \mathrm{Br}(J/\psi \to \mu^+\mu^-)$ [nb/GeV]				
p_T	$\langle p_T \rangle$	$\|y\| < 0.75$				
(GeV)	(GeV)	Value	± (stat.)	± (syst.)	± (spin)	FONLL prediction
7.0-7.5	7.3	2.4	±0.4	±0.4	±0.08	$1.7 \pm^{0.7}_{0.4}$
7.5-8.0	7.8	1.8	±0.3	±0.3	±0.06	$1.4 \pm^{0.5}_{0.3}$
8.0-8.5	8.3	1.2	±0.2	±0.1	±0.03	$1.1 \pm^{0.4}_{0.3}$
8.5-9.0	8.8	1.1	±0.1	±0.1	±0.03	$0.9 \pm^{0.3}_{0.2}$
9.0-9.5	9.3	0.8	±0.1	±0.1	±0.02	$0.7 \pm^{0.3}_{0.2}$
9.5-10.0	9.8	0.69	±0.07	±0.08	±0.02	$0.62 \pm^{0.22}_{0.15}$
10.0-11.0	10.5	0.49	±0.03	±0.05	±0.01	$0.47 \pm^{0.16}_{0.11}$
11.0-12.0	11.5	0.34	±0.02	±0.04	±0.01	$0.34 \pm^{0.11}_{0.08}$
12.0-14.0	12.9	0.19	±0.01	±0.02	±0.004	$0.21 \pm^{0.06}_{0.05}$
14.0-16.0	14.9	0.111	±0.008	±0.011	±0.003	$0.117 \pm^{0.033}_{0.024}$
16.0-18.0	16.9	0.060	±0.005	±0.006	±0.002	$0.069 \pm^{0.018}_{0.013}$
18.0-22.0	19.7	0.032	±0.003	±0.003	±0.001	$0.035 \pm^{0.008}_{0.006}$
22.0-30.0	25.0	0.0091	±0.0010	±0.0011	±0.0002	$0.0109 \pm^{0.0022}_{0.0018}$
30.0-70.0	37.2	0.0008	±0.0001	±0.0001	±0.0000	$0.0009 \pm^{0.0001}_{0.0001}$

Table .7. Non-prompt J/ψ production cross-sections as a function of J/ψ p_T for $0.75 < |y|_{J/\psi} < 1.5$ under the assumption that prompt and non-prompt J/ψ production is unpolarised ($\lambda_\theta = 0$), and the spin-alignment envelope spans the range of non-prompt cross-sections within $\lambda_\theta = \pm 0.1$. The first uncertainty is statistical, the second uncertainty is systematic. Comparison is made to FONLL predictions.

		$\frac{d^2\sigma^{non-prompt}}{dp_T dy} \cdot \mathrm{Br}(J/\psi \to \mu^+\mu^-)$ [nb/GeV]				
p_T	$\langle p_T \rangle$	$0.75 < \lvert y \rvert < 1.5$				
(GeV)	(GeV)	Value	± (stat.)	± (syst.)	± (spin)	FONLL prediction
5.0-5.5	5.3	4.9	±1.7	±1.2	±0.15	$3.8 \pm ^{1.6}_{1.1}$
5.5-6.0	5.8	2.4	±0.8	±0.5	±0.07	$3.0 \pm ^{1.3}_{0.8}$
6.0-6.5	6.3	2.5	±0.5	±0.4	±0.07	$2.4 \pm ^{1.0}_{0.7}$
6.5-7.0	6.8	3.3	±0.5	±0.5	±0.09	$1.9 \pm ^{0.6}_{0.5}$
7.0-7.5	7.2	1.9	±0.3	±0.3	±0.05	$1.5 \pm ^{0.6}_{0.4}$
7.5-8.0	7.8	1.6	±0.2	±0.2	±0.04	$1.2 \pm ^{0.5}_{0.3}$
8.0-8.5	8.3	0.9	±0.1	±0.1	±0.02	$1.0 \pm ^{0.4}_{0.3}$
8.5-9.0	8.8	0.81	±0.09	±0.09	±0.02	$0.83 \pm ^{0.30}_{0.20}$
9.0-9.5	9.3	0.75	±0.07	±0.08	±0.02	$0.68 \pm ^{0.24}_{0.17}$
9.5-10.0	9.8	0.65	±0.06	±0.07	±0.02	$0.56 \pm ^{0.20}_{0.13}$
10.0-11.0	10.5	0.49	±0.03	±0.05	±0.01	$0.43 \pm ^{0.15}_{0.10}$
11.0-12.0	11.5	0.35	±0.02	±0.04	±0.01	$0.30 \pm ^{0.10}_{0.07}$
12.0-14.0	12.9	0.19	±0.01	±0.02	±0.00	$0.19 \pm ^{0.06}_{0.04}$
14.0-16.0	14.9	0.100	±0.007	±0.011	±0.002	$0.104 \pm ^{0.029}_{0.021}$
16.0-18.0	16.9	0.054	±0.005	±0.006	±0.001	$0.061 \pm ^{0.016}_{0.012}$
18.0-22.0	19.7	0.025	±0.002	±0.003	±0.001	$0.030 \pm ^{0.007}_{0.006}$
22.0-30.0	25.2	0.0086	±0.0009	±0.0010	±0.0001	$0.0093 \pm ^{0.0019}_{0.0015}$
30.0-70.0	38.0	0.0007	±0.0001	±0.0001	±0.0000	$0.0007 \pm ^{0.0001}_{0.0001}$

Table .8. Non-prompt J/ψ production cross-sections as a function of J/ψ p_T for $1.5 < |y|_{J/\psi} < 2$ under the assumption that prompt and non-prompt J/ψ production is unpolarised ($\lambda_\theta = 0$), and the spin-alignment envelope spans the range of non-prompt cross-sections within $\lambda_\theta = \pm 0.1$. The first uncertainty is statistical, the second uncertainty is systematic. Comparison is made to FONLL predictions.

		$\frac{d^2\sigma^{non-prompt}}{dp_T dy}\cdot \mathrm{Br}(J/\psi \to \mu^+\mu^-)$ [nb/GeV]				
p_T	$\langle p_T \rangle$	$1.5 < \lvert y \rvert < 2$				
(GeV)	(GeV)	Value	± (stat.)	± (syst.)	± (spin)	FONLL prediction
1.0-4.0	2.8	14.3	±7.9	±5.5	±0.37	$9.4 \pm ^{4.5}_{3.9}$
4.0-5.0	4.5	8.3	±2.0	±1.9	±0.21	$4.9 \pm ^{2.2}_{1.6}$
5.0-5.5	5.2	3.8	±1.0	±0.9	±0.09	$3.4 \pm ^{1.5}_{1.0}$
5.5-6.0	5.7	2.4	±0.5	±0.4	±0.06	$2.7 \pm ^{1.1}_{0.7}$
6.0-6.5	6.3	2.3	±0.5	±0.6	±0.05	$2.1 \pm ^{0.9}_{0.6}$
6.5-7.0	6.8	2.0	±0.3	±0.3	±0.05	$1.7 \pm ^{0.7}_{0.4}$
7.0-7.5	7.3	1.2	±0.2	±0.2	±0.03	$1.3 \pm ^{0.5}_{0.4}$
7.5-8.0	7.8	1.1	±0.1	±0.1	±0.02	$1.1 \pm ^{0.4}_{0.3}$
8.0-8.5	8.3	0.82	±0.10	±0.10	±0.02	$0.87 \pm ^{0.33}_{0.22}$
8.5-9.0	8.8	0.82	±0.08	±0.10	±0.02	$0.71 \pm ^{0.26}_{0.18}$
9.0-9.5	9.3	0.65	±0.07	±0.07	±0.01	$0.58 \pm ^{0.21}_{0.14}$
9.5-10.0	9.8	0.50	±0.05	±0.05	±0.01	$0.48 \pm ^{0.17}_{0.11}$
10.0-11.0	10.5	0.43	±0.03	±0.05	±0.01	$0.36 \pm ^{0.12}_{0.08}$
11.0-12.0	11.5	0.25	±0.02	±0.03	±0.01	$0.25 \pm ^{0.08}_{0.06}$
12.0-14.0	12.9	0.14	±0.01	±0.01	±0.002	$0.16 \pm ^{0.05}_{0.03}$
14.0-16.0	14.9	0.081	±0.007	±0.009	±0.001	$0.085 \pm ^{0.024}_{0.017}$
16.0-18.0	16.9	0.053	±0.005	±0.007	±0.001	$0.049 \pm ^{0.013}_{0.009}$
18.0-22.0	19.6	0.023	±0.002	±0.002	±0.0000	$0.024 \pm ^{0.006}_{0.004}$
22.0-30.0	25.0	0.0064	±0.0009	±0.00081	±0.0001	$0.0071 \pm ^{0.0014}_{0.0012}$

Table .9. Non-prompt J/ψ production cross-sections as a function of J/ψ p_T for $2 < |y|_{J/\psi} < 2.4$ under the assumption that prompt and non-prompt J/ψ production is unpolarised ($\lambda_\theta = 0$), and the spin-alignment envelope spans the range of non-prompt cross-sections within $\lambda_\theta = \pm 0.1$. The first uncertainty is statistical, the second uncertainty is systematic. Comparison is made to FONLL predictions.

		$\frac{d^2\sigma^{non-prompt}}{dp_T dy}\cdot \mathrm{Br}(J/\psi \to \mu^+\mu^-)$ [nb/GeV]				
p_T	$\langle p_T \rangle$	$2 < \lvert y \rvert < 2.4$				
(GeV)	(GeV)	Value	± (stat.)	± (syst.)	± (spin)	FONLL prediction
5.0-6.0	5.5	3.2	±1.3	±1.0	±0.04	$2.7 \pm ^{1.1}_{0.7}$
6.0-7.0	6.5	2.2	±0.4	±0.4	±0.02	$1.7 \pm ^{0.7}_{0.4}$
7.0-7.5	7.3	0.5	±0.2	±0.1	±0.01	$1.2 \pm ^{0.5}_{0.3}$
7.5-8.0	7.8	0.9	±0.2	±0.2	±0.01	$0.9 \pm ^{0.4}_{0.2}$
8.0-8.5	8.3	0.6	±0.1	±0.1	±0.01	$0.7 \pm ^{0.3}_{0.2}$
8.5-9.0	8.8	0.35	±0.09	±0.06	±0.01	$0.60 \pm ^{0.22}_{0.15}$
9.0-9.5	9.2	0.39	±0.06	±0.06	±0.01	$0.49 \pm ^{0.18}_{0.12}$
9.5-10.0	9.7	0.30	±0.06	±0.04	±0.005	$0.40 \pm ^{0.14}_{0.10}$
10.0-11.0	10.5	0.22	±0.03	±0.03	±0.003	$0.30 \pm ^{0.10}_{0.07}$
11.0-12.0	11.5	0.18	±0.02	±0.02	±0.003	$0.21 \pm ^{0.07}_{0.05}$
12.0-14.0	12.9	0.11	±0.01	±0.01	±0.002	$0.13 \pm ^{0.04}_{0.03}$
14.0-18.0	15.6	0.042	±0.006	±0.005	±0.0004	$0.053 \pm ^{0.015}_{0.011}$
18.0-30.0	21.3	0.0059	±0.0010	±0.0007	±0.0001	$0.0097 \pm ^{0.0022}_{0.0017}$

Table .10. Prompt J/ψ production cross-sections as a function of J/ψ p_T for $|y|_{J/\psi} < 0.75$. The central value assumes unpolarised ($\lambda_\theta = 0$) prompt and non-prompt production, and the spin-alignment envelope spans the range of possible prompt cross-sections under various polarisation hypotheses. The first quoted uncertainty is statistical, the second uncertainty is systematic. Comparison is made to the Colour Evaporation Model prediction.

		$\frac{d^2\sigma^{prompt}}{dp_T dy}\cdot\mathrm{Br}(J/\psi \to \mu^+\mu^-)$ [nb/GeV]				
p_T	$\langle p_T \rangle$	$\lvert y\rvert < 0.75$				
(GeV)	(GeV)	Value	± (stat.)	± (syst.)	± (spin)	CEM prediction
7.0-7.5	7.3	6.8	±0.8	$\pm^{1.1}_{1.1}$	$\pm^{4.3}_{2.2}$	2.8
7.5-8.0	7.8	5.9	±0.6	$\pm^{0.9}_{0.9}$	$\pm^{2.7}_{1.9}$	2.2
8.0-8.5	8.3	3.3	±0.3	$\pm^{0.4}_{0.4}$	$\pm^{1.3}_{1.0}$	1.7
8.5-9.0	8.8	2.6	±0.2	$\pm^{0.4}_{0.4}$	$\pm^{0.9}_{0.8}$	1.3
9.0-9.5	9.2	2.2	±0.2	$\pm^{0.3}_{0.3}$	$\pm^{0.9}_{0.6}$	1.0
9.5-10.0	9.8	1.5	±0.1	$\pm^{0.2}_{0.2}$	$\pm^{0.5}_{0.4}$	0.8
10.0-11.0	10.5	1.04	±0.05	$\pm^{0.11}_{0.11}$	$\pm^{0.32}_{0.29}$	0.60
11.0-12.0	11.5	0.71	±0.03	$\pm^{0.08}_{0.08}$	$\pm^{0.19}_{0.20}$	0.41
12.0-14.0	12.9	0.34	±0.01	$\pm^{0.04}_{0.04}$	$\pm^{0.08}_{0.09}$	0.24
14.0-16.0	14.9	0.163	±0.010	$\pm^{0.016}_{0.016}$	$\pm^{0.036}_{0.042}$	0.128
16.0-18.0	16.9	0.076	±0.006	$\pm^{0.008}_{0.008}$	$\pm^{0.015}_{0.018}$	0.071
18.0-22.0	19.7	0.035	±0.003	$\pm^{0.004}_{0.004}$	$\pm^{0.006}_{0.008}$	0.035
22.0-30.0	25.0	0.0078	±0.0009	$\pm^{0.0009}_{0.0009}$	$\pm^{0.0010}_{0.0014}$	0.0109
30.0-70.0	37.2	0.0004	±0.0001	$\pm^{0.0001}_{0.0001}$	$\pm^{0.0000}_{0.0000}$	0.0008

Table .11. Prompt J/ψ production cross-sections as a function of J/ψ p_T for $0.75 < |y|_{J/\psi} < 1.5$. The central value assumes unpolarised ($\lambda_\theta = 0$) prompt and non-prompt production, and the spin-alignment envelope spans the range of possible prompt cross-sections under various polarisation hypotheses. The first quoted uncertainty is statistical, the second uncertainty is systematic. Comparison is made to the Colour Evaporation Model prediction.

		$\frac{d^2\sigma^{prompt}}{dp_T dy}\cdot\mathrm{Br}(J/\psi \to \mu^+\mu^-)$ [nb/GeV]				
p_T	$\langle p_T \rangle$	$0.75 < \lvert y \rvert < 1.5$				
(GeV)	(GeV)	Value	± (stat.)	± (syst.)	± (spin)	CEM prediction
5.0-5.5	5.3	21.9	±4.7	$\pm^{4.8}_{4.6}$	$\pm^{8.7}_{6.5}$	10.4
5.5-6.0	5.8	16.8	±2.6	$\pm^{3.0}_{2.9}$	$\pm^{7.5}_{5.0}$	7.2
6.0-6.5	6.2	11.0	±1.0	$\pm^{1.4}_{1.4}$	$\pm^{5.8}_{3.2}$	5.2
6.5-7.0	6.7	9.2	±0.9	$\pm^{1.4}_{1.4}$	$\pm^{2.9}_{2.6}$	3.7
7.0-7.5	7.2	6.3	±0.5	$\pm^{0.8}_{0.8}$	$\pm^{1.7}_{1.8}$	2.8
7.5-8.0	7.7	5.0	±0.3	$\pm^{0.6}_{0.6}$	$\pm^{1.2}_{1.4}$	2.1
8.0-8.5	8.2	3.2	±0.2	$\pm^{0.3}_{0.3}$	$\pm^{1.4}_{0.7}$	1.6
8.5-9.0	8.7	2.8	±0.2	$\pm^{0.3}_{0.3}$	$\pm^{0.8}_{0.6}$	1.3
9.0-9.5	9.3	2.1	±0.1	$\pm^{0.2}_{0.2}$	$\pm^{0.5}_{0.5}$	1.0
9.5-10.0	9.7	1.57	±0.09	$\pm^{0.17}_{0.17}$	$\pm^{0.30}_{0.35}$	0.79
10.0-11.0	10.5	1.06	±0.04	$\pm^{0.12}_{0.12}$	$\pm^{0.19}_{0.24}$	0.59
11.0-12.0	11.5	0.67	±0.03	$\pm^{0.08}_{0.08}$	$\pm^{0.12}_{0.15}$	0.39
12.0-14.0	12.9	0.34	±0.01	$\pm^{0.04}_{0.04}$	$\pm^{0.06}_{0.08}$	0.23
14.0-16.0	14.9	0.149	±0.008	$\pm^{0.016}_{0.016}$	$\pm^{0.024}_{0.031}$	0.120
16.0-18.0	16.9	0.066	±0.005	$\pm^{0.007}_{0.007}$	$\pm^{0.009}_{0.013}$	0.067
18.0-22.0	19.7	0.028	±0.002	$\pm^{0.003}_{0.003}$	$\pm^{0.004}_{0.005}$	0.032
22.0-30.0	25.2	0.0073	±0.0008	$\pm^{0.0008}_{0.0008}$	$\pm^{0.0008}_{0.0011}$	0.0100
30.0-70.0	38.0	0.0004	±0.0001	$\pm^{0.0001}_{0.0001}$	$\pm^{0.0000}_{0.0000}$	0.0007

Table .12. Prompt J/ψ production cross-sections as a function of J/ψ p_T for $1.5 < |y|_{J/\psi} < 2$. The central value assumes unpolarised ($\lambda_\theta = 0$) prompt and non-prompt production, and the spin-alignment envelope spans the range of possible prompt cross-sections under various polarisation hypotheses. The first quoted uncertainty is statistical, the second uncertainty is systematic. Comparison is made to the Colour Evaporation Model prediction.

		$\frac{d^2\sigma^{prompt}}{dp_T dy}\cdot\mathrm{Br}(J/\psi \to \mu^+\mu^-)$ [nb/GeV]				
p_T	$\langle p_T \rangle$	$1.5 < \lvert y \rvert < 2$				
(GeV)	(GeV)	Value	± (stat.)	± (syst.)	± (spin)	CEM prediction
1.0-4.0	2.8	129	±22	$\pm^{25}_{35}$	$\pm^{246}_{35}$	43
4.0-5.0	4.5	31.1	±4.6	$\pm^{4.5}_{4.5}$	$\pm^{54.7}_{7.7}$	17.7
5.0-5.5	5.2	13.8	±2.7	$\pm^{3.4}_{3.2}$	$\pm^{13.5}_{3.2}$	10.0
5.5-6.0	5.7	11.8	±1.1	$\pm^{1.5}_{1.5}$	$\pm^{11.6}_{2.6}$	6.7
6.0-6.5	6.3	10.5	±0.9	$\pm^{1.2}_{1.1}$	$\pm^{8.2}_{2.2}$	4.8
6.5-7.0	6.8	6.9	±0.5	$\pm^{1.0}_{1.0}$	$\pm^{4.2}_{1.6}$	3.4
7.0-7.5	7.2	5.1	±0.4	$\pm^{0.7}_{0.7}$	$\pm^{2.5}_{1.2}$	2.6
7.5-8.0	7.7	4.0	±0.3	$\pm^{0.5}_{0.4}$	$\pm^{1.8}_{0.7}$	1.9
8.0-8.5	8.3	3.0	±0.2	$\pm^{0.3}_{0.3}$	$\pm^{1.2}_{0.4}$	1.5
8.5-9.0	8.7	2.3	±0.1	$\pm^{0.3}_{0.2}$	$\pm^{0.7}_{0.3}$	1.2
9.0-9.5	9.2	1.61	±0.09	$\pm^{0.17}_{0.17}$	$\pm^{0.46}_{0.26}$	0.89
9.5-10.0	9.7	1.18	±0.08	$\pm^{0.13}_{0.12}$	$\pm^{0.32}_{0.21}$	0.72
10.0-11.0	10.5	0.86	±0.04	$\pm^{0.10}_{0.09}$	$\pm^{0.21}_{0.16}$	0.53
11.0-12.0	11.5	0.51	±0.03	$\pm^{0.05}_{0.05}$	$\pm^{0.11}_{0.10}$	0.35
12.0-14.0	12.9	0.26	±0.01	$\pm^{0.03}_{0.02}$	$\pm^{0.05}_{0.04}$	0.21
14.0-16.0	14.9	0.112	±0.008	$\pm^{0.012}_{0.011}$	$\pm^{0.016}_{0.019}$	0.106
16.0-18.0	16.9	0.050	±0.005	$\pm^{0.007}_{0.005}$	$\pm^{0.006}_{0.008}$	0.057
18.0-22.0	19.6	0.026	±0.003	$\pm^{0.002}_{0.002}$	$\pm^{0.003}_{0.004}$	0.028
22.0-30.0	25.0	0.0042	±0.0007	$\pm^{0.0005}_{0.0005}$	$\pm^{0.0003}_{0.0005}$	0.0084

Table .13. Prompt J/ψ production cross-sections as a function of J/ψ p_T for $2 < |y|_{J/\psi} < 2.4$. The central value assumes unpolarised ($\lambda_\theta = 0$) prompt and non-prompt production, and the spin-alignment envelope spans the range of possible prompt cross-sections under various polarisation hypotheses. The first quoted uncertainty is statistical, the second uncertainty is systematic. Comparison is made to the Colour Evaporation Model prediction.

		$\frac{d^2\sigma^{prompt}}{dp_T dy}\cdot\mathrm{Br}(J/\psi \to \mu^+\mu^-)$ [nb/GeV]				
p_T	$\langle p_T \rangle$	$2 < \lvert y \rvert < 2.4$				
(GeV)	(GeV)	Value	± (stat.)	± (syst.)	± (spin)	CEM prediction
5.0-6.0	5.5	11.5	±2.5	$\pm^{2.5}_{2.6}$	$\pm^{12.1}_{2.0}$	7.8
6.0-7.0	6.5	5.6	±0.6	$\pm^{0.6}_{0.6}$	$\pm^{3.3}_{0.9}$	3.9
7.0-7.5	7.3	3.5	±0.5	$\pm^{0.6}_{0.5}$	$\pm^{2.3}_{0.6}$	2.3
7.5-8.0	7.7	3.1	±0.4	$\pm^{0.5}_{0.4}$	$\pm^{2.2}_{0.5}$	1.8
8.0-8.5	8.3	2.1	±0.3	$\pm^{0.3}_{0.3}$	$\pm^{0.7}_{0.5}$	1.4
8.5-9.0	8.7	1.6	±0.2	$\pm^{0.2}_{0.2}$	$\pm^{0.5}_{0.3}$	1.1
9.0-9.5	9.2	1.1	±0.1	$\pm^{0.1}_{0.1}$	$\pm^{0.3}_{0.2}$	0.9
9.5-10.0	9.7	0.91	±0.09	$\pm^{0.13}_{0.12}$	$\pm^{0.33}_{0.12}$	0.68
10.0-11.0	10.5	0.61	±0.05	$\pm^{0.07}_{0.07}$	$\pm^{0.21}_{0.06}$	0.47
11.0-12.0	11.5	0.42	±0.04	$\pm^{0.05}_{0.06}$	$\pm^{0.12}_{0.05}$	0.32
12.0-14.0	12.9	0.21	±0.02	$\pm^{0.02}_{0.02}$	$\pm^{0.05}_{0.03}$	0.18
14.0-18.0	15.6	0.079	±0.007	$\pm^{0.007}_{0.005}$	$\pm^{0.012}_{0.007}$	0.071
18.0-30.0	21.2	0.008	±0.001	$\pm^{0.001}_{0.001}$	$\pm^{0.001}_{0.001}$	0.012

Additional Information on J/ψ Cross-Section Measurement

.1 Detector Acceptance and J/ψ Spin-alignment

The general angular distribution for the decay $J/\psi \to \mu\mu$ in the J/ψ decay frame is given by:

$$\frac{d^2N}{d\cos\theta^\star d\phi^\star} \propto 1 + \lambda_\theta \cos^2\theta^\star + \lambda_\phi \sin^2\theta^\star \cos 2\phi^\star + \lambda_{\theta\phi} \sin 2\theta^\star \cos\phi^\star \qquad (.1)$$

where $\theta^\star$ is the angle between the direction of the positive muon momentum in the J/ψ decay frame and the J/ψ line of flight, while $\phi^\star$ is defined as the angle between the J/ψ production and decay planes in the lab frame (see Figure .1, reference [107] and references therein).

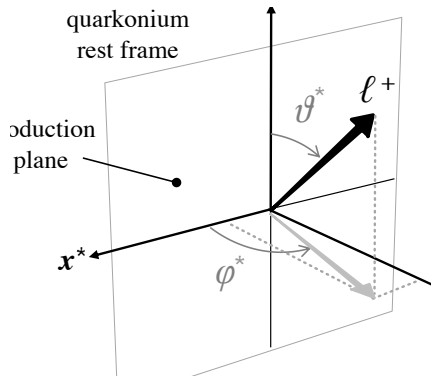

Figure .1. Definitions of the J/ψ spin-alignment angles, in the J/ψ decay frame. $\theta^\star$ is the angle between the direction of the positive muon in that frame and the direction of J/ψ in the laboratory frame, which is directed along the $z^\star$-axis. $\phi^\star$ is the angle between the J/ψ production ($x^\star - z^\star$) plane and its decay plane formed by the direction of the J/ψ and the lepton ℓ^+ (from [107]).

A large number of possible combinations of the coefficients $\lambda_\theta, \lambda_\phi, \lambda_{\theta\phi}$ have been studied, including some with $\lambda_{\theta\phi} \neq 0$. Five extreme cases have been identified that lead to the biggest variation of acceptance within the kinematics of the ATLAS detector and define an envelope in which the results may vary under all possible polarisation assumptions:

1. Isotropic distribution, independent of $\theta^\star$ and $\phi^\star$, with $\lambda_\theta = \lambda_\phi = \lambda_{\theta\phi} = 0$, labelled as “FLAT". This is used as the main (central) hypothesis.
2. Full longitudinal alignment with $\lambda_\theta = -1, \lambda_\phi = \lambda_{\theta\phi} = 0$, labelled as “LONG".
3. Transverse alignment with $\lambda_\theta = +1, \lambda_\phi = \lambda_{\theta\phi} = 0$, labelled as T_{+0}.
4. Transverse alignment with $\lambda_\theta = +1, \lambda_\phi = +1, \lambda_{\theta\phi} = 0$, labelled as T_{++}.
5. Transverse alignment with $\lambda_\theta = +1, \lambda_\phi = -1, \lambda_{\theta\phi} = 0$, labelled as T_{+-}.

Two-dimensional acceptance maps are produced in bins of p_T and y of the J/ψ, for each of these five scenarios, and are illustrated in Figure .2. The maps are obtained by reweighting the flat distribution at the generator level using Equation .1.

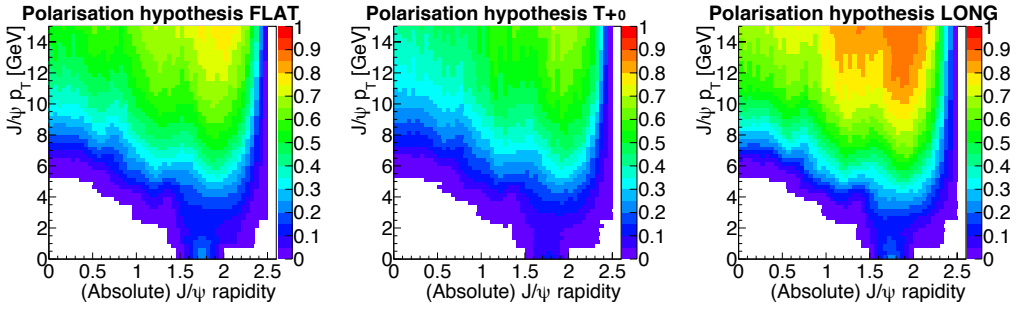

(a) $\lambda_\theta = \lambda_\phi = \lambda_{\theta\phi} = 0$ (b) $\lambda_\theta = +1, \lambda_\phi = \lambda_{\theta\phi} = 0$ (c) $\lambda_\theta = -1, \lambda_\phi = \lambda_{\theta\phi} = 0$

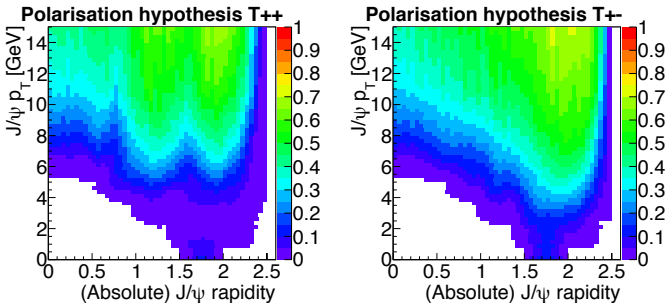

(d) $\lambda_\theta = +1, \lambda_\phi = +1, \lambda_{\theta\phi} = 0$ (e) $\lambda_\theta = +1, \lambda_\phi = -1, \lambda_{\theta\phi} = 0$

Figure .2. Kinematic acceptance maps as a function of J/ψ transverse momentum and rapidity for specific spin-alignment scenarios considered, which are representative of the extrema of the variation of the measured cross-section due to spin-alignment configurations. Differences in acceptance behaviour, particularly at low p_T, occur between scenarios and can significantly influence the cross-section measurement in a given bin.

Additional Information on Non-Prompt to Prompt J/ψ Cross-Section Fraction

.2 Test of the Fitting Technique: Results

Table .14. Results of a Gaussian fit of the obtained pull distributions in $|y| < 0.75$ bins.

p_T (J/ψ) [GeV]	pull mean value	pull σ
6 – 7	-0.03 ± 0.11	1.13 ± 0.08
7 – 7.5	-0.08 ± 0.09	0.90 ± 0.06
7.5 – 8	0.01 ± 0.10	1.00 ± 0.07
8 – 8.5	-0.01 ± 0.08	0.85 ± 0.06
8.5 – 9	0.05 ± 0.10	1.01 ± 0.07
9 – 9.5	0.01 ± 0.09	0.90 ± 0.06
9.5 – 10	-0.12 ± 0.11	1.09 ± 0.08
10 – 11	-0.09 ± 0.10	1.02 ± 0.07
11 – 12	0.26 ± 0.10	1.00 ± 0.07
12 – 14	-0.04 ± 0.10	1.03 ± 0.07
14 – 16	-0.15 ± 0.10	1.01 ± 0.07
16 – 18	0.15 ± 0.09	0.92 ± 0.06
18 – 22	0.01 ± 0.10	0.98 ± 0.07
22 – 30	-0.04 ± 0.10	1.00 ± 0.07
30 – 70	0.15 ± 0.11	1.10 ± 0.08

Table .15. Results of a Gaussian fit of the obtained pull distributions in $0.75 < |y| < 1.5$ bins.

p_T (J/ψ) [GeV]	pull mean value	pull σ
4 – 5	0.16 ± 0.10	0.96 ± 0.07
5 – 5.5	-0.09 ± 0.11	1.05 ± 0.07
5.5 – 6	-0.08 ± 0.10	1.02 ± 0.07
6 – 6.5	-0.04 ± 0.10	1.02 ± 0.07
6.5 – 7	-0.015 ± 0.10	1.02 ± 0.07
7 – 7.5	0.19 ± 0.11	1.09 ± 0.08
7.5 – 8	0.05 ± 0.10	0.97 ± 0.07
8 – 8.5	-0.03 ± 0.12	1.20 ± 0.08
8.5 – 9	0.05 ± 0.11	1.06 ± 0.07
9 – 9.5	0.08 ± 0.09	0.88 ± 0.06
9.5 – 10	-0.02 ± 0.09	0.92 ± 0.06
10 – 11	-0.01 ± 0.09	0.94 ± 0.07
11 – 12	0.08 ± 0.09	0.93 ± 0.07
12 – 14	0.03 ± 0.09	0.90 ± 0.06
14 – 16	0.13 ± 0.09	0.95 ± 0.07
16 – 18	0.01 ± 0.08	0.82 ± 0.06
18 – 22	-0.01 ± 0.11	1.06 ± 0.07
22 – 30	0.04 ± 0.11	1.13 ± 0.08
30 – 70	-0.02 ± 0.11	1.07 ± 0.08

Table .16. Results of a Gaussian fit of the obtained pull distributions in $1.5 < |y| < 2$ bins.

p_T (J/ψ) [GeV]	pull mean value	pull σ
1 – 4	0.18 ± 0.09	0.87 ± 0.06
4 – 5	-0.14 ± 0.10	0.96 ± 0.07
5 – 5.5	-0.03 ± 0.11	1.07 ± 0.07
5.5 – 6	-0.00 ± 0.09	0.91 ± 0.06
6 – 6.5	-0.01 ± 0.09	0.95 ± 0.07
6.5 – 7	0.04 ± 0.10	0.97 ± 0.07
7 – 7.5	0.16 ± 0.10	1.05 ± 0.07
7.5 – 8	0.11 ± 0.10	1.02 ± 0.07
8 – 8.5	-0.02 ± 0.11	1.06 ± 0.07
8.5 – 9	-0.02 ± 0.10	1.01 ± 0.07
9 – 9.5	-0.02 ± 0.08	0.82 ± 0.06
9.5 – 10	0.03 ± 0.09	0.91 ± 0.06
10 – 11	0.15 ± 0.11	1.06 ± 0.07
11 – 12	0.08 ± 0.09	0.87 ± 0.06
12 – 14	0.18 ± 0.09	0.92 ± 0.06
14 – 16	0.07 ± 0.10	0.98 ± 0.07
16 – 18	-0.24 ± 0.10	1.00 ± 0.07
18 – 22	0.03 ± 0.11	1.06 ± 0.07
22 – 30	-0.05 ± 0.11	1.08 ± 0.08

Table .17. Results of a Gaussian fit of the obtained pull distributions in $2 < |y| < 2.4$ bins.

p_T (J/ψ) [GeV]	pull mean value	pull σ
1 – 5	0.00 ± 0.11	1.8 ± 0.08
5 – 6	0.06 ± 0.10	0.97 ± 0.07
6 – 7	-0.08 ± 0.10	1.04 ± 0.07
7 – 7.5	-0.05 ± 0.10	1.02 ± 0.07
7.5 – 8	-0.09 ± 0.11	1.1 ± 0.08
8 – 8.5	0.10 ± 0.10	1.05 ± 0.07
8.5 – 9	0.00 ± 0.10	0.99 ± 0.07
9 – 9.5	0.23 ± 0.09	0.92 ± 0.06
9.5 – 10	0.13 ± 0.10	1.04 ± 0.07
10 – 11	0.21 ± 0.11	1.05 ± 0.07
11 – 12	-0.12 ± 0.09	0.94 ± 0.07
12 – 14	-0.05 ± 0.10	1.04 ± 0.07
14 – 18	-0.13 ± 0.10	1.02 ± 0.07
18 – 30	-0.06 ± 0.10	1.04 ± 0.07

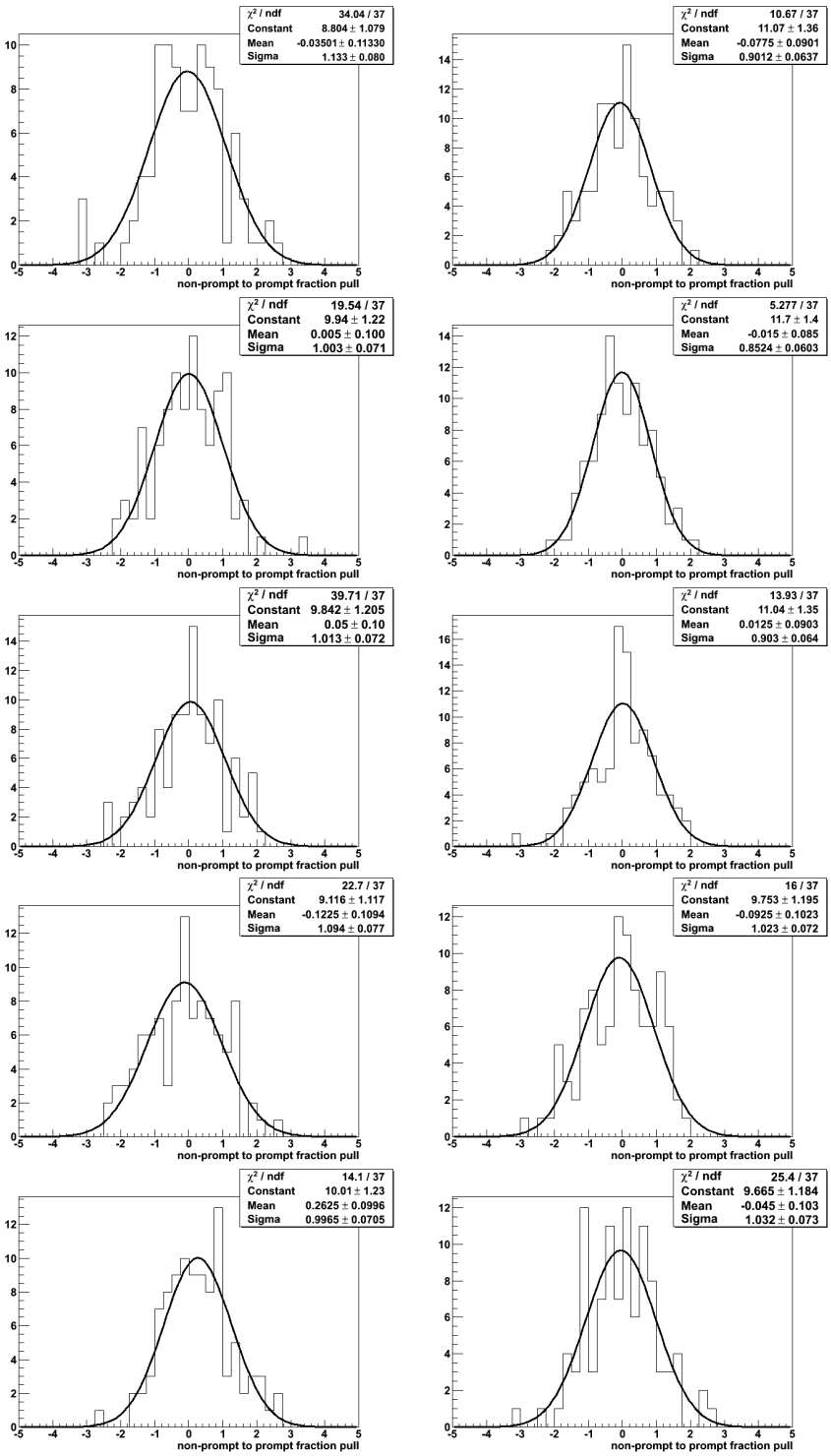
χ² / ndf 34.04 / 37
Constant 8.804 ± 1.079
Mean -0.03501 ± 0.11330
Sigma 1.133 ± 0.080
non-prompt to prompt fraction pull
χ² / ndf 10.67 / 37
Constant 11.07 ± 1.36
Mean -0.0775 ± 0.0901
Sigma 0.9012 ± 0.0637
non-prompt to prompt fraction pull
χ² / ndf 19.54 / 37
Constant 9.94 ± 1.22
Mean 0.005 ± 0.100
Sigma 1.003 ± 0.071
non-prompt to prompt fraction pull
χ² / ndf 5.277 / 37
Constant 11.7 ± 1.4
Mean -0.015 ± 0.085
Sigma 0.8524 ± 0.0603
non-prompt to prompt fraction pull
χ² / ndf 39.71 / 37
Constant 9.842 ± 1.205
Mean 0.05 ± 0.10
Sigma 1.013 ± 0.072
non-prompt to prompt fraction pull
χ² / ndf 13.93 / 37
Constant 11.04 ± 1.35
Mean 0.0125 ± 0.0903
Sigma 0.903 ± 0.064
non-prompt to prompt fraction pull
χ² / ndf 22.7 / 37
Constant 9.116 ± 1.117
Mean -0.1225 ± 0.1094
Sigma 1.094 ± 0.077
non-prompt to prompt fraction pull
χ² / ndf 16 / 37
Constant 9.753 ± 1.195
Mean -0.0925 ± 0.1023
Sigma 1.023 ± 0.072
non-prompt to prompt fraction pull
χ² / ndf 14.1 / 37
Constant 10.01 ± 1.23
Mean 0.2625 ± 0.0996
Sigma 0.9965 ± 0.0705
non-prompt to prompt fraction pull
χ² / ndf 25.4 / 37
Constant 9.665 ± 1.184
Mean -0.045 ± 0.103
Sigma 1.032 ± 0.073
non-prompt to prompt fraction pull

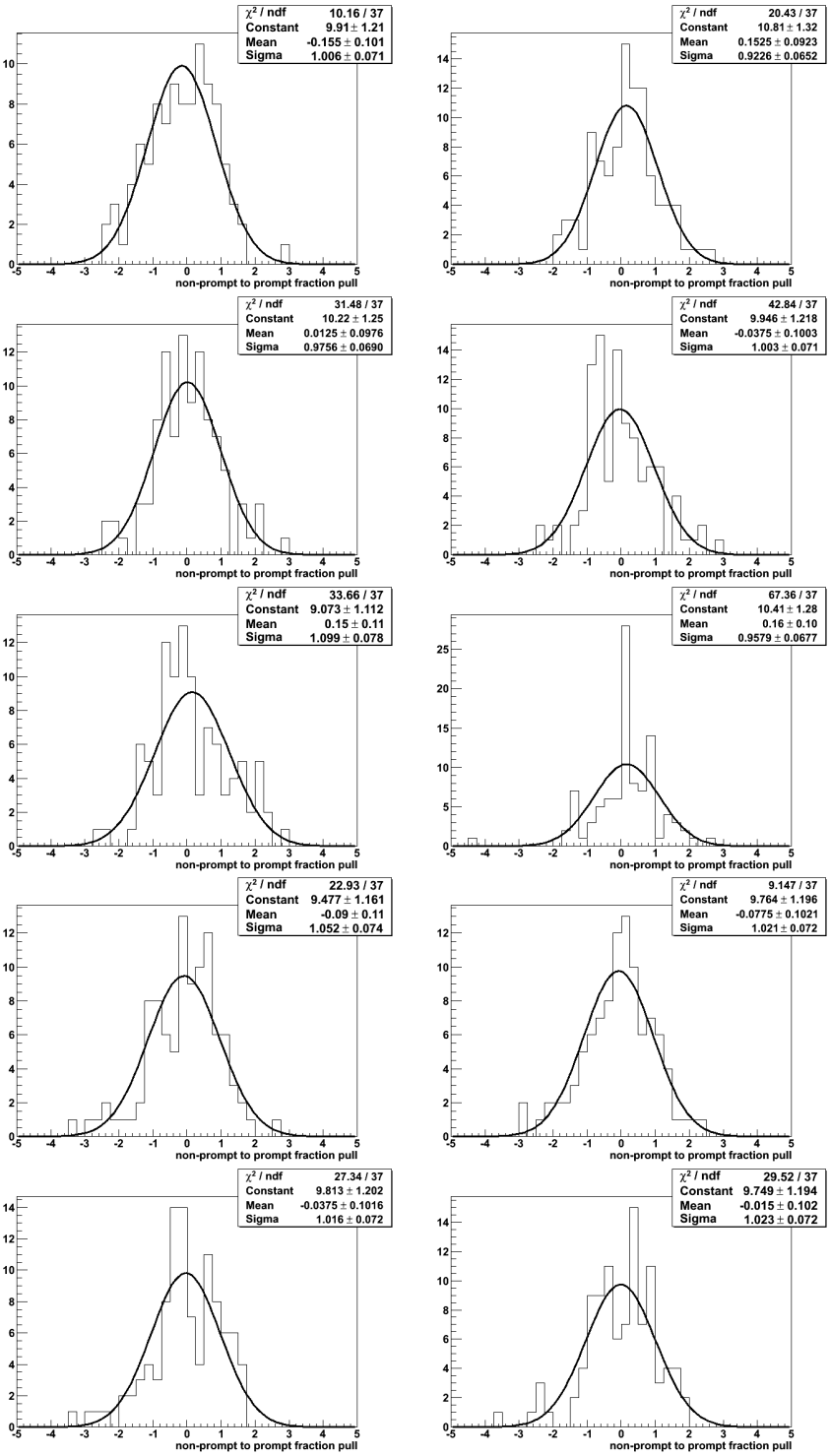
χ² / ndf 10.16 / 37
Constant 9.91 ± 1.21
Mean -0.155 ± 0.101
Sigma 1.006 ± 0.071
non-prompt to prompt fraction pull
χ² / ndf 20.43 / 37
Constant 10.81 ± 1.32
Mean 0.1525 ± 0.0923
Sigma 0.9226 ± 0.0652
non-prompt to prompt fraction pull
χ² / ndf 31.48 / 37
Constant 10.22 ± 1.25
Mean 0.0125 ± 0.0976
Sigma 0.9756 ± 0.0690
non-prompt to prompt fraction pull
χ² / ndf 42.84 / 37
Constant 9.946 ± 1.218
Mean -0.0375 ± 0.1003
Sigma 1.003 ± 0.071
non-prompt to prompt fraction pull
χ² / ndf 33.66 / 37
Constant 9.073 ± 1.112
Mean 0.15 ± 0.11
Sigma 1.099 ± 0.078
non-prompt to prompt fraction pull
χ² / ndf 67.36 / 37
Constant 10.41 ± 1.28
Mean 0.16 ± 0.10
Sigma 0.9579 ± 0.0677
non-prompt to prompt fraction pull
χ² / ndf 22.93 / 37
Constant 9.477 ± 1.161
Mean -0.09 ± 0.11
Sigma 1.052 ± 0.074
non-prompt to prompt fraction pull
χ² / ndf 9.147 / 37
Constant 9.764 ± 1.196
Mean -0.0775 ± 0.1021
Sigma 1.021 ± 0.072
non-prompt to prompt fraction pull
χ² / ndf 27.34 / 37
Constant 9.813 ± 1.202
Mean -0.0375 ± 0.1016
Sigma 1.016 ± 0.072
non-prompt to prompt fraction pull
χ² / ndf 29.52 / 37
Constant 9.749 ± 1.194
Mean -0.015 ± 0.102
Sigma 1.023 ± 0.072
non-prompt to prompt fraction pull

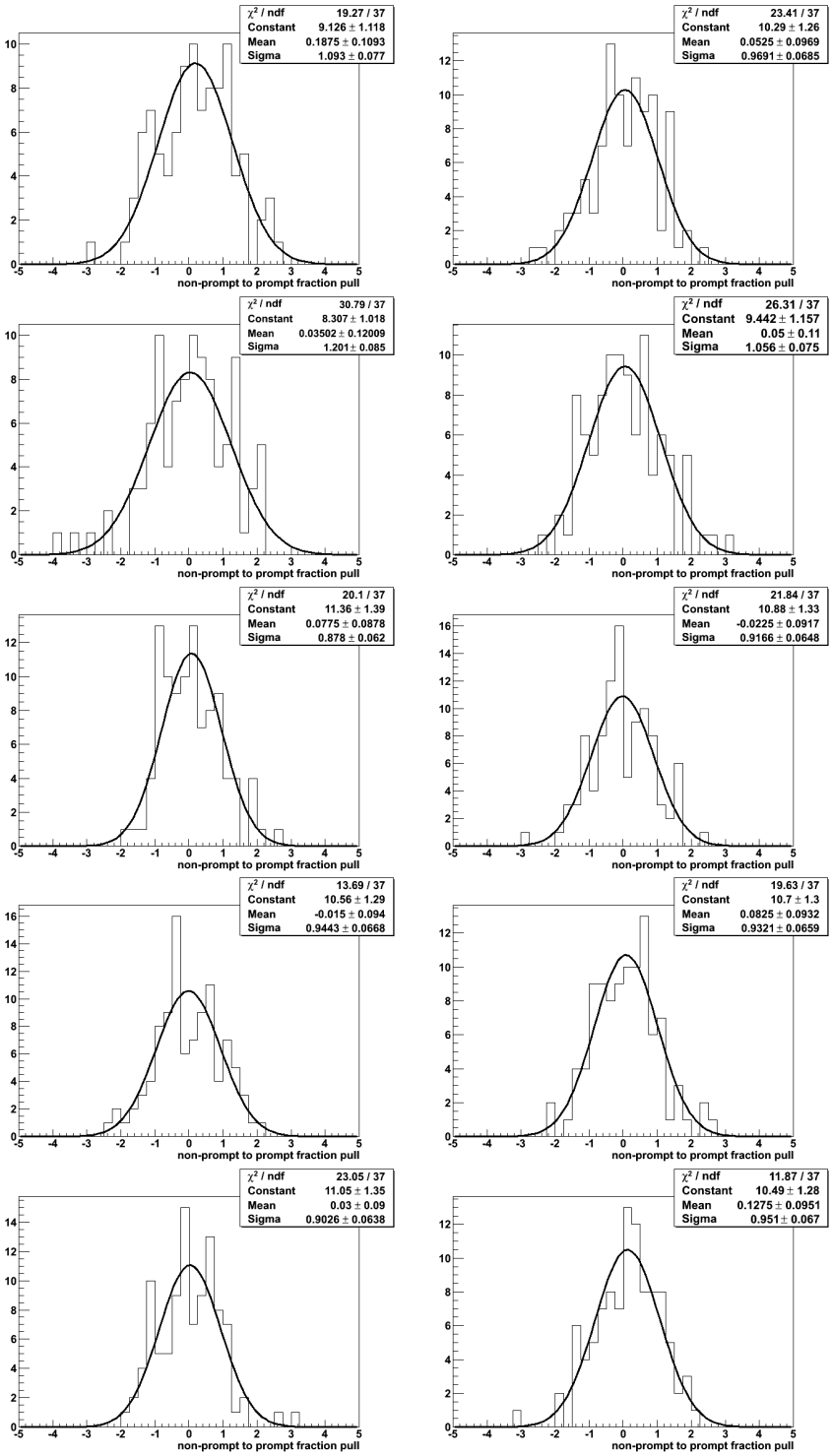
χ² / ndf 19.27 / 37
Constant 9.126 ± 1.118
Mean 0.1875 ± 0.1093
Sigma 1.093 ± 0.077
non-prompt to prompt fraction pull
χ² / ndf 23.41 / 37
Constant 10.29 ± 1.26
Mean 0.0525 ± 0.0969
Sigma 0.9691 ± 0.0685
non-prompt to prompt fraction pull
χ² / ndf 30.79 / 37
Constant 8.307 ± 1.018
Mean 0.03502 ± 0.12009
Sigma 1.201 ± 0.085
non-prompt to prompt fraction pull
χ² / ndf 26.31 / 37
Constant 9.442 ± 1.157
Mean 0.05 ± 0.11
Sigma 1.056 ± 0.075
non-prompt to prompt fraction pull
χ² / ndf 20.1 / 37
Constant 11.36 ± 1.39
Mean 0.0775 ± 0.0878
Sigma 0.878 ± 0.062
non-prompt to prompt fraction pull
χ² / ndf 21.84 / 37
Constant 10.88 ± 1.33
Mean -0.0225 ± 0.0917
Sigma 0.9166 ± 0.0648
non-prompt to prompt fraction pull
χ² / ndf 13.69 / 37
Constant 10.56 ± 1.29
Mean -0.015 ± 0.094
Sigma 0.9443 ± 0.0668
non-prompt to prompt fraction pull
χ² / ndf 19.63 / 37
Constant 10.7 ± 1.3
Mean 0.0825 ± 0.0932
Sigma 0.9321 ± 0.0659
non-prompt to prompt fraction pull
χ² / ndf 23.05 / 37
Constant 11.05 ± 1.35
Mean 0.03 ± 0.09
Sigma 0.9026 ± 0.0638
non-prompt to prompt fraction pull
χ² / ndf 11.87 / 37
Constant 10.49 ± 1.28
Mean 0.1275 ± 0.0951
Sigma 0.951 ± 0.067
non-prompt to prompt fraction pull

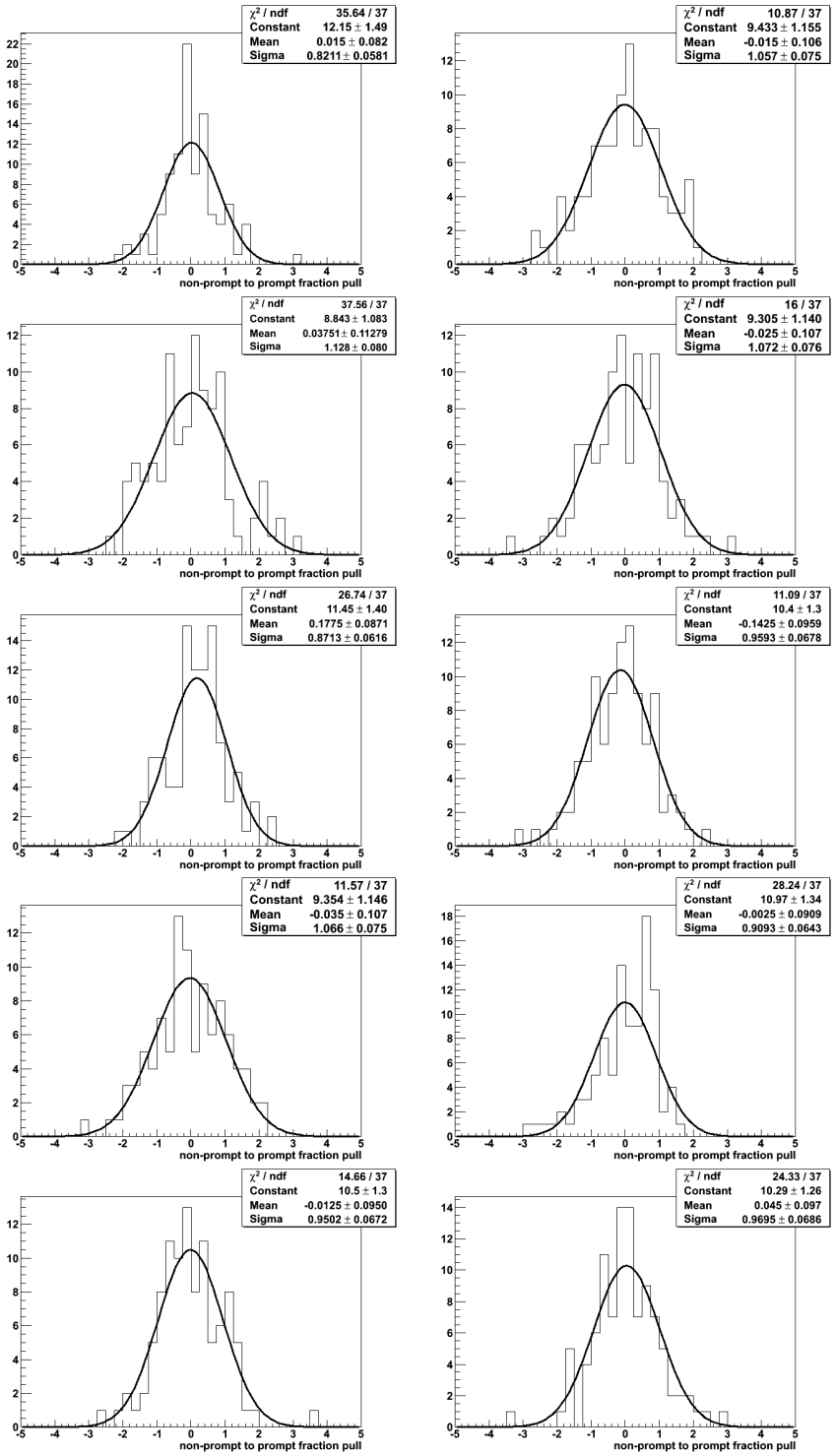
χ² / ndf 35.64 / 37
Constant 12.15 ± 1.49
Mean 0.015 ± 0.082
Sigma 0.8211 ± 0.0581
non-prompt to prompt fraction pull
χ² / ndf 10.87 / 37
Constant 9.433 ± 1.155
Mean -0.015 ± 0.106
Sigma 1.057 ± 0.075
non-prompt to prompt fraction pull
χ² / ndf 37.56 / 37
Constant 8.843 ± 1.083
Mean 0.03751 ± 0.11279
Sigma 1.128 ± 0.080
non-prompt to prompt fraction pull
χ² / ndf 16 / 37
Constant 9.305 ± 1.140
Mean -0.025 ± 0.107
Sigma 1.072 ± 0.076
non-prompt to prompt fraction pull
χ² / ndf 26.74 / 37
Constant 11.45 ± 1.40
Mean 0.1775 ± 0.0871
Sigma 0.8713 ± 0.0616
non-prompt to prompt fraction pull
χ² / ndf 11.09 / 37
Constant 10.4 ± 1.3
Mean -0.1425 ± 0.0959
Sigma 0.9593 ± 0.0678
non-prompt to prompt fraction pull
χ² / ndf 11.57 / 37
Constant 9.354 ± 1.146
Mean -0.035 ± 0.107
Sigma 1.066 ± 0.075
non-prompt to prompt fraction pull
χ² / ndf 28.24 / 37
Constant 10.97 ± 1.34
Mean -0.0025 ± 0.0909
Sigma 0.9093 ± 0.0643
non-prompt to prompt fraction pull
χ² / ndf 14.66 / 37
Constant 10.5 ± 1.3
Mean -0.0125 ± 0.0950
Sigma 0.9502 ± 0.0672
non-prompt to prompt fraction pull
χ² / ndf 24.33 / 37
Constant 10.29 ± 1.26
Mean 0.045 ± 0.097
Sigma 0.9695 ± 0.0686
non-prompt to prompt fraction pull

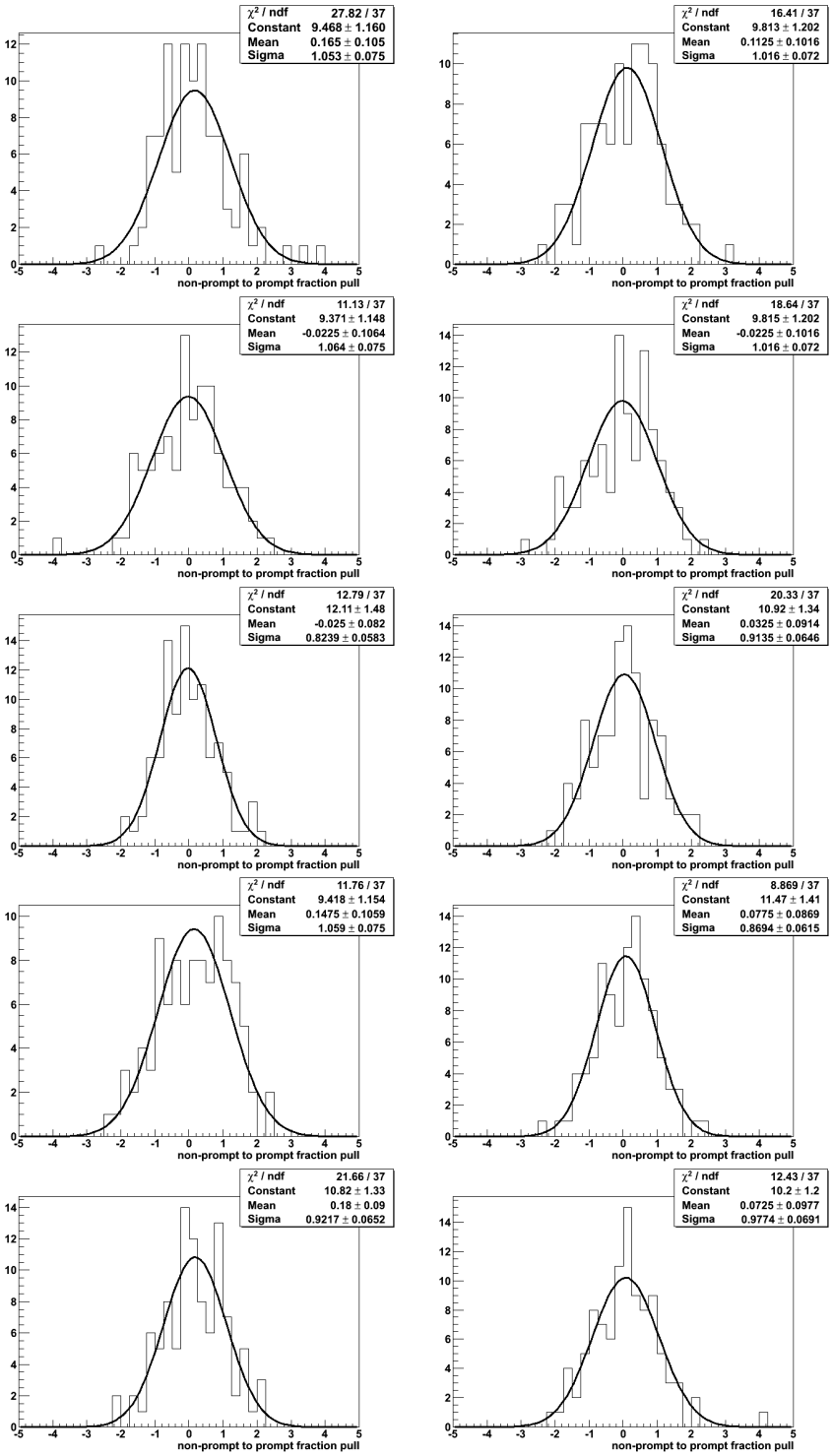
χ² / ndf 27.82 / 37
Constant 9.468 ± 1.160
Mean 0.165 ± 0.105
Sigma 1.053 ± 0.075
non-prompt to prompt fraction pull
χ² / ndf 16.41 / 37
Constant 9.813 ± 1.202
Mean 0.1125 ± 0.1016
Sigma 1.016 ± 0.072
non-prompt to prompt fraction pull
χ² / ndf 11.13 / 37
Constant 9.371 ± 1.148
Mean -0.0225 ± 0.1064
Sigma 1.064 ± 0.075
non-prompt to prompt fraction pull
χ² / ndf 18.64 / 37
Constant 9.815 ± 1.202
Mean -0.0225 ± 0.1016
Sigma 1.016 ± 0.072
non-prompt to prompt fraction pull
χ² / ndf 12.79 / 37
Constant 12.11 ± 1.48
Mean -0.025 ± 0.082
Sigma 0.8239 ± 0.0583
non-prompt to prompt fraction pull
χ² / ndf 20.33 / 37
Constant 10.92 ± 1.34
Mean 0.0325 ± 0.0914
Sigma 0.9135 ± 0.0646
non-prompt to prompt fraction pull
χ² / ndf 11.76 / 37
Constant 9.418 ± 1.154
Mean 0.1475 ± 0.1059
Sigma 1.059 ± 0.075
non-prompt to prompt fraction pull
χ² / ndf 8.869 / 37
Constant 11.47 ± 1.41
Mean 0.0775 ± 0.0869
Sigma 0.8694 ± 0.0615
non-prompt to prompt fraction pull
χ² / ndf 21.66 / 37
Constant 10.82 ± 1.33
Mean 0.18 ± 0.09
Sigma 0.9217 ± 0.0652
non-prompt to prompt fraction pull
χ² / ndf 12.43 / 37
Constant 10.2 ± 1.2
Mean 0.0725 ± 0.0977
Sigma 0.9774 ± 0.0691
non-prompt to prompt fraction pull

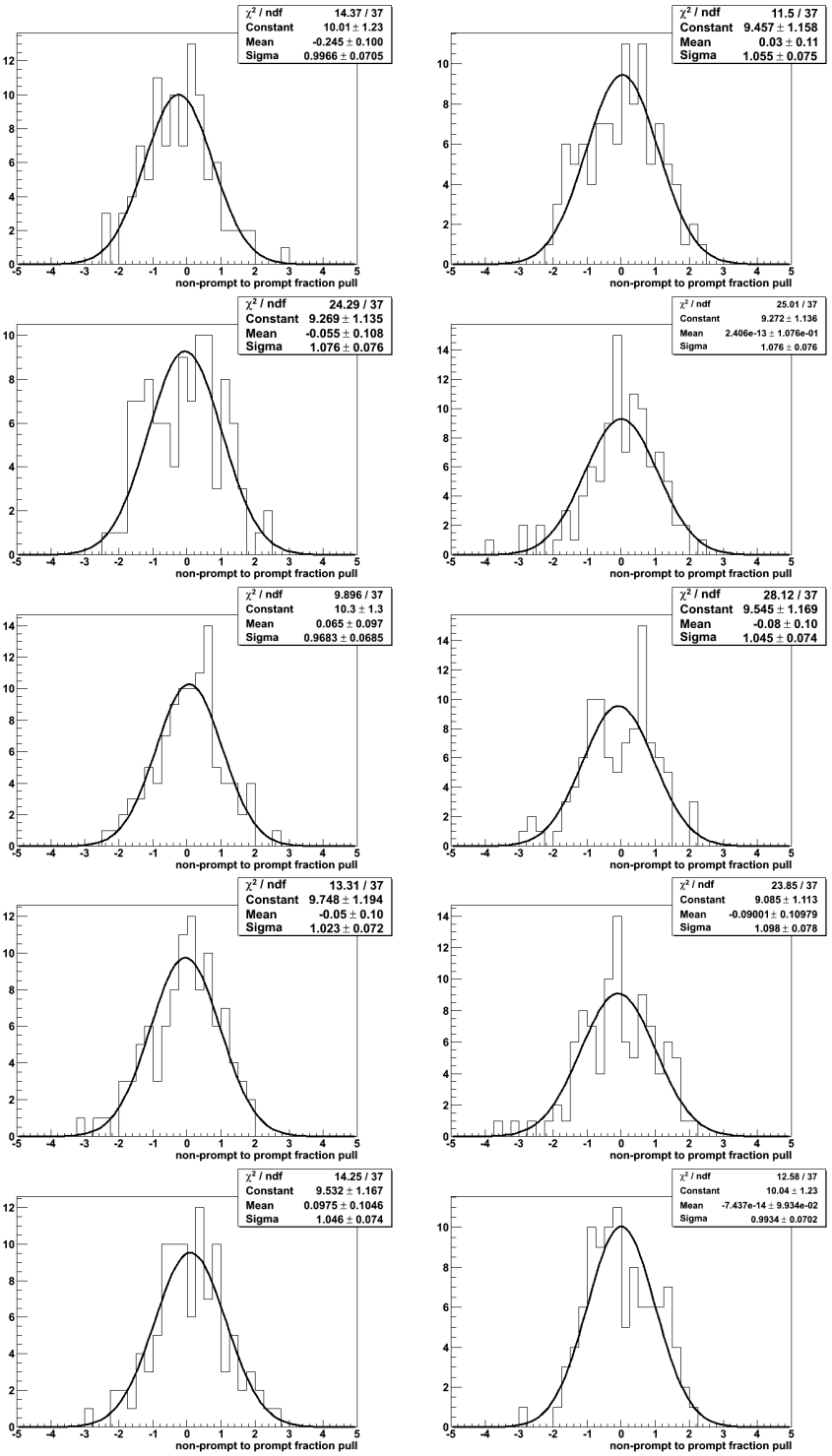
χ² / ndf 14.37 / 37
Constant 10.01 ± 1.23
Mean -0.245 ± 0.100
Sigma 0.9966 ± 0.0705
non-prompt to prompt fraction pull
χ² / ndf 11.5 / 37
Constant 9.457 ± 1.158
Mean 0.03 ± 0.11
Sigma 1.055 ± 0.075
non-prompt to prompt fraction pull
χ² / ndf 24.29 / 37
Constant 9.269 ± 1.135
Mean -0.055 ± 0.108
Sigma 1.076 ± 0.076
non-prompt to prompt fraction pull
χ² / ndf 25.01 / 37
Constant 9.272 ± 1.136
Mean 2.406e-13 ± 1.076e-01
Sigma 1.076 ± 0.076
non-prompt to prompt fraction pull
χ² / ndf 9.896 / 37
Constant 10.3 ± 1.3
Mean 0.065 ± 0.097
Sigma 0.9683 ± 0.0685
non-prompt to prompt fraction pull
χ² / ndf 28.12 / 37
Constant 9.545 ± 1.169
Mean -0.08 ± 0.10
Sigma 1.045 ± 0.074
non-prompt to prompt fraction pull
χ² / ndf 13.31 / 37
Constant 9.748 ± 1.194
Mean -0.05 ± 0.10
Sigma 1.023 ± 0.072
non-prompt to prompt fraction pull
χ² / ndf 23.85 / 37
Constant 9.085 ± 1.113
Mean -0.09001 ± 0.10979
Sigma 1.098 ± 0.078
non-prompt to prompt fraction pull
χ² / ndf 14.25 / 37
Constant 9.532 ± 1.167
Mean 0.0975 ± 0.1046
Sigma 1.046 ± 0.074
non-prompt to prompt fraction pull
χ² / ndf 12.58 / 37
Constant 10.04 ± 1.23
Mean -7.437e-14 ± 9.934e-02
Sigma 0.9934 ± 0.0702
non-prompt to prompt fraction pull

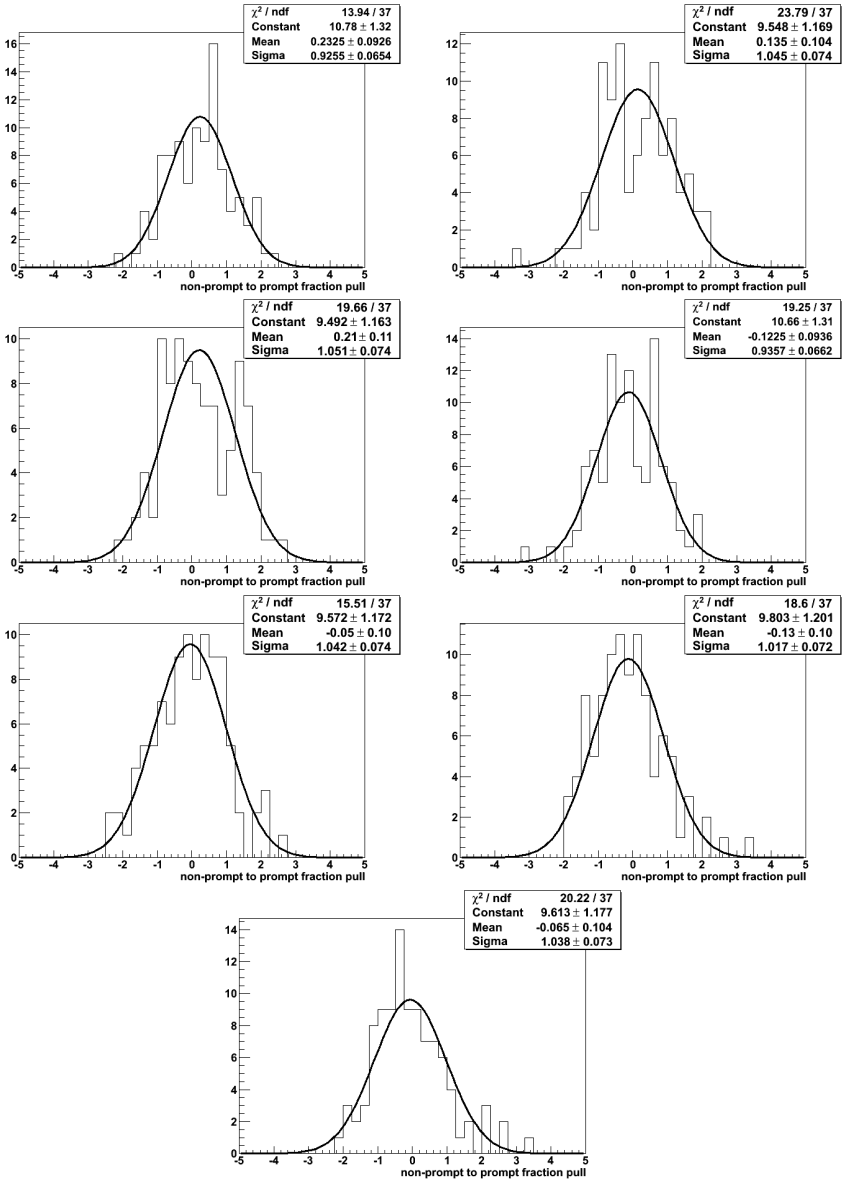

Figure .3. Pull distributions for all the p_T and y bins used in the ratio measurement, with a Gaussian fit superimposed

.3 Pearson χ^2 Definition

In order to evaluate the quality of the maximum likelihood fit, the Pearson χ^2 is computed. In order to do so, the binned data histogram and the relative fit curve that are to be tested are considered. The binning is dynamic (i.e. it can vary with the observable) so that in each bin, the data histogram contains enough statistics: here at least ten entries are required.

The χ^2 of the fit is then computed as follows:

$$\chi^2 = \sum_{i=1}^{N} \frac{(y_i - y_i^{exp})^2}{y_i^{exp}},$$

where N is the total number of bins, y_i is the number of entries in the data histogram, y_i^{exp} is the number of expected entries from the fit curve. When a bin is larger than the fine initial binning, an interpolation is performed between the bins' maximum and minimum values.

.4 Results of the Likelihood Fits

This section contains the complete set of mass and lifetime fits obtained in all of the p_T and y bins. First all of the plots are provided in Figures from .4 to .11. Then the parameters and fit quality results are listed in Tables .18, .19, .20 and .21.

.4.1 Complete set of mass and lifetime plots

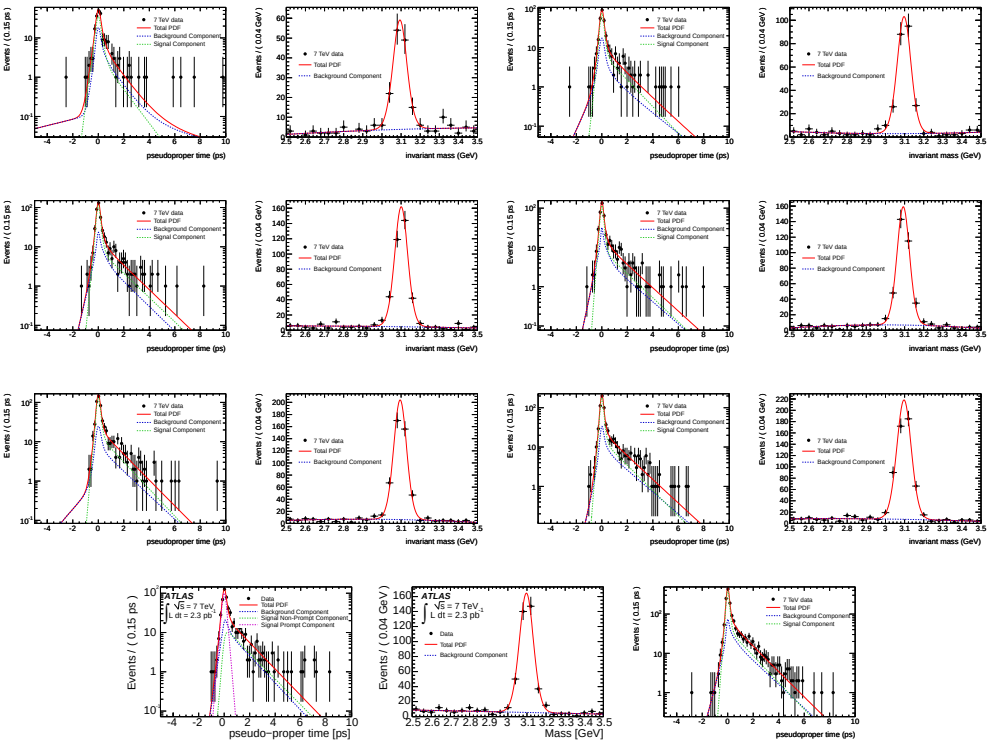

Figure .4. Masses and lifetimes in the $0.0 < y < 0.75$ bin (1)

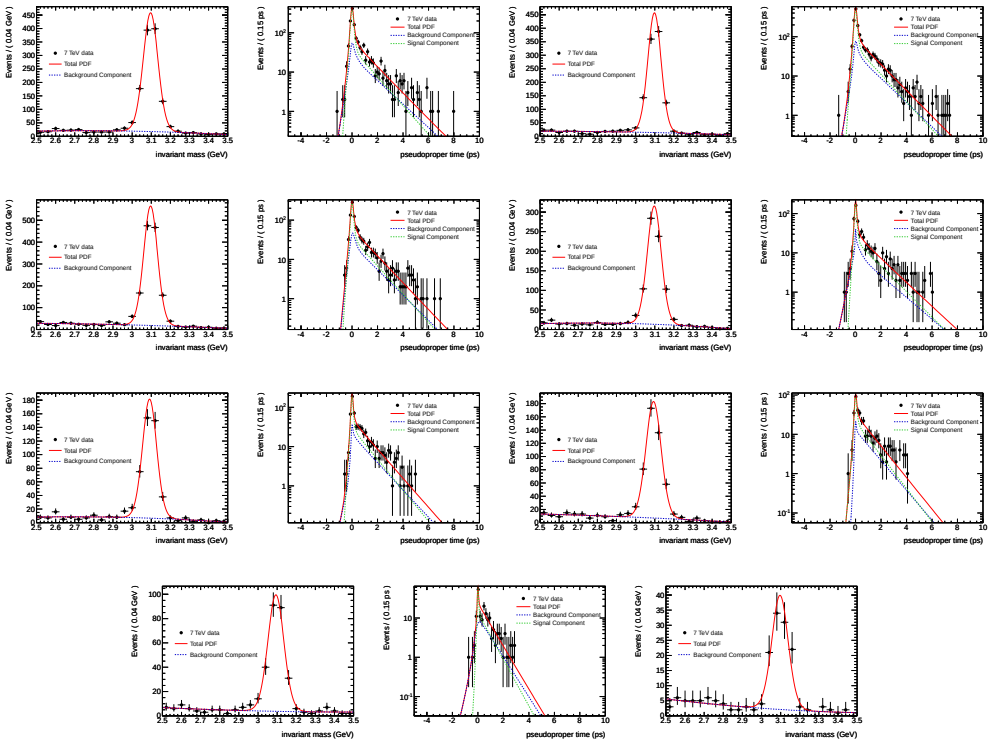

Figure .5. Masses and lifetimes in the $0.0 < y < 0.75$ bin (2)

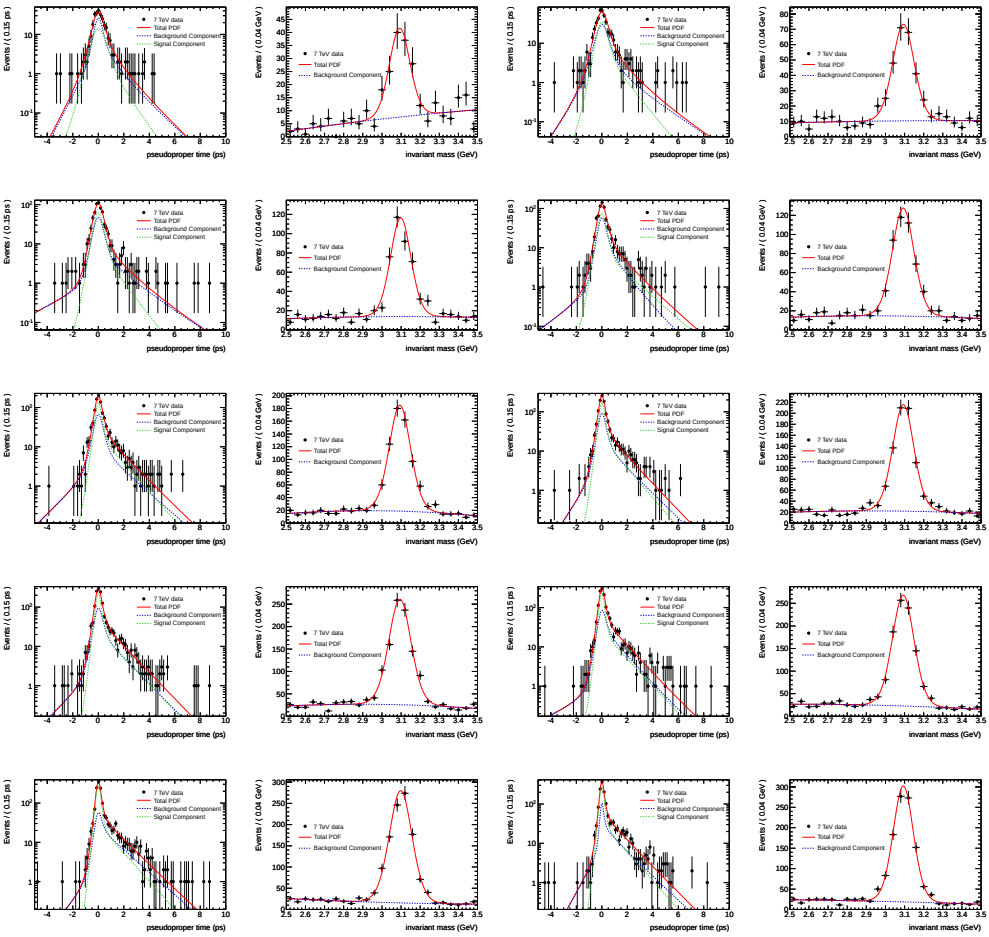

Figure .6. Masses and lifetimes in the $0.75 < y < 1.5$ bin (1)

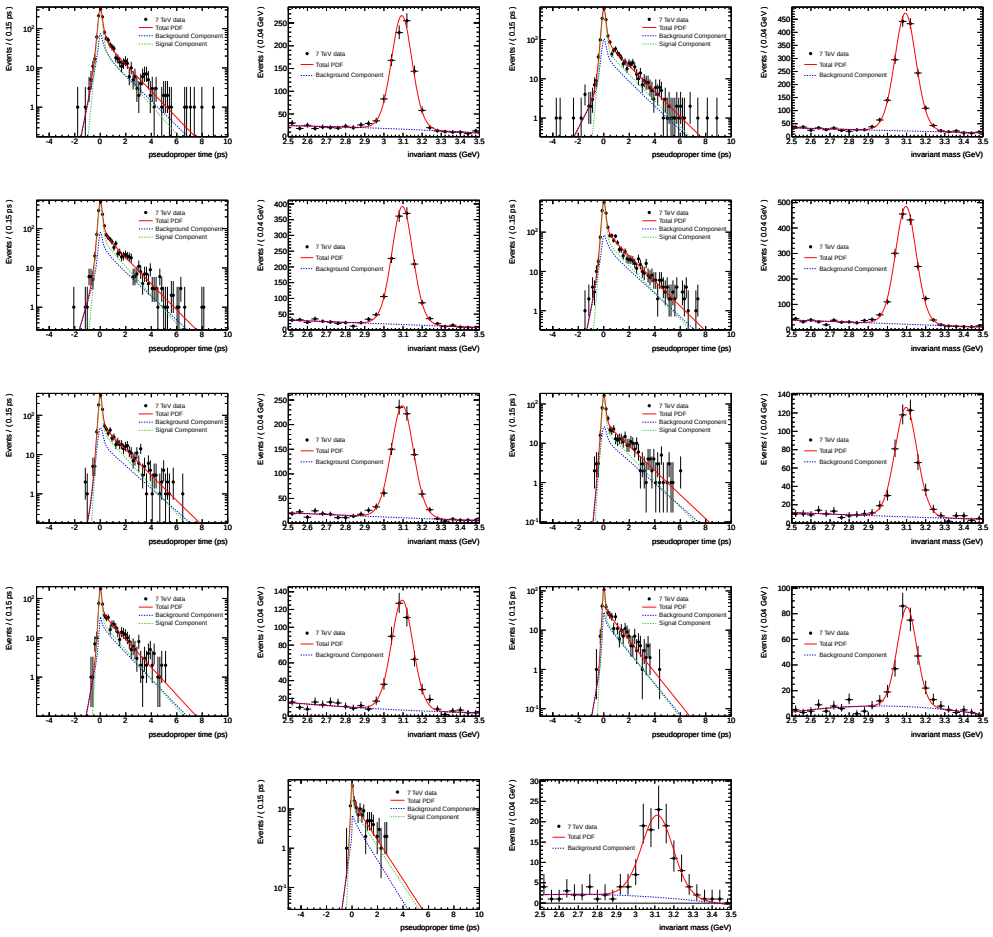

Figure .7. Masses and lifetimes in the $0.75 < y < 1.5$ bin (2)

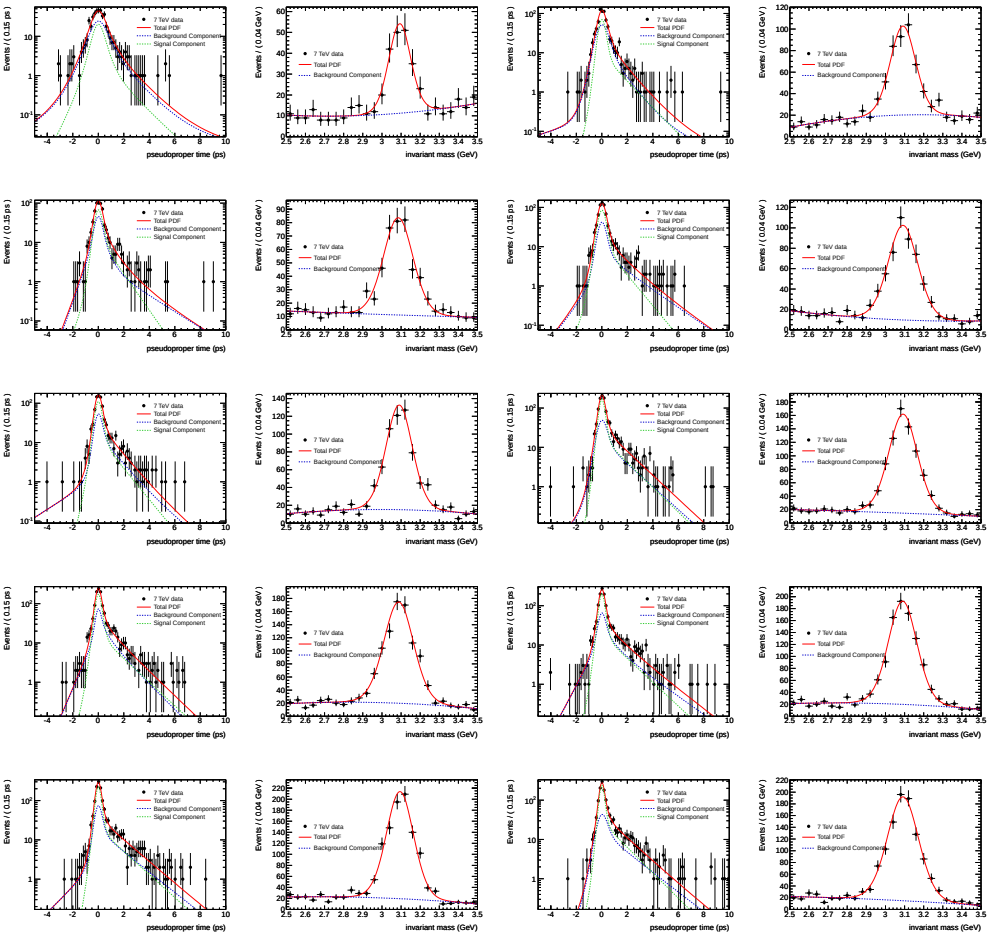

Figure .8. Masses and lifetimes in the $1.5 < y < 2.0$ bin (1)

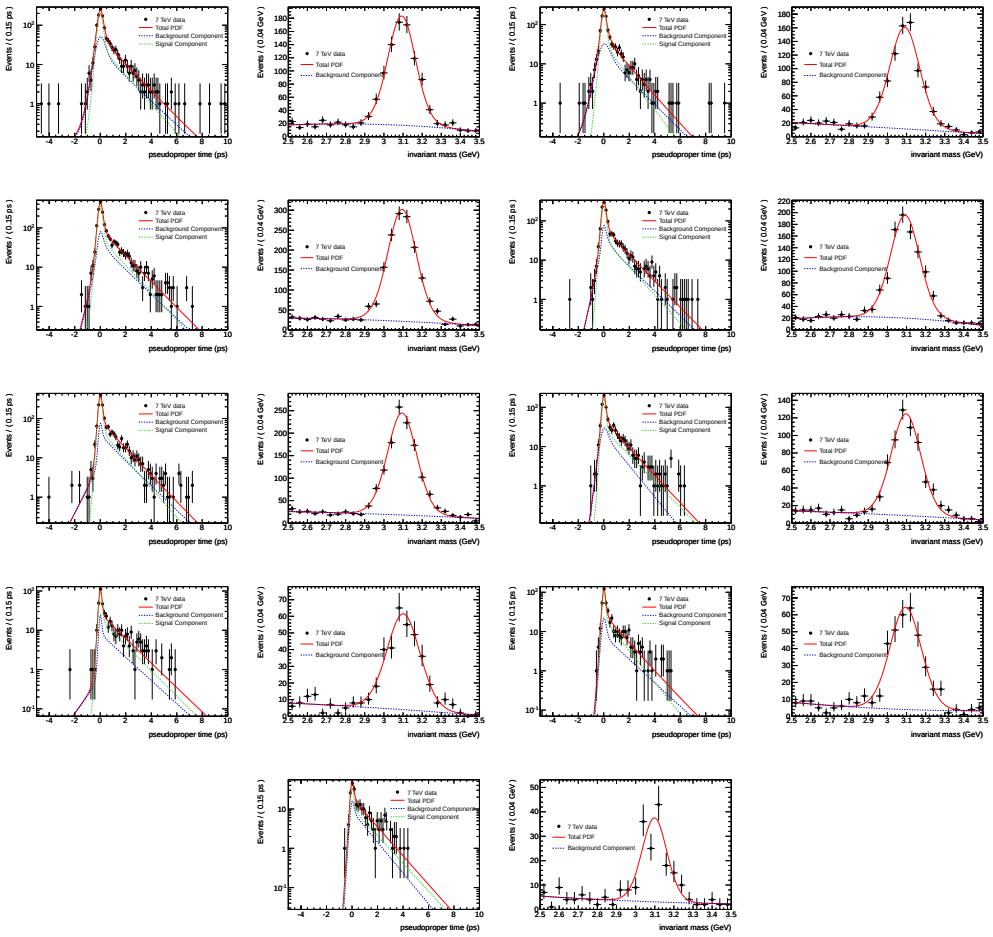

Figure .9. Masses and lifetimes in the $1.5 < y < 2.0$ bin (2)

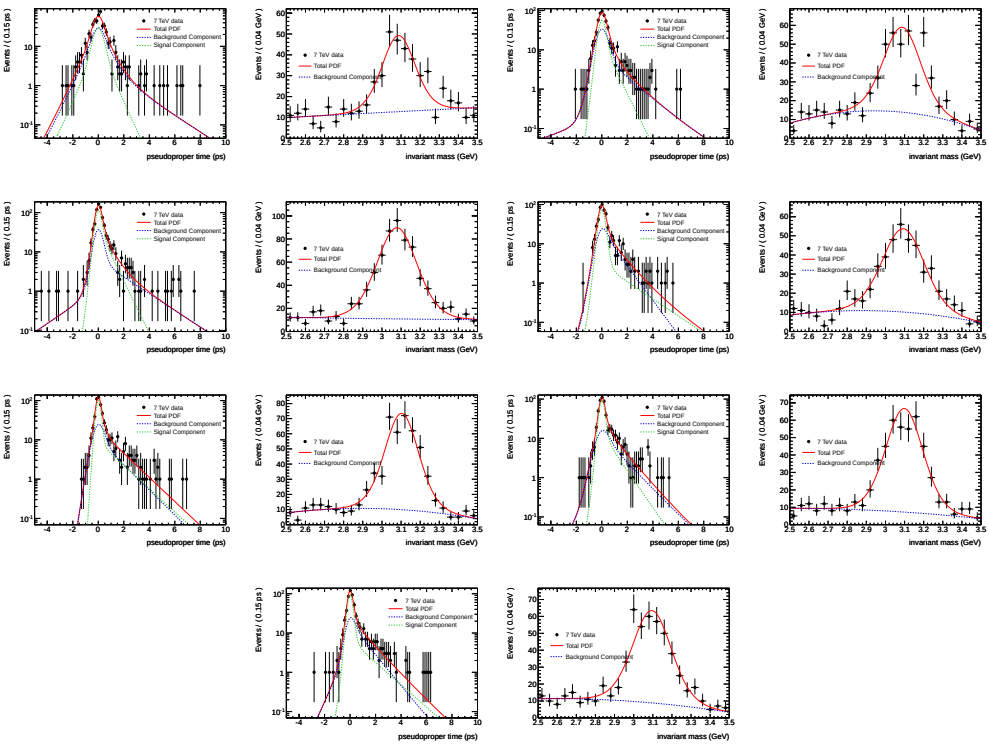

Figure .10. Masses and lifetimes in the $2.0 < y < 2.4$ bin (1)

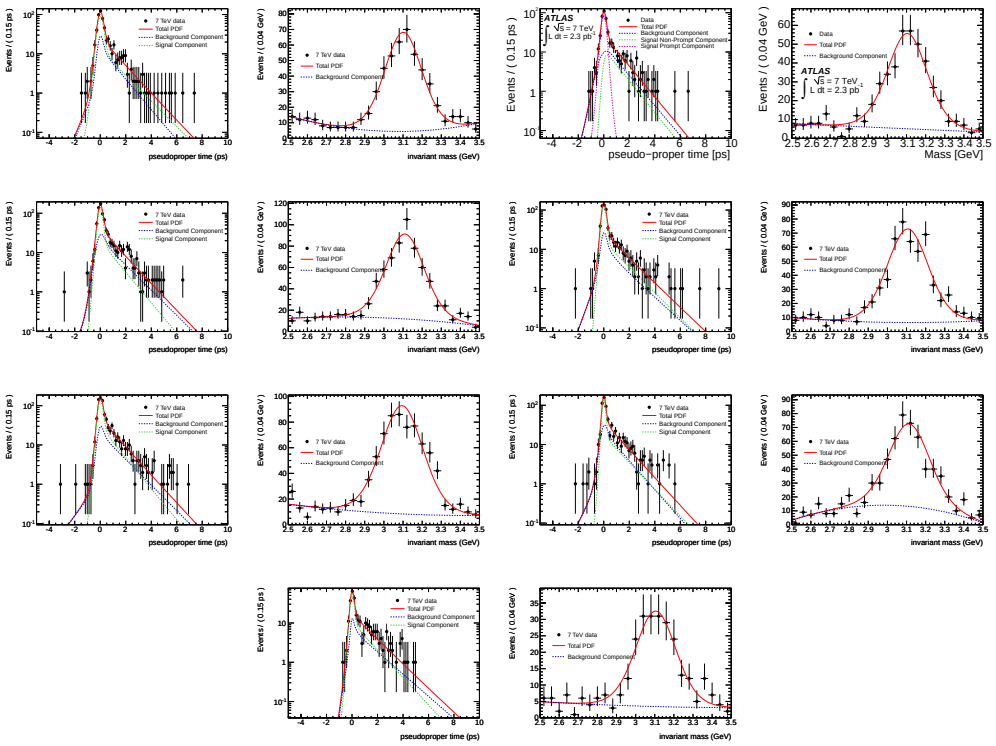

Figure .11. Masses and lifetimes in the $2.0 < y < 2.4$ bin (2)

.4.2 Complete set of fraction results

Table .18. Non-prompt fraction measurement for the $0 \leq |y| < 0.75$ bin

p_T (J/ψ) (GeV)	Non-prompt fraction	χ^2/ndof	χ^2 p-value	Kolmogorov	Mean p_T
$6 < p_T < 7$	0.175 ± 0.057	10.3/14	0.74	0.99	6.64 ± 0.27
$7 < p_T < 7.5$	0.259 ± 0.038	9.9/18	0.93	1	7.28 ± 0.14
$7.5 < p_T < 8$	0.236 ± 0.030	12.0/21	0.94	0.98	7.75 ± 0.14
$8 < p_T < 8.5$	0.258 ± 0.032	21.1/22	0.52	1	8.26 ± 0.14
$8.5 < p_T < 9$	0.291 ± 0.030	20.5/24	0.67	1	8.77 ± 0.14
$9 < p_T < 9.5$	0.268 ± 0.025	20.3/26	0.78	0.99	9.25 ± 0.15
$9.5 < p_T < 10$	0.320 ± 0.026	37.3/27	0.09	0.97	9.75 ± 0.14
$10 < p_T < 11$	0.321 ± 0.018	26.7/35	0.84	0.94	10.49 ± 0.29
$11 < p_T < 12$	0.327 ± 0.019	49.0/33	0.04	1	11.48 ± 0.29
$12 < p_T < 14$	0.359 ± 0.017	39.7/36	0.31	0.69	12.93 ± 0.57
$14 < p_T < 16$	0.406 ± 0.024	33.0/32	0.42	1	14.91 ± 0.58
$16 < p_T < 18$	0.443 ± 0.030	36.1/29	0.17	0.84	16.92 ± 0.57
$18 < p_T < 22$	0.479 ± 0.030	30.8/27	0.28	1	19.70 ± 1.13
$22 < p_T < 30$	0.538 ± 0.039	26.2/24	0.34	0.40	25.05 ± 2.24
$30 < p_T < 70$	0.663 ± 0.059	21.4/17	0.21	0.41	37.74 ± 7.34

Table .19. Non-prompt fraction measurement for the $0.75 \leq |y| < 1.5$ bin

p_T (J/ψ) (GeV)	Non-prompt fraction	χ^2/ndof	χ^2 p-value	Kolmogorov	Mean p_T
$4 < p_T < 5$	0.142 ± 0.094	21.3/18	0.26	1	4.68 ± 0.25
$5 < p_T < 5.5$	0.183 ± 0.049	24.5/23	0.38	0.26	5.28 ± 0.14
$5.5 < p_T < 6$	0.127 ± 0.038	24.0/26	0.57	0.87	5.76 ± 0.14
$6 < p_T < 6.5$	0.188 ± 0.033	26.3/27	0.50	0.40	6.26 ± 0.14
$6.5 < p_T < 7$	0.261 ± 0.029	27.3/31	0.66	0.98	6.77 ± 0.14
$7 < p_T < 7.5$	0.230 ± 0.025	14.4/31	0.99	1	7.25 ± 0.14
$7.5 < p_T < 8$	0.238 ± 0.023	39.9/34	0.22	0.87	7.75 ± 0.14
$8 < p_T < 8.5$	0.226 ± 0.022	53.4/33	0.01	0.72	8.24 ± 0.14
$8.5 < p_T < 9$	0.226 ± 0.021	35.2/36	0.50	0.94	8.75 ± 0.14
$9 < p_T < 9.5$	0.261 ± 0.021	42.7/36	0.20	1	9.25 ± 0.14
$9.5 < p_T < 10$	0.292 ± 0.023	29.3/33	0.65	0.93	9.75 ± 0.15
$10 < p_T < 11$	0.315 ± 0.016	41.6/41	0.44	1	10.47 ± 0.29
$11 < p_T < 12$	0.343 ± 0.018	30.9/37	0.84	0.75	11.48 ± 0.28
$12 < p_T < 14$	0.352 ± 0.016	41.8/41	0.44	0.53	12.90 ± 0.57
$14 < p_T < 16$	0.402 ± 0.022	34.2/33	0.41	0.89	14.90 ± 0.56
$16 < p_T < 18$	0.450 ± 0.031	22.3/30	0.84	1	16.88 ± 0.58
$18 < p_T < 22$	0.477 ± 0.031	23.1/28	0.73	1	19.71 ± 1.10
$22 < p_T < 30$	0.541 ± 0.042	25.1/24	0.40	1	25.15 ± 2.16
$30 < p_T < 70$	0.595 ± 0.060	13.8/15	0.54	0.97	37.81 ± 7.95

Table .20. Non-prompt fraction measurement for the $1.5 \leq |y| < 2.0$ bin

p_T (J/ψ) (GeV)	Non-prompt fraction	χ^2/ndof	χ^2 p-value	Kolmogorov	Mean p_T
$1 < p_T < 4$	0.103 ± 0.053	22.1/26	0.68	0.69	2.78 ± 0.86
$4 < p_T < 5$	0.211 ± 0.042	32.4/27	0.22	0.87	4.59 ± 0.26
$5 < p_T < 5.5$	0.218 ± 0.043	27.9/24	0.26	1	5.27 ± 0.15
$5.5 < p_T < 6$	0.170 ± 0.034	26.1/26	0.46	0.98	5.75 ± 0.14
$6 < p_T < 6.5$	0.180 ± 0.034	34.0/28	0.20	0.97	6.26 ± 0.14
$6.5 < p_T < 7$	0.222 ± 0.028	30.9/31	0.47	1	6.76 ± 0.14
$7 < p_T < 7.5$	0.195 ± 0.025	31.5/33	0.54	1	7.26 ± 0.14
$7.5 < p_T < 8$	0.210 ± 0.024	27.1/37	0.88	0.94	7.75 ± 0.14
$8 < p_T < 8.5$	0.216 ± 0.022	31.8/37	0.71	1	8.25 ± 0.14
$8.5 < p_T < 9$	0.264 ± 0.023	32.0/35	0.61	1	8.75 ± 0.14
$9 < p_T < 9.5$	0.287 ± 0.026	21.0/32	0.93	1	9.25 ± 0.14
$9.5 < p_T < 10$	0.297 ± 0.028	20.9/30	0.89	1	9.74 ± 0.15
$10 < p_T < 11$	0.335 ± 0.019	30.5/38	0.80	1	10.47 ± 0.29
$11 < p_T < 12$	0.326 ± 0.026	37.7/34	0.30	0.93	11.48 ± 0.29
$12 < p_T < 14$	0.358 ± 0.022	31.4/38	0.77	1	12.89 ± 0.58
$14 < p_T < 16$	0.420 ± 0.029	26.9/29	0.58	1	14.90 ± 0.58
$16 < p_T < 18$	0.516 ± 0.038	19.5/25	0.77	1	16.93 ± 0.57
$18 < p_T < 22$	0.468 ± 0.038	30.7/24	0.16	0.97	19.67 ± 1.13
$22 < p_T < 30$	0.604 ± 0.058	14.9/20	0.78	0.97	24.88 ± 2.20

Table .21. Non-prompt fraction measurement for the $2.0 \leq |y| < 2.4$ bin

p_T (J/ψ) (GeV)	Non-prompt fraction	χ^2/ndof	χ^2 p-value	Kolmogorov	Mean p_T
$1 < p_T < 5$	0.098 ± 0.065	57.7/26	0.0003	0.87	3.59 ± 1.25
$5 < p_T < 6$	0.217 ± 0.077	21.1/23	0.57	0.94	5.53 ± 0.29
$6 < p_T < 7$	0.289 ± 0.047	30.8/25	0.20	0.38	6.55 ± 0.28
$7 < p_T < 7.5$	0.125 ± 0.035	29.0/24	0.21	1	7.25 ± 0.14
$7.5 < p_T < 8$	0.231 ± 0.037	24.6/27	0.59	1	7.75 ± 0.14
$8 < p_T < 8.5$	0.209 ± 0.042	20.1/24	0.69	0.99	8.25 ± 0.14
$8.5 < p_T < 9$	0.183 ± 0.041	15.4/24	0.91	0.95	8.74 ± 0.14
$9 < p_T < 9.5$	0.268 ± 0.037	23.0/25	0.58	0.99	9.24 ± 0.14
$9.5 < p_T < 10$	0.249 ± 0.045	9.9/22	0.99	1	9.73 ± 0.15
$10 < p_T < 11$	0.269 ± 0.037	33.5/29	0.26	0.97	10.49 ± 0.28
$11 < p_T < 12$	0.297 ± 0.034	20.9/26	0.75	0.92	11.47 ± 0.29
$12 < p_T < 14$	0.353 ± 0.034	29.1/29	0.46	1	12.87 ± 0.57
$14 < p_T < 18$	0.348 ± 0.044	28.6/28	0.43	1	15.59 ± 1.12
$18 < p_T < 30$	0.419 ± 0.058	19.9/21	0.53	0.84	21.74 ± 3.00

.5 Systematic Uncertainties Assessment

Additional information on systematic uncertainties calculation discussed in section 4.5.4.

.5.1 Spin-Alignment

The different spin-alignments in the numerator and denominator of the non-prompt-to-prompt fraction are imposed as follows. For each $p_T - y$ bin, the average acceptance is weighted by a factor w, where w is the ratio of the average acceptance for a FLAT spin-alignment to the average acceptance for another spin-alignment model. This is repeated for each spin-alignment scenario, and the prompt to non-prompt fraction is recalculated in each case. The revised fraction f' is given by

$$f' = \frac{1}{1 + w \times \frac{N_{prompt}}{N_{nonprompt}}}, \tag{.2}$$

where

$$\frac{N_{prompt}}{N_{nonprompt}} = \frac{1}{f} - 1. \tag{.3}$$

Here f is the prompt to non-prompt fraction with both numerator and denominator assuming the same spin-alignment. It can be trivially seen that $f = f'$ if $w = 1$.

Additional Information on Average B Lifetime Measurement

.6 Fit Results: Covariance Matrix

In Table .22 in Appendix .6 the complete covariance matrix is provided.

Table .22. Correlation matrix of the parameters from the mass and lifetime simultaneous fit.

parameters	global	A	B	C	D	E	F	G	H	I	J	K	L	M	N
A: f_{bkg}	0.48190	1.000	-0.126	-0.047	-0.075	-0.083	0.315	-0.087	-0.009	-0.157	-0.012	-0.027	-0.013	-0.023	-0.020
B: $f_{B,bkg}$	0.69497	-0.126	1.000	0.549	-0.091	0.053	-0.148	0.039	0.002	0.051	0.499	-0.050	-0.499	-0.004	0.023
C: b_1	0.68271	-0.047	0.549	1.000	0.042	0.006	-0.031	0.009	0.003	0.016	0.477	0.177	-0.529	-0.067	-0.002
D: f_B	0.28739	-0.075	-0.091	0.042	1.000	-0.008	-0.010	0.004	0.003	0.020	-0.027	0.048	-0.011	-0.146	-0.192
E: α	0.86897	-0.083	0.053	0.006	-0.008	1.000	-0.783	0.030	-0.344	0.422	-0.012	0.007	0.000	-0.006	-0.001
F: n	0.85644	0.315	-0.148	-0.031	-0.010	-0.783	1.000	-0.145	0.160	-0.198	0.016	-0.028	-0.001	0.008	0.001
G: $C_1(m_{\mu\mu})$	0.20378	-0.087	0.039	0.009	0.004	0.030	-0.145	1.000	-0.023	-0.029	-0.002	0.006	0.000	-0.001	0.002
H: $m_{\mu\mu}$	0.40042	-0.009	0.002	0.003	0.003	-0.344	0.160	-0.023	1.000	-0.265	-0.003	0.009	-0.001	-0.003	-0.006
I: S_m	0.53433	-0.157	0.051	0.016	0.020	0.422	-0.198	-0.029	-0.265	1.000	0.015	0.013	0.004	0.013	0.002
J: S_{bkg}	0.58339	-0.012	0.499	0.477	-0.027	-0.012	0.016	-0.002	-0.003	0.015	1.000	0.023	-0.345	0.131	0.014
K: $\tau_{eff\,1}$	0.32974	-0.027	-0.050	0.177	0.048	0.007	-0.028	0.006	0.009	0.013	0.023	1.000	-0.063	-0.025	-0.206
L: $\tau_{eff\,2}$	0.59306	-0.013	-0.499	-0.529	-0.011	0.000	-0.001	0.000	-0.001	0.004	-0.345	-0.063	1.000	0.048	0.001
M: S_t	0.25272	-0.023	-0.004	-0.067	-0.146	-0.006	0.008	-0.001	-0.003	0.013	0.131	-0.025	0.048	1.000	0.085
N: τ_B	0.28867	-0.020	0.023	-0.002	-0.192	-0.001	0.001	0.002	-0.006	0.002	0.014	-0.206	0.001	0.085	1.000